1996

Friction and wear of nanocrystalline materials and nanolaminated composites.

Zoheir N. Farhat
University of Windsor

Recommended Citation

Farhat, Zoheir N., "Friction and wear of nanocrystalline materials and nanolaminated composites." (1996). *Electronic Theses and Dissertations.* Paper 2161.

INFORMATION TO USERS

This manuscript has been reproduced from the microfilm master. UMI films the text directly from the original or copy submitted. Thus, some thesis and dissertation copies are in typewriter face, while others may be from any type of computer printer.

The quality of this reproduction is dependent upon the quality of the copy submitted. Broken or indistinct print, colored or poor quality illustrations and photographs, print bleedthrough, substandard margins, and improper alignment can adversely affect reproduction.

In the unlikely event that the author did not send UMI a complete manuscript and there are missing pages, these will be noted. Also, if unauthorized copyright material had to be removed, a note will indicate the deletion.

Oversize materials (e.g., maps, drawings, charts) are reproduced by sectioning the original, beginning at the upper left-hand corner and continuing from left to right in equal sections with small overlaps. Each original is also photographed in one exposure and is included in reduced form at the back of the book.

Photographs included in the original manuscript have been reproduced xerographically in this copy. Higher quality 6" x 9" black and white photographic prints are available for any photographs or illustrations appearing in this copy for an additional charge. Contact UMI directly to order.

UMI

A Bell & Howell Information Company
300 North Zeeb Road, Ann Arbor MI 48106-1346 USA
313/761-4700 800/521-0600

FRICTION AND WEAR OF NANOCRYSTALLINE MATERIALS AND NANOLAMINATED COMPOSITES

by

Zoheir N. Farhat

A Dissertation
Submitted to the Faculty of Graduate Studies and
Research Through the Engineering Materials
Program of the Department of Mechanical
Engineering in Partial Fulfilment of the
Requirements for the Degree of
Doctor of Philosophy at the
University of Windsor

Windsor, Ontario, Canada

1996

0-612-30282-2

ABSTRACT

In the search of new wear resistant coatings for applications such as cutting tools and turbine refurbishing, a wide range of coatings, belonging to emerging classes of materials, namely, nanocrystalline materials and nanolayered composites, have been produced and tested. These coatings were produced using an rf magnetron sputtering system and include monolithic nanocrystalline metals (Al,Ti,Cu), nanolaminated composites composed of alternating layers of metal/ceramic (Al/Al_2O_3, Ti/TiN) and metal/metal (Ti/Cu). The metal layer thickness in the as-sputtered films of Al/Al_2O_3 ranged from 70 to 500 nm, and 150 to 450 nm in Ti/TiN. The nonmetals (Al_2O_3 ,TiN) layer thicknesses ranged from 10 to 40 nm and total film thicknesses of 10-15 μm. As-sputtered nanocrystalline aluminum films with an average grain size of 16.4 nm were isothermally annealed at 573 K to increase the grain size up to 98.0. nm.

All materials were characterized and tested for their tribological properties. Friction and wear tests were performed under unlubricated sliding conditions using pin-on-disc type tribometer which was designed and constructed for measuring wear rates and coefficients of friction of thin films in air and in vacuum. The coefficient of friction of the materials tested against the stainless steel pin varied with the sliding distance. At the early stages of sliding the coefficient of friction rose to a peak, followed by a decrease to a steady-state value. The transition to the steady-state in the friction curve corresponded to a transition from severe wear to

mild wear. These were discussed in terms of work hardening, texture evolution and roughness of worn surface in monolithic materials.

In aluminum the value of the peak coefficient of friction decreased from μ_p=1.4 for a coarse grain size of 10^6nm to μ_p=0.6 for a grain size of 16.4 nm when tested under ambient conditions. The coefficient of friction of nanocrystalline aluminum showed a 30% increase when tested in vacuum (10^{-6} torr). Within the grain size range of 15-100 nm, the wear rates were found to be linearly dependent on the square root of the grain size ($W_s = 8.5 \times 10^{-4} + (2.44 \times 10^{-4})\ .\ D^{1/2}$ for severe wear and $W_m = -1.9 \times 10^{-4} + (5.1 \times 10^{-5})\ .\ D^{1/2}$ for mild wear). The peak value of the coefficient of friction decreased about 70% in Al/Al_2O_3 (with 200 nm Al layer thickness) while a 60% improvement in the steady-state coefficient of friction was measured in Ti/TiN (with 150 nm Ti layer thickness) in comparison to the as-sputtered monolithic aluminum and titanium films, respectively. An increase in wear resistance with decreasing layer thickness was also observed (for example, $W_s = 7.0 \times 10^{-5} + (2.9 \times 10^{-7})\ .\ \lambda^{0.5}_{Ti}$).

Mechanical properties (hardness and elastic moduli) of the films were measured using an ultra-microindentation system. Hardness measurement of nanocrystalline aluminum revealed that within the grain size range 15-100 nm the hardness-grain size data obeys a Hall-Petch type relationship (i.e., $H = 34$ [MPa] $+ 0.21$ [MPa . $m^{0.5}$] $D^{-0.5}$ [$m^{-0.5}$]). The hardness of Al/Al_2O_3 and Ti/TiN could also be described in the formalism of the Hall-Petch type indicating that ceramic layers

inhibit slip transfer across metallic layers.

Recommendations are made, based on a proposed modified Archrad's law which directly relates wear rate to structure refinement, on future directions for producing improved wear resistant coatings.

ACKNOWLEDGMENTS

The author wishes to express his sincere gratitude to his advisors Dr. A. Alpas and Dr. D. Northwood, who were a constant source of inspiration throughout this work. Their friendship, guidance, supervision and encouragement are deeply appreciated.

Greatest thanks go to Dr. S. A. Hackney for reviewing this dissertation and for his informative remarks on it. I am also grateful to Dr. W. Youdelis, Dr. D. Watt and Dr. A. Asfour for their critical review and helpful comments on this dissertation.

Acknowledgments are extended to Dr. Y. Ding for his help in the fabrication of the coatings. I would like to thank Mr. J. Robinson for his technical assistance and Mrs. B. Denomey for all the help she provided the author during his entire studies at the University of Windsor.

Last but not least, I would like to express my deepest appreciation to all my family for their patience, support and encouragement throughout the years of my education. Sincere thanks go to my parents, my wife, my daughter, Iman, and my son, Nureddin.

CONTENTS

LIST OF FIGURES

Chapter 2

Chapter 3

Chapter 4

Chapter 5

CHAPTER 1

INTRODUCTION

Recent advances in materials processing have made it possible to fabricate materials in which the scale of structure is of the order of 5-500 nm. These production techniques include rapid solidification, vapour deposition and sputtering. The study of the mechanical properties of these materials is important to delineate the validity of Hall-Petch relation (i.e., $\sigma_y = \sigma_o + kD^{-0.5}$, where σ_y is the yield stress, σ_o is the lattice frictional stress, k is a constant representing the measure of strength of a barrier to dislocation motion and D is the grain size) to extremely fine structures and to explore the upper limit of strengthening that can be achieved by microstructural refinement. An important aspect of strengthening by microstructural refinement is that the strength increase need not be on the expense of the loss of ductility.

On the other hand, ceramic coatings such as carbides, nitrides and oxides have been studied for many years because of their high hardness and resistance to wear and corrosion. Titanium nitride, in particular, has received considerable attention as a wear resistant coating. Surface coatings incorporating alternating layers of metallic and ceramic phases can present an alternative to the monolithic materials because of the high strength levels attainable and because they combine superior wear resistance compared to monolithic metal films, and high toughness compared to ceramic coatings.

Because nanoscale materials have been synthesized only recently their strengthening mechanisms are not well known, for example, the applicability of the Hall-Petch relationship is a subject of controversy. However, despite these complexities in, and the lack of full understanding of, the mechanical behaviour, it is important to initiate studies on the friction and wear characteristics of nanocrystalline and nanolayered structures because of the perceived potential engineering applications of these materials as tribological surface coatings. It can be expected that microstructural refinement should lead to an improvement in the wear resistance according to Archard's law of wear, i.e., $W=KF_N/H$, where W is the volume worn per unit sliding distance, F_N is the applied load, H is the hardness of the softer of the materials in contact and K is the wear coefficient. Experimental data relating wear resistance and coefficient of friction to grain size and interlayer spacing is almost non-existent in the open literature.

Depending on the applied load, speed, geometry of contact, environmental conditions and properties of the materials in contact, friction and wear may proceed by a number of mechanisms. These mechanisms include abrasion, adhesion and delamination and can act individually or in concert. Friction and wear are dynamic processes and transitions in their behaviour from one mechanism to another can be understood in terms of microstructural and crystallographic changes occurring at the contact surface.

In this work, mechanical and tribological properties of nanocrystals and nanolayered composites were studied in order to identify strengthening and wear mechanisms which operate in nanocrystalline materials and nanolaminated composites. Thereby exploiting the wear controlling parameters which could be used to develop new and improved materials for potential wear resistant surface coating applications.

This study was focused on two types of materials, namely: i) nanocrystalline aluminum films with grain size range 15-100 nm; ii) nanolaminated Al/Al_2O_3, Ti/TiN and Ti/Cu composites consisting of nanocrystalline metallic layers. The deformation, friction and wear characteristics under unlubricated sliding conditions of these materials were investigated for the first time and compared to those of the more conventional materials. Transitions in the coefficient of friction and wear as a function of sliding distance were related to the development of crystallographic textures and changes in work hardening and surface topography during wear.

The dissertation is divided to six chapters. This introduction is followed by a literature survey (Chapter 2) which gives a review of the recent literature on nanocrystalline materials and nanolaminated composites. This is followed by a review of friction and wear mechanisms and transitions. Chapter 3 covers the experimental methodology used for the production, characterization, and testing of mechanical and tribological properties. Presentation of results and their analysis were given in Chapter 4. Chapter 5 is the discussion: in this chapter an attempt is made to relate all the results in order to develop a general explanation of friction and wear behaviour of nanocrystalline materials and nanolaminated composites. The final chapter (Chapter 6) summarizes the main conclusions and also gives a summary of original contributions to the field made by this dissertation. Recommendations for future work is given at the end of the chapter

CHAPTER 2

LITERATURE REVIEW

2.1. Nanocrystalline Materials

In recent years, nanocrystalline materials have been the subject of intensive research. These materials are polycrystalline in nature, but have an ultra-fine grain size in the order of 1-100 nm. In such materials the volume fraction of the grain boundaries becomes comparable to the volume fraction of the crystals themselves. As many as 50% of the atoms are located at grain or interfacial boundaries. Due to this large volume fraction of grain boundaries, and the very small grain size of these materials, they exhibit different properties than conventional engineering alloys (1-5).

Nanocrystalline materials can be synthesized by various techniques. In principle, any method capable of producing fine grained materials can be utilized to produce nanoscale materials. These methods include gas-condensation (6), electron beam vapour deposition (7), chemical vapour deposition (8), mechanical alloying (9), molecular beam epitaxy (10) and rapid solidification (11).

Many experimental studies have indicated that a considerable increase in the strength and hardness of metals can be obtained by refining the grain size to nanometre scale. For example, Hughes et al (12) found an increase from 0.9 to 6.9 GPa in the hardness of electrodeposited nickel when the grain size was decreased from 10^4 to 12 nm. Grain sizes of electrodeposited nickel tested were in the as-deposited condition, that is, the crystallite size was varied during the electrodeposition process by varying deposition parameters. Grain size measurements were estimated from counts including both twin and large angle grain boundaries by the mean linear intercept method on optical, scanning, and for the smallest grain size, transmission electron microscopes. Hardness has been found to follow a Hall-Petch relationship down to the smallest grain size.

Similarly, Nieman and Weertman (13) observed an increase from 0.5 to 1.2 GPa in the hardness of nanocrystalline copper when reducing the grain size from 5×10^5 to 25 nm. Furthermore, they found a four fold increase in the hardness of palladium, an increase from 0.7 to 3.1 GPa as the grain size decreases from 100 μm to 5 nm. The palladium and copper were produced by an inert-gas condensation method which is capable of producing small crystallites with a narrow crystal size distribution. This process involves evaporation of material in a high purity noble gas atmosphere followed by condensation. The mean grain size was controlled by the evaporation temperature and the inert-gas pressure. Palladium and copper powders were then compacted in a vacuum of approximately 10^{-6} Pa using uniaxial pressure of 1.4 GPa to form 9 mm diameter discs approximately 300 µm thick. Density measurements on the compacted nanocrystalline palladium discs indicated that the density ranged from 82-96 % of a coarse-grained standard. The grain sizes were varied by annealing in vacuum (0.13 Pa) for 100 minutes in the temperature range 100-1000 °C. The crystallite size was determined by an X-ray-line-broadening method. Vickers hardness measurements (using a 100 g load) was found to obey the Hall-Petch behaviour in the nanocrystalline grain size range. However the slope of the hardness versus $D^{-0.5}$ for palladium was two times smaller than that observed in the coarse-grained range. The Vickers hardness (VH) in both ranges was expressed as: $VH=1030$ MPa + 0.19 ($MPa.m^{0.5}$) $D^{-0.5}$ in the coarse-grained range, while $VH=2236$ MPa + 0.08 ($MPa.m^{0.5}$) $D^{-0.5}$ in the nanocrystalline grain size range.

Jang and Koch (14) have recently studied the hardness as a function of grain size for nanocrystalline iron synthesized by a ball milling method. Initially an iron powder with a 99.5% purity was screened to <45 μm size. Mechanical milling was then carried out in a mill using martensitic stainless steel balls in an argon atmosphere. After milling for 100 hours, the oxygen and nitrogen content of the fine iron powder were 3.5 and 1.8 at%, respectively. The grain size was varied by varying the milling time and was estimated by an X-ray-line-broadening method. Microstructural evolution during milling was monitored by a transmission electron microscope (TEM). Specimens for the TEM were prepared by making powder pellet compacts. TEM examination revealed that a random nanocrystalline structure had evolved from dislocation cell structures within the shear bands. After only 0.5

hours of milling a fine dislocation cell structure was observed with an average cell diameter of about 25 nm and after 2 hours the cell dimension was 10 nm. Vickers microhardness with a 25 g load was used on metallographically mounted individual powder particles. Hardness was observed to increase dramatically with reducing grain size, i.e., about a factor of 5 from grain size of $3x10^3$ to 6 nm. It was shown that the hardness of nanocrystalline iron followed a Hall-Petch relationship but with a flatter slope than that measured in the conventional grain size range.

Valiev et al (15), produced a submicron grained Al-1.5%Mg alloy by a high plastic torsional straining at a low strain rate (10^{-4} s^{-1}), and simultaneously applying a pressure of 4 GPa to a true strain of 7. The specimens were then annealed for 30 minutes at various temperatures (from 323 to 673 K) to obtain a variety of grain sizes. TEM investigation showed a structure of granular type and equiaxed grains having a mean grain size of 150 nm. This structure was reported to be "fairly uniform" along the entire sample. Grain growth occurred only during the annealing at 393 K and higher and the structure remained unchanged. Nevertheless, specimens annealed at 393 K or higher temperatures revealed few dislocations inside the grains. Vickers microhardness measurements performed using 50 g load showed an increase from 0.4 GPa to 1.6 GPa as the grain size was reduced from $1.3x10^4$ to 150 nm and obeyed the Hall-Petch relationship. However annealing between 373 to 393 K did not effect the grain size while the hardness decreased:

This caused a break-down in the Hall-Petch behaviour. Based on these observations, it was suggested that the strength and hardness of ultra-fine grain size materials may be dependent not only on the grain size, but other structural parameters such as the substructure of grain interiors (such as subgrains) which might influence the Hall-Petch strength even without a change in the grain size.

Mechanical behaviour of a nanocrystalline $(Fe_{0.99}Mo_{0.01})_{78}Si_9B_{13}$ alloy was investigated by Liu et al (16). The raw material was in the form of amorphous ribbon 30-50 mm wide and about 25 μm thick. Calorimetric measurements performed in a differential scanning calorimeter (DSC) revealed two crystallization reactions at 841 and 858 K. Nanocrystallites were produced by isothermal annealing of the amorphous ribbon in argon atmosphere. The annealing temperatures were between 753 to 1023 K and an annealing time of 1 hour was used. X-ray diffraction confirmed the precipitation of many metastable phases such as $(Fe,Mo)_3B$, $(Fe,Mo)_{23}B$ and $(Fe,Mo)_3Si$ with increasing annealing temperature which were subsequently transformed to two stable phases (α-Fe and Fe_2B). Due to the existence of many overlapping peaks from many phases, α-Fe(Si,Mo) phase grain size was selected as a representative of the average grain size of the whole specimen. TEM observation of the annealed specimen (at 833 K) showed a homogenous distribution of precipitate particles. The hardness increased from 6.3 to 10 GPa as the grain size of the precipitates decreased from 200 to 45 nm in agreement with Hall-Petch relationship. However, below 45 nm precipitate size softening occurred with decreasing grain size down to 15 nm. Liu et al (16) suggested that the reason why the Hall-Petch breaks-down below 45 nm was because the precipitation process was still taking place. An increase in the number of precipitates with annealing temperature (up to 893 K) increased the hardness. Above 45 nm, the precipitation process was completed and grain growth started to take effect on hardness as predicted by the Hall-Petch relationship.

Chokshi et al (2) examined the validity of the Hall-Petch relationship in pure nanocrystalline copper and palladium prepared by the inert-gas condensation method. Copper and palladium were evaporated in high purity helium (about 0.1-1 KPa pressure). The evaporated metal condensate in the form of nanometre sized crystals which accumulated at a surface of a cold finger in a powder form. Crystals were then scraped off the cold finger and consolidated (pressure of 5 GPa) into a dense polycrystalline material with an average grain size of 5 to 10 nm depending on the pressure and the evaporation rate. The grain size was then varied by subsequent annealing of the nanocrystals. Grain size determination was performed using an X-ray-line broadening method. The hardness was measured using a Vickers indenter and a load of 200 g. Chokshi et al (2) found that in the nanocrystalline grain size range (5-15 nm) both copper and palladium exhibited a negative Hall-Petch slope. This resulted in a clear contradiction with the experimental observations reported by Nieman and Weertman (13) for copper and palladium produced by the same method. Chokshi et al (2) suggested that the decrease in strength with decrease in grain size for nanocrystalline materials occurred as a result of a rapid diffusional creep and grain boundary sliding. The fine grain size and high diffusivity observed in nanocrystalline materials suggested that considerable creep deformation could occur even at room temperature. This was attributed to Coble's creep model, which states that the creep rate is proportional to D_b^{diff}/D^3, where D_b^{diff} is the grain boundary diffusivity and D is the grain size diameter.

Lu et al (17) have synthesized Ni-P alloy from an amorphous $Ni_{80}P_{20}$ (at%) alloy by crystallization at different annealing temperatures. TEM observations revealed that amorphous alloy specimens were completely crystallized during the annealing (annealing temperature ranged from 300 to 400° C) and no amorphous regions were detected. The sizes of the crystallized nanocrystalline Ni_3P grains were determined by means of TEM observation and X-ray diffraction line-broadening method. The grain size was found to remain unchanged at a grain size of 7.5 nm up to an annealing temperature of 330° C. Annealing at higher temperatures increased the grain size. Microhardness measurements showed that amorphous Ni-P alloy had 40% lower hardness (6.5 GPa) than nanocrystalline Ni-P alloy (10.4 GPa) with the same composition. A Hall-Petch plot of the hardness as a function of Ni_3P grain size over a range of grain sizes from 9 to 120 nm showed a softening of the material as the grain size was reduced. SEM observation of the fractured surface of amorphous Ni-P alloy showed evidence for a ductile behaviour while the fractured surface of crystallized Ni-P alloy revealed that brittle fracture had taken place. The extent of plastic deformation was found to diminish with increasing grain size, i.e., as the grain size increased the material became progressively more brittle. This behaviour was used to explain the break-down of the Hall-Petch relation, i.e., the specimen with smaller grain size had lower resistance to plastic deformation (smaller microhardness value than coarse-grained specimen).

A plateau was observed in hardness versus grain size curves for electrodeposited nanocrystalline nickel (99.9%) which was electroplated onto a titanium substrate to a thickness of 0.3 mm (18). Experimental parameters were adjusted to produce a series of nickel films with a grain size range 10-100 nm. TEM was used for grain size determination which showed a uniform structure with fairly narrow grain size distribution and no evidence of porosity. Vickers hardness measurements were performed using a 100 g load. Below 20 nm grain size a deviation from the regular Hall-Petch behaviour was observed down to 11 nm grain size. This behaviour was attributed to a triple line disclination effect, i.e., the increase in the triple junction volume fraction leading to softening of the material.

Moreover, the type of processing method used for varying the grain size, such as heat treatment (19) as well as presence of imperfections such as triple junctions (20-21) or porosity (22) have been cited among the possible causes for the observed inverse Hall-Petch behaviour. For example, Fougere et al (19) compared the hardness data for copper and palladium prepared by the inert-gas condensation method in which the nanocrystalline grain size (10-40 nm) was varied in the as-prepared condition with those in which grain size was varied by subsequent annealing. Annealing was carried out in an argon gas atmosphere at 0.315 T_m (423 K for Cu and 569 K for Pd) for up to 10 hours for copper and 9 hours for palladium. Fougere et al (19) found that the annealed copper and palladium specimens exhibited an increase in hardness with increasing annealing time (i.e., increasing grain size) due to neck development during early stages of sintering of consolidated powder. On the other hand, copper and palladium specimens in the as prepared form in the same grain size range show an increase in hardness with decreasing gain size in agreement with Hall-Petch relationship. Fougere et al (19) concluded that hardening and softening of nanocrystalline materials could depend upon the method used to vary the grain size.

An important aspect of strengthening by microstructural refinement is that the strength increase does not occur at the expense of the ductility. Fan (23) recently proposed that the plane strain fracture toughness, K_{IC}, of metals and alloys were inversely dependent on grain size. This means that reducing the grain size increases both strength and ductility. Experimental evidence for increased ductility in ceramics had been reviewed by Siegel (24) and Karch et al (3). They propose that reducing the grain size (D) of ceramics to the nanocrystalline range will increase grain boundary diffusivity (D^{diff}_b). This translated to an increase in the diffusional creep rate (ϵ) by a factor of 10^{12} (i.e., $\epsilon \propto D^{diff}_b/D^3$). Karch et al (3) examined the deformation of nanocrystalline specimens of CaF_2 and TiO_2 ceramics having an average grain size of about 8 nm. Bending tests performed on nanocrystalline CaF_2 and TiO_2 revealed enhanced ductility over coarse-grained ceramics.

In summary, the mechanical properties of nanocrystalline material have been investigated by many researchers in recent years. These materials were produced by a wide range of methods, such as inert-gas condensation, electroplating, ball milling and by crystallization from amorphous martials. Nanocrystals with a broad range of grain sizes were obtained either by varying the fabrication parameters during the production stage or by isothermal annealing of the as-prepared nanocrystalline specimens. Hardness measurements performed on these materials have led to a controversy over the applicability of the Hall-Petch relationship. Tables 2.1 and 2.2 summarize the Hall-Petch and the "inverse" Hall-Petch parameters for nanocrystalline materials. Many interpretations of why a particular type of softening or hardening behaviour occurs in nanocrystalline materials were given, but, a generally accepted theory is yet to be developed. A possible reason for the controversy over the applicability of nanocrystalline materials in the literature is that the grain size (or range of grain sizes) at which softening commences is not well defined and this depends on factors such as the type of material tested and the preparation method used. Published literature does not present sufficient hardness data below 10 nm grain size where the softening behaviour was often reported to occur. In such a fine grain size only few number of dislocations can be accommodated, therefore, dislocations may play a limited role in deformation compared to the coarse-grained crystals. A better understanding of the deformation process in nanoscale materials should involve a closer investigation of the grain boundary structure and how they behave during deformation. In the following section, theories on the grain boundary controlled deformation processes are reviewed.

2.1.1. The Hall-Petch Theory

The study of the methods that can provide an increase in strength of materials had been a subject of interest for many years. The Hall-Petch (25,26) relationship proposes that the yield strength is proportional to $D^{-1/2}$, where D is the characteristic microstructural parameter such as the grain diameter, the subgrain diameter and/or thickness of the laminae. Ever since Hall and Petch introduced their well known relationship between the lower yield point of low carbon steel and grain size, a great deal of effort had been devoted to explain it from a fundamental point of view (27-35) and to apply it to different metals and alloy systems (36-45).

The Hall-Petch equation has the following form

$$\sigma_y = \sigma_o + kD^{-0.5} \qquad 2.1$$

where σ_y is the yield stress, σ_o is the lattice frictional stress required to move dislocations in the absence of an obstacle (i.e., grain boundary), k is a constant representing the measure of strength of a barrier to dislocation motion and D is the grain size. The basic idea behind the original Hall-Petch model was that a dislocation pile-up can burst through a grain boundary due to stress concentrations at the head of the pile-up. If τ_a is the resolved shear stress applied on the slip plane, then the stress acting in the head of the pile-up containing n dislocations is $n\tau_a$. The number of dislocations in a pile-up depends on the length of the pile-up, which, in turn, is proportional to the grain diameter D. According to Eshelby et al (27),

$$n = \alpha \pi l \tau_a / Gb \qquad 2.2$$

where l is the length of the pile-up, i.e., for a pile-up with two ends (generated, for an instance, by Frank-Read source in the centre of the grain) equal to half the grain diameter D; and α is a geometrical constant equal to one for the pile-up of screw dislocations and equal to $(1-\nu)$ for edge dislocations; G is the shear modulus and b is Burgers vector. If τ_c is the critical stress required to overcome the grain boundary obstacles, the dislocations of the pile-up will be able to traverse the grain boundary if $n\tau_a=\tau_c$, then, from equation 2.2

$$\tau_c = \alpha \pi D \tau_a^2 / 2Gb \qquad 2.3$$

When the friction stress τ_o is taken into account equation 2.3 becomes,

$$\tau_a = \tau_o + kD^{-0.5} \qquad 2.4$$

where

$$k = (2Gb\tau_c / \alpha\pi)^{0.5}$$

Equation 2.4 provides a physical explanation for equation 2.1. It should be noted that equation 2.2 is valid only for a large number of dislocations.

Cottrell (28), recognizing that it was virtually impossible for dislocations to "burst" through boundaries, proposed a different mechanism for the Hall-Petch behaviour. It was assumed that the stress concentrations produced by a pile-up in one grain activated dislocation sources in the adjacent grain. A Frank-Read source at a distance r from the boundary is activated by the pile-up produced by a Frank-Read source in the adjacent grain. The propagation of yield is thought to occur as follows (28): when a dislocation source is unpinned it releases an avalanche of dislocations into its slip plane and these pile-up at the grain boundary. Their stress concentration acts with the applied stress on the dislocations of the next grain and unpins the nearest of these, so that the process is repeated in the next grain. The applied shear stress τ_a at which this yield propagates is given by

$$\tau_a = [\tau_o + \tau_c(2r/D)^{0.5}] / [1 + (2r/D)^{0.5}] \qquad 2.5$$

For yield to propagate in the manner described, it is necessary that $\tau_c > \tau_o$. For most grain sizes, where $D >> r$, equation 2.5 simplifies to

$$\tau_a = \tau_o + kD^{-0.5} \qquad 2.6$$

where $k = \tau_c\ (2r)^{0.5}$

Equation 2.6 is of the Hall-Petch form (equation 2.1).

Li (29) used a different approach to obtain the same relationship. Instead of using the concept of dislocation pile-up, he considered the grain boundary to be a source of dislocation generation. The onset of yielding in polycrystals is thought to be associated with the activation of these sources. Li (29) suggested that the grain boundary ledges generate dislocations, by "pumping" them into the grains. This increased dislocations density in regions close to the boundary. According to Li (29), the yield stress was, the stress required to move dislocations through these regions. For many metals the applied stress is related, under most conditions, to the dislocation density (ρ) by the relationship

$$\tau_a = \tau_o + Gb\rho^{0.5} \qquad 2.7$$

ρ was taken as proportional to the grain diameter D. Li (29) rationalized this as follows. The ledges "pump" dislocations into the grains. The number of dislocations generated per unit deformation was proportional to the number of ledges, or to the grain boundary surface per unit volume (S_v) assuming the same ledge density per unit area for different grain sizes, $\rho \propto S_v$. The grain boundary surface per unit volume, S_v, is inversely proportional to D. Hence, $\rho \propto 1/D$. Substituting into equation 2.7,

$$\tau_a = \tau_o + GbD^{-0.5} \qquad 2.8$$

Conrad (30) proposed a different theory, known as the work hardening theory. This theory started from the assumption that small-grain-sized specimens had a higher dislocation density than the larger-grain-sized specimens at a given value of plastic strain. The higher density generated higher internal stress. The overall stress required to move dislocation was the sum of two components: the thermal stress τ^* (short range obstacles) and the athermal stress τ_G (long range obstacles). The athermal stress can be regarded as the sum of a component independent of dislocation density, τ_{Go}, and a component that showed the increase in dislocation density, $\tau_{G\rho}$. Conrad (30) assumes that $\tau_{G\rho} = Gb\rho^{0.5}$. He also considered the effect of grain size on the average free slip distance and obtained a relationship between ρ and D,

$$\rho = \gamma / K_1bD \tag{2.9}$$

where γ is the shear strain and K_1 is a proportionality constant. Hence, Conrad obtained an equation similar to that of Hall-Petch,

$$\tau = \tau^* + \tau_{Go} + Gb(\gamma/K_1bD)^{0.5} \tag{2.10}$$

Conrad's model emphasized the motion of dislocations through the grain rather than the behaviour in the immediate vicinity of the grain boundary.

One important draw-back of the Hall-Petch equation is that it predicts an infinite yield stress at infinitely small grain size. Armstrong et al (31) have examined the dislocation pile-up model and predicted that the Hall-Petch relationship will become discontinuous for small number of dislocations in the pile-up (<50). They concluded that the Hall-Petch analysis was only valid for grain sizes greater than few microns.

Lloyd (40) examined the deformation behaviour of fine grained aluminum alloy (Al-6wt%N) (<1 μm) by conducting a series of stress-strain tests. Lloyd (40) found that at grain sizes approaching 1 μm there was little dislocation interaction within the grains and no dislocation cell formation even at large deformations. Instead, dislocations were concentrated around the grain boundaries. At large grain sizes a dislocation cell structure was formed which approached a 1 μm size after large deformations. Lloyd (40) also found that at low strains the work hardening rate was very similar for all grain sizes and a significant decrease, for small grain sizes, occur only at large strains. The large grain size specimens, even though they form a dislocation cell structure, had a lower dynamic recovery rate at large strains than very fine grain sizes. This suggested that the difference in the stress-strain behaviour between fine and large grain sizes may be better considered in terms of dislocation annihilation and rearrangement rather than the dislocation accumulation arguments of the previous models. It was clear from Lloyd's work that material with grain size ≤ 1 μm had a very high capacity for dynamic recovery, and the expected hardening due to the dislocation envelope around the grain boundary was not present. From this it was concluded that the gradient of the Hall-Petch plot decreases slowly with strain because of the more rapid decrease in the work-hardening rate as the grain size approaches 1 μm or smaller.

More recent theories have been developed in order to relate strength to grain size in the nanoscale range. It had been pointed out by Palumbo et al (20) that triple junctions form an important component of the microstructure of very small grain sizes. Palumbo et al (20) showed that the triple junction volume fraction displayed a greater grain size dependence than the grain boundary volume fraction and suggested that increasing the triple junctions volume fraction promoted softening. In their attempt to evaluate the grain size dependence of volume fraction associated with both grain boundaries and triple junctions, Palumbo et al (20) considered the regular fourteen sided tetrakaidecahedron as the grain shape, where the hexagonal face represent grain boundaries, and edges correspond to triple junctions. By considering the grain size to be represented by maximum diameter (D) of an inscribed sphere, and the intercrystalline component assumed as an outer "skin" of the tetrakaidecahedron having a thickness of $\Delta/2$, where Δ is the grain boundary thickness, the following relation was obtained for the total intercrystalline volume fraction (V_t^{ic}),

$$V_t^{ic} = 1 - [(D - \Delta) / D]^3 \qquad 2.11$$

The grain boundary component could be assumed as a hexagonal prism of thickness, $\Delta/2$, extending from the faces of the inner tetrakaidecahedron which defines the interface between perfect crystals and the interfacial "skin". This yielded the following relation for grain boundary volume fraction (V_t^{gb}),

$$V_t^{gb} = [3\Delta(D - \Delta)^2] / D^3 \qquad 2.12$$

The volume fraction associated with triple junctions (V_t^{tj}) is then given by,

$$V_t^{tj} = V_t^{ic} - V_t^{gb} \qquad 2.13$$

Equations (2.11), (2.12) and (2.13) are valid under conditions where $D > \Delta$. Thus, Palumbo et al (20) explained the negative Hall-Petch slope at very small grain sizes on the basis of increased triple junction volume fraction.

2.1.2. Nanolaminated Composites

In addition to leading to the production of monolithic nanocrystalline materials, new processing routes such as vapour deposition and sputtering also enabled laminated composites to be fabricated in which the intrinsic scale of the microstructure was extremely fine (of the order of 5 to 500 nm). Layered composite materials may offer high strength and high toughness with isotropic properties in the plane of the sheet. In view of these mechanical properties, microlaminates have been investigated in recent years to establish their structure/properties relationship.

A new type of strengthening was proposed by Koehler (46) in dealing with a fine laminated structure. The theory proposed by Koehler predicts that strengthening in multilayered structures arises from the difference of shear moduli of the constituents such that a large externally applied force is required to move dislocations from a layer with a low shear modulus into a layer with a higher modulus. Consequently, the multilayered material exhibits a resistance to plastic deformation well in excess of that predicted by the rule of mixtures.

According to Lehoczky (47,48) in the case of dislocations moving on a slip plane in a metallic layer (B) into a layer with higher elastic modulus (A) the minimum stress required for yielding (σ_y) is given by

$$\sigma_y = [f_B + f_A (E_A/E_B)] (\sigma_m + \sigma_\infty^B) \qquad 2.14$$

where

$$\sigma_m = (\mu_B/8\pi) [(\mu_A-\mu_B)/(\mu_A+\mu_B)] \qquad 2.15$$

f is the volume fractions, E is Young's modulus, σ_∞^B is the frictional stress in the B layer and μ is the shear modulus. The subscripts A and B denote the layers A and B, respectively. By following Lehoczky's analysis, Kelly (49) proposed that below a critical layer thickness, λ^C, a Frank-Read source will be restricted from operating and Koehler's strengthening is expected to occur. This critical layer thickness, λ_B^C, can be calculated using (49)

$$\lambda_B^C = 32\pi b_B [(\mu_A+\mu_B)/(\mu_A-\mu_B)] \qquad 2.16$$

where b_B is Burgers vector for layer B.

For layer thicknesses greater than those required for dislocation generation, Lehoczky (48) have extended the Koehler model to include dislocation pile-up groups. In contrast to the Hall-Petch type inverse-square-root variation commonly observed for interlaminar spacing ($\lambda^{-0.5}$) dependence of yield stress, Lehoczky predicted that above the appropriate critical layer thickness, the stress at yield for each laminate system showed a linear dependence on the inverse layer thickness (λ^{-1}). Assuming that the generation of new dislocations occurs only in B layer (i.e., $\lambda_B>\lambda_B^C$), the condition for yield in the laminate becomes,

$$\sigma_y = [f_B + f_A (E_A/E_B)]\,[(C_B\sigma_m\lambda_B^C/\lambda_B) + \sigma_\infty^B], \quad \lambda_B>\lambda_B^C\,,\ \lambda_A<\lambda_A^C \qquad 2.17$$

where C_B is a constant. The resolved tensile stress in B required for yielding (σ_y^B) is,

$$\sigma_y^B = \sigma_y\,[f_B + f_A (E_A/E_B)]^{-1} = (C_B\sigma_m\lambda_B^C/\lambda_B) + \sigma_\infty^B, \quad \lambda_B>\lambda_B^C\,,\ \lambda_A<\lambda_A^C \qquad 2.18$$

Lehoczky (47,48) had experimentally confirmed the predictions made by Koehler for the yield strength of the Al-Cu system. Aluminum and copper specimens were used to prepare Al/Cu laminates by vapour deposition in vacuum. The substrate onto which the metals were deposited was an NaCl single crystal. NaCl substrate was used because it can be dissolved in water after a specimen is mounted for tensile testing. Specimens had 10 mm gauge length and 3.2 mm width and a thickness of 2 μm. A specially designed microtensile tester was used for tensile measurements. The copper layer thickness was kept constant at 50 nm while the aluminum layer thickness was varied over a wide range of layer thickness (40-1000 nm). The grain size of aluminum was 10-20 nm and about 60 nm for copper. The strength in the Al/Cu laminate increased from 0.193 to 0.496 GPa when the aluminum layer thickness was reduced from 1000 to 232 nm. The data for the yield stress in the Al/Cu laminates shown in Figure 2.1 confirms the inverse layer thickness dependence of the yield stress predicted by equation 2.18. The critical aluminum layer thickness is about 232 nm corresponding to the minimum thickness required for Frank-Read type dislocation source operation in the aluminum layers. For aluminum layer thickness lower than 232 nm the strength level in the Al laminate remains unchanged, i.e., independent of the aluminum layer thickness, in accordance with Koehler's theory. The maximum tensile stress in the Al layer at yielding of the Al/Cu laminate calculated from equation 2.14 (i.e., $\sigma_y^{Al} = \sigma_y [f_{Al} + f_{Cu} (E_{Cu}/E_{Al})]^{-1} = \sigma_m + \sigma_\infty^{Al}$) ,0.534 GPa, was in good agreement with the measured strength of 0.496 GPa.

Springer and Catlett (50) investigated the structure and mechanical properties of Al/Al_xO_y vacuum deposited laminates. Prior to deposition of the laminates, a thin layer of CsI approximately 50 nm thick was deposited as a parting agent onto a glass slide substrate. The samples were then released from the substrate by immersing the slide in water. TEM showed the periodicity of the Al/Al_xO_y layers, however, the Al/Al_xO_y interface was smooth at layer thicknesses < 200 nm but became rough for larger spacings. Strength of the laminates was determined by performing tensile testing on the 7-10 μm thick films, which were 3 mm wide and had a gauge length of approximately 20 mm. The mechanical behaviour of the laminates was described by a Hall-Petch relationship over a range of aluminum layer thickness of 50 to 1000 nm. The ductility of the material appeared to be inversely related to the yield strength with the elongation ranging from approximately 20% to less than 0.2% for the strongest sample. However, the yield stress predicted by Koehler analysis overestimated the maximum yield stress measured experimentally. However, computations were based on the elastic modulus of pure alumina, rather than that of the nonstoichiometric oxygen deficient Al_xO_y layers which could not be measured but which were presumably lower.

Structure/property relationship in multilayered Ni/Cu and Fe/Cu composite systems were investigated by Bunshah et al (51). Multilayers of Ni/Cu and Fe/Cu composites were prepared by the evaporation of copper and nickel or of copper and iron and subsequent condensation of the vapour on a substrate. Both Ni/Cu and Fe/Cu composites were deposited on a stainless steel substrate. A 10μm thick ZrO_2 or a 0.1 μm thick CaF_2 intermediate layers were deposited on the stainless steel substrates prior to evaporation, so that after deposition the multilayers could be separated from the substrate. The layer thicknesses in each component were kept equal and varied between 88 to $5x10^4$ nm in both types of laminates. The variation in the microhardness with thickness of the laminate followed a Hall-Petch type relationship. The observed strengthening was attributed to the reduction in the distance between interfaces, i.e., between the layers that were considered to act as barriers to dislocation motion.

In another study, by Bunshah et al (52), examined a metal/ceramic laminated system (Ni/TiC). The laminate was deposition by an evaporation method to a total thickness of 250 μm. The individual layer thicknesses of Ni and TiC were varied between 0.1 to 11 μm. The yield strength of the microlaminate increased from 0.4 GPa at 11 μm thickness to 0.55 GPa at 1.4 μm. Tensile tests were also carried out at 600°C and it was found that the strength levels only decreased slightly, i.e., they were about 0.08 GPa lower than those measured at room temperature. Bunshah et al (52) concluded that Ni/TiC (metal/ceramic) composite provided high strength and good thermal stability for high temperature applications.

Yoshi et al (53) studied the influence of dislocations on the mechanical properties of multiple layer films composed of nickel and copper. Ni/Cu (having thickness between 50 and 500 nm) were prepared by evaporating high purity (99.99%) Ni and Cu on NaCl substrates. TEM and SEM observations revealed that the Ni/Cu films having thicknesses of more than 120 nm were continuous and porosity free. Those observations also showed the existence of micro-twins in very thin Ni and Cu layers which tended to disappear as the film thickness was increased. A dislocation density of about $10^{11}/cm^2$ was observed in the individual layers of the Ni/Cu laminate. When the stress in the laminate increased to a level equal to the yield strength of copper layers, dislocations in the copper layers began to move on the {111) planes. However, the stress-strain curve of the laminate showed yielding at much higher stress than that of copper. Yoshi et al (53) concluded that the Ni/Cu interface could be considered to restrict the movement of dislocations. TEM examination showed pile-ups of dislocations at the interface which were not present prior to the tensile test. This was attributed to the generation of a repulsive force due to image forces at the interface. Again SEM and TEM observations of fractured surfaces revealed that fracture might be caused by interfacial splitting due to the dislocation pile-ups. The yield strength of the Ni/Cu film were found to be independent of Cu and Ni layer thicknesses and varied from 0.6 to 0.7 GPa which were 2.5 and 5 times higher than those for monolithic nickel and copper films respectively.

Ni/Cu multilayer composites were produced by electrodeposition by Tench and White (54). They observed a great enhancement in the tensile strength in the Ni/Cu laminate when the copper layer thickness fell below 0.4 μm. The tensile strength was seen to remain constant at about 0.6 GPa down to a thickness of about 0.4 μm, and then increased sharply to 1.3 GPa for thickness in the 0.01 μm range. The tensile strength enhancement was attributed to the epitaxial growth of Cu and

Ni layers.

Metallic-glass/metal laminated composite structures had been produced, using thin ribbon (thickness=55 μm) of a melt spun $Ni_{78}Si_{10}B_{12}$ amorphous alloy (tensile strength = 2.1 GPa) and copper sheets, by Alpas and Embury (55). Layers of copper 0.07-0.15 mm thick were electrodeposited on metallic glass strips and sandwiched between annealed copper sheets. The copper/copper interfaces were diffusion bonded under a pressure of 250 MPa and temperature of 560 K. Alpas and Embury (55) found that the constraint of metallic glass layers by adjacent copper layers modified their deformation behaviour relative to that of the monolithic ribbon. The major effect of the constraint provided by the copper layers was to impede the propagation of a large number of shear bands and increase the overall ductility by facilitating the nucleation of new bands (in contrast with the behaviour of monolithic $Ni_{78}Si_{10}B_{12}$ ribbons where tensile fracture immediately followed the development of an intense shear band).

In a separate study, Alpas et al (56) investigated the mechanical properties of laminated microscale composites of Al/Al_xO_y. Laminated composites of Al/Al_xO_y were prepared in an electron beam deposition system using a pulsed-gas process. As 99.999% aluminum was evaporated onto CsI-coated glass slide, oxygen was pulsed into the vacuum system producing an oxygen-containing layer at predetermined intervals. The total film thickness was 25 μm and the aluminum layer thickness ranged from 50 to 500 nm. The aluminum oxide layer was 5 nm thick and had a composition close to Al_2O_3 but substoichiometric with respect to oxygen. Tensile tests performed on the microlaminates were found to obey a Hall-Petch type of equation. The tensile strength level obtained (for aluminum layer thickness of 50 nm) was about 0.45 GPa while that for 500 nm had a strength of 0.16 GPa. Annealing experiments indicated that these structures were stable after annealing at 450° C for 24 hrs. Tear tests performed to evaluate the fracture resistance of the laminates revealed enhanced fracture resistance with decreasing spacing between the oxide layers. These layers were resistant to cavitation during tensile tests at elevated temperatures. Alpas et al (56) summarized the deformation mechanisms of the laminated composites by constructing a deformation mechanism map.

Foecke and Lashmore (57) examined the ultimate tensile strength (UTS) of compositionally modulated alloys of electrodeposited copper and nickel. They found that the ultimate tensile strength of multilayers strongly depended on the modulation wavelength, which was defined as the thickness of a pair of film layers. Experimental results showed that the strength increased to a peak value when the wavelength was decreased to 20 nm. Below 20 nm, the strength decreased to less than the bulk hardness of nickel. The peak in the UTS versus modulation wavelength plot occurred roughly at the point where these structures were known to lose coherency and began to form interfacial misfit dislocations.

Weihs et al (58), on the other hand, examined the hardness of Cu/Cu-Zr multilayers using the rule of mixtures. A series of Cu/Zr multilayred foils were produced by magnetron sputtering deposition. A solid state amorphorization occurred, during deposition, between the copper and the zirconium layers. Differential scanning calorimeter (DSC) tests and metallographic studies revealed the transformation reaction of all the Zr and a fraction of each copper layer to amorphous Cu-Zr alloy. The hardness of Cu/Cu-Zr multilayered foils were found to increase as the volume fraction of the Cu-Zr layers increased according to a modified rule of mixtures which incorporated the Hall-Petch relationship into the rule of mixtures as follows

$$H_{\text{laminate}} = X_A * (H_A^O + K_A \lambda_A^{-0.5}) + X_B * (H_B^O + K_B \lambda_B^{-0.5}) \qquad 2.19$$

where X_A and X_B are volume fractions of A and B components, respectively.

Nanolayers of Ru/Cu and Ru/Ti were prepared by electron beam evaporation technique by Kung et al (59). One set of composites had Ru thickness varying from 25 to 250 nm alternating with Cu or Ti layers of 1.5 nm. The other set had 25 nm thick Ru layers and the Cu or Ti layers thickness varied between 1.5 and 20 nm. TEM observations of the microstructure of Ru/Cu composite showed that the layers exhibited more waviness as the deposition process proceeded which was seen by the gradual change in layer morphology from planer to wavy away from the substrate. On the other hand, Ru/Ti composite possessed a more uniform layer geometry. In addition to the difference in the layer morphologies, the Ru/Ti composite seemed to have higher percentage of voids. Nanoindentation measurements showed that there was no significant change in hardness as Cu and Ti layer thicknesses varies. The hardness was constant below a critical thickness as predicted by Koehler (46). However, the Ru/Cu multilayer had twice the hardness of Ru/Ti. The strengthening mechanism proposed by Koehler predicted that Ru/Ti composites should have higher strength than Ru/Cu due to the larger modulus difference between Ru and Ti. Kung et al (59) suggested that the discrepancy indicated the break-down of the Koehler model in cases where the thickness of the softer material was extremely small. They proposed a model which suggested that if the softer material was thin enough to inhibit dislocation motion to contribute to the deformation process, then the deformation will have to be accommodated by "shearing" of the softer layer. There were two possible ways to shear the Cu or Ti layers. One possibility was to have dislocation plasticity in the thick Ru layers, in which case, the dislocation would have to propagate through the softer layer by shearing mechanisms. The thin softer layer would then serve as barrier to dislocation motion as in the case of grain boundary strengthening. Another possibility required fracture in the Ru layer to accommodate the shear of the Cu or Ti. Since the shear modulus of Ti is smaller than that of Cu, hence, the Ru/Ti exhibited lower hardness than Ru/Cu.

Table 2.3 summarizes the equations in the literature that were used to predict the strength of multilayered composites.

2.2. Friction and Wear

2.2.1. Definitions

Friction and wear are elements of the field of tribology. Tribology is a discipline involving the physics, chemistry and engineering of moving and contacting bodies. Friction is defined as the resistance to relative motion between two surfaces in contact and wear is the volume loss and/or damage resulting from that contact (60,61). Friction and wear are not intrinsic material properties but are characteristic of a tribosystem. According to Zum-Gahr (62), friction and wear of sliding pairs can be divided into 5 categories:

1) Micro-geometrical paring properties.
2) Loading and macro-geometrical properties.
3) Tribochemical properties.
4) Environmental properties.
5) Metallurgical and microstructural properties.

Surface roughness and topography of mating surfaces belong to the micro-geometrical paring properties, while load, sliding speed, vibration, shape and dimensions of mating surfaces belong to the loading and macro-geometrical properties. The tribochemical properties of the surfaces, such as adsorbed atoms, amount and type of surface films (i.e., oxides), chemical reactivity and thermal conductivity are not independent of environmental properties such as lubricants, humidity, temperature, composition and partial pressure of gaseous atmosphere. Finally, wear is significantly influenced by the metallurgical properties of the tribosystem which include hardness, work-hardening, crystal structure, crystallographic orientation (texture), ductility and fracture toughness. All these factors work simultaneously in a complex dynamic fashion and, ultimately, determine the type of wear mechanism(s) taking place.

2.2.2. Sliding Wear

Sliding wear is defined as the continuous (unidirectional or reciprocating) relative motion between two moving bodies in contact under load. Two modes of sliding wear can be identified; these are termed "severe" and "mild" (63). Severe wear is associated with high wear rates and high coefficients of friction and occurs under conditions of high velocities, loads and temperatures. Mild wear usually occurs at low loads and low velocities and is associated with lower wear rates and lower coefficients of friction than the severe wear. Sliding wear can well be described by Archard's law of wear (64),

$$W = KF_N / H \qquad 2.20$$

where W is the volume worn per unit sliding distance, F_N is the applied load, H is the hardness of the softer of the materials in contact and K is the wear coefficient. Equation 2.20 is valid for either severe or mild wear, but does not predict any transition in the wear rate. During sliding a transition from severe to mild wear is commonly observed (65,66). This type of transition known as "distance-dependant" transition is attributed to a combination of work-hardening, the formation of surface oxides and smoothening out of the initial surface roughness (63). The last factor is equivalent to gradual, but continuous, reduction in the true contact pressure during sliding, which would result in reduction in the measured rate of wear.

Most metal surfaces are covered by an oxide film, even after cleaning by machining. Grinding the metal can cause buildup of an oxide film several molecular layers thick in a few minutes. Thus, if an oxide film covering an asperity is removed by rubbing in normal atmosphere the clean metallic surface will be covered by a monomolecular oxide layer almost instantaneously. Numerous studies performed in both an SEM vacuum chamber (67-72) and atmospheric pressure consistently revealed that the coefficient of friction and wear rates are much higher in vacuum (60,62,73-77). These studies indicated that a hard oxide layer covering a metallic surface acts as a protective coating against wear. Hence, the transition from severe to mild wear is caused at least in part by the formation of oxide films.

There are several possible mechanisms of sliding wear, which are identified based on the type of material removal process taking place (78). Many different mechanisms of sliding wear are proposed in the literature (79-84). However, the most commonly cited mechanisms of wear in the literature include abrasion, adhesion and delamination. The three mechanisms of sliding wear are discussed, here, in more detail.

2.2.2.1. Abrasion

Abrasion is the most common mechanism of wear and may be described as damage to a surface by a hard material (85-89). It is also sometimes called scratching, scoring and gouging depending on the degree of severity. Abrasion covers two general situations. In both situations wear occurs by the removal of material from the softer surface by a harder surface. In the first instance, asperities of a harder material sliding against a softer one, are known as "two-body-abrasion". In the second case, abrasion is caused by loose hard particles sliding between rubbing surfaces (three-body-abrasion).

The abrasive wear process occurs by combined effects of microploughing, microcutting and microcracking (62,85). In the ideal case, microploughing due to a simple pass of one hard asperity does not result in any detachment of material from a surface being worn. The material is usually displaced sideways forming a ridge adjacent to the groove. Material loss can occur by microcracking of ridges as a result of repeated passing of the slider on the same wear track (90). Pure microcutting occurs by cutting of a material ahead of the asperities and results in a formation of a chip equal in volume to the wear groove produced. Microploughing and microcutting are common in ductile materials. The proportion of microploughing to microcutting depends on both the hardness and the attack angle of the asperity (88) (the angle between the asperity and the wearing surface). When the hardness of the harder material is much larger than the softer one and the attack angle is high, microcutting will dominate resulting in higher wear rates than microploughing.

The shape and the size of the wear debris also contribute to the ploughing of the softer surface (three-body-abrasion), especially, when these debris come from the harder surface or from the hard oxide debris forming. The wear rate is expected to be higher for "sharp" pointed debris (i.e., abrasive particle) than for "blunt" rounded abrasive. The wear rate also increases as the abrasive particle size increases.

Many investigators (91-93) have confirmed that hardness is an important parameter in abrasive wear. For example, Kruschov (91) plotted resistance to wear against hardness for a range of pure metals, obtaining a linear relationship. He also found that prior work-hardening of pure metals had no effect on wear rate. These experiments have led to the conclusion that during abrasion a metal surface work-hardens to a maximum value, and it is this value of hardness that is appropriate when investigating wear resistance.

Richardson (94) has shown that if wear resistance is studied as a function of the ratio of the hardness H_m/H_a, where H_m is the hardness of the metal surface and H_a is the hardness of the abrasive, then the wear resistance increases rapidly as H_m/H_a approaches unity. The region of abrasive wear where $H_m/H_a < 1$ is known as "hard abrasion" and where $H_m/H_a > 1$ as "soft abrasion". It has been suggested that the criterion for abrasion wear to be negligible is when $H_m/H_a = 1$.

Rabinowicz (73) derived an expression for abrasive wear rate by assuming that the asperities of the harder surface are conical (Fig. 2.2) and the wear rate (W) is given by

$$W = V/L = K_{ab} (F_N / \pi H) \tan \theta \qquad 2.21$$

where (V) is the volume loss, (L) is the sliding distance, $\tan \theta$ is the slope of the penetrating asperity, K_{ab} is a proportionality constant known as the wear coefficient for abrasion, (H) is the hardness of the abraded material and F_N is the normal applied load. It is interesting to note that this equation is of exactly the same form as the adhesive wear equation formulated by Archard's (64) (equation 2.20). This equation represents a general law of sliding wear.

A more rigorous analysis of abrasion mechanism was made by Zum- Gahr (62). He considered the detailed processes of microcutting and microploughing in the abrasive wear of ductile materials and found that,

$$W = V/L = A_{ab}[(F_N / 5H_{def})(1+10\ \mu^2)^{1/2} + (R^2_{asp} / \tan\psi)((\pi \tan\psi / 2) - 1)] \qquad 2.22$$

where A_{ab} is a factor relating the groove cross-sectional area and cross-sectional area of the material plastically displaced to the sides of the wear grooves. H_{def} is the hardness value of the wearing material in the deformed state after the abrasion action, R_{asp} is the tip radius of the abrasive asperity, ψ is the half tip angle of the asperity and μ is the coefficient of friction between the mating surfaces.

2.2.2.2. Adhesion

According to the early theory of Bowden and Tabor (95), adhesion occurs as a result of relative sliding between two surfaces under a normal contact load. It is assumed that when asperities come into contact, they adhere strongly to each other and form asperity junctions (96-98). Continued sliding causes the junctions to be sheared and separation of the surfaces occur in the bulk of the softer material. This process leads to fragments of the softer material adhering to the harder one.

2.2.2.3. Delamination

The delamination theory of wear (90,99-101) proposes that wear takes place by the deformation of the surface layer, nucleation of cracks at the subsurface and propagation of these cracks nearly parallel to the surface. Eventually loose sheet-like wear particles are generated. The detailed delamination process is as follows

(102,103):

1) When two sliding surfaces come into contact, normal and tangential loads are transmitted through the contact region. The asperities of the softer surface are easily deformed and fractured by repeated loading. A relatively smooth surface is generated, either when these asperities are deformed or removed.

2) Once the surface becomes smooth, the contact is not just an asperity/asperity contact, but rather an asperity/plane contact, each point along the softer surface experiences cyclic loading. The surface traction exerted by the harder asperity on the softer surface includes plastic deformation which accumulates with repeated loading.

3) As the subsurface deformation continues, voids are nucleated below the surface. Void nucleation below the contact is controlled by two factors. Deformation by shear component of stress promotes void nucleation, while the triaxial state of compressive stress opposes nucleation. Since the compressive stress is maximum at the surface, voids can not nucleate at the surface. However, below a certain depth, where the deformation induced stress exceeds the compressive stress, void nucleation becomes possible (104).

4) Upon further deformation and repeated loading, cracks extend and propagate, joining the neighbouring ones. Cracks tend to propagate parallel to the surface since the state of loading is repeated along the surface.

5) When these subsurface cracks reach a critical length they become unstable and

propagate to the surface, generating thin sheet-like wear debris.

2.2.3. Friction

Friction is the resistance to relative motion of contacting bodies. The degree of the resistance to motion is expressed as a "coefficient of friction", μ,

$$\mu = F_N / F_T \tag{2.23}$$

where F_N is the normal applied load and F_T is the tangential force required to sustain sliding.

The value of the coefficient of friction is determined by the sum of the individual contributions of the principal friction components (73,90); namely, adhesion (μ_a), ploughing (μ_{pl}) and deformation (μ_d). Hence,

$$\mu = f_a \mu_a + f_{pl} \mu_{pl} + f_d \mu_d \tag{2.24}$$

where the coefficients f_a, f_{pl} and f_d indicate the relative contribution of each component. The actual values of the contributions are determined by the characteristics of the wear mechanism(s) taking place, which is a function of material properties, and environmental and testing conditions. Many investigators (76,95,105-112) attempted to model friction, however, there is, as yet, no comprehensive model of predicting the coefficient of friction. Adhesion, ploughing and deformation components of friction are discussed below in more details.

i) Adhesion component of friction

Bowden and Tabor (76,95) suggested that the adhesion component of friction is due to the formation and rupture of interfacial bonds. These bonds are the result of interfacial interatomic forces developing between two surfaces in contact. If sliding is to take place, a friction force is needed to shear the weakest tangential planes at the area of contact.

If the shear strength at the interface is τ_i, which is assumed to be the bulk shear strength of the weaker material, the force required to beak a junction, between two asperities in contact, will be given by $\tau_i A_r$, that is F_T.

Using the relationship, $A_r=F_N/H$, the adhesion component of friction (μ_a) becomes,

$$\mu_a = F_T / F_N = \tau_i / H \qquad 2.25$$

where H is the hardness of the softer material.

Rabinowicz (73) extended Bowden and Tabor's model by taking into account the surface energy of contacting bodies, which gives

$$\mu_a = (\tau_i / H)[1 - 2(W_{12} \cot \theta / R_j H)]^{-1} \qquad 2.26$$

where θ is the angle that the asperity makes with the surface and R_j is the junction radius. The term W_{12} represents the energy that must be applied to separate a unit area of the interface between bodies 1 and 2, involving the need to create two surfaces of energy, γ_1 and γ_2 but destroying an interface that had interfacial energy of amount γ_{12}. Hence,

$$W_{12} = \gamma_1 + \gamma_2 - \gamma_{12} \qquad 2.27$$

W_{12} is generally referred to as the work of adhesion of the contacting surfaces.

ii) Ploughing component of friction

Ploughing occurs when two bodies in contact have different hardness. The asperities on the harder surface penetrates the softer surface and in the presence of relative motion it produces microgrooves. Because of the resistance to the ploughing action, a certain force is required to maintain motion.

Consider a hard conical asperity in contact with a soft surface (Fig. 2.2). During sliding only the front surface of each conical asperity is in contact with the opposing material, thus, the horizontally projected area of contact is

$$A = \pi x^2 / 2 \qquad 2.28$$

where x is the distance shown on the diagram in Figure 2.2. Also we have, F_N =

$A_r H = \pi x^2 H / 2$, where A_r is the real area of contact supporting F_N. The friction force F_T is obtained in a simple manner by considering the vertically projected area supporting F_T, the area of material which is being displaced by plastic flow, i.e.,

$$F_T = x\, h\, H \qquad 2.29$$

where h is the asperity depth of penetration of the harder material into the softer one. Therefore, the ploughing component of friction can be written as (114),

$$\mu_{pl} = F_T / F_N = 2h / \pi\, x \qquad 2.30$$

A more elaborate model of the ploughing component of friction, proposed by Zum-Gahr (62), predicts that

$$\mu_{pl} = (4 / 5\pi B)(F_N \sin\theta / R^2_{asp}\, H_{def}) \qquad 2.31$$

where B is a constant which depends on the number of slip systems and is influenced by surface texture, R_{asp} is the tip radius of the asperity, H_{def} is the hardness of the softer material after deformation and θ is the attack angle. From equation 2.31 it follows that the ploughing term of the coefficient of friction decreases strongly with increasing hardness of the highly deformed structure of the wearing surface. This relationship has been supported by experimental friction studies on different materials (62).

iii) Deformation component of friction

Heilmann and Rigney (105) suggested a model for the deformation component of friction that relates friction to plastic deformation. The main assumption is that the frictional work is equal to the work of plastic deformation. The deformation component of friction is given by

$$\mu_d = f(\tau_{ss} / \tau_{max})(A_r \ \tau_{max} / F_N) \qquad 2.32$$

where $f(\tau_{ss}/\tau_{max}) = 1 - 2[((\ln(1+(\tau_{ss}/\tau_{max}))-(\tau_{ss}/\tau_{max}))/\ln(1-(\tau_{ss}/\tau_{max})^2)]$, τ_{ss} is the average interfacial shear strength and τ_{max} is the ultimate shear strength of the material.

2.2.4. The Effect of Sliding Distance on the Coefficient of Friction

Friction is a time dependent phenomenon, however, it is commonly reported as an average single value. Friction versus sliding distance (time) curve gives the variation of coefficients of friction as a function of time. Three important parameters can be obtained from a friction curve; namely, peak value of the coefficient of friction, steady-state value of the coefficient of friction and the time required to reach a steady-state. Figure 2.3 shows a schematic diagram of a common (114-117) coefficient of friction versus sliding distance curve. However, the shape of this friction curve is only one amongst several shapes cited in the literature (117). In choosing a material for a specific application all three parameters are taken into consideration.

Until recently, the time-dependant friction behaviour had not been explored (66,90,117-120) and is still not well understood. Suh (90,120) proposed a theory to explain different stages on the friction curve (Fig. 2.3). Suh's proposal is briefly reviewed below:

Stage I. In this early stage of dynamic friction the coefficient of friction is largely dominated by ploughing of the soft surface by the hard asperities and debris particles. This stage is characterized by a steep slope because of the rapid increase in the number of wear particles entrapped between the sliding surfaces as a result of wear. The slope is also affected by adhesion arising from the increase in clean interfacial areas as a result of deformation. The force required to deform the asperities will continue to contribute to the frictional force as new asperities are generated, as a consequence of delamination.

Stage II. This stage is reached when the number of wear particles entrapped within the interface remains constant. This occurs when the number of newly entrapped particles entering the interface equals the number of entrapped particles leaving the interface. Both ploughing and deformation contribute to the coefficient of friction at this stage.

Stage III. When a hard slider is slid against a softer surface, the asperities of both surfaces are gradually removed, creating a mirror finish. In this case the friction force decreases because of the decrease in ploughing of the surfaces by the wear particles and the reduction of surface asperities. Wear particles can not plough since they can not penetrate and anchor into the hard surface.

Stage IV. Eventually, when the hard surface becomes mirror smooth to the maximum extent, the softer surface also acquires the same mirror finish and the frictional force levels off. The surface of the softer material is never completely smooth since there are always a somewhat rougher areas caused by the detachments of delamination wear particles.

Blau (66,117), on the other hand, developed a semi-empirical model to account for some of the transitions observed in the coefficient of friction with time. The framework for Blau's model was constructed from the view point of observed behaviour rather than being created based on assumed asperity shape. It relies on finding the physical attributes of a sliding system that would produce the shape of the friction as a function of time curve.

Other factors that influence the friction curve are the evolution of crystallographic texture (121) and the work-hardening (118) that takes place during the wear process. Texture and work-hardening of the "near-surface" are examined below in more detail.

2.2.4.1. Crystallographic Texture

The mechanical properties of single crystals are markedly anisotropic. The anisotropy of plastic properties are more pronounced in hexagonal than in cubic crystals. Non-random array of grains in polycrystal are called texture. Crystallographic texture can be used successfully to strengthen metals. Preferred orientation or texture may arise during the fabrication of metals (122) or may be induced by deformation processes such as wear (121,123).

A type of flow softening (124-126), which does not necessarily involve work softening, however, is that due to texture changes. Texture softening occurs most dramatically in single crystals deforming by single slip. For a simple tensile test, at the beginning of straining, there is a little or no work-hardening (the critical resolved shear stress τ_c is approximately constant), and the tensile flow stress, σ, is given by

$$\sigma = \tau_c / \cos \theta_g \cos \phi_g \qquad 2.33$$

where the factor $\cos \theta_g \cos \phi_g$ is known as the Schmid factor, θ_g is the angle between the slip plane normal and the stress axis and ϕ_g that between the slip direction and the stress axis. If the angle between the tensile axis and the glide plane normal is initially small (e.g., 10 to 20°), then during extension, the normal is gradually tilted away from the tensile axis. Under those conditions, the Schmid factor increases towards its maximum value of 0.5 at 45°, and the axial yield stress decreases in direct proportion, as given by equation 2.33. Such geometrical softening can attain relative values as high as 70% (124).

In polycrystalline hcp materials, because of the dispersion of crystallite orientation, the proportions of flow softening that can be produced by texture modifications are smaller. These are reduced even further in fcc and bcc metals. Nevertheless, texture softening can be significant, particularly, in processes where large plastic deformation has taken place, such as wear.

Kuhlmann-Wilsdorf (119) used the concept of texture softening to explain the transitions in the coefficient of friction as a function of sliding distance. She suggested that the crystallographic reorientation (i.e., texture evolution) below a contact surface may be a possible cause for the reduction in the coefficient of friction during sliding wear. Crystallographic reorientation can produce a reduction in the effective shear stress in near-surface regions and a reduction in the required friction force to maintain relative motion. Kuhlmann-Wilsdorf's model will be discussed below in more detail.

Only a limited amount of research has been conducted to determine the influence of texturing on friction and wear. Texture evolution during wear often resembles that of a rolling texture (122). It has been reported (121,127,128) that for hexagonal metals, sliding tends to produce an alignment of basal slip planes (0001) parallel to the worn surface, the basal poles being actually tilted by up to 10° down towards the direction from which sliding occurred. For fcc metals, Wheeler and Buckley (123) found a texture of (111) (a slip plane in fcc) tilted about 10° towards the sliding direction for rubbed copper and nickel. A similar texture evolution during sliding wear for stainless steel and aluminum has been observed by Hirth and Rigney (121).

Studies in the literature have shown that the wear and friction between a hard slider and the surface depends markedly on crystallographic orientation (129). For example, the influence of texture on abrasion resistance of Ti-8.5%Al was investigated by Zum-Gahr (62). He prepared samples with basal texture and transversal texture from sheet with inherent texture. A case where the preferred basal planes were oriented parallel to the surface was referred to as basal texture and orientation perpendicular to it was referred to as transversal texture. A scratch test revealed that larger wear rates were recorded on surfaces with inherent basal texture than with transversal texture. Similar results were obtained on hexagonal cobalt (62) which suggested that plastic deformation during wear is easier on surfaces showing basal textures.

Static friction between two oriented crystals of copper (130) showed that the coefficient of friction on the (100) face was more than 4 times larger than that on the (111) face. The lower coefficient of friction was attributed to the ease of shearing the crystal parallel to its slip planes.

2.2.4.2 Work-Hardening

Contact between metallic surfaces nearly always produces plastic deformation in and around the real areas of solid/solid contact. This is particularly true when relative sliding motion occurs between unlubricated surfaces. The deformation is caused by normal and shear traction at the contact interface and is an integral part of the friction and wear processes (118,131-134). This irreversible deformation is a major mechanism by which mechanical energy is dissipated, and thus it is responsible for most frictional energy losses.

When a ductile material is deformed plastically below its recrystallization temperature dislocations are produced in numbers proportionate to the degree of deformation. A complicated network of interlocking dislocations is thereby created which impedes the dislocation movement and the metal is strengthened or "work-hardened" (135).

Metals work-harden during sliding wear and the amount of work-hardening depends on the specific metal (i.e., the rate of work-hardening is lower for hexagonal than for cubic metals) and its microstructure and on the testing conditions (such as normal applied load, sliding speed).

During dry sliding wear, strains accumulate in a loaded surface due to the repeated passage of asperities of the counterface. These strains decay with increasing depth below the surface (104), and will decay more strongly the greater the rate of work-hardening of the surface. The extent of surface and subsurface strains depend mainly on the flow stress of the material, the applied load and the coefficient of friction (90). For a given metal, the deformations are enhanced by increasing the coefficient of friction and the applied load.

The subsurface microstructure of severely worn metals often reveals three distinct zones (136,137). Zone 1 being the deepest followed by zone 2 then 3 near the surface. In zone 1, bulk materials remain undeformed. Zone 2 contains plastically deformed metal, with plastic shear strains increasing towards the surface. Grain reorientation and refinement may be found towards the boundary of zones 2 and 3. The metal nearest to the surface, in zone 3, consists of fine grains (sometimes in the nanometre range (138)) and containing components not present in the bulk material such as material transferred from the counterface and oxides.

The subsurface work-hardening effect is represented by hardness gradient being maximum at the surface and diminishing with increasing depth below the worn surface. Cracks can be initiated in the heavily deformed zone when the applied strains exceed the capability of deformation (ductility) of the material. Several studies (90,104) have shown that the strain accumulation results in subsurface crack initiation and propagation. The effect of work-hardening on the shape of the friction as a function of sliding distance has also been investigated (117-119).

2.2.4.3. Kuhlmann-Wilsdorf's Friction Model

Kuhlmann-Wilsdorf (119) proposed a deformation-based model that contains contributions from both work-hardening and near surface crystallographic reorientation resulted from sliding-induced deformation. Based on this model the coefficient of friction is found to be

$$\mu = c\,(\tau_s / \tau_b)(m_b / m_s) \qquad 2.34$$

where c is a factor derived from consideration of hardness, contact geometry and loading conditions. τ(s,b) are the critical resolved shear stresses near the surface and in the bulk material, respectively. m(s,b) are the Schmid factors near the surface and in the bulk material and are given by

$$m_b = \cos\theta_b \cos\phi_b \qquad 2.35$$

$$m_s = \cos\theta_s \cos\phi_s \qquad 2.36$$

where θ_b and ϕ_b are the angles made by the compression axis with the active slip direction and slip plane normal, respectively. θ_s is the angle which the slip direction includes with the sliding direction and ϕ_s is the angle which the slip plane makes with the plane of sliding.

The maximum value of m_s is unity when θ_s and ϕ_s are both equal to zero;

that is, when the slip plane and direction coincide with the sliding plane and direction, respectively. In polycrystalline materials, the possible number of slip planes that can be oriented favourably in different grains increases with the number of slip systems (in polycrystal θ and ϕ are averaged over all grains). It follows that the value of Schmid factor also increases with the number of, crystallographically possible, "easy" glide systems.

Equation 2.34 allows one the ability to let the work-hardening rate to vary independently from the rate of near surface crystallographic reorientation. Generally, m_s tends to rise perhaps up to unity during sliding, while m_b remains constant. This should cause the coefficient of friction to drop towards steady-state. Conversely, work-hardening through surface deformation increases τ_s while τ_b remains rather stable, causing the coefficient of friction to rise proportionately. Depending on whether crystallographic reorientation or work-hardening happens faster, several possible shapes of the friction curve can be observed (66,117).

While the Kuhlmann-Wilsdorf model displays some of the features of observed frictional behaviour, there is some concern that it is not general enough to handle a variety of actual sliding conditions. Factors such as hardness and roughness that also vary during sliding friction were not taken into account. The coefficient of friction versus sliding distance curve is, ultimately, determined by all of these factors occurring simultaneously at different rates.

2.2.5. Experimental Work on the Friction and Wear of Nanocrystalline and Nanolayered Composite Materials

Ceramic coatings such as aluminum oxide, titanium nitride, silicon carbide, silicon nitride and zirconium oxide have been studied extensively for their tribological properties in the last decade (139-149). Hard ceramic coatings exhibit high hardness, high melting point and extreme chemical stability. They provide low wear and generally capable of sustaining heavy loads, high speeds and high temperatures for extended periods without any deterioration in performance. Ceramic coatings have been used extensively in industry in the recent years. For example, Al_2O_3 coatings are used in various wear applications such as gas bearings, electrical insulation and thin film structure of magnetic heads for tape and disc drives. In particular, TiN has received considerable attention as a wear resistant coating for cutting and forming tools such as drill bits and saws. Because of its excellent lubricancy and tendency to reduce friction, TiN coatings are being used for extrusion and drawing dies and injection molds. TiN coatings are also commonly used as decorative coating material for watch cases, watch bands, eye glass frames, etc., due to their distinct bright golden colour. In view of their high hardness and resistance to erosion and wear as well as to corrosion, TiN coatings are being considered for application to gas turbine engine components to provide erosion resistance, thereby extending the useful life of these components (145).

The mechanical properties of ceramic coatings such as hardness, ductility, elastic modulus, porosity and interlayer adhesion of the coating to the substrate are crucial for good friction and wear performance. Intrinsic (residual) stresses can cause coating rupture and loss of adhesion to substrate (84).

Furthermore, the wear resistance of these coatings appears to be closely related to their thermal diffusivity characteristics (146). A coating with high diffusivity (or thermal conductivity) rapidly dissipates the frictional heat and avoids local high temperatures which would result in high local thermal stresses. The large local thermal stresses will include spalling in these local regions. Apart from thermal properties, the pore size, shape, and distribution as well as cracks in the coating, that might have developed during the fabrication process, also effect significantly the wear resistance because of their influence on stress concentrations (84).

A major disadvantage of monolithic ceramic coatings is their brittleness (low toughness) and their tendency to fracture during wear when a critical contact load is exceeded. The dominant failure mechanism in these cases would be by the initiation and propagation of lateral cracks which ultimately result in spalling or delamination of the coating (139,142, 147-149). However, subsurface damage, plastic deformation and grooving are also observed, to a limited degree, during sliding wear of ceramics, despite their brittleness (150-152).

Modern production techniques allow the toughening of ceramic coatings by incorporating alternating metallic and ceramic layers to combine the effect of the high strength of ceramics with the ductility of the metallic layers. Only a limited number of publications on the friction and wear of laminated composites (mostly, metal/metal) are available in the open literature (153-158). Alpas et al. (154) found that, in the sliding wear of laminated composites of copper/amorphous $Ni_{78}Si_{10}B_{12}$ metallic glass, the wear resistance increases with increasing volume fraction of the metallic glass. The wear rate of the laminate was found to fit an equation of the form;

$$W=[(W_{Cu}-W_A)\exp(-\gamma V_A)]+W_A \qquad 2.37$$

where W, W_{Cu} and W_A are the wear rates of the composite, the wear rate of Cu and the wear rate of $Ni_{78}Si_{10}B_{12}$, respectively, γ is a constant (=24.6), V_A is the volume fraction of $Ni_{78}Si_{10}B_{12}$. These experiments confirmed that the amorphous layers were effective in increasing the wear resistance of the composite by supporting the load with less deformation and by obstructing the damage process initiated in copper layers.

Ruff and Lashmore (155) found that a metal/metal multilayered composites of copper and nickel offered substantially increased wear resistance to sliding wear when compared to monolithic copper and nickel. Coefficients of friction of the multilayer composites were intermediate between the coefficient of friction for copper and nickel. Wear tests performed on gold/molybdenum and gold/stainless steel by Courtridge et al (156) showed that decreasing the gold layer thickness resulted in a decrease in wear rate. The study also found that the alternate layers of Au/Mo did not wear by gradual wearing of successive layers, but rather by delamination in underlying layers as a result of plastic deformation and fracture at the interfaces. Norose et al (157,158) prepared metal/metal laminates by depositing thin plates of metal A and metal B. As a result of wear experiments carried out on 33 metal combinations rubbed against pure Fe and pure Cu, they found that laminated composites consistently exhibited higher wear resistance than the pure metals.

Another type of coating, monolithic nanocrystalline films, are being tested as potential wear resistant coatings. It is well established that grain size has a considerable influence on the strength of metals. It can also be expected that grain size may have an appreciable effect on the wear resistance. However, at the present time there is not sufficient experimental data, even in the conventional grain size range, relating wear resistance to grain size. Korshunov et al. (159) reported an increase of 2-5 times in wear resistance of quenched and tempered steel when the grain size was reduced from 100 to 10 μm. They have also observed a 15% reduction in the average value of the coefficient of friction within this grain size range. Miranda-Martinez et al. (160) studied the grain size effect on the wet erosive wear of high purity polycrystalline alumina. They found that there is almost two orders of magnitude decrease in the wear rate as the grain size is reduced from 12 to 1 μm. They also found that there is a strong linear relationship between the wear rate and the square root of the grain size.

Table 2.1. Summary of Hall-Petch parameters for nanocrystalline materials.

Material	Production method	Method used to vary grain size	Grain size range (nm)	Hardness range (GPa)	$^*\sigma_o$ (MPa)	k (MPa. $m^{0.5}$)	Ref.
Ni	electro-deposition	as-deposited	$12\text{-}10^4$	0.9-6.9	300	0.22	12
Cu	gas-condensation	annealing	$25\text{-}5x10^4$	0.5-1.2	161	1.2	13
Pd	gas-condensation	annealing	$5\text{-}10^5$	0.7-3.1	745	0.3	13
Fe	ball milling	as-prepared	$6\text{-}3x10^3$	2-10	371	0.7	14
Al-1.5%Mg	torsional straining	annealing	$150\text{-}10^4$	0.4-1.6	118	0.16	15
$(Fe_{.99}Mo_{.01})_{78}$ Si_9B_{13}	isothermal annealing	annealing	45-200	6.3-10	1426	0.4	16
Ni	electro-deposition	as-deposited	$20\text{-}10^5$	1.4-6.4	443	0.22	18

* H is converted to σ using the relation σ=H/3.

Table 2.2. Summary of inverse-Hall-Petch parameters for nanocrystalline materials.

Material	Production method	Method used to vary grain size	Grain size range (nm)	Hardness range (GPa)	*σ_o (MPa)	k (MPa. $m^{0.5}$)	Ref.
Cu	gas-condensation	annealing	6.5-12.3	1.5-2.25	1250	- 0.07	2
Pd	gas-condensation	annealing	7.5-13.5	2.25-3.75	2500	- 0.14	2
$(Fe_{.99}Mo_{.01})_{78}Si_9B_{13}$	isothermal annealing	annealing	15-45	7.8-10	4583	- 0.25	16
$Ni_{80}P_{20}$	isothermal annealing	annealing	9-120	10.4-11.3	3933	- 0.04	17
Ni	electro-deposition	as-deposited	11-20	6.4-6.5	hardness plateau		18

* H is converted to σ using the relation σ=H/3.

Table 2.3. Equations describing the strength of multilayered composites.

Material	Yield strength range (GPa)	Yield strength equation (MPa)	Ref.
Al(40-1000nm)/ Cu(50nm)	0.19-0.49	$\sigma_y=[f_{Al}+1.5\ f_{Cu}][(10^{-4}/\lambda_{Al})+23]$ Lehoczky relation.	48
Al(50-1000nm)/ Al_x/O_y(25nm)	0.10-0.40	$\sigma_y=27+0.086\ \lambda^{-.05}{}_{Al}$ Hall-Petch.	50
*Ni(80-5x10^4nm)/ Cu(80-5x10^4nm)	**0.33-0.90	$\sigma_y=300+0.17\ \lambda^{-.05}$ Hall-Petch.	51
Ni(1-11μm)/ TiC(1-11μm)	0.40-0.55	$\sigma_y=128\ f_{Ni}+862\ f_{TiC}$ Rule of mixtures.	52
$Ni_{78}Si_{10}B_{12}$(55μm)/ Cu(550-1100μm)	0.22-0.38	$\sigma_y=2100\ f_{Ni78Si10B12}+203\ f_{Cu}$ Rule of mixtures.	55
Al(50-500nm)/ Al_x/O_y(5nm)	0.16-0.48	$\sigma_y=80.7+0.1\ \lambda^{-.05}{}_{Al}$ Hall-Petch.	56

[*] layer thicknesses of both components were kept equal for all laminates.

[**] H is converted to σ using the relation $\sigma=H/3$.

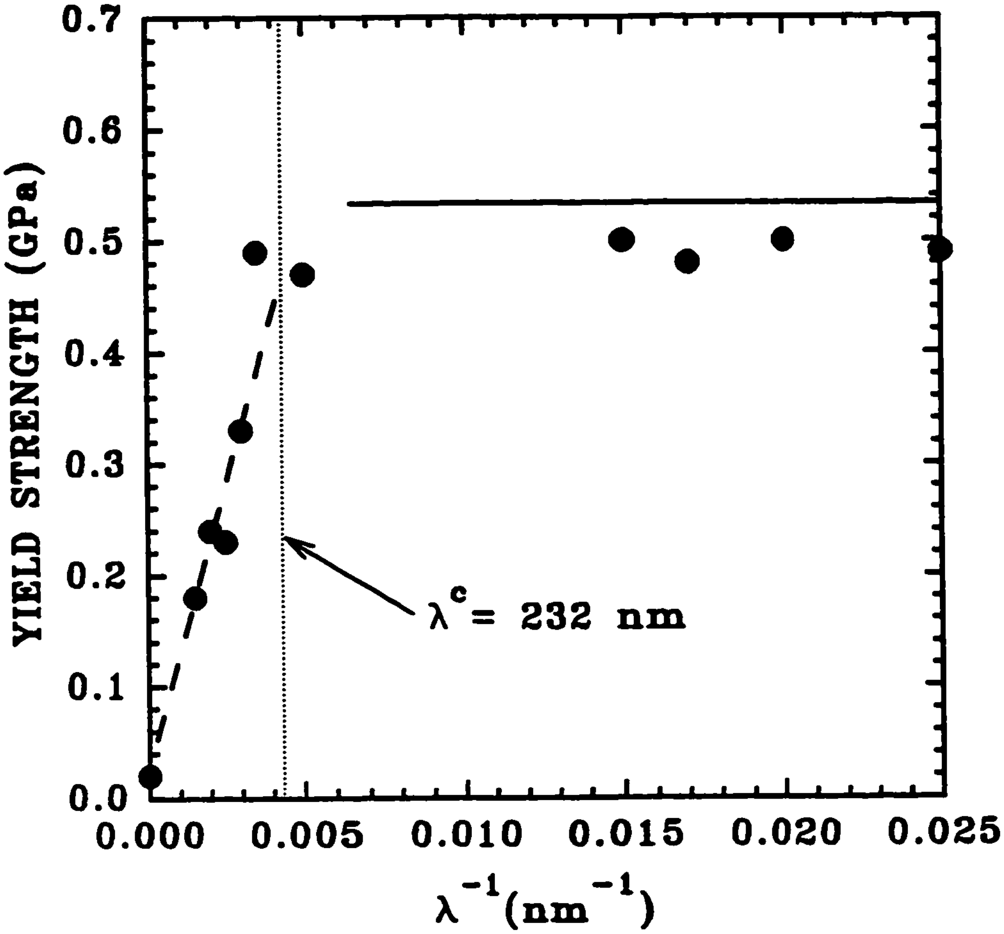

2.1. Inverse Al-layer thickness dependence of the yield stress for Al/Cu laminates (43). At a critical layer thickness (232 nm), the yield strength becomes independent of the interlayer spacing.

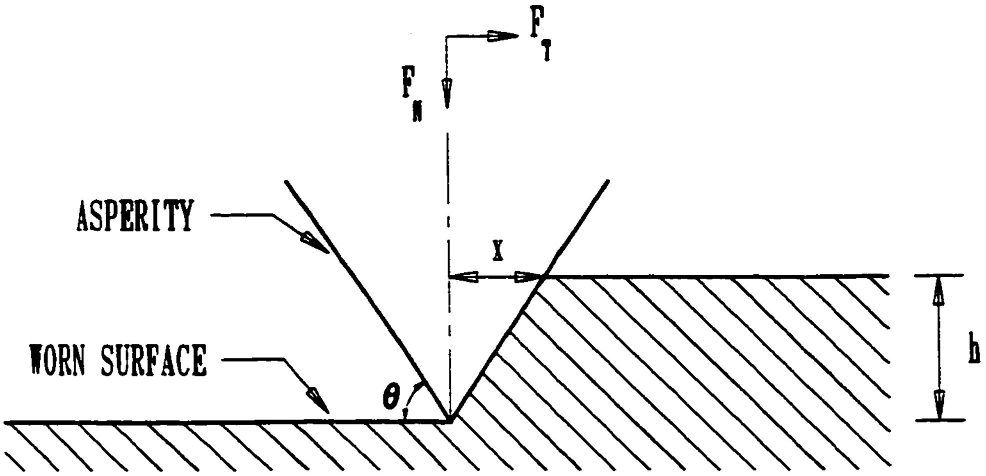

2.2. Schematic diagram showing a hard conical asperity sliding against a softer surface.

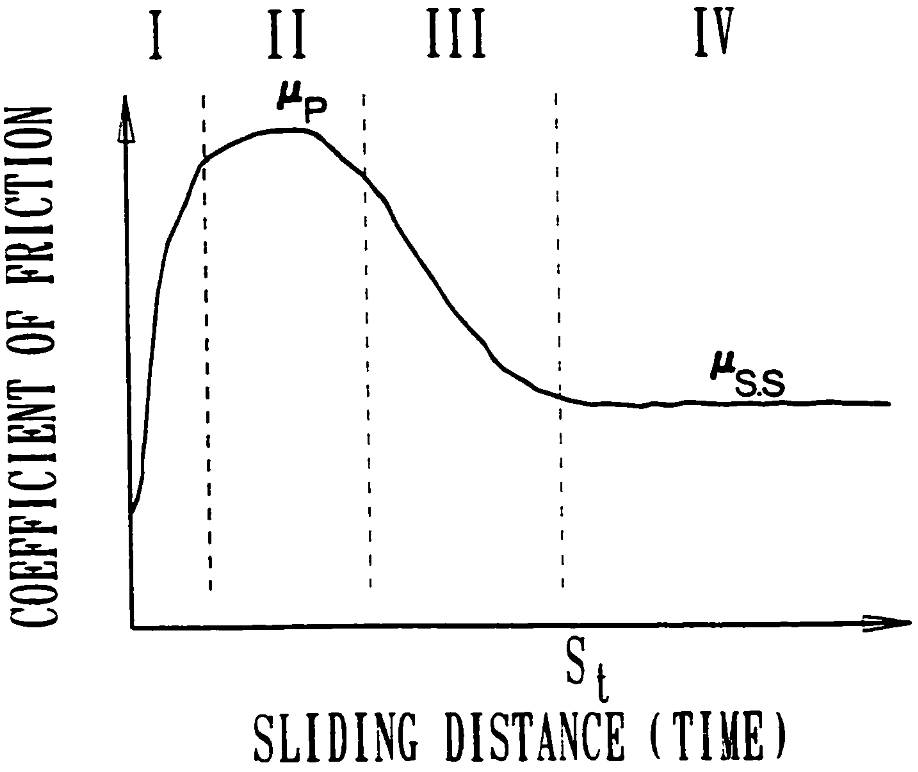

2.3. Schematic diagram showing a typical coefficient of friction as a function of sliding distance. The friction curve increases rapidly to a peak value (μ_p) followed by a gradual decrease to steady state ($\mu_{s.s}$). See text for the explanation of regions I-IV.

CHAPTER 3

EXPERIMENTAL METHODS

3.1. Materials

3.1.1. Target Materials

Monolithic nanocrystalline (Al, Ti, and Cu) and nanolaminated Al/Al_2O_3, Ti/TiN and Ti/Cu composites consisting of nanocrystalline Al, Ti and Cu layers were fabricated by a radio frequency (r.f.) magnetron sputtering technique. Microstructural and mechanical characterizations of materials used as sputtering targets (Al, Ti, Cu and Al_2O_3) were performed using X-ray diffraction, optical metallography and hardness measurements. X-ray diffraction patterns of Al, Ti, Cu and Al_20_3 are shown in Figures. 3.1(a-d), respectively. The microstructures of Al, Al_20_3, and Cu showed uniform equiaxed grains. However, the grains of the Ti specimen are larger in the transverse section than in the normal section (Table 3.1). The grain size was determined using linear intercept method. Table 3.1 also shows the average Vickers hardness values (of 15 measurements) of the materials used as sputtering targets from which the nanoscale materials were produced.

3.1.2. Sputtering System

The vacuum chamber of the r.f. triode magnetron sputtering system is shown schematically in Figure 3.2. The material to be sputtered is used as a cathode in the system in which glow discharge (plasma state) is established in an inert gas (such as argon). The vacuum system was pumped down to a pressure of 10^{-7} torr prior to sputtering, and a pressure of $1.5\text{-}4.5\times10^{-3}$ torr was maintained during the deposition process. The substrate on which the film to be deposited is placed on a substrate table located above the sputtering target. The system is also equipped with a thermionic emission source (a Ta cathode) to further assist the glow discharge process. The use of the radio frequency (r.f.) allows sputtering of non-conductive materials. This coating method provides a higher degree of control over the film thickness and uniformity compared to electron-beam deposition, but the deposition rate were rather slow (0.6-10 nm/min) compared to electron-beam deposition technique.

3.1.3. Nanocrystalline Aluminum and Nanolaminated Al/Al_2O_3

Nanocrystalline Al films were fabricated in order to study the effect of grain size on friction and wear. These films were produced from high purity (99.999%) cast aluminum targets. The films were deposited on substrates made of a commercial 1100 aluminum alloy (VH=0.85 GPa, using 0.1 N load). Specimens were produced in the form of 20x20 mm^2 coupons suitable for friction and wear tests. Aluminum films with different grain sizes were also investigated. The grain size of the as-sputtered nanocrystalline Al was increased by annealing at 573 K for the time intervals of 5, 10 and 50 hrs. in vacuum sealed quartz tubes.

Nanolayered Al/Al_2O_3 composites were fabricated in order to compare their mechanical and tribological properties with those of the monolithic nanocrystalline aluminum as the composites were expected to provide higher strength levels than the monolithic aluminum. Investigation of the role of the structure, i.e., distance between Al_2O_3 layers on the mechanical properties was also an important objective of this work. Alternating Al and Al_2O_3 layers were deposited by positioning the substrate (mounted on a rotating substrate table, Fig. 3.2) over each target source for a predetermined time, which depended on the required thickness of the layer. Aluminum and Al_2O_3 target sources were prepared from pure aluminum and high purity (99.99%) sintered Al_2O_3 (Table 3.2). Al films (16 nm grain size) were deposited using only high purity Ar (99.999%) as a sputtering gas, whereas the Al_2O_3 films were deposited using a sputter gas containing both Ar and O_2 (99.999%). Oxygen injection was required because without compensation of the O_2 partial pressure, the resulting Al_2O_3 films were oxygen deficient. The multilayered Al_2O_3 composites were deposited on 20x20 mm^2 1100 Al alloy coupons.

3.1.4. Ti/TiN nanolaminated films

Monolithic TiN films are of great commercial importance as hard and wear resistant coatings for tribological applications. However, their brittle behaviour under certain loading conditions and their poor adhesion to the substrate necessitates the search for new ways to increase their ductility and at the same time maintain high wear resistance and a low coefficient of friction. In this project, alternating nanolayer Ti/TiN films were produced in order to compare their mechanical and tribological properties to those of the monolithic TiN films. The Ti layers (30 nm grain size, estimated from TEM observations) in the Ti/TiN composites were directly sputter deposited from a Ti (99.999%) target. The TiN layers were deposited using the same Ti target, but this time nitrogen was used as a reactive sputtering gas.

Monolithic TiN films (total thickness of 10 μm) were produced by Liburdi Engineering Ltd., Hamilton, Ontario using a reactive ion plating (RIP) process (145) on a stainless steel substrate. The principles of the RIP method are similar to those of the sputtering technique. A stainless steel coupon to be coated is suspended from a rack above a crucible filled with titanium pellets inside a vacuum chamber. A tungsten filament acts as a thermionic emitter which injects electrons to support the plasma during operation of the coating process. The titanium is melted and evaporated by an electron beam originating from a tungsten cathode deflected into the crucible by suitable magnetic coils. Prior to depositing TiN a thin interlayer (< 1 μm) of pure Ti was deposited onto the stainless steel to improve the adhesion between TiN and the substrate. Nitrogen used as reactive gas is then injected at predetermined rate into the system and TiN is subsequently deposited on the stainless steel substrate.

The structure of the TiN coating was characterized by X-ray diffraction (Fig. 3.3) which shows clearly defined TiN diffraction peaks. Scanning electron microscope (SEM) micrograph in Figure 3.4 show the cross-section of the stainless steel substrate and the TiN coating of thickness of about 7 μm. The figure also shows a Ti interlayer having a thickness of about 3 μm. The different layers (i.e., steel, Ti, TiN) were identified by energy dispersive spectroscopy (EDS).

Metal/metal type (Ti/Cu) layered films were produced for comparison with the metal/ceramic (Ti/TiN and Al/Al_2O_3) multilayered composites. The advantage of producing metal/metal type composite over metal/ceramic layered composites was that the materials could be deposited at much higher rate (Table 3.2). For Ti/Cu composites, the Ti layers were sputter deposited from a Ti target and the Cu layers (40 nm grain size, estimated from TEM observations) from a Cu target (99.999%).

Pure Ti and Cu nanocrystalline monolithic films were also fabricated from their respective targets. Ti, Ti/TiN, Cu and Ti/Cu films were deposited on 20x20 mm^2 silica glass slides (VH=5.5 GPa, using 0.1 N load). The total thickness of all films were 10-15 μm. Details of the sputtering conditions are given in Table 3.2.

3.2. Grain Size Determination

An X-ray line broadening technique (161) was used to determine the grain size of the as-sputtered and the annealed Al films. The aluminum films were removed from the substrate and X-ray diffraction patterns of the (111) peaks were obtained using a Rigaku X-ray diffractometer with Cuk_α radiation. In order to accurately record the diffraction profile, a scanning step of 0.02° was chosen. The data was recorded to a computer, both as analog charts showing the diffraction peaks and as a digital output to be used for further analysis of the profile.

Since k_α X-ray radiation was used, separation of the $k_{\alpha1}$ and $k_{\alpha2}$ contributions of the profile was necessary. A method of separating $k_{\alpha1}$ and $k_{\alpha2}$ known as Rachinger correction (162) was employed. The Rachinger correction assumes that the intensity of the $k_{\alpha2}$ component is half that of the $k_{\alpha1}$ component, so that the contribution of $k_{\alpha2}$ towards a diffraction line has the same shape as that of $k_{\alpha1}$ except that it is half the height and shifted towards larger angles by $\Delta(2\theta)$. If I_n is the total intensity at position "n" on the profile and $I_n(k_{\alpha1})$ is the contribution of $k_{\alpha1}$ alone then

$$I_n(k_{\alpha1})=I_n-I_n(k_{\alpha2})=I_n-(I_{n-m}(k_{\alpha1})/2) \qquad 3.1$$

where $I_n(k_{\alpha2})$ is $k_{\alpha2}$ contribution to the total intensity, m is the number of intervals in a $\Delta 2\theta$ range and is equal to 5 ($\Delta 2\theta/0.02°$, where 0.02° is the scanning step).

The peak profiles were then smoothed by subtracting the background noise, and the points where the baseline intersected the peak tails were defined. The scatter in the data was reduced using a computer program that calculates a running average for each point on the profile, that is, taking an average of every 3 neighbouring points.

An integral breadth method was used to analyze the broadening of the profile. The integral breadth (β) is defined as

$$\beta = A_P / H_P \qquad 3.2$$

where A_P is the total area under the peak and H_P is the peak height. The total area under the peak was calculated using the Trapezoidal Rule method. The broadening of the peak is usually a result of three factors, namely: i) presence of fine crystallite size which show up in the tails, ii) microstrains which shows up in the upper part of the peak and iii) instrumental broadening which has to be subtracted from the profile. To determine the amount of instrumental broadening, a standard fully annealed polycrystalline aluminum powder, having grain size of about 2 μm, was used. The separation of the instrumental broadening was accomplished using the empirical relation given by Wagner and Aqua (163)

$$\beta^*_{specimen} = \beta^*_{total} - ((\beta^*_{instrumental})^2 / \beta^*_{total}) \qquad 3.3$$

where $\beta^*=\beta\cos\theta_{k\alpha 1}/\lambda_{k\alpha 1}$ and $\beta_{instrumental}=\beta_{standard\ specimen}$. After the determination of the broadening in the specimen alone, it was desirable to separate the contribution to the broadening from both the crystallite size and the microstrains. In Wagner and Aqua method (163) a Gaussian distribution of the profile for both effects was assumed as follows.

$$(\beta^*_{specimen})^2=(\beta^*_D)^2+(\beta^*_\epsilon)^2 \qquad 3.4$$

where β^*_D is the broadening due to crystallite size and β^*_ϵ is the broadening due to microstrains. In this investigation the assumption was made that the broadening in the (111) is due to crystallite size only, since the broadening observed was mostly in the tails. Then the crystallite size (D) could be calculated from the Scherrer formula

$$D=1/\beta^*_{specimen} \qquad 3.5$$

TEM examinations were carried out using a JEOL 100 to confirm the grain sizes of the as sputtered and annealed aluminum films. The films examined by TEM were sputter deposited on NaCl substrates which were then separated by dissolving the NaCl substrate. The grain size was measured using the conventional linear intercept method on the TEM micrographs.

3.3. Measurement of Mechanical Properties

The mechanical properties of the nanolaminated and the nanocrystalline films were measured using a nanohardness indentation system (UMIS 2000 developed by CSIRO, Australia) since this was the most reliable hardness measurement technique for thin films. Figure 3.5 is a schematic diagram showing the operating principles of the nanoindentation system. A member carrying a specially developed elastic elements is driven downwards by a piezodriver. The elastic elements support a shaft with a diamond pyramid indenter attached. The instrument uses a Berkovich diamond pyramid with an angle of 65.3° between the tip axis and the faces of the triangular pyramid. An LVDT (Linear Variable Differential Transformer) records the position of the shaft (depth LVDT) and a second LVDT (force LVDT) records the force applied. With this instrument, the displacement of the indentation and the load could be measured independently with a resolution of 1.0 nm and 0.1 mN, respectively (164). The force applied was in a square root increments to produce approximately equal increments of penetration. A schematic of the loading/unloading cycle produced by the nanoindentation instrument is shown in Figure 3.6. An average of 20 measurements were produced on a given specimen. Hardness (H) at the maximum applied load was determined using the relationship between plastic depth of penetration (h_p) and the maximum applied load (P) as follows (164,165)

$H=P/A$ 3.6

where A is the area of contact, and $A=kh_p^2$ (the constant k for the Berkovich indenter is 24.5). The total depth of penetration was always kept less than 10% of the total thickness of the films.

The total penetration depth consists of a plastic component and an elastic recovery component which occurs during the unloading. The unloading curve was used to determine the elastic modulus (E) of the films using equations developed by Doerner and Nix (166) and Sneddon (167). The slope of the force (P) versus displacement (h) curve on unloading is:

$dP/dh=1.67\ E^{*}A^{0.5}$ 3.7

where E^{*} is defined as the effective modulus of the system and given by:

$1/E^{*}=(1-\nu^{2})/E + (1-\nu_{i}^{2})/E_{i}$ 3.8

where E and ν are elastic modulus and Poisson's ratio for the specimens, while E_i and ν_i are the same parameters for the Berkovich indenter. In the current analysis E_i and ν_i were taken as 1050 GPa and 0.3, respectively (168).

Microhardness measurements were also performed using a Vickers diamond pyramidal indenter with a load of 0.10 N. An average of 15 measurements were recorded.

3.4. Measurement of Coefficient of Friction and Wear

3.4.1. Design and Construction of a Friction and Wear Tester "Tribometer"

Friction and wear tests were performed under unlubricated sliding conditions using a miniature pin-on-disc type tribometer built for this purpose. The tribometer was designed to measure friction and wear of thin films (a few microns in thickness) for sliding distances in excess of 100 m. The schematic of the tribometer is shown in Figures 3.7(a,b). It consists of a specimen holder (disc) rotated by an A.C. motor and a stationary pin.

Two 120 Ohms strain gauges were mounted on the wear rig arms to measure the normal and tangential displacements of the pin. The strain gauges were, in turn, connected to two high precision 120 Ohms bridge circuits activated by two regulated power supplies with an output voltage of 5 Volts and fed to a computer interface (Fig. 3.7(b)). The whole setup was insulated to minimize temperature fluctuations. Using a data acquisition system, the output voltage across the bridge was collected at a sampling rate of one data point every 2 seconds. The tribometer was calibrated for a load range of 1 to 1500 g and found to exhibit a linear relationship between the voltage measured and the applied normal and tangential loads (Figs. 3.8(a,b)).

A warm-up period (prior to testing) of about one hour was required to obtain a stable response as shown in Figure 3.9. Figure 3.9 also shows that the background noise (fluctuations around a mean value) was low, i.e., about ±2 g. The background noise may come from many sources, such as, instrumental (wires, gauges, resistors, etc.), mechanical vibrations, electromagnetic interference and temperature fluctuations. This noise was further reduced by smoothing the recorded data using running averages.

The sliding pin was made of AISI 304 stainless steel (19wt% Cr, 11wt% Ni, 1.5wt% Mn, 0.07wt% C, 0.02wt% N, the balance Fe). The X-ray diffraction pattern of the material is given in Figure 3.10. The pin had rounded tip with a radius of 2.15 mm. The stainless steel slider pin has a uniform equiaxed grains with an average grain size of 15±3 μm, measured by linear intercept method. The Vickers microhardness of the pin was measured (using 0.1 N load) as 4.5 GPa. It is because of this high hardness and also high oxidation resistance that AISI 304 stainless steel was selected as a counterface material. The material also has high stiffness which makes it possible to transmit the applied load to the sample with minimum deflection. AISI 304 steel is known to have tendency for galling at high loads but did not show galling under the current testing conditions.

3.4.2. Data Acquisition

Unlubricated sliding tests were made under a constant load of 1.0±0.1N. The load was applied to the tip of the stainless steel pin. Films to be tested were ultrasonically cleaned in acetone and methanol to remove any organic residue and mounted on the rotating specimen holder. The sliding of the pin created a circular wear track of about 6 mm diameter on the surface of the films. A constant sliding speed of $1.3\text{x}10^{-2}$ m.s^{-1} was maintained at the centre of the track. The width of the wear track was measured at a regular intervals during the test using a low power optical microscope (magnification x20) and the volume loss (V) of the material during wear was calculated according to the ASTM standard G99 (169) as follows,

$$V=2\pi R[r^2 \sin^{-1}(d_{TW}/2r)-(d_{TW}/4)(4r^2-d_{TW}{}^2)^{1/2}] \qquad 3.9$$

where V is the volume loss (mm^3), R is the wear track radius (mm), r is the radius of the rounded tip of the pin (mm) and d_{TW} is the wear track width (mm). The instantaneous values of the calibrated normal (F_N) and tangential (F_T) forces were measured and continuously recorded to a data acquisition system as a function of test time (sliding distance). The data was then processed to determine the variation of the coefficient of friction ($\mu=F_T/F_N$) as a function of sliding distance.

Most tests were performed under the ambient conditions (21° C, 60% relative humidity). However, to study the effect of vacuum on the friction and wear, the pin-on-disc wear rig was mounted in the specimen chamber of a SEMCO Nanolab 7 scanning electron microscope whose stage was rotated by an external A.C. motor at a speed of $4.2X10^{-4}$ $m.s^{-1}$ (Fig. 3.11). The pressure inside the scope during the wear tests was 10^{-6} torr.

3.5. Topographical Evaluation of Worn Surfaces

Surface roughness of wear tracks at a selected sliding distances were performed using a Mitutoyo Surftest MST-301. The instrument was set to a sampling length of 0.8 mm which is the distance the detector travels and collects data. Surface roughness (Ra) is then calculated from the roughness profile.

The roughness (Ra) is the arithmetic mean of the absolute values of the profile deviation from a centre line. The centre line is defined as a reference line placed in a way such that the sum of the areas limited by it and the roughness profile are equal on both sides (Fig. 3.12). The profile roughness is calculated as:

$$Ra=\left(\int_{0}^{L_s} | Y(x) | \, dx \right) / L_s \qquad 3.10$$

where the roughness profile is given by Y(x) with the X-axis coinciding with the centre line and L_s is the data sampling length. An average of 20 roughness profile measurements were taken for each sliding distance in a tangential direction at the centre of the wear track.

Morphological and microstructural changes in the wear tracks during wear were characterized by a scanning electron microscope (SEM) equipped with an energy dispersive spectroscope (EDS) for semi-quantitative chemical analysis. Microhardness measurements (average of 10 data points) in the bulk materials (aluminum and titanium) below the worn surfaces were made using a Knoop indenter and a load of 0.10 N. These measurements were made as a function of sliding distance and at different depths to monitor the subsurface hardening behaviour.

3.6. Texture Measurements

Texture measurements during the wear process were made by X-ray diffraction inverse-pole-figure technique. The purpose of texture measurements was to relate changes in the friction and wear behaviours to the microstructural changes. Dry sliding wear tests were performed on Al and Ti specimens of 5x5 mm^2. For the Ti the tests were performed on both normal and transverse directions of the disc. A block-on-ring type wear machine as shown in Figure 3.13 was used for these particular experiments. The block-on-ring configuration was chosen over the pin-on-disc wear machine because it provides larger wear surface area for the subsequent X-ray texture analysis. The block-on-disc wear machine consists of a rotating ring, made a of 52100 bearing steel (VH=9.0 GPa) with an outside radius of 37.5 mm. A specimen holder was used to hold the specimen in contact with the ring. The sliding speed was set to a $1.3X10^{-1}$ $m.s^{-1}$. The applied normal load was 10 N and this was provided by the weights placed on top of the specimen holder. The wear tests were performed on a single specimen in ambient conditions and the texture of samples was tested at selected sliding distances and evaluated using X-ray diffraction.

The X-ray diffraction patterns were recorded using a Rigaku X-ray diffractometer and CuK_{α} radiation. Wear specimens were placed in a specimen holder exposing their worn surfaces to the X-ray beam. The patterns were recorded over the range 2θ from 5 to 150° using a scan rate of 2° per minute.

Crystallographic texture is most often characterized by constructing an inverse pole figure from X-ray diffraction data. An inverse pole figure is a stereographic projection showing the intensities of all planes in a specific direction. Harris (170) introduced this technique which incorporates in a single diagram all the information given conventionally in pole charts for various (hkil) reflections and, therefore, it represents a considerable degree of condensation.

To understand how the inverse pole figure may be derived from peak intensities, it is first necessary to examine some of the factors which influence the diffractometer trace. The geometric relationship between the X-ray beam, the sample surface and the detector is of prime importance. These are arranged in such a way that as a scan of θ (Bragg angle) is made, only crystal planes parallel to the plane of the specimen surface contribute to the measured diffracted intensity. For example, for the hexagonal system, the measured intensity of any [hkil] pole, having a tilt angle Φ from the basal pole [0001], represents the intensity of the basal pole [0001] at an angle Φ from the reference direction (normal to the specimen surface), see Figure 3.14.

Measurement of the intensity, I, for all of the (hkil) peaks of a test sample, and comparison with the corresponding intensities, I°, for a random sample, will therefore indicate the preferred orientation existing in the test sample. The randomly oriented sample is a powder with the particles having all possible orientations with respect to the X-ray beam, have diffraction intensities that define the crystallographic isotropy. These orientations are shown on the (0001) and (111) standard stereographic projection of Ti (hcp) and Al (fcc), respectively, shown in Figure 3.15(a,b). The angle ∝ indicates a pole rotation about the [0001] (or [111]) pole and the angle Φ is the tilt of a diffraction pole from the [0001] (or [111]) pole. The significance of monitoring the (0001) and (111) planes during texture evolution is that they represent slip planes in the Ti and Al crystals.

To plot an inverse pole figure, the intensities from the sample and those from randomly oriented sample (taken from the Powder Diffraction File for both Al and Ti) were determined. Then a texture coefficient (T.C.) for each (hkil) is calculated using the equation:

$$T.C._{i} = (I_i / I^{\circ}_i) / [(1/n) * \sum (I_i / I^{\circ}_i)] \qquad 3.11$$

where I_i is the intensity of the ith reflection for the textured sample, I°_i is the intensity of the ith reflection from the randomly oriented sample, n is the number of reflections. The T.C. values are then entered on a stereographic projection.

Pole density distribution curves, T.C.(Φ) versus Φ, were then determined from the inverse pole figures (171). As indicated by the stereographic projections in Figures 3.15(a,b), each of the reflection planes is at some tilt angle, Φ, from the [0001] and [111] poles, respectively. However, the diffraction planes are located along lines at only three positions of rotation angle $\propto$: at 0, 19.1 and 30° for Ti and at 0, 30 and 60° for Al.

First, average T.C. values were calculated at tilt angles (Φ) at 3° (for Ti and 2° for Al) increments for all three lines, separately. Assuming that the intensity between diffraction points varies linearly with the tilt angle Φ. Thus,

$$T.C._{j}(\Phi)=T.C._{dj}+[(\Phi-\Phi_d)/(\Phi_{d+1}-\Phi_d)]*(T.C._{(d+1)j}-T.C._{dj}) \qquad 3.12$$

where $T.C._{j}(\Phi)$ is the texture coefficient at some tilt angle Φ for line j. $T.C._{dj}$ and $T.C._{(d+1)j}$ are the texture coefficients of two consecutive diffraction planes, d and d+1, on the same line j. Φ_d and Φ_{d+1} are the tilt angles of the d and d+1 diffraction planes.

Assuming that the intensity varies linearly with the rotation angle $\propto$. Thus, the T.C(Φ) value is averaged over the range of $\propto$ which is 30 and 60° for Ti and Al on an inverse pole figure, respectively. The average texture coefficient at an angle Φ where all three lines are defined is calculated for Ti and Al by equations 3.13(a,b), respectively.

$$T.C.(\Phi)_{average}=(1/30)\{19.1[(T.C._1(\Phi) + T.C._2(\Phi))/2) + 10.9[(T.C._2(\Phi) + T.C._3(\Phi))/2]\} \qquad 3.13a$$

$$T.C.(\Phi)_{average}=(1/2)\{[(T.C._1(\Phi)+T.C._2(\Phi))/2]+[(T.C._2(\Phi)+T.C._3(\Phi))/2]\} \qquad 3.13b$$

Where $T.C._1(\Phi)$, $T.C._2(\Phi)$ and $T.C._3(\Phi)$ are the texture coefficients of lines 1, 2 and 3, respectively, at the same tilt angle (Φ). If only two lines were defined, for example, lines 1 and 2, then the $T.C.(\Phi)_{average}$ is calculated by simple averaging,

$$T.C.(\Phi)_{average} = (T.C._1(\Phi) + T.C._2(\Phi))/2 \qquad 3.14$$

TEM examination on coarse-grained Al were conducted on both worn and unworn surfaces. Specimens were prepared by polishing the specimen from the back of the worn surface. A 3 mm discs (thickness of about 0.1 mm) from the wear track area and from the unworn surface were cut. The discs were then electropolished using a current of 0.5 A and a voltage of 15 V for 3 minutes. Jet electropolishing was done using a 90% methanol and 10% nitric acid as an electrolyte and the solution maintained at a temperature of about -30° C using dry ice. Thin foils were then examined under a JEOL 100 TEM operated at 100 KeV. selected area electron diffraction (SAED) patterns were taken from worn and unworn surfaces.

Table 3.1. Summary of microstructural and mechanical properties of materials used as sputtering targets.

Material	*Vickers Hardness (Kg/mm^2)	(GPa)	Grain size (μm)
Al	28.5±3.9	0.28±0.04	$(1\pm0.2)10^3$
Al_2O_3	612.2±20.4	6.00±0.20	70±5
Ti (normal)	242.9±12.2	2.38±0.12	20±4
Ti (transverse)	219.4±12.2	2.15±0.12	60±9
Cu	96.9±5.1	0.95±0.05	25±5

* using a load of 0.10 N.

Table 3.2. Fabrication conditions of monolithic and laminated composites prepared by an rf magnetron sputtering system.

	Al/Al_2O_3 laminated composites		Ti/TiN laminated composites		Ti/Cu laminated composites	
	Al layer	Al_2O_3 layer	Ti layer	TiN layer	Ti layer	Cu layer
Sputtering gas	Ar(99.999%)	Ar(99.999%)	Ar(99.999%)	Ar(99.999%)	Ar(99.999%)	Ar(99.999%
Reactive gas	---	O_2	---	N_2		
Pressure (Torr)	$(1.5\text{-}5.0)\times10^{-3}$	$(1.5\text{-}5.0)\times10^{-3}$	$(2.0\text{-}4.5)\times10^{-3}$	$(2.0\text{-}4.5)\times10^{-3}$	$(2..0\text{-}4.5)\times10^{-3}$	$(2.0\text{-}4.5)\times10^{-3}$
Target	Al(99.999%)	Sintered Al_2O_3(99.99%)	Ti(99.999%)	Ti(99.999%)	Ti(99.999%)	Cu(99.999%)
Target diameter	25.4 mm	25.4 mm	25.4 mm	25.4 mm	25.4 mm	25.4 mm
T-S distance*	50 mm	50 mm	50 mm	50 mm	50 mm	50 mm
Substrate temperature	320 K	350 K	320 K	350 K	320 K	320 K
Deposition rate	~ 10nm/min	~ 0.6nm/min	~10nm/min	~0.6nm/min	~10nm/min	10-20nm/min
Power density	15~20 W/cm^2	10~15 W/cm^2	10~20 W/cm^2	10~20 W/cm^2	10-20W/cm^2	10-20W/cm^2

* target to substrate distance.

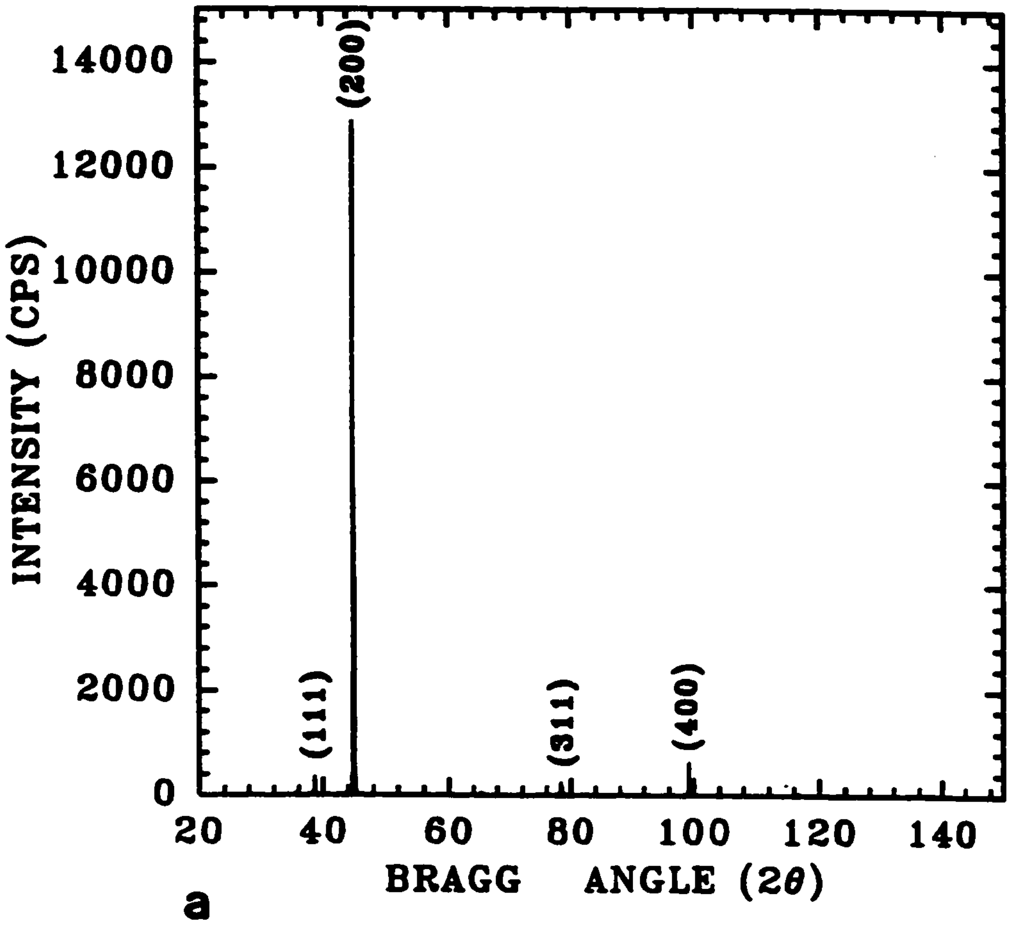

3.1. X-ray diffraction patterns for materials used as sputtering targets, the diffraction peaks are labelled according to the material scanned: (a)Al ; (b)Ti; (c)Cu; (d)Al_2O_3.

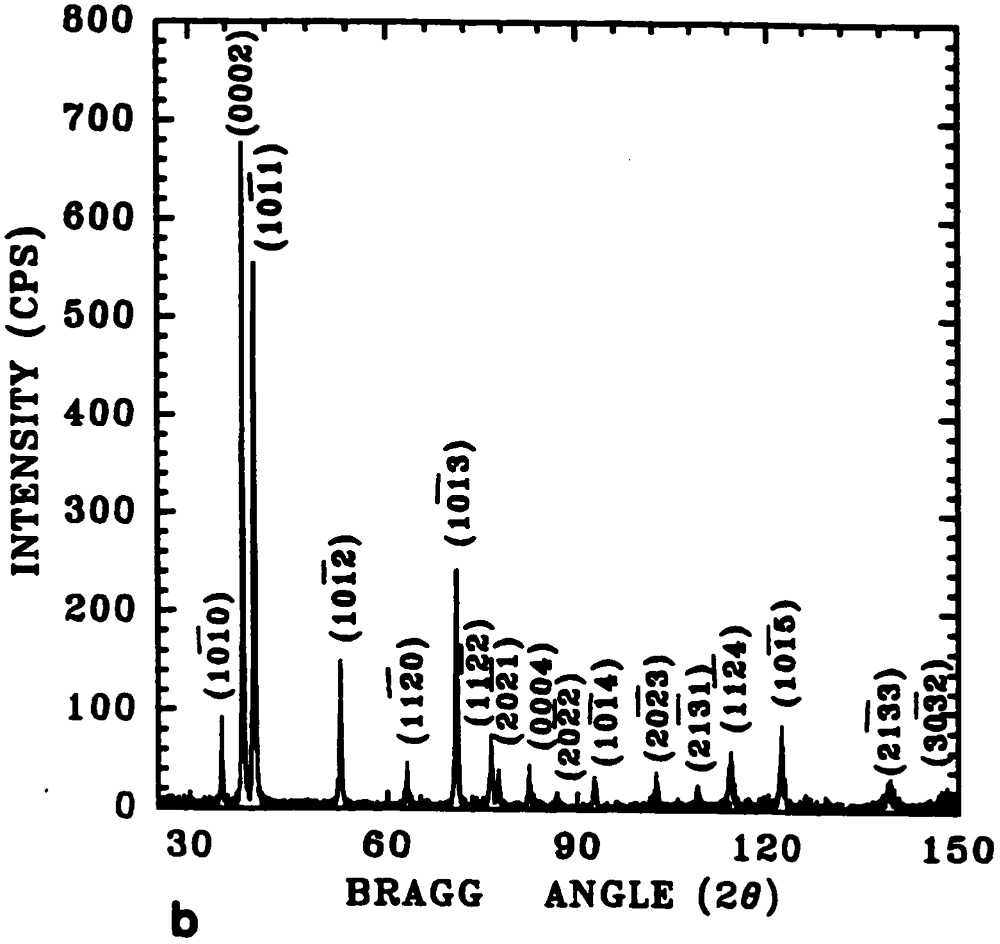

3.1. (continued).

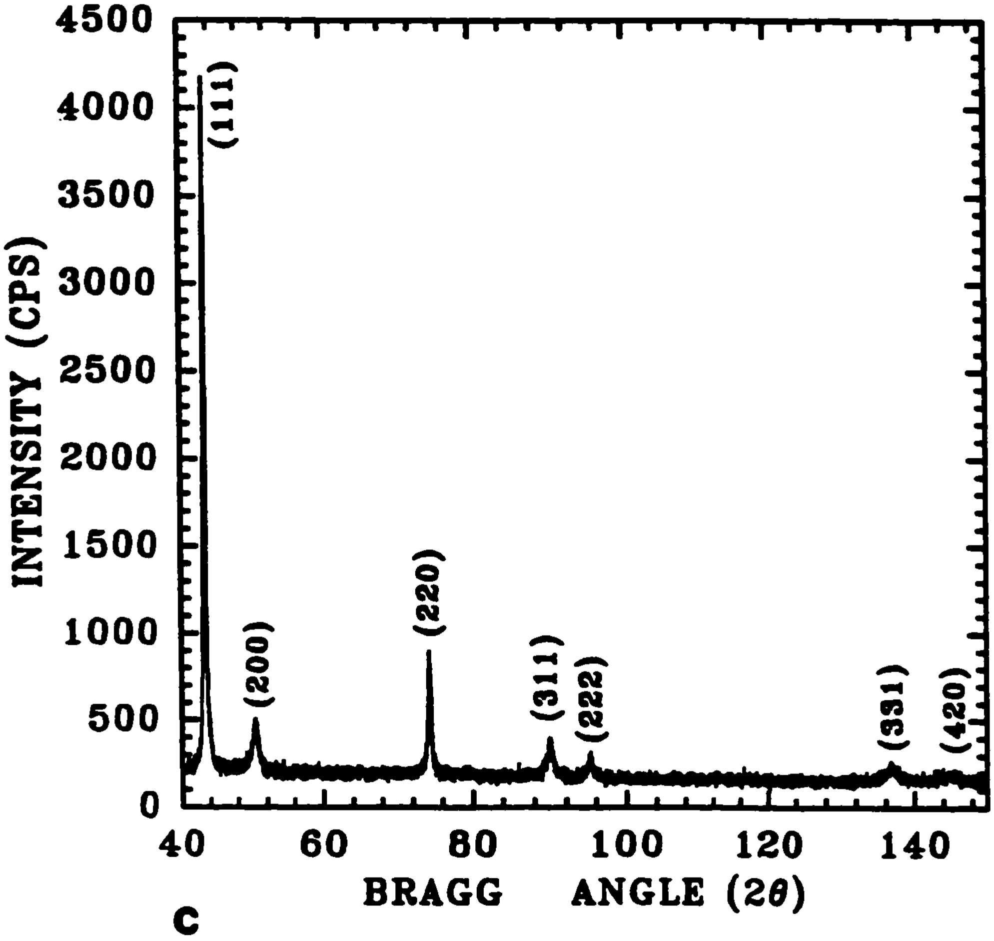

3.1. (continued).

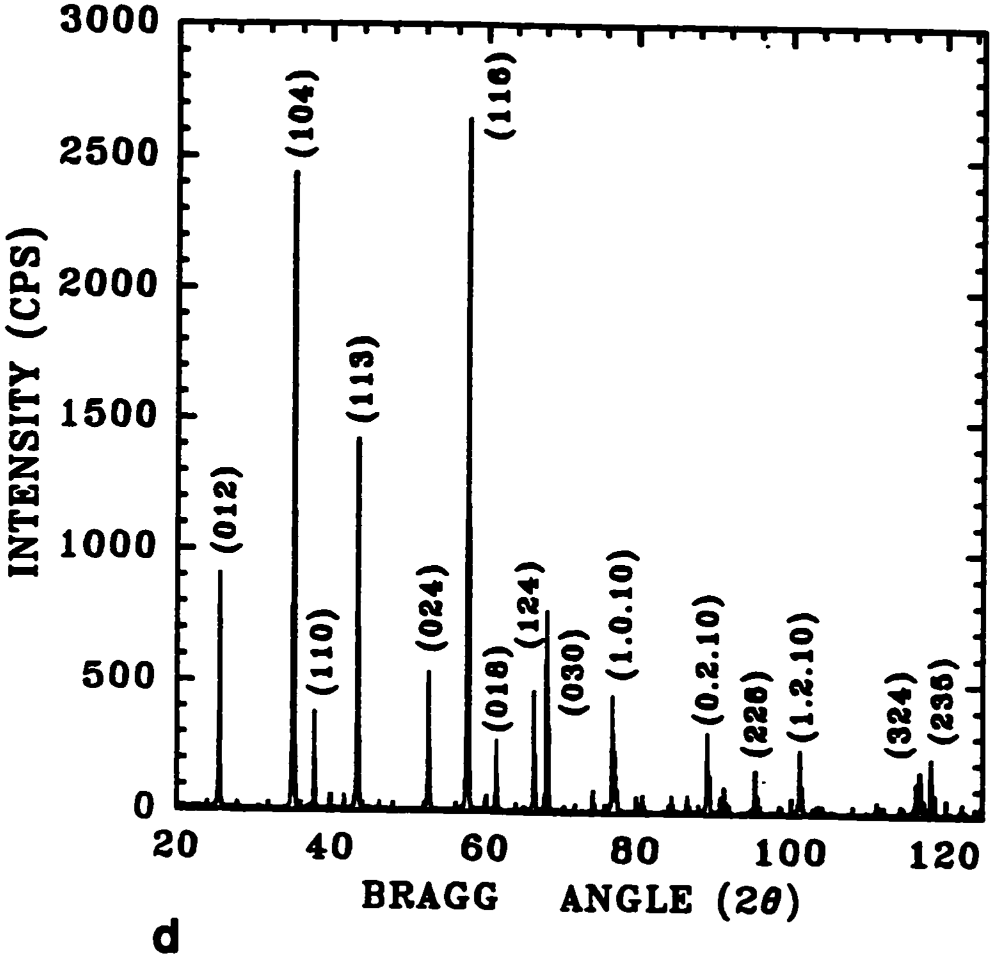

3.1. (continued).

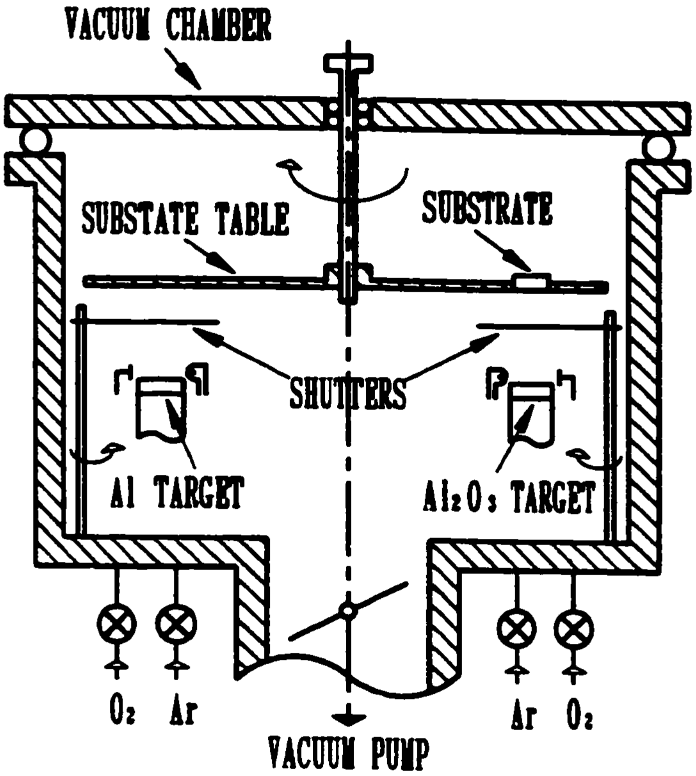

3.2. Schematic of the vacuum chamber of the sputtering unit. The substrate is mounted on a rotating table and switched between target sources.

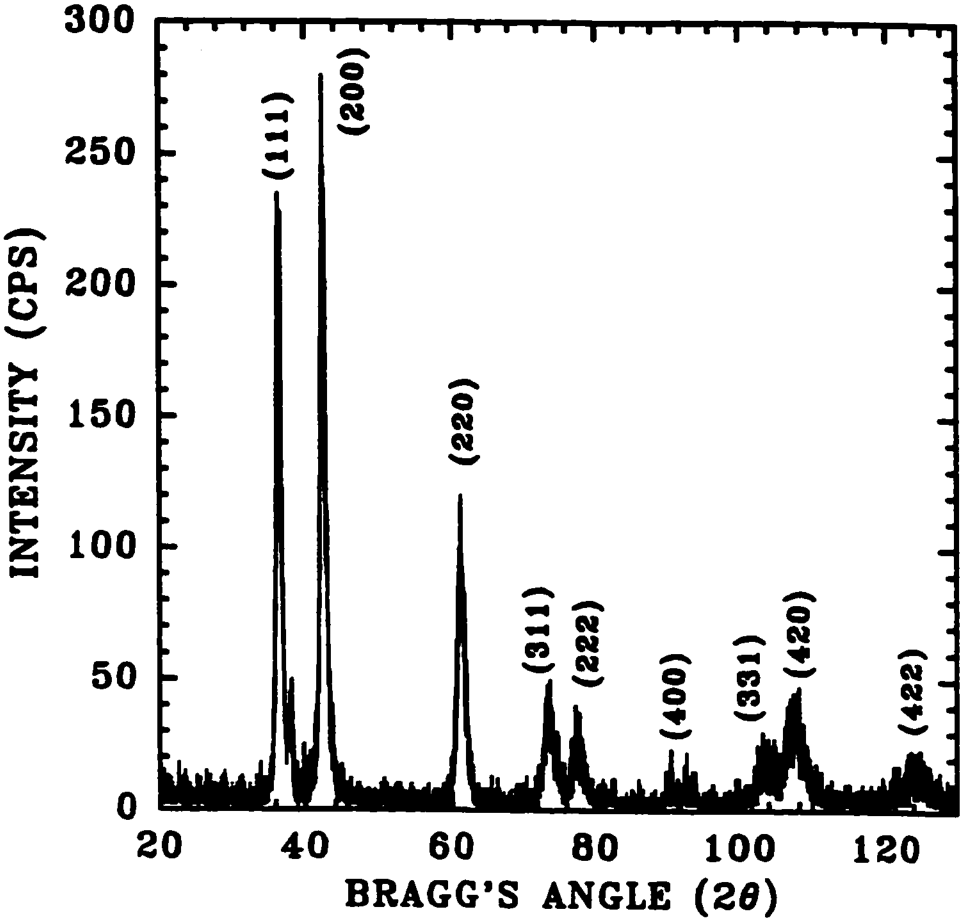

3.3. X-ray diffraction pattern of TiN coating, on a stainless steel substrate, produced by reactive ion plating (RIP) method.

3.4. SEM micrograph of a cross-section of the TiN coating on stainless steel substrate. The coating reveals a thin intermediate monolayer of Ti between a stainless steel substrate and the TiN coating.

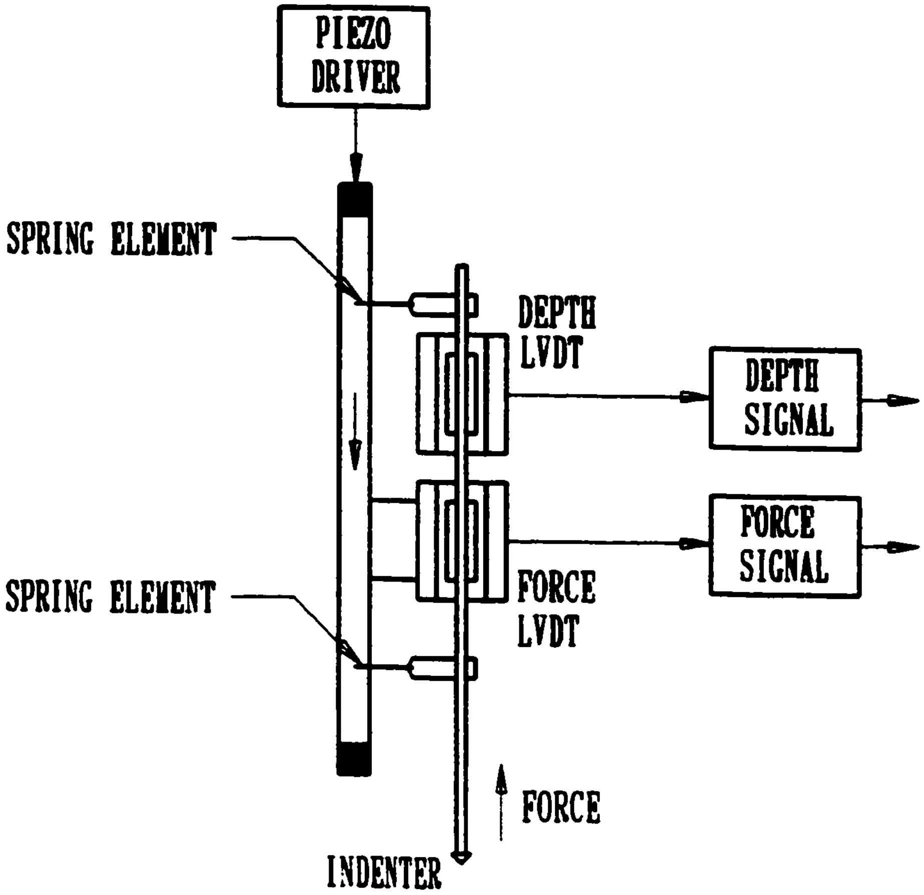

3.5. Schematic diagram showing the operating principles of the nanohardness indenter system. The load is applied to the specimen through a Berkovich indenter.

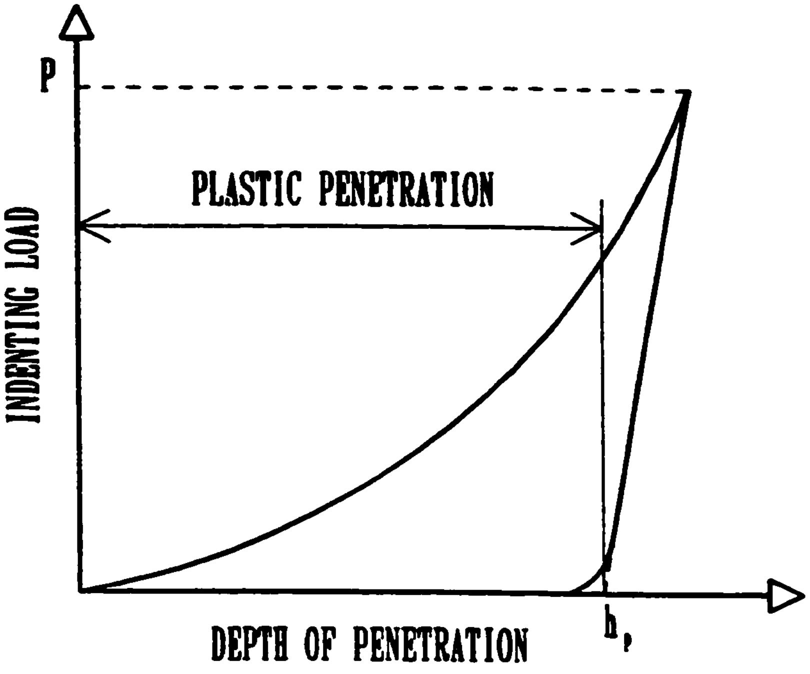

3.6. Typical loading/unloading curve produced by a nanoindentation system. The hardness is calculated using the maximum hardness (P) and plastic deformation (h_p).

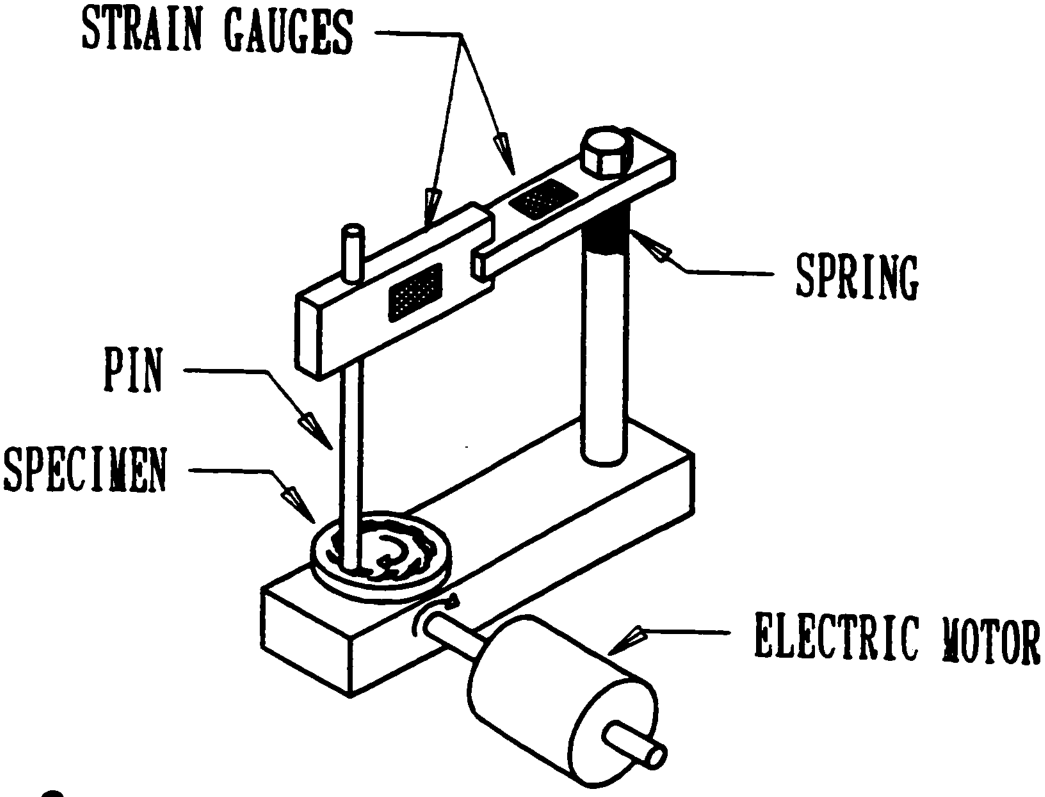

a

3.7. (a)Pin-on-disc wear rig. The load is applied, parallel to the pin axis, through a spring located below the rig arm ; (b)schematic diagram of the electronics of the pin-on-disc set-up.

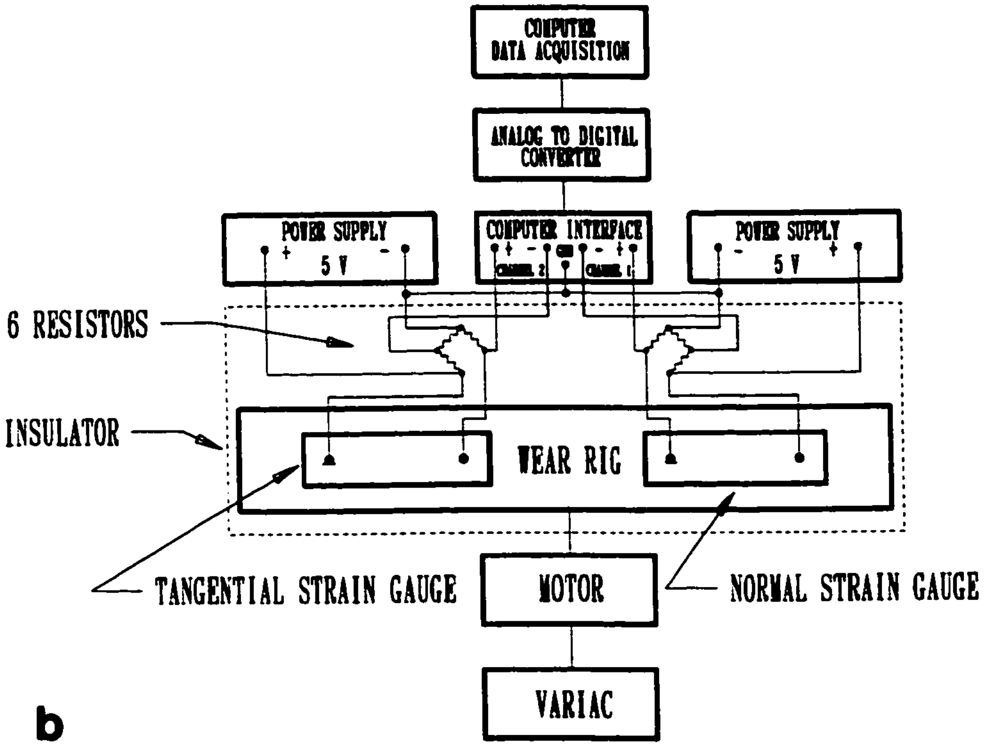

3.7. (continued).

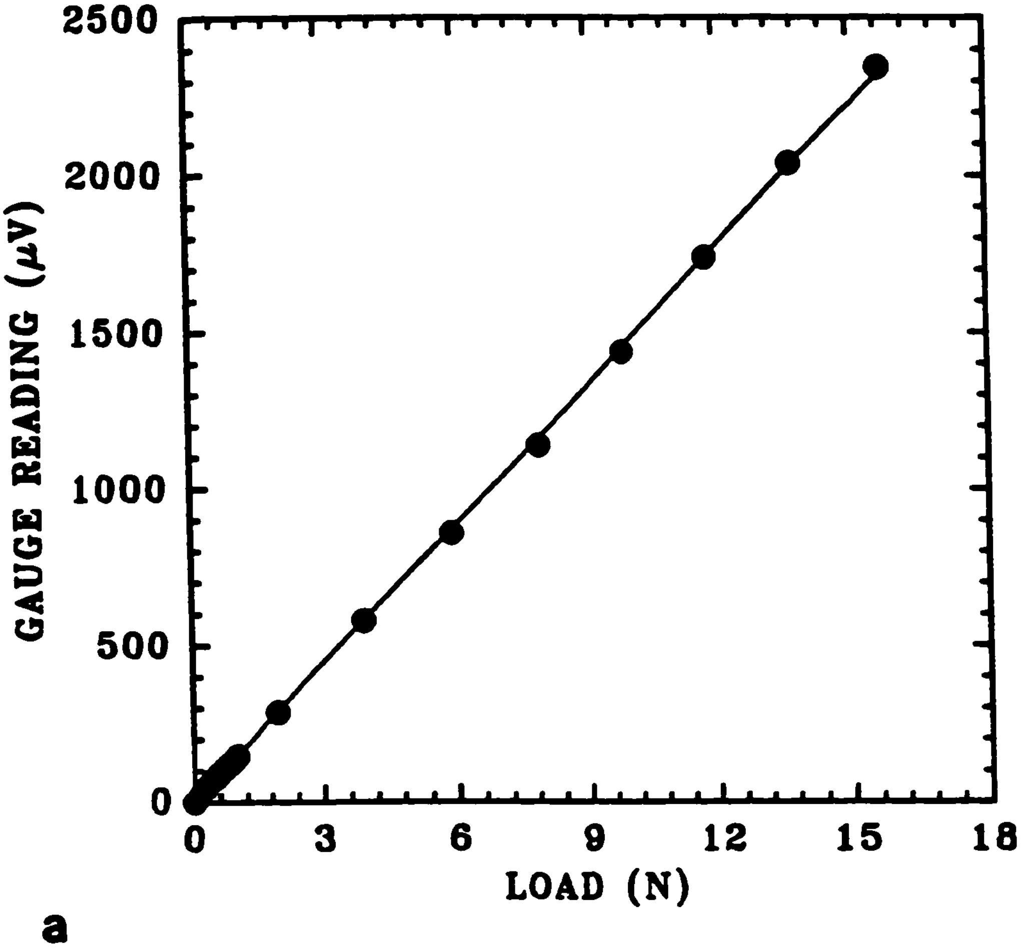

3.8. The tribometer load calibration curves. The tribometer is calibrated by applying a discrete increments of loads (hanging weights) and recording the corresponding output signal from the strain gauges for; (a)normal load; (b)tangential load.

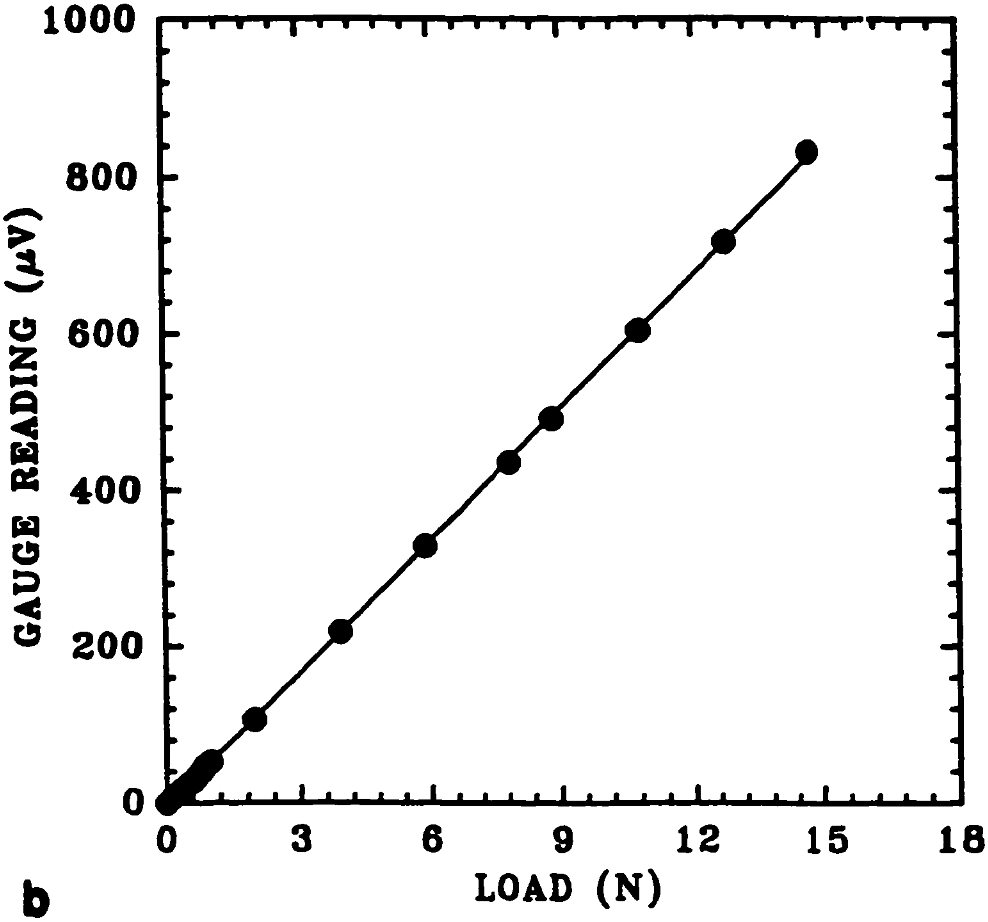

3.8. (continued).

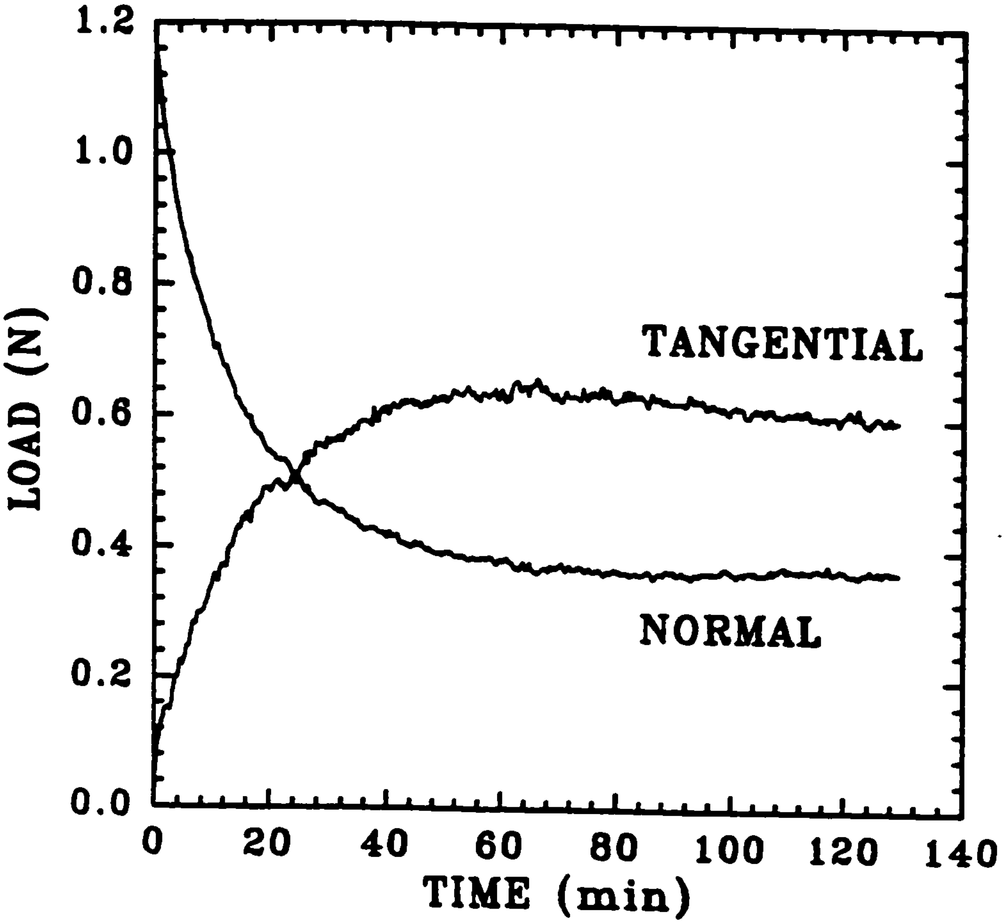

3.9. Diagram showing the stability of the tribometer. The signal from the tangential and normal strain gauges becomes stable after a warm-up period of 40 minutes.

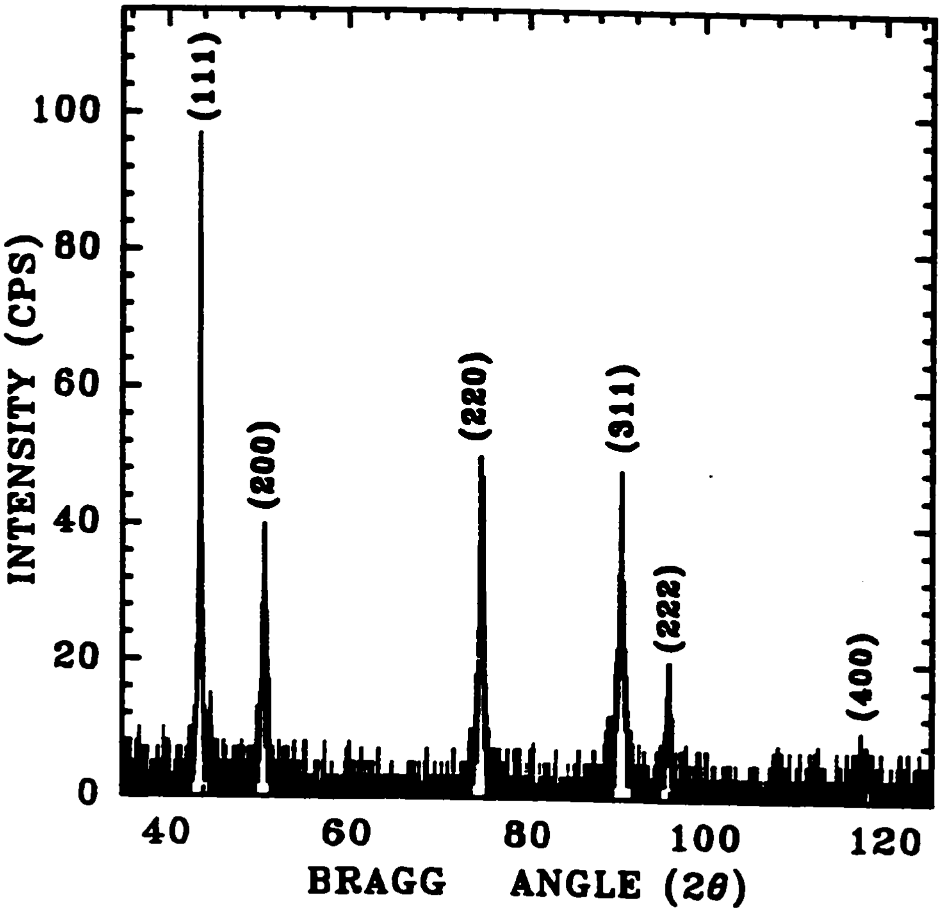

3.10. X-ray diffraction pattern of the AISI 304 stainless steel sliding pin (19wt%Cr, 11wt%Ni, 1.5wt%Mn, 0.07wt%C, 0.02wt%N, the balance Fe).

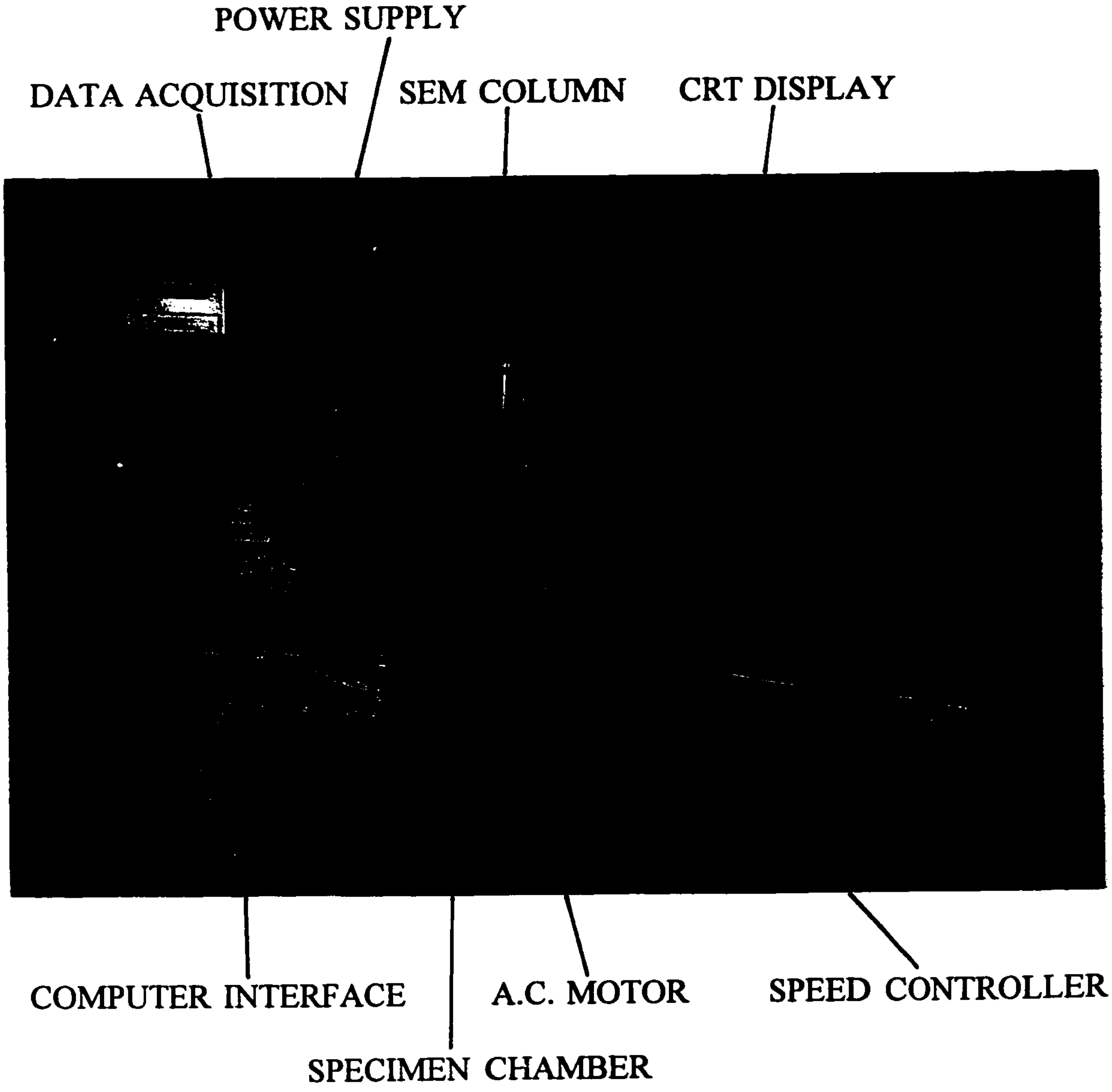

3.11 Experimental set-up for friction and wear measurements inside a scanning electron microscope.

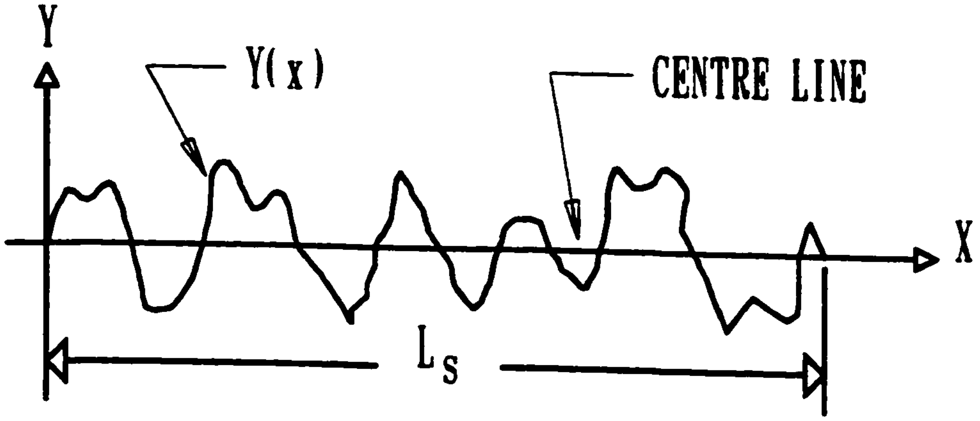

3.12. Illustrative diagram of a typical roughness profile. The Y-direction represents changes in the hight of asperities and the X-direction represents a distance parallel to the sample surface.

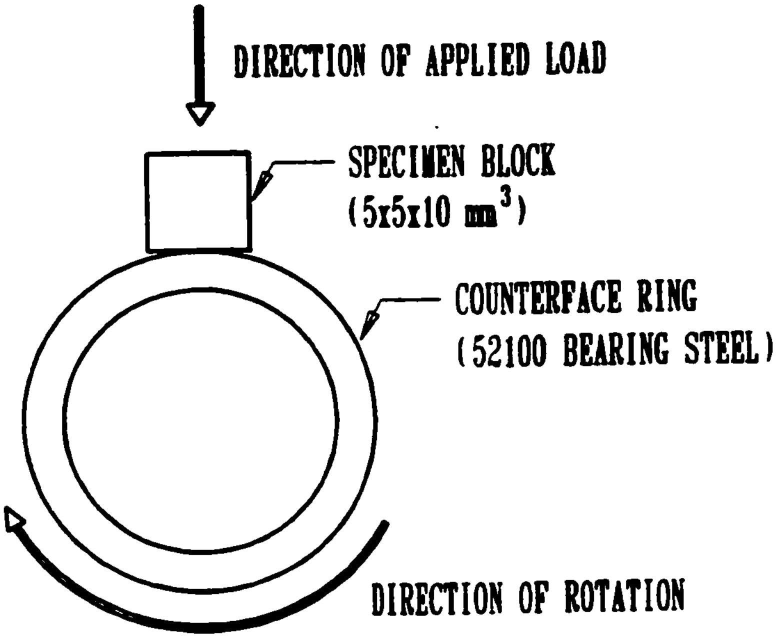

3.13. Schematic of the block-on-ring wear machine. A stainless steel ring rotates clockwise at a speed of $1.3\text{x}10^{-1}$ m.s^{-1} against a specimen block under an applied normal load.

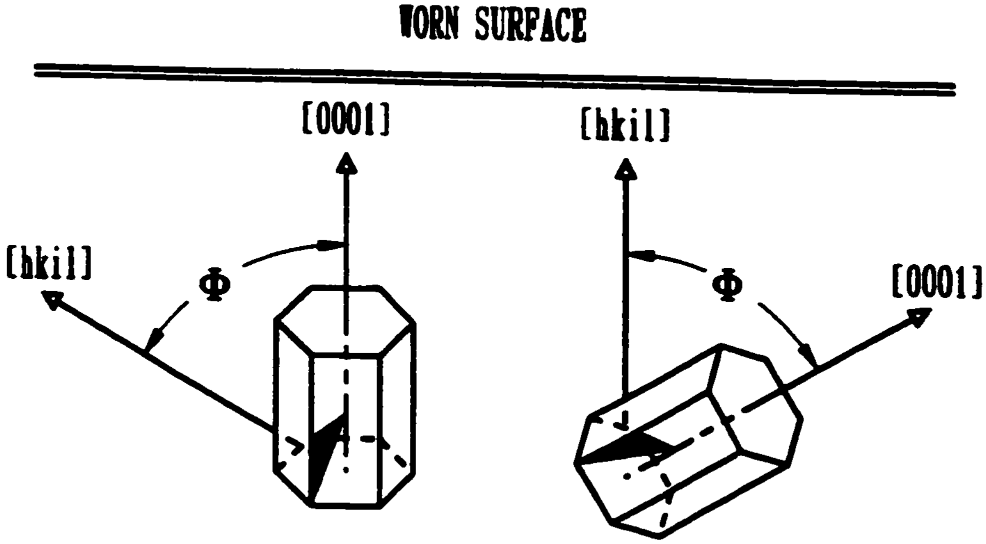

3.14. Schematic diagram showing the relationship between the worn surface exposed to the x-ray beam, the tilt angle (Φ), the basal pole [0001] and an [hkil].

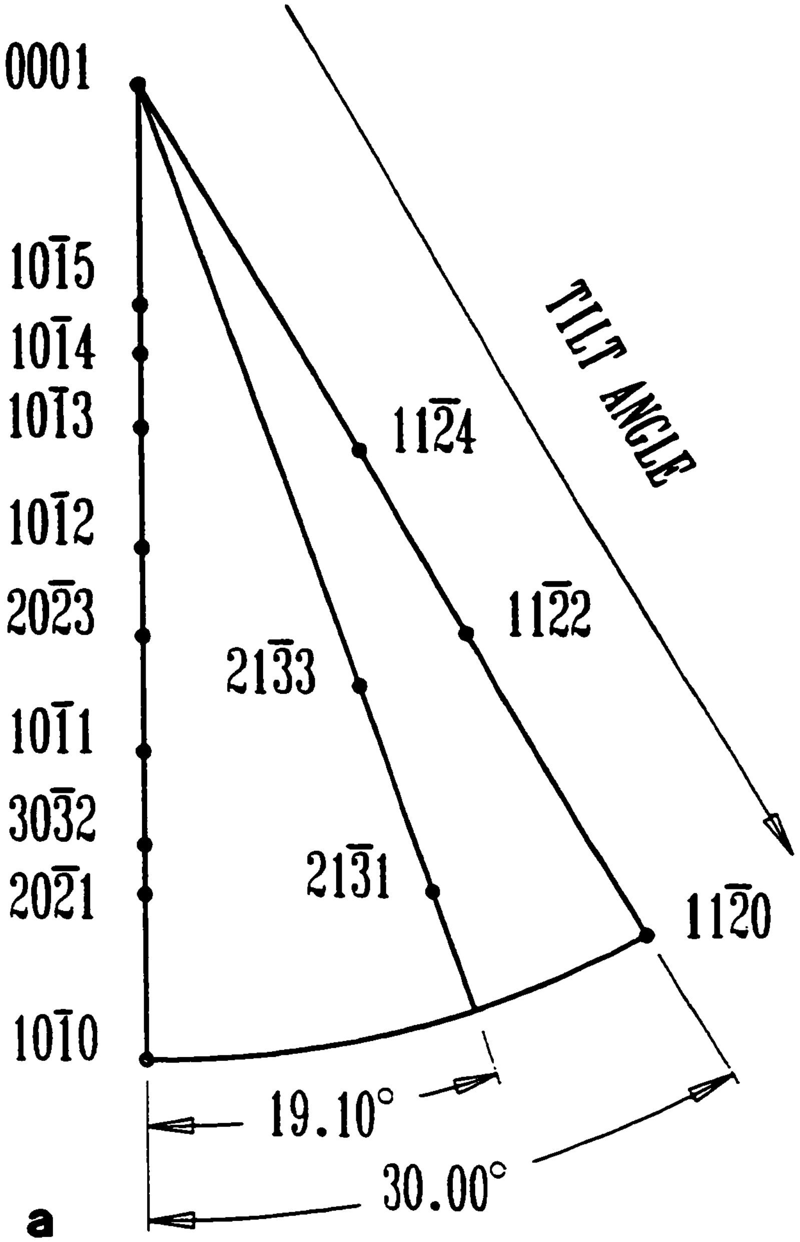

a

3.15. (a)A standard (0001) stereographic projection for titanium (hcp); (b)a standard (111) stereographic projection for aluminum (fcc).

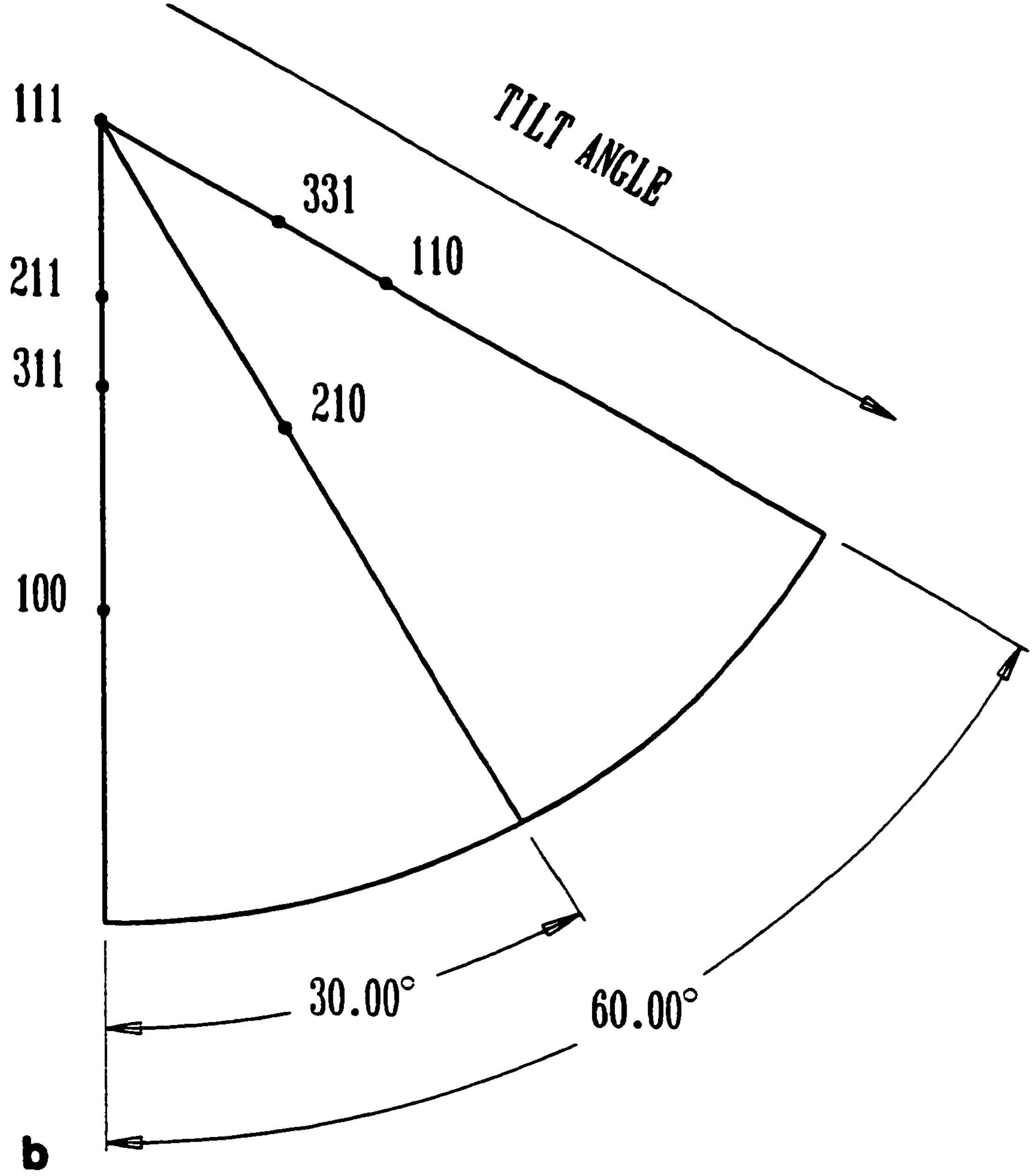

3.15. (continued)

CHAPTER 4

EXPERIMENTAL RESULTS

4.1. Microstructures

The (111) diffraction peaks, obtained from the as sputtered and annealed (at 573 K for 5 and 50 hrs.) aluminum films in order to determine their grain size, are shown in Figures 4.1(a-c), respectively. Figure 4.1(d) shows the (111) diffraction peak for the "standard" aluminum powder of grain size ~2 μm. The standard specimen has the sharpest $k_{\alpha 1}$ peak with a broadening ($\beta_{standard}=\beta_{instrumental}=\beta_{Total}$) of 0.1°, while the as sputtered film has a broader peak, $\beta_{specimen}=0.6°$. Using the method described in section 3.2 the grain size of the as-sputtered aluminum can be calculated as 16.4±1.5 nm and it is found that the grain size had increased to 31.7±3.0 nm after annealing 5 hrs. at 573 K and 98.0±5.0 nm after annealing to 50 hrs. at 573 K. The specimen peak broadening is determined by subtracting the broadening due to instruments from the total peak broadening (i.e., total peak broadening is the total area under the peak/peak height). The broadening due to the specimen is attributed to fine grain size and is calculated using equation 3.5. The peak broadening due to specimens is listed in Table 4.1.

Figure 4.2(a) shows the dependence of grain size of as-sputtered aluminum films on the annealing time. Measurements made by X-ray line broadening technique are in good agreement with the TEM measurements using linear intercept method. TEM bright field micrographs of the as-sputtered and annealed (for 50 hrs.) films are shown in Figures 4.2(b,c). It is seen that the microstructure before and after annealing are effectively free of porosity and consist of a uniform distribution of equiaxed grains. The SAED (Selected Area Electron Diffraction) patterns in the insert belong to aluminum. A pattern of continuous rings for the as-sputtered aluminum is an indicative of fine grain size (16.4 nm) as compared to a pattern of spotty rings for the annealed specimen (98.0 nm).

Cross-sectional specimens were prepared for the SEM examination to confirm the thickness of each layer in Al/Al_2O_3, Ti/TiN and Ti/Cu laminated composites (see Figs. 4.3(a-c)). The periodicity and continuity of the layers are clearly seen. The layer thicknesses of the films are given in Table 4.2. X-ray diffraction (XRD) patterns of Al, Al/Al_2O_3, Ti, Ti/TiN and Ti/Cu films were obtained using a Rigaku X-ray powder diffractometer and CuK_α radiation. It is seen that Ti/TiN films (Fig. 4.4(a)) exhibit clearly defined TiN peaks. Thus Ti (Fig. 4.4(b)) and TiN layers in these films have crystalline structures. On the other hand, XRD pattern of Al/Al_2O_3 composites (Fig. 4.5(a)) is identical to that of the as-sputtered monolithic Al (Fig. 4.5(b)) and does not reveal presence of a crystalline oxide phase. The non-crystalline nature of the Al_2O_3 layers (deposited on NaCl substrate) is shown by selected area diffraction studies by TEM in Figure

4.6 which shows no ring pattern which is an indication of an amorphous structure. The X-ray diffraction pattern of Ti/Cu laminate composite (Fig. 4.7) reveals the existence of diffraction peaks from both polycrystalline titanium and copper layers.

4.2. Micromechanical Properties

Force-displacement (penetration depth of indenter) curves for monolithic aluminum with different grain sizes show the loading/unloading cycles of the nanoindentation test (Fig. 4.8(a)). Similar curves for Al/Al_2O_3, Ti, TiN, Ti/TiN and Ti/Cu with different layer thicknesses are shown in Figures 4.8(b,c,d). In these tests nanoindentations were made perpendicular to the plane of the layers. Each curve in these figures represents an average of 20 loading/unloading curves each taken from a different area on a single specimen. The effective plastic depth of penetration, h_p, was computed by a regression line through the unloading curve over the upper one-third of the data, then the hardness at the maximum load was calculated from the value of h_p using equation 3.6. The elastic moduli, however, were calculated from the slope of the upper one-third portion of the unloading part of the curve using equations 3.7 and 3.8. Tables 4.3 and 4.4 summarize the mechanical properties of monolithic and nanolaminated composite films, respectively.

4.2.1. Monolithic Nanocrystalline Aluminum

According to Figure 4.9(a), within the 16-100 nm grain size, the hardness data obeys a Hall-Petch type equation,

$$H(Al) = 34\ [MPa] + 0.21\ [MPa\ .\ m^{0.5}]\ D^{-0.5}\ [m^{-0.5}] \qquad 4.1$$

where D is the grain size of aluminum. Equation 4.1 suggests that Hall-Petch strengthening in polycrystalline aluminum extends to grain sizes as small as 16 nm. Data in Figure 4.9(a) also shows that the extrapolation of the Hall-Petch plot to coarse grain range underestimates the measured hardness. Caution must be exerted in comparing hardness results over a broad range of grain sizes because when a load of 20 mN is applied (as in Fig. 4.8(a)) the indentation impression covers approximately 5-50 grains for the nanocrystalline material which is clearly not the case for the material with a grain size of 1 mm.

4.2.2. Nanolayered Composites

The nanoindentation measurements for Al/Al_2O_3 and Ti/TiN show a consistent trend: as the spacing between the non-metallic layers becomes smaller, the hardness increases. The hardness data for Al/Al_2O_3 and Ti/TiN composites are plotted as a function of both reciprocal (λ^{-1}) and reciprocal-square-root ($\lambda^{-0.5}$) of metallic layer thickness (Fig. 4.9(b,c)). The exponent of the layer thickness might vary between -0.5 to -1 but tends to be closer to -0.5. Thus, the hardness dependence on the layer thickness can be described better by a Hall-Petch type equation. For Al/Al_2O_3 (with the exception of laminates with the smallest aluminum layer thickness), this can be expressed as:

$$H(Al/Al_2O_3) = 1653\ [MPa] + 1.25\ [MPa\ .\ m^{0.5}]\ \lambda^{-0.5}_{Al}\ [m^{-0.5}] \qquad 4.2$$

and for Ti/TiN,

$$H(Ti/TiN) = 10965\ [MPa] + 0.71\ [MPa\ .\ m^{0.5}]\ \lambda^{-0.5}_{Ti}\ [m^{-0.5}] \qquad 4.3$$

Ti/Cu laminated composite, on the other hand, exhibits an inverse Hall-Petch relationship, as shown in Figure 4.9(d).

$$H(Ti/Cu) = 6230\ [MPa] - 1.00\ [MPa\ .\ m^{0.5}]\ \lambda^{-0.5}_{Ti}\ [m^{-0.5}] \qquad 4.4$$

The negative slope indicates a softening of the Ti/Cu laminates as the layer thickness decreases.

4.3. Coefficient of Friction and Wear

Coefficient of friction versus sliding distance curves give details on the change in the friction behaviour of a material as a function of sliding distance. These curves are obtained using a load of 1 N and speed of $1.3\text{x}10^{-2}$ m.s^{-1} under ambient conditions. Prior to examining the data for the materials tested it should be noted that three important parameters can be obtained from such a curve. These are the peak value of the coefficient of friction (μ_p), the steady-state value of the coefficient of friction (μ_{ss}) and the sliding distance (time) at which transition to steady-state (S_t) occurs.

The coefficient of friction curves for all materials tested had the same overall shape (Fig. 4.10). Each curve was characterized by two friction regimes; initially, the coefficient of friction increases rapidly until reaching a maximum value μ_p. This was followed by a gradual decrease to a steady-state value μ_{ss} where the coefficient of friction became independent of sliding distance.

The cumulative volume loss versus sliding distance curves (Fig. 4.11) showed two wear regimes. Initially, the wear rates (slope of the cumulative volume loss versus sliding distance curves) were high (severe wear) but after a certain sliding distance, the slope decreased to a lower value (mild wear). Severe wear was characterized by high wear rate, high coefficient of friction and heavy surface deformation. Mild wear, on the other hand, was associated with low wear rate and coefficient of friction as well as small amount of plastic deformation. The transition from severe to mild wear generally corresponded to a similar (i.e., about the same sliding distance) transition from the peak to steady state coefficient of friction regime.

4.3.1. Nanocrystalline Monolithic Aluminum

The principal effect of reducing the grain size of aluminum is to decrease the value of the peak coefficient of friction (Fig. 4.10(a-d)). For a grain size of 98 nm, μ_p is 0.94. This is reduced to 0.62 in a sample with a grain size of 16.4 nm. Compared to the coarse-grained aluminum (D=1 mm) which exhibits the highest value for μ_p (1.34) this represents a total decrease of about 54%. On the other hand, only a slight variation in the values of the steady-state coefficient of friction were observed. Within the broad grain size range studied, μ_{ss} varied only between 0.10 to 0.25. According to Figure 4.10, aluminum with a grain size of 16.4 nm shows a transition to steady-state in a shorter time (S_t≈50 m) compared to coarse grained aluminum, for which S_t≈80 m. The friction curve for 1100 aluminum alloy used as a substrate material (Fig. 4.10(e)) shows a higher value for the peak coefficient of friction than the nanocrystalline aluminum films tested (Fig. 4.10(a-c)). The values of the parameters which characterize friction curves for different grain sizes are given in Table 4.5.

Wear rate data for aluminum with different grain sizes (Table 4.5) shows that grain refinement has a significant influence on the wear resistance. Aluminum with a grain size of 16.4 nm shows approximately a one order of magnitude decrease in the severe wear rate and two orders of magnitude decrease in the mild wear rate with respect to coarse-grained aluminum.

In order to assess the role of the test atmosphere, friction tests were also performed in the vacuum chamber of an SEM. Results of friction tests performed in vacuum (10^{-6} torr) are given in Figures 4.12(a-c). These figures show the initial stages (up to 4 m) of the friction curves for aluminum tested using a speed of 4.2×10^{-4} $m.s^{-1}$ (This speed is 30 times slower compared to the regular test). In vacuum, the coefficient of friction increases from an initial value towards a maximum, but the rate of increase is higher compared to tests performed in air under the same sliding speed (Fig. 4.13(a-c)). There is over 40% increase in the coefficient of friction measured in vacuum compared to tests in air for all the grain sizes investigated (see Table 4.6). The volume loss versus sliding distance curves for nanocrystalline and coarse-grained aluminum tested in vacuum and air at a sliding speed of 4.2×10^{-4} $m.s^{-1}$ (Fig. 4.14) show that wear rates (Table 4.6) exhibit a systematic decrease as the grain size is decreased and that the specimens tested in vacuum consistently show higher wear rates.

4.3.2. Nanolaminated Al/Al_2O_3 Composites

Friction curves for nanolaminated Al/Al_2O_3 composites with aluminum layer thickness of 200 and 500 nm show the same trend as monolithic aluminum

(Fig. 4.15). The effect of introducing Al_2O_3 layers to monolithic Al is to reduce the peak coefficient of friction. For example, μ_p=0.62 for monolithic aluminum (D=16.4 nm) is reduced to 0.36 for Al/Al_2O_3 with 200 nm Al layer thickness. In fact Al/Al_2O_3 laminated composites exhibit lower peak coefficients of friction than both their pure components (peak coefficient of friction of Al_2O_3 is 0.84, Fig. 4.16). An even further reduction (about 73%) in the peak coefficient of friction is observed when comparing Al/Al_2O_3 to aluminum (D=1 mm).

Decreasing the layer thickness also causes a reduction in the peak value of the coefficient of friction. The steady state coefficient of friction, however, does not vary significantly by reducing the aluminum layer thickness. For example, as the aluminum layer thickness decreases from 500 to 200 nm the peak coefficient of friction decreases from 0.52 to 0.36. In Figure 4.15(a) a systematic decrease in the sliding distance, at which transition to steady-state (S_t) occurs, is observed with decreasing aluminum layer thickness.

Values of wear rates in Table 4.7 (obtained from Figure 4.17) indicate that reducing the aluminum layer thickness translates to a reduction in the wear rate. Both severe and mild wear rates are reduced by 10 and 35%, respectively, as the aluminum layer thickness is reduced from 500 to 200 nm.

In summary, nanolaminated Al/Al_2O_3 composite (with 500 nm Al layer thickness) provides a reduced peak coefficient of friction as compared to its monolithic components, Al and Al/Al_2O_3. Further decreases in the peak coefficient of friction and the wear rates can be achieved by reducing the aluminum layer thickness in layered Al/Al_2O_3 composite.

4.3.3. Monolithic TiN and Nanolaminated Ti/TiN Composites

Friction data for titanium-based coatings (Fig. 4.18(a-d)) can be described as follows. In Ti/TiN nanolaminated composites, reducing the layer thickness causes a reduction in the steady-state value of the coefficient of friction. The steady-state coefficient of friction is reduced from 0.39 to 0.23 as the titanium layer decreases from 450 to 150 nm. Comparison of commercial TiN (RIP) coating with Ti/TiN nanolaminated composites having a Ti layer thickness of 150 nm shows that monolithic TiN exhibits lower steady state coefficient of friction ($\mu_{s.s}$(TiN)=0.1, $\mu_{s.s}$(Ti/TiN)=0.23). On the other hand, Ti/TiN laminated composite exhibits a lower peak coefficient of friction and lower transition time to steady state than monolithic TiN, i.e., μ_p=0.67, S_t=62 m for Ti/TiN as compared to μ_p=0.93 and S_t=115 m for monolithic TiN.

Coarse grained titanium was tested for friction behaviour on both normal and transverse (at a right angle to the plane of the disc) sections (Fig. 4.19(a,b)). Friction curves of the titanium normal section show a sharp increase in the coefficient of friction up to a value of 0.69 and remains steady afterwards. However, the friction curve of the titanium transverse section show a peak coefficient of friction of 1.04 followed by a transition to a steady state ($\mu_{s.s}$=0.59).

The transition in the coefficient of friction was not observed from the tests performed on the normal section.

Coefficient of friction of silica glass used as a substrate material (Fig. 4.20) is characterized by a peak coefficient of friction of 0.68 and a steady state coefficient of friction of 0.5 in comparison to Ti and Ti/TiN films which show different coefficient of friction parameters.

Volume loss versus sliding distance curves for Ti-based materials (Fig. 4.21) show two regions similar to Al and Al/Al_2O_3. A systematic decrease in the severe and mild wear rates is observed as the titanium layer thickness in Ti/TiN composites is reduced from 450 to 150 nm (Table 4.8). Monolithic TiN exhibits a remarkably low wear rate both in severe and mild regimes as compared to all other materials tested.

4.3.4. Nanolaminated Ti/Cu Composites

Figure 4.22 gives the friction curves for coarse-grained copper, used as a sputtering target, and Ti/Cu laminates with Ti layer thickness of 150 nm. Ti/Cu laminated composite shows a reduction in the peak coefficient of friction as compared to conventional copper. Comparison of the laminated Ti/TiN to the laminated Ti/Cu composites having similar layer thickness reveals that Ti/TiN exhibits lower peak and lower steady-state coefficients of friction (reductions of 24 and 50%, respectively). The effect of incorporating TiN layers to monolithic Ti is to reduce the coefficient of friction while incorporating (Cu) layers seems to increase the peak coefficient of friction. Both the severe and mild wear rates (Fig. 4.23) of the Ti/TiN are an order of magnitude lower compared to the Ti/Cu nanolaminated composite having the same layer thickness (Table 4.9).

4.4. Examination of Worn Surfaces

4.4.1. Monolithic Aluminum

Worn surfaces were examined at two characteristic distances, namely, at 12 m which corresponds to a sliding distance where coefficient of friction and wear rates are high and at 90 m where wear becomes mild and proceeds under steady-state conditions.

Worn surface of coarse-grained aluminum tested to 12 m was subjected to severe deformation and was heavily damaged (Fig. 4.24(a)). The surface consisted of a series of parallel grooves, of about 100 μm wide each, extending longitudinally towards the sliding direction (as a result of a microploughing process). The material within the grooves was displaced to the edges forming a topography which can be described as extruded ridges. It is not clear whether one or more wear mechanisms were responsible for the formation of the observed grooves and ridges but the origin of microploughing can be attributed to a process of abrasive wear by the hard steel counterface. On the other hand, the presence of continuous scratch marks along and inside the grooves can be regarded as compelling evidence for the abrasive wear. The large scale deformation process observed on the worn surface appears to have led to the removal of the wear particles by the fracture of the extruded ridges. An example for the microcracking is shown in Figure 4.24(a,b). The loose debris particles detached from the worn surface were in the form of plate-like particles of approximately 10-25 μm diameter. Examples of debris particles adhered on the wear track can be seen in Figure 4.24(c). A large ribbon-like chip about 250 μm long which appears to be cut and removed from the edge of the wear track leaving behind a deep groove (Fig. 4.24(d)). Figure 4.24(e) shows shear flow of material pointing in the sliding direction as it is being dragged ahead of the counterface. Material ahead of the interface curls-up, separates from the surface (Fig. 4.24(f)) and then breaks-up, generating large wear debris particles (Fig. 4.24(g)).

In contrast, nanocrystalline aluminum samples tested under the same conditions displayed smoother wear tracks. Microgrooves and ridges can also be seen on the worn surface of 16.4 nm aluminum (Fig. 4.25), but these are now much narrower (and shallower) indicating that the nanocrystalline aluminum resisted damage caused by plastic deformation and abrasion more effectively. Furthermore, the debris particles are finer in size (<1 μm) than those for coarse-grained (D=1 mm) specimen.

Figure 4.26(a,b) show, respectively, the worn surface morphologies of coarse and fine grain sizes at 90 m, i.e., within the mild wear regime. The most noticeable feature of the wear track of coarse-grained aluminum is its smoothness (Fig. 4.26(a)). The surface is almost featureless and the wear grooves are hardly visible which suggests that during sliding the surface of aluminum becomes polished by the stainless steel pin. Debris particles rejected from both sides of worn area consist of submicroscopic particles. Thus, the surface of the coarse-grained aluminum gradually assumes a similar morphology to that of its nanocrystalline counterpart (Fig. 4.26(b)). The contact surface of the stainless steel pin run against aluminum (D=1 mm) shows (Fig. 4.27) no evidence of wear or material transfer after 90 m.

4.4.2. Nanolaminated Al/Al_2O_3, Ti/TiN and Ti/Cu Composites

The worn surface of Al/Al_2O_3 (having 200 nm aluminum layer thickness) tested to a sliding distance of 12 m (Fig. 4.28(a)) reveals shalow microgrooves, as well as microscratches and ridges along the wear track as a result of microploughing by the counterface asperities. Al/Al_2O_3 shows, however, a lesser degree of damage and deformation compared to coarse-grained aluminum (Fig. 4.24). Fine wear debris particles (<1μm) pushed along the sides of the wear track are also observed. Figure 4.28(b) is a wear track tested under the same conditions but at a sliding distance of 90 m. The latter shows features comparable to those developed after sliding to 12 m but now the worn surface is smoother and the microgrooves are shallower.

The wear track of the coarse-grained titanium specimens shows the same type of features for both sliding distances of 12 and 90 m (Fig. 4.29). Shallow microgrooves covered with finely dispersed wear debris particles are evident. The worn surface of the nanolaminated Ti/TiN (having 150 nm Ti layer thickness) shown in Figure 4.30 reveals shallow worn surfaces having sharp wear track edges and fine wear debris particles (~5μm) for the 12 m sliding distance wear surface and even finer wear debris (<1μm) for the 90 m. The wear track morphologies of both pure Ti and Ti/TiN seem to be similar, although Ti/TiN composite has a narrower wear track than pure Ti.

An SEM micrograph of the wear track of Ti/Cu (having 150 nm Ti layer thickness) at 12 m sliding distance shows that layers of Ti and Cu were delaminated at the edges of the wear track (Fig. 4.31). The nanolaminated Ti/Cu composite also shows a zigzagged wear track edge as opposed to a straight wear track edge observed for nanolaminated Ti/TiN having the same interlayer spacings and tested under the same conditions.

4.5. Roughness of Worn Surfaces

Surface roughness of worn surfaces as a function of sliding distance has been determined in an effort to understand the changes in the coefficient of friction and wear rates with distance. Surface roughness (Ra) versus sliding distance plots for the coarse-grained aluminum and titanium are shown in a Figure 4.32 and Table

4.10. The roughness of the wear track of coarse-grained aluminum (Fig. 4.32(a)) appears to rapidly increase up to a considerable average roughness value of 10 μm at a sliding distance of 5-10 m. This followed by a gradual decrease to Ra=4 μm at a sliding distance of about 90 m and remains steady afterwards. Coarse-grained titanium (Fig. 4.32(b)), however, increases to a steady roughness value of about Ra=3.5 μm which persists up to a sliding distance of 100 m.

4.6. Subsurface Hardness

In order to study the change in the flow strength of the material adjacent to the worn surfaces, as a function of sliding distance, the hardness below the centre of the wear track were measured in coarse-grained aluminum and titanium samples (Fig. 4.33). There is a considerable hardening of the material layers near the contact surface. For a given sliding distance, the subsurface hardness increases near the surface and decreases as the depth below the worn surface increases until it reaches the bulk hardness. For example, for coarse grained aluminum, the hardness measured as 350 MPa at depth 35 μm increases to almost 450 MPa at 5 μm beneath the wear track after a sliding distance of 1 m. The figures also show how the hardness increases with sliding distance, for a given depth. The effect of the sliding distance on the subsurface hardness (measured at 10 μm) is given in Figure 4.34. The rate of hardening is rapid at the initial stages of wear (up to 20 m, for coarse-grained aluminum) but then starts to increase at a lower rate with the sliding distance (reaching 550 MPa after 120 m).

The thickness of the plastically deformed and hardened subsurface layer is defined as the depth of material where subsurface hardening is first detected. For the coarse-grained aluminum, the depth of plastic zone is about 20 μm after sliding to 1 m and extends to 60 μm at 110 m. The thickness of the deformed layer as a function of sliding distance, for both coarse-grained aluminum and titanium (Fig. 4.35), increases with sliding distance. Both curves reveal a sharp rise in the deformed zone thickness followed by a slower one. However, aluminum is characterized by a deformed layer that is thicker than that of titanium at any given sliding distance.

4.7. Texture Evolution

Texture evolution during sliding wear was monitored and subsequently related to the friction and wear behaviour. Texture was determined by constructing (111) inverse-pole-figures at different sliding distances for coarse-grained aluminum. The texture coefficients of the (111) plane increases with sliding distance (from 0.08 at 0 sliding distance to 0.63 at 2714 m sliding distance), Figure 4.36. This means that the number of the (111) planes being parallel to the worn surface increases with sliding distance. The figure also shows that the texture coefficients of different poles that make a small tilt angle with the reference direction (perpendicular to the worn surface) increases with sliding distance. This indicates that the [111] poles tend to concentrate around the reference direction. Figure 4.37 is the pole density distribution of the [111] pole with respect to the reference direction. Prior to the wear test, the initial texture (0 m sliding distance) shows that the (111) planes are oriented at a high angle from the surface. The figure also reveals how the (111) plane changes orientation from high tilt angle, at 0 sliding distance, towards smaller tilt angle at 4524 m.

The inverse pole figures for nanocrystalline aluminum (grain size of 16.4 and 43.1 nm) at a 0 sliding distance were also constructed (Fig. 4.38). Both pole figures show high concentration of [111] poles around the reference direction than the coarse-grained aluminum (at 0 sliding distance). The average texture coefficient versus tilt angle compares the [111] pole orientation distribution for different grain size aluminum prior to the wear test as well as 4524 m sliding distance for coarse-grained aluminum (Fig. 4.39). The texture index (an index number that gives an indication on the preferred orientation in a certain direction) is calculated and plotted as a function of sliding distance of coarse-grained aluminum for $0 \leq \Phi \leq 35^\circ$ (texture index=$\sum_{0}^{35^\circ} \mathrm{T.C.}(\Phi)_{average}$) and $40^\circ \leq \Phi \leq <90^\circ$ (texture index=$\sum_{40^\circ}^{90^\circ} \mathrm{T.C.}(\Phi)_{average}$), Figure 4.40. The texture index is the sum of the [111] poles within 35° angle from the reference direction and 50° angle from the normal to the reference direction. The figure also give the initial texture index for the nanocrystalline aluminum (D=16.4 and 43.1 nm) at 0 sliding distance. The texture index within 35° from the reference direction increases while that within 50° from the normal to the reference direction decreases with sliding distance. That is, more (111) planes become parallel to the worn surface as sliding continues.

The inverse pole figures for coarse-grained titanium (Fig. 4.41) reveal that the initial texture has a preferred orientation of the basal pole, [0001], in the reference direction. This indicates that a high density of (0001) planes are parallel to the specimen surface prior to testing. Increasing the sliding distance does not seem to effect the texture which is also observed in the average texture coefficient versus tilt angle curve (Fig. 4.42).

Texture evolution on the transverse section of coarse-grained titanium (Fig. 4.43) show that [0001] poles increase around the reference direction with sliding distance. The average texture coefficient versus tilt angle (Fig. 4.44) shows how the [0001] pole density at low tilt angle increases as the sliding distance. The as-sputtered titanium pole figure, prior to wear testing, is given in Figure 4.45. The [0001] poles are depleted around the reference direction and concentrated away from it, that is, most of the (0001) planes are at right angle to the specimen surface. Figure 4.46 compares coarse-grained (normal and transverse sections) and as-sputtered titanium. The figure gives initial textures prior to wear as a function of tilt angle.

SAED patterns of the coarse-grained aluminum surface before and after wear at the longest sliding distance (4524 m) show that a change in the microstructure has occurred (Fig. 4.47). The micrographs reveal that the initial surface prior to testing consists of large grain size indicated by the diffraction spots characteristic of single crystal SAED pattern. However, after wear testing, the SAED pattern takes the form of spotty rings which are an indication of small grain size.

Table 4.1. (111) x-ray peak broadening of nanocrystalline aluminum films.

Aluminum	$\beta_{specimen}$ (rad)	Grain size (nm)
As-sputtered	9.955×10^{-3}	16.4±1.5
Annealed (for 5 hrs.)	5.145×10^{-3}	31.7±3.0
Annealed (for 50 hrs.)	1.664×10^{-3}	98.0±5.0

Table 4.2. Layer thicknesses and volume fractions of nanolayered composites.

	λ_1(nm)	λ_2(nm)	f_1	f_1
Al/Al_2O_3	500	20	0.96	0.04
	200	20	0.91	0.09
	70	10	0.88	0.12
Ti/TiN	450	40	0.92	0.08
	150	20	0.88	0.12
Ti/Cu	1000	120	0.89	0.11
	500	60	0.89	0.11
	250	30	0.89	0.11
	150	20	0.88	0.12

λ_1 and λ_2 are layer thicknesses of components 1 and component 2, respectively.
f_1 and f_2 are volume fractions of components 1 and component 2, respectively.
Resolution of measurement is ±15 nm.

Table 4.3. Nanohardness of nanocrystalline aluminum films with different grain sizes.

Material	Grain size(nm)	H(GPa)
Nanocrystalline		
	16.4	1.70±0.06
	31.7	1.21±0.12
	98.0	0.72±0.13
Conventional		
	10^6	0.30±0.06

Table 4.4. Mechanical properties of nanolaminated composite films.

Nanolaminates	λ_1(nm)	λ_2(nm)	*H(GPa)	E(GPa)
Al/Al_2O_3	500	20	3.29±0.06	61.69±1.50
	200	20	4.52±0.08	66.99±1.50
	70	10	4.83±0.08	84.75±2.00
Ti/TiN				
	450	40	12.04±0.20	117.42±2.70
	150	20	12.80±0.25	119.55±2.70
as-sputtered Ti			10.96±0.20	113.10±2.50
coarse-grained Ti			2.57±0.10	112.32±2.50
TiN (RIP)			34.09±0.24	299.33±2.09
Ti/Cu	1000	120	5.40±0.10	101.63±2.50
	500	60	4.57±0.08	111.02±2.60
	250	30	4.29±0.08	102.30±2.50
	150	20	3.69±0.08	105.39±2.60
as-sputtered Cu			2.48±0.03	102.46±2.50
coarse-grained Cu (VH)			0.95±0.05	

* all hardness values are determined by a nanoindentation system unless indicated otherwise.

λ_1 and λ_2 are layer thicknesses of components 1 and component 2, respectively.

Table 4.5. Coefficients of friction and wear rates of aluminum obtained using a load of 1 N and a sliding speed of 1.3×10^{-2} m.s^{-1} in ambient conditions.

Grain size (nm)	μ_p	$\mu_{s.s}$	$\Delta\mu_p$	S_t (m)	W_s($X10^{-3}$) (mm^3/m)	W_m($X10^{-5}$) (mm^3/m)
Nanocrystalline						
16.4	0.62±0.06*	0.25±0.05	0.37±0.11	52	1.82±0.37	2.77±0.39
43.1	0.58±0.03	0.14±0.03	0.44±0.06	71	2.37±0.38	11.36±0.69
98.0	0.92±0.02	0.14±0.02	0.78±0.04	73	3.24±0.50	32.36±1.57
Conventional						
10^6	1.34±0.02	0.12±0.06	1.22±0.08	81	10.08±1.78	342.46±6.94

μ_p = peak coefficient of friction.
$\mu_{s.s}$ = steady-state coefficient of friction.
$\Delta\mu_p$ = $(\mu_p - \mu_{s.s})$.
S_t = transition distance to steady-state.
W_s = severe wear rate.
W_m = mild wear rate
*denotes fluctuation around the mean.

Table 4.6. Coefficients of friction and wear rates of aluminum obtained using a load of 1 N and a siding speed of $4.2\text{x}10^{-4}$ m.s^{-1} performed in both vacuum and air.

Grain size (nm)	Vacuum, 10^{-6}torr		Ambient, 1 atm	
	μ	W(X10^{-4}) (mm^3/m)	μ	W(X10^{-4}) (mm^3/m)
<u>Nanocrystalline</u>				
16.4	1.06±0.04	1.77±0.11	0.69±0.06	0.45±0.20
98.0	1.30±0.05	8.10±0.46	0.88±0.10	3.63±0.27
<u>Conventional</u>				
10^6	1.60±0.36	33.33±2.50	1.12±0.15	18.67±1.63

μ and W are measured at sliding distance of 3.5 m (number of cycles = 190).

Table 4.7. Coefficients of friction and wear rates of Al/Al_2O_3 nanolaminated composite obtained using a load of 1 N and a sliding speed of $1.3x10^{-2}$ $m.s^{-1}$ in ambient conditions.

Al layer thickness (nm)	μ_p	$\mu_{s.s}$	$\Delta\mu_p$	S_t (m)	$W_s(X10^{-3})$ (mm^3/m)	$W_m(X10^{-5})$ (mm^3/m)
200	0.36±0.03*	0.08±0.04	0.28±0.07	48	1.31±0.29	1.57±0.19
500	0.52±0.02	0.10±0.03	0.42±0.05	53	1.46±0.24	2.35±0.33

μ_p = peak coefficient of friction.
$\mu_{s.s}$ = steady-state coefficient of friction.
$\Delta\mu_p$ = $(\mu_p - \mu_{s.s})$.
S_t = transition distance to steady-state.
W_s = severe wear rate.
W_m = mild wear rate
*denotes fluctuation around the mean.

Table 4.8. Coefficients of friction and wear rates of Ti/TiN nanolaminated composite obtained using a load of 1 N and a sliding speed of 1.3×10^{-2} m.s^{-1} in ambient conditions.

Ti-based materials	μ_p	$\mu_{s.s}$	$\Delta\mu_p$	S_t (m)	$W_s (X10^{-3})$ (mm^3/m)	$W_m (X10^{-5})$ (mm^3/m)
<u>Ti/TiN</u>						
150$^+$	0.67±0.03*	0.23±0.03	0.44±0.06	62	0.07±0.02	0.10±0.02
450	0.75±0.03	0.39±0.03	0.36±0.06	75	0.08±0.02	0.18±0.01
<u>As-sputtered Ti</u>						
	0.75±0.04	0.54±0.03	0.21±0.07	83	0.09±0.02	0.32±0.01
$^\#$<u>Coarse-grained Ti</u>						
	0.69±0.03	0.69±0.04	0.00±0.00	---	2.34±0.66	9.83±0.52
<u>TiN (RIP)</u>						
	0.93±0.03	0.10±0.03	0.83±0.06	115	0.05±0.002	0.03±0.01

μ_p = peak coefficient of friction.
$\mu_{s.s}$ = steady-state coefficient of friction.
$\Delta\mu_p$ = $(\mu_p - \mu_{s.s})$.
S_t = transition distance to steady-state.
W_s = severe wear rate.
W_m = mild wear rate
*denotes fluctuation around the mean.
$^+$denotes Ti layer thickness (nm)
$^\#\mu_p$ to $\mu_{s.s}$ transition not observed.

Table 4.9. Coefficients of friction and wear rates of coarse-grained Cu and Ti/Cu nanolaminated composite (having 150 nm Ti layer thickness) obtained using a load of 1 N and a sliding speed of 1.3x10^{-2} m.s^{-1} in ambient conditions.

	μ_p	$\mu_{s.s}$	$\Delta\mu_p$	S_t (m)	W_s(X10^{-3}) (mm^3/m)	W_m(X10^{-5}) (mm^3/m)
<u>Ti/Cu</u>						
	0.91±0.02*	0.40±0.05	0.51±0.07	60	0.81±0.12	1.25±0.14
<u>Conventional Cu</u>						
	1.12±0.02	0.26±0.05	0.86±0.07	70	4.87±0.50	205.43±4.11

μ_p = peak coefficient of friction.
$\mu_{s.s}$ = steady-state coefficient of friction.
$\Delta\mu_p$ = $(\mu_p - \mu_{s.s})$.
S_t = transition distance to steady-state.
W_s = severe wear rate.
W_m = mild wear rate
*denotes fluctuation around the mean.

Table 4.10. Average roughness of worn surfaces of coarse-grained aluminum and titanium.

Sliding distance (m)	Aluminum Ra(μm)*	Titanium Ra(μm)
0	0.15±0.08	0.10±0.02
1	4.14±0.50	0.89±0.11
4	9.93±1.40	1.94±0.32
30	9.21±1.10	3.01±0.42
60	6.98±0.60	3.43±0.51
90	3.91±0.54	----------
100	----------	3.51±0.53
110	4.10±0.65	----------

*Ra = surface roughness calculated from equation 3.10.

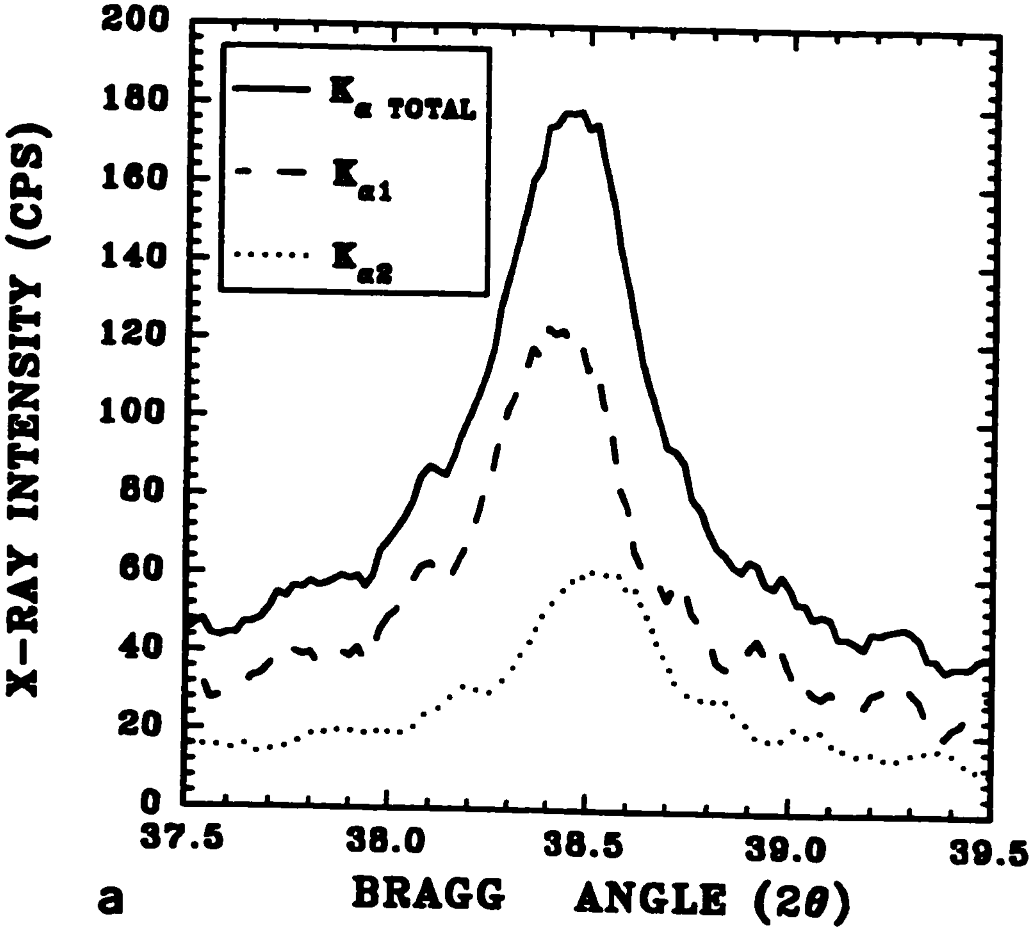

4.1. (111) diffraction peak for: (a)as-sputtered aluminum; (b)annealed at 573K for 5 hrs.; (c)annealed at 573 K for 50 hrs.; (d)"standard" aluminum powder.

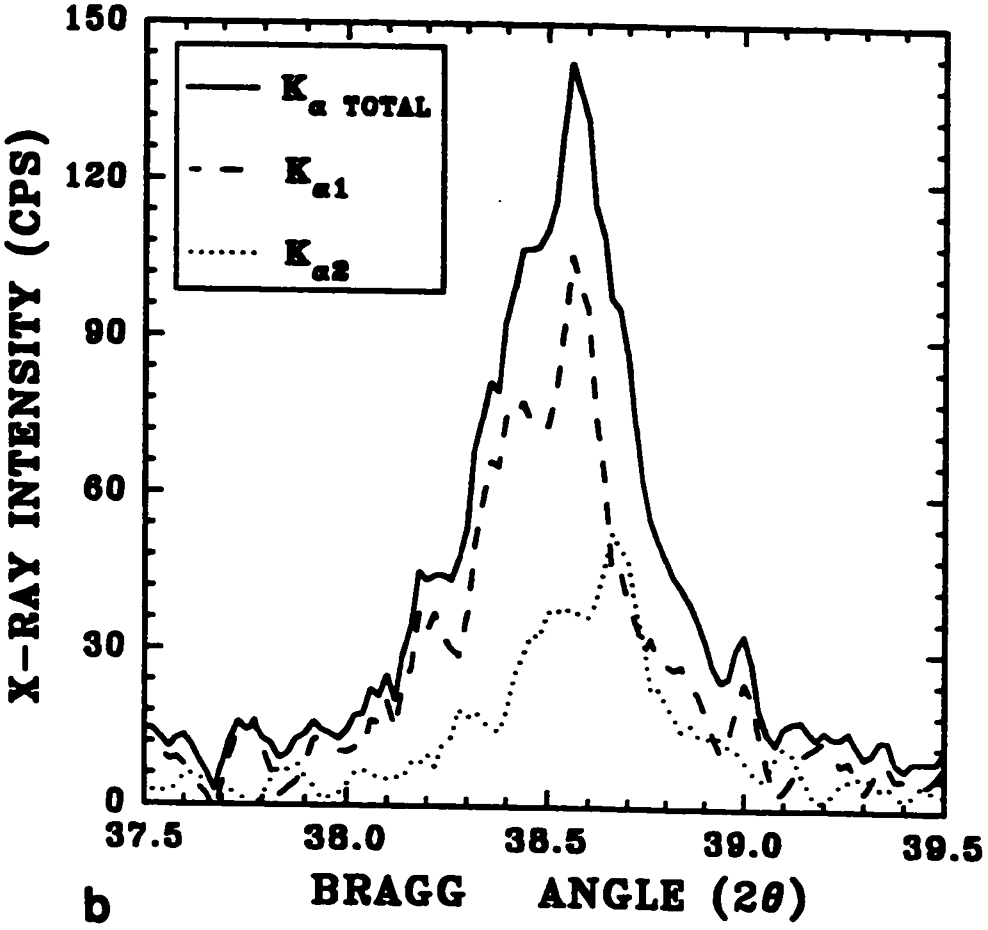

4.1. (continued).

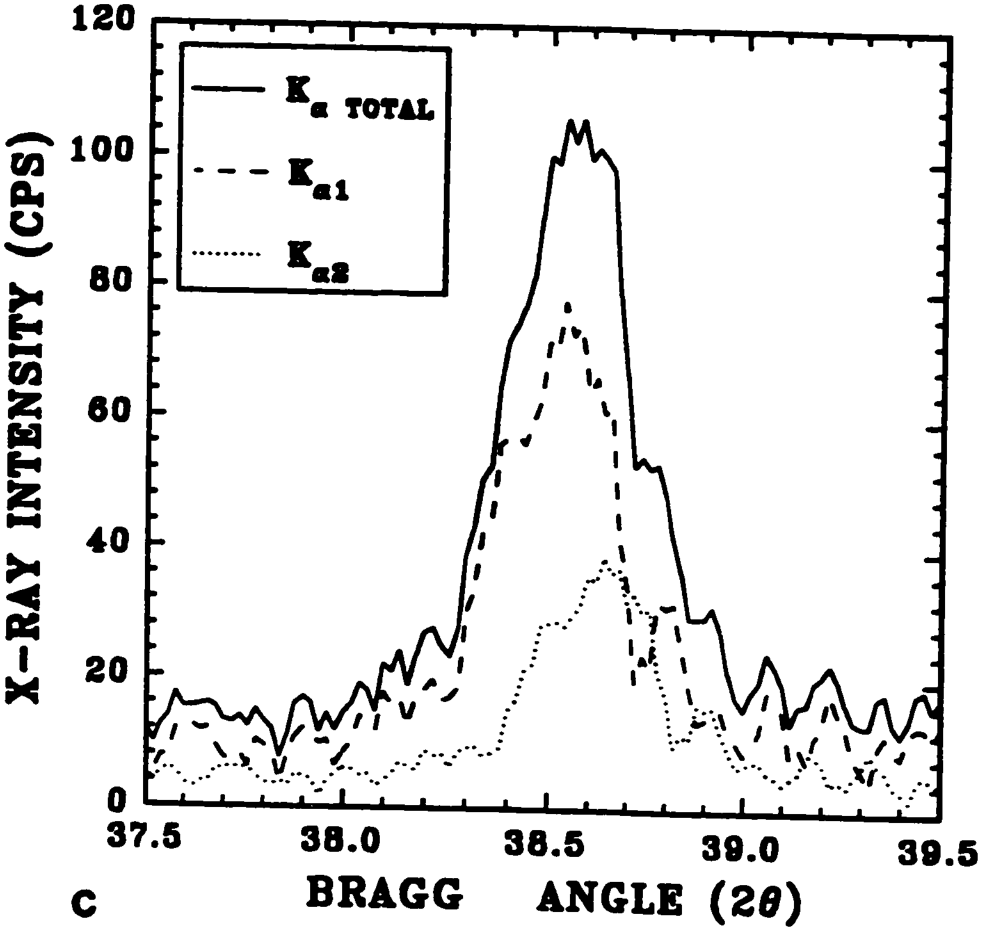

4.1. (continued).

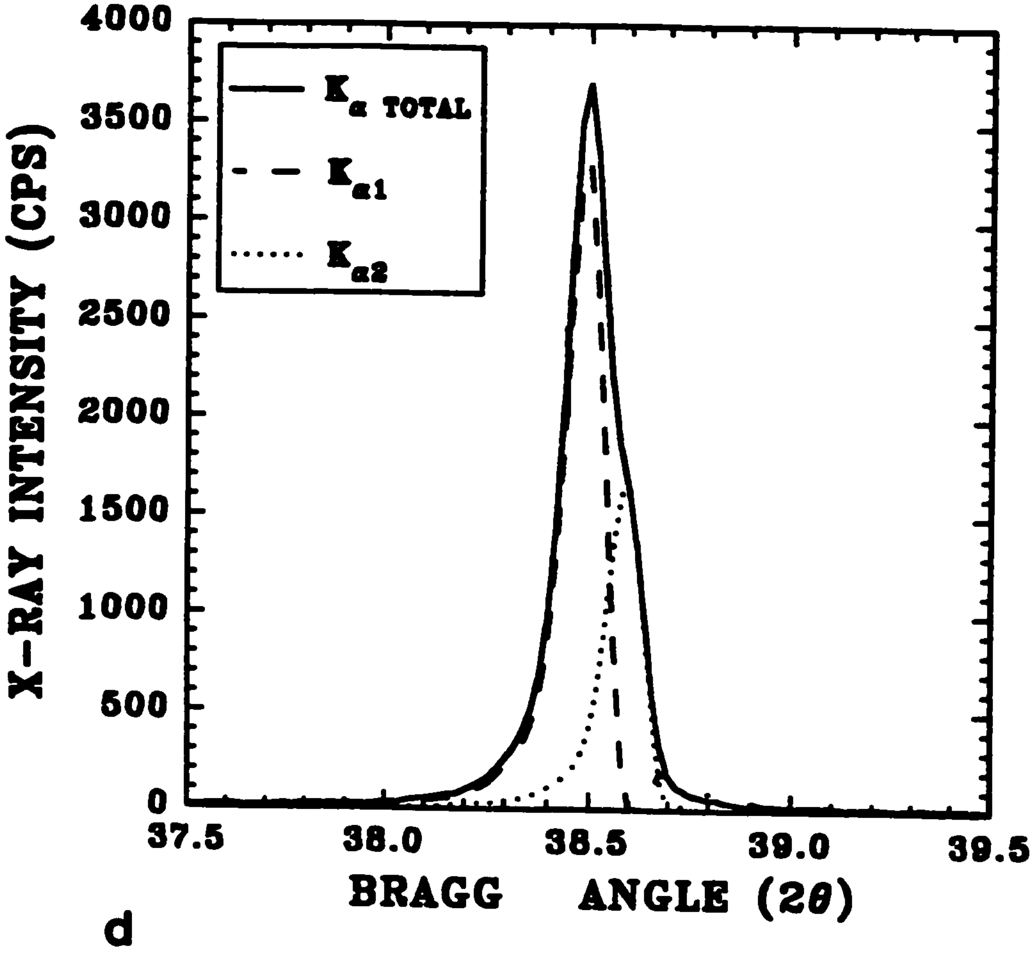

4.1. (continued).

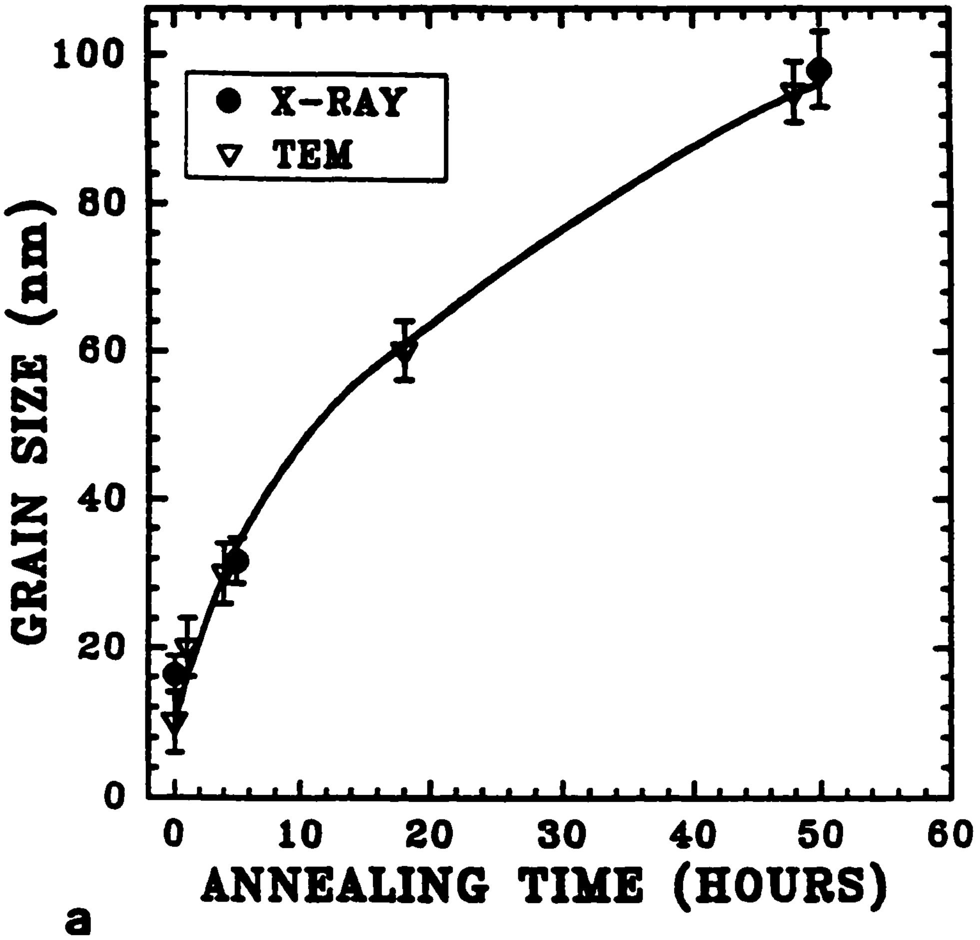

4.2. (a)Aluminum grain size as a function of annealing time; (b)TEM micrograph of as-sputtered aluminum; (c)TEM micrograph of aluminum annealed at 573 K for 50 hrs.

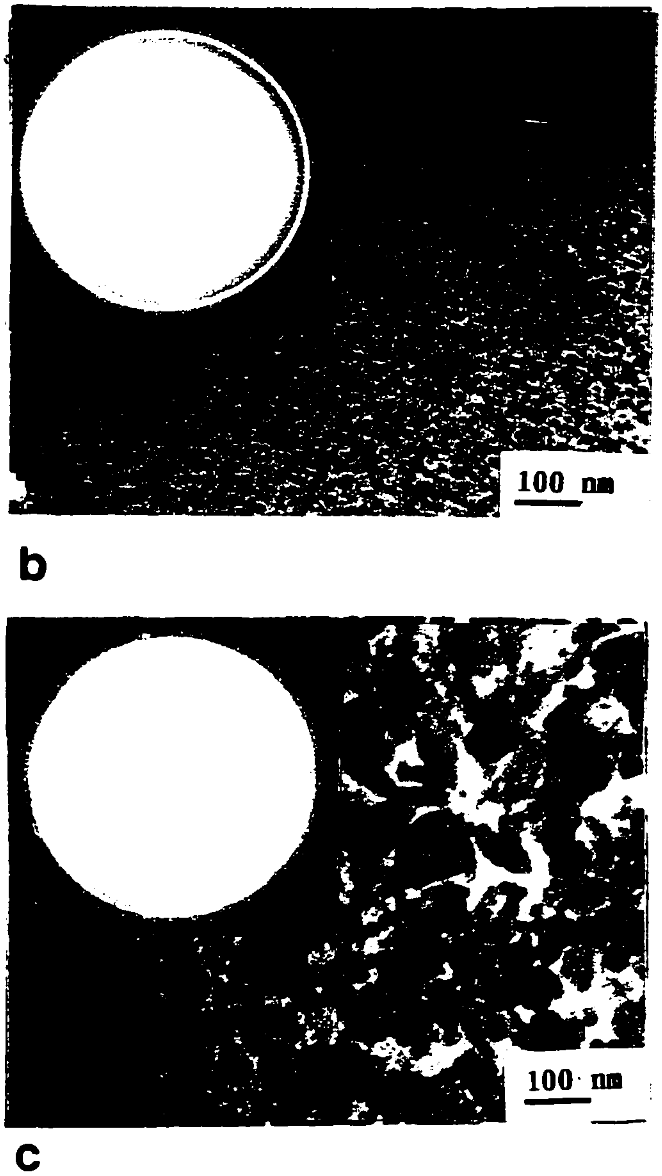

4.2. (continued).

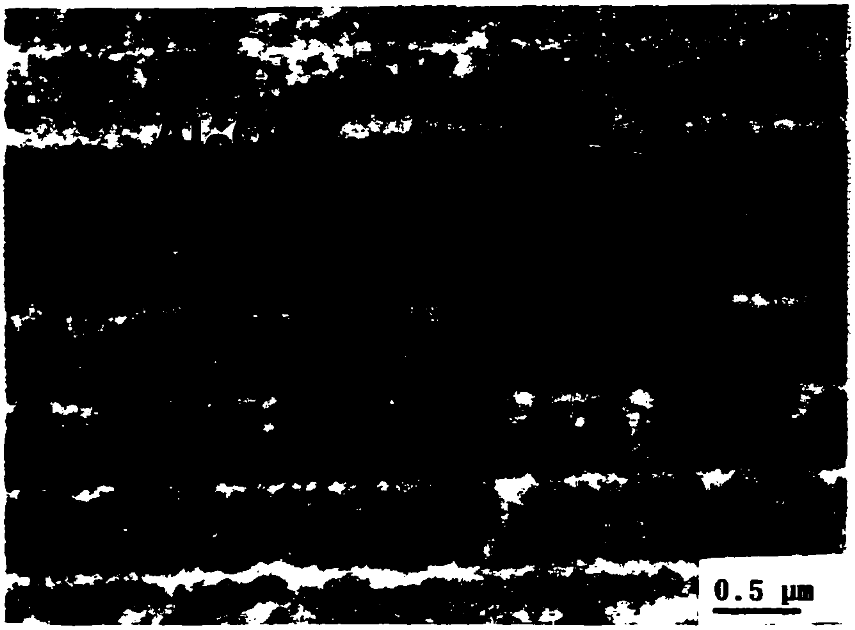

4.3. A scanning electron microscope (SEM) image of the cross-section of laminated composites of: (a)Al/Al_2O_3 ; (b)Ti/TiN; (c)Ti/Cu.

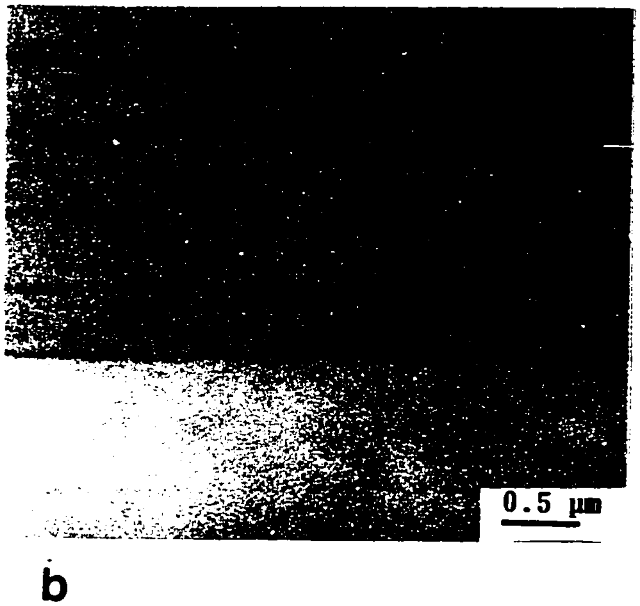

4.3. (continued).

4.3. (continued).

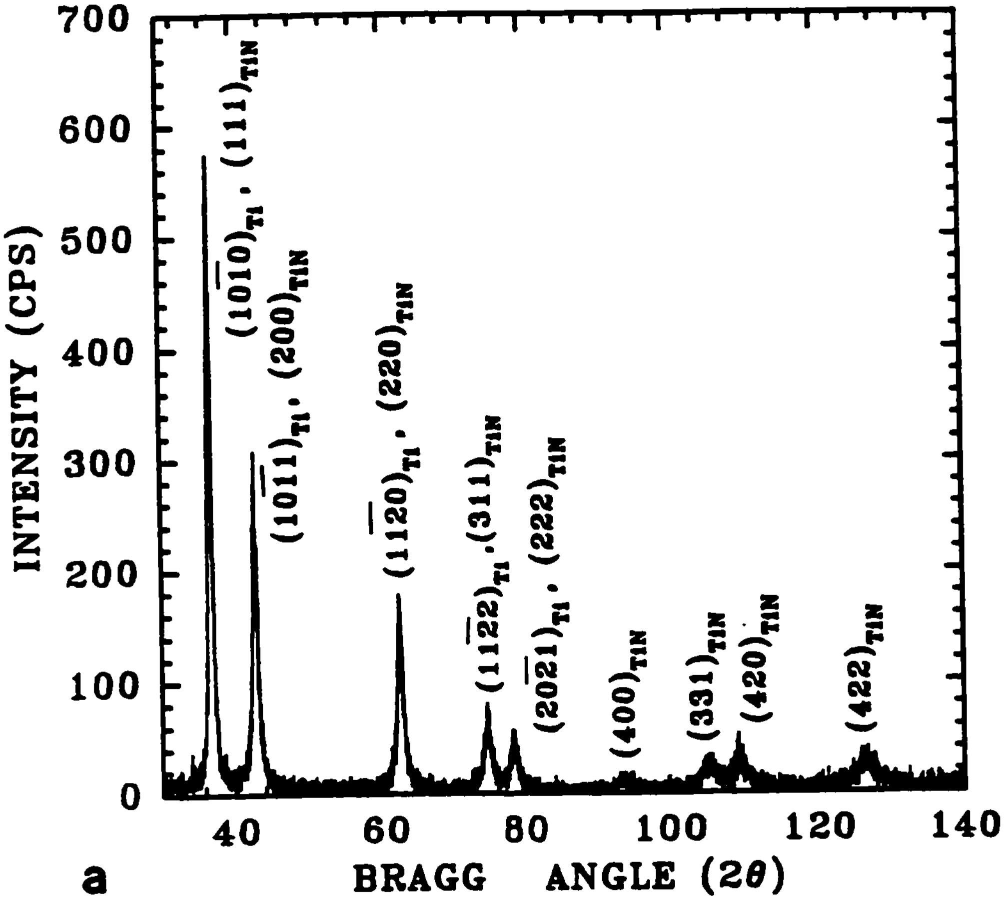

4.4. X-ray diffraction (XRD) patterns of: (a)Ti(150 nm)/TiN(20 nm) composite; (b)Ti film.

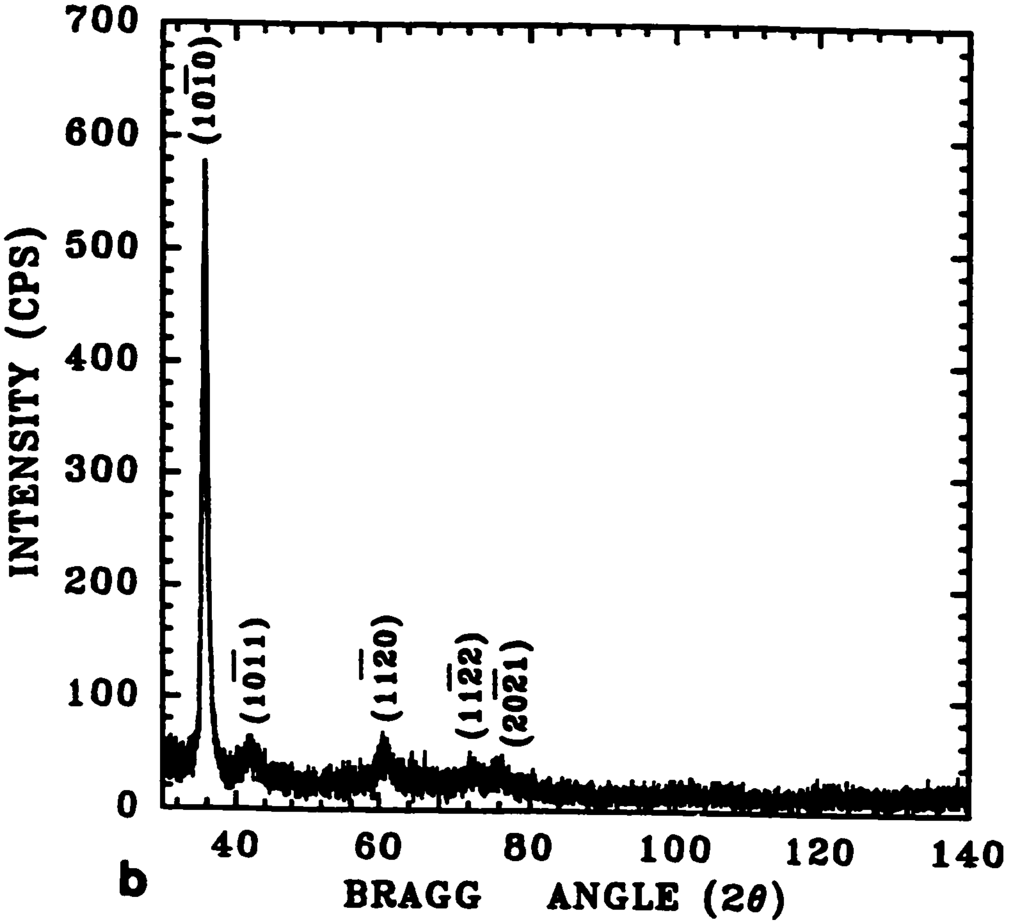

4.4. (continued).

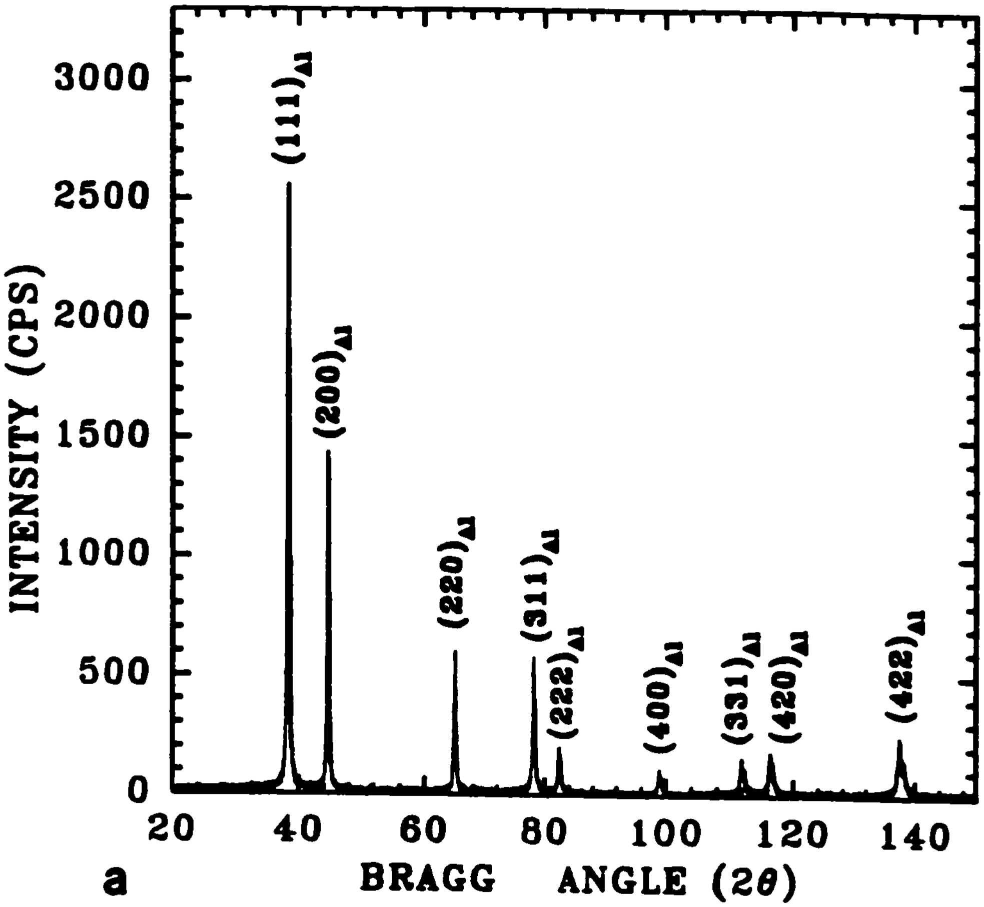

4.5. X-ray diffraction (XRD) patterns of: (a)Al(200 nm)/Al_2O_3 (20 nm) composite; (b)Al film.

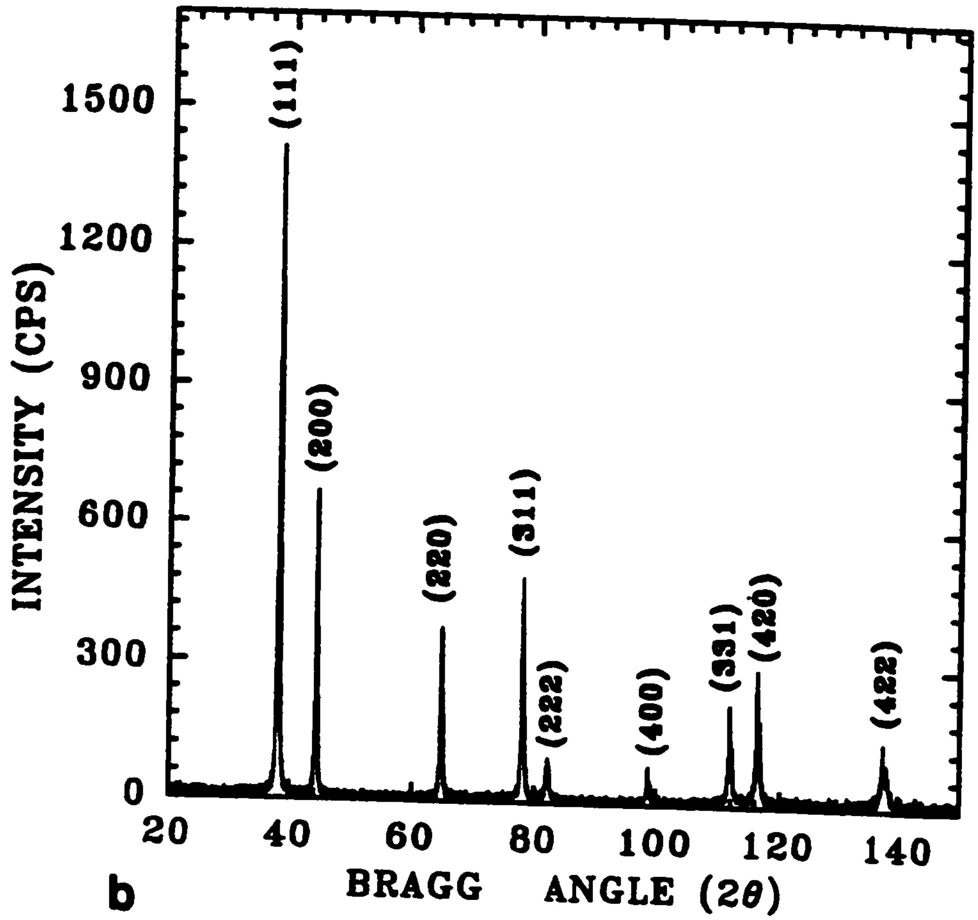

4.5. (continued).

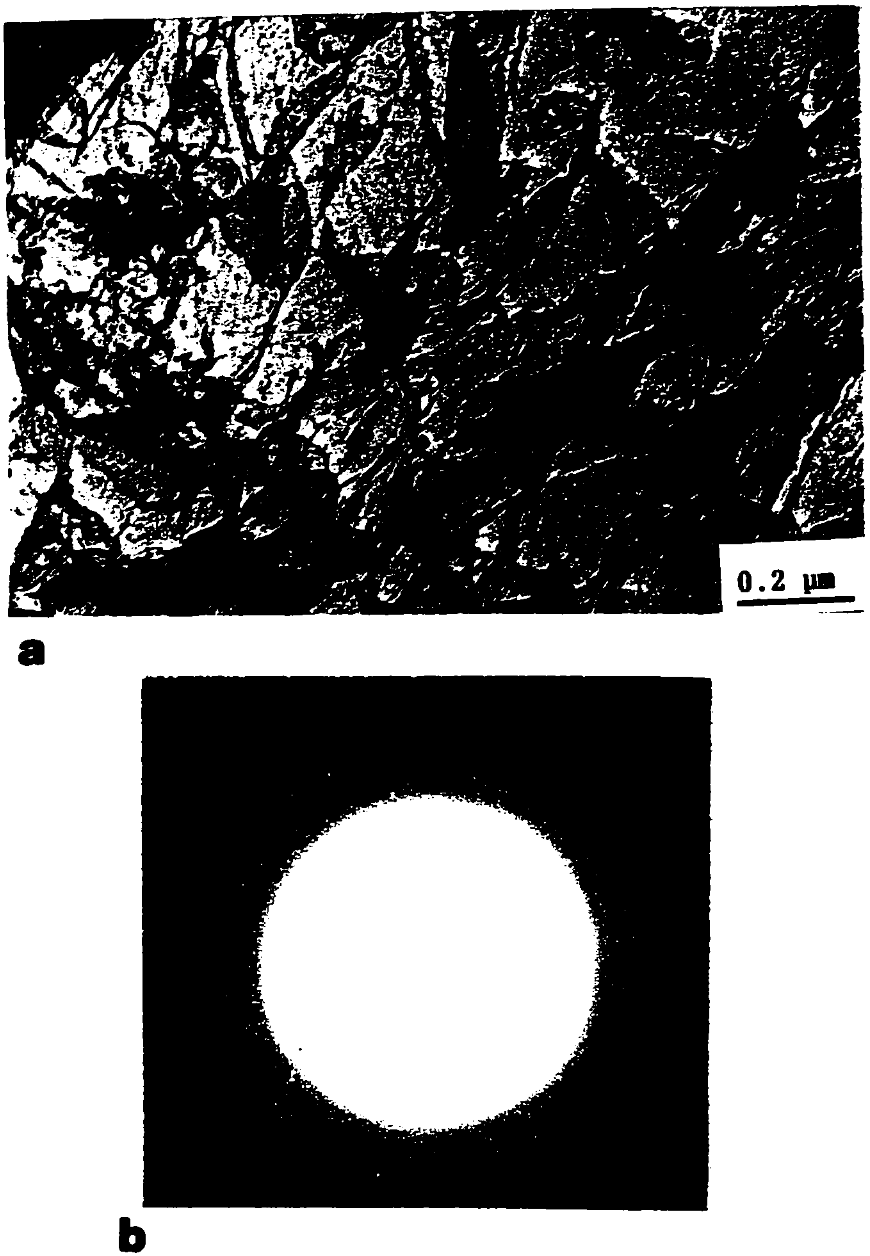

4.6 (a)TEM micrographs of Al_2O_3 layer film; (b)selected area electron diffraction (SAED) pattern of Al_2O_3 showing amorphous structure.

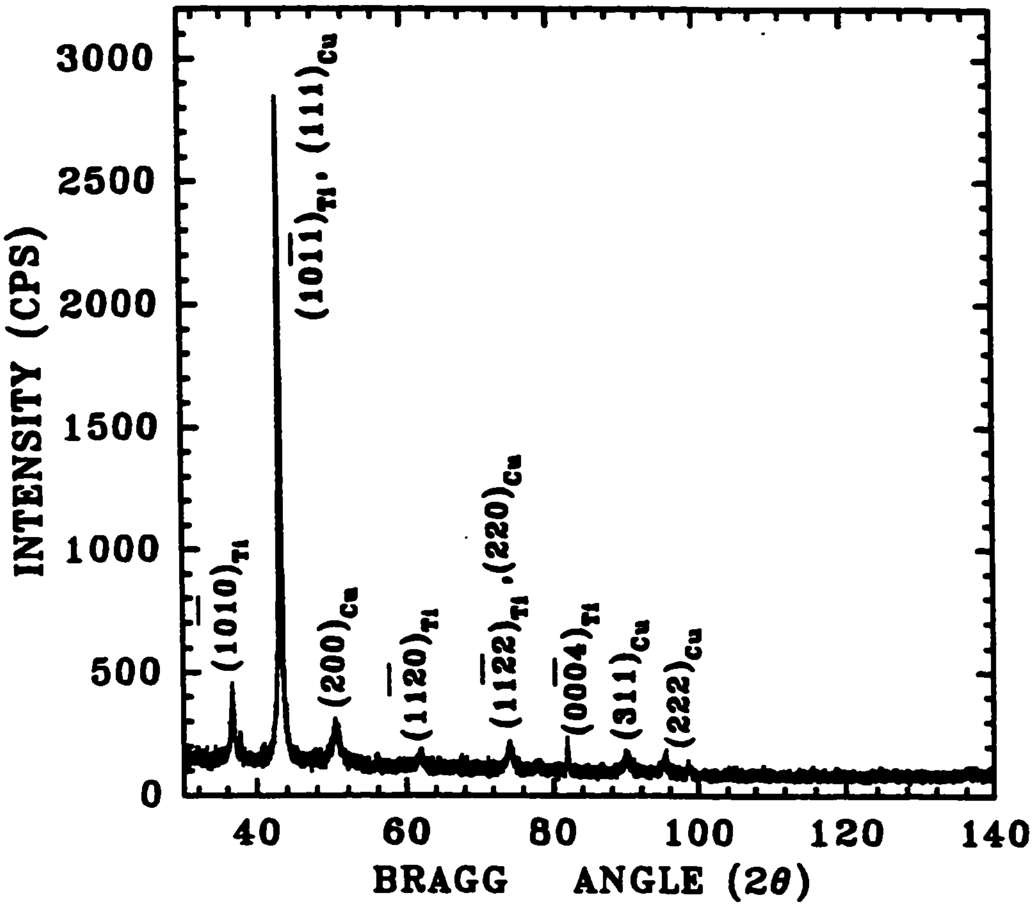

4.7. X-ray diffraction (XRD) pattern of Ti(150 nm)/Cu(20 nm) laminated composite.

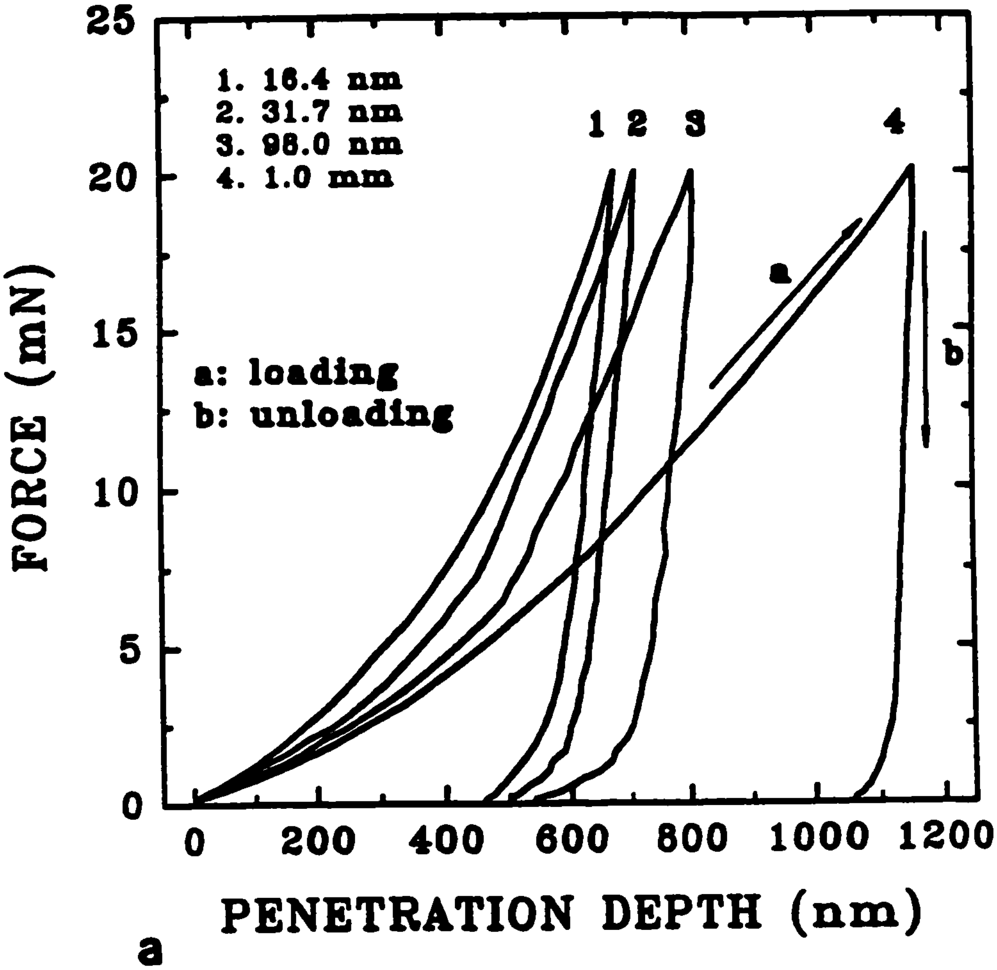

4.8. Force-displacement curves for: (a)monolithic nanocrystalline aluminum (b)Al/Al_2O_3; (c)Ti/TiN; (d)Ti/Cu.

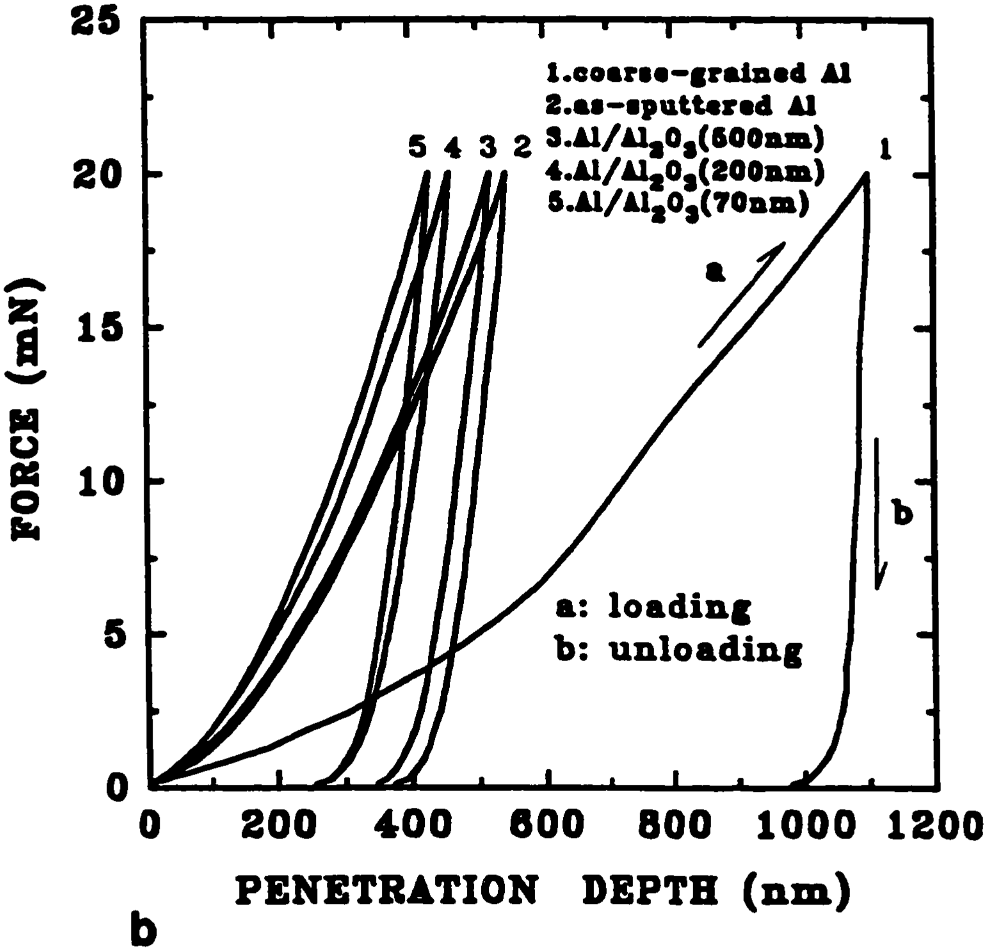

4.8. (continued).

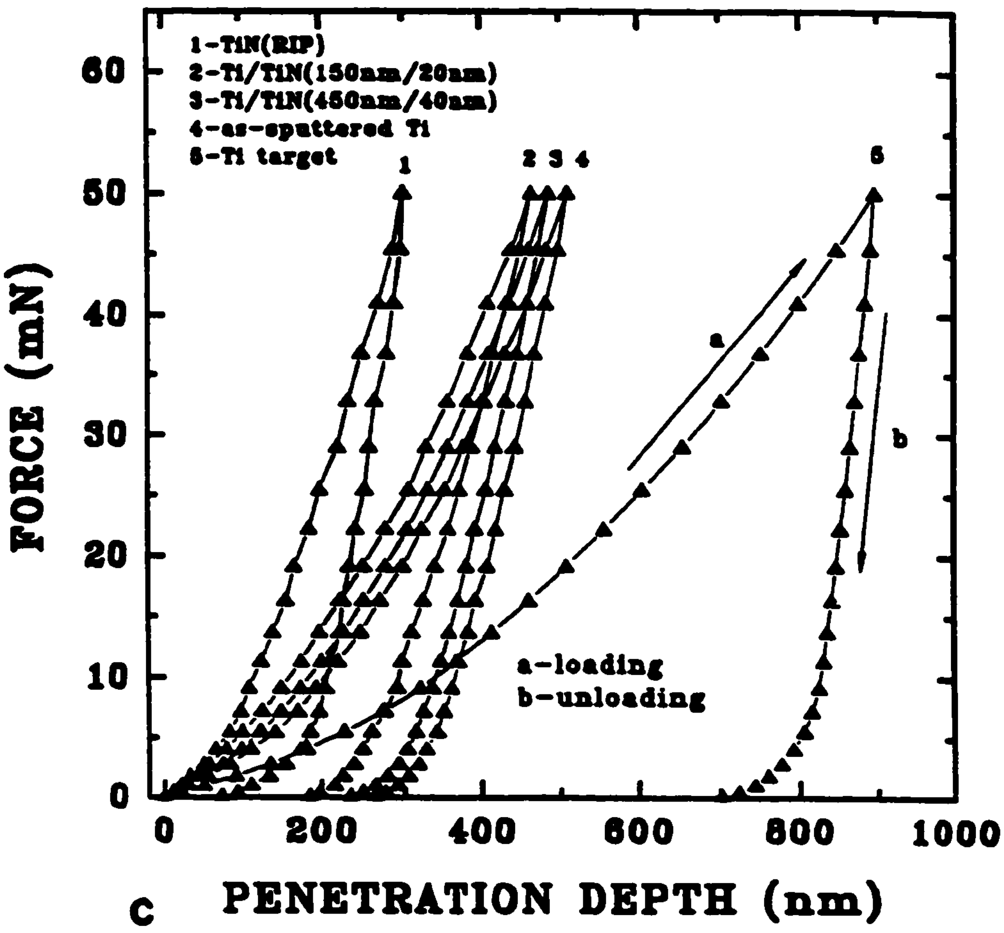

4.8. (continued).

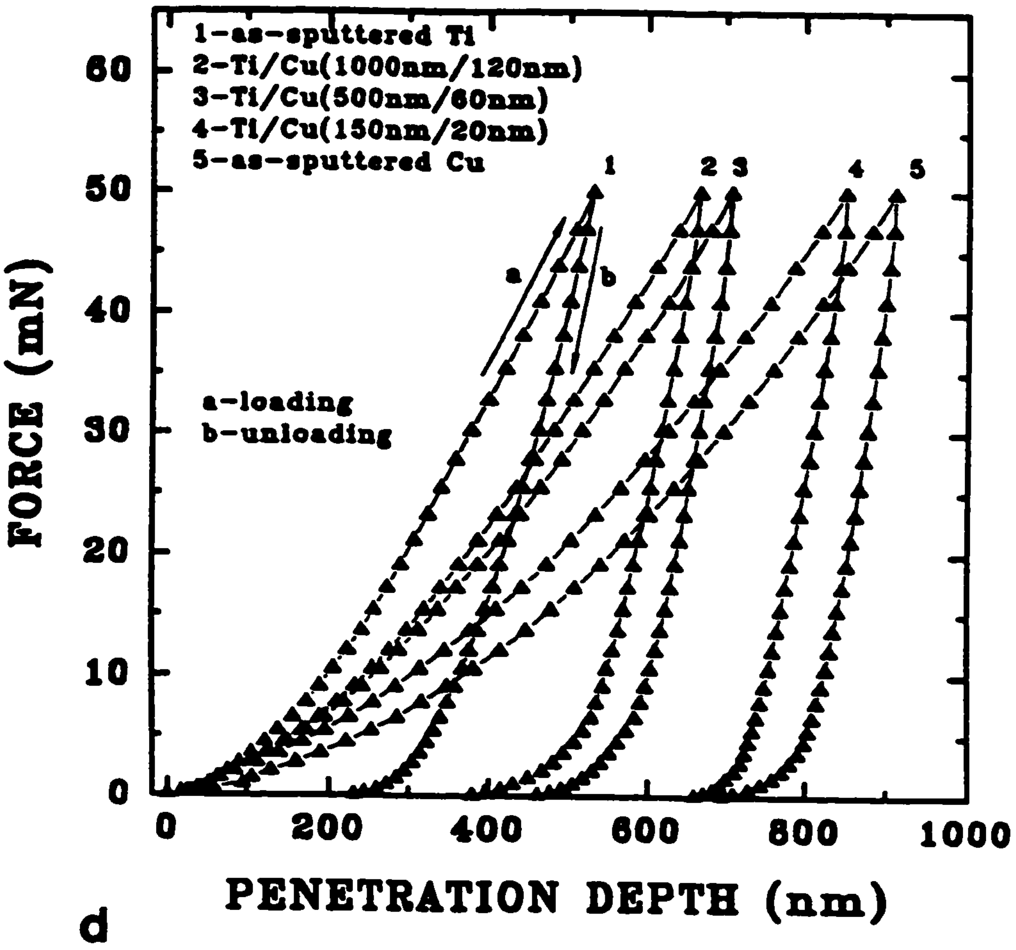

4.8. (continued).

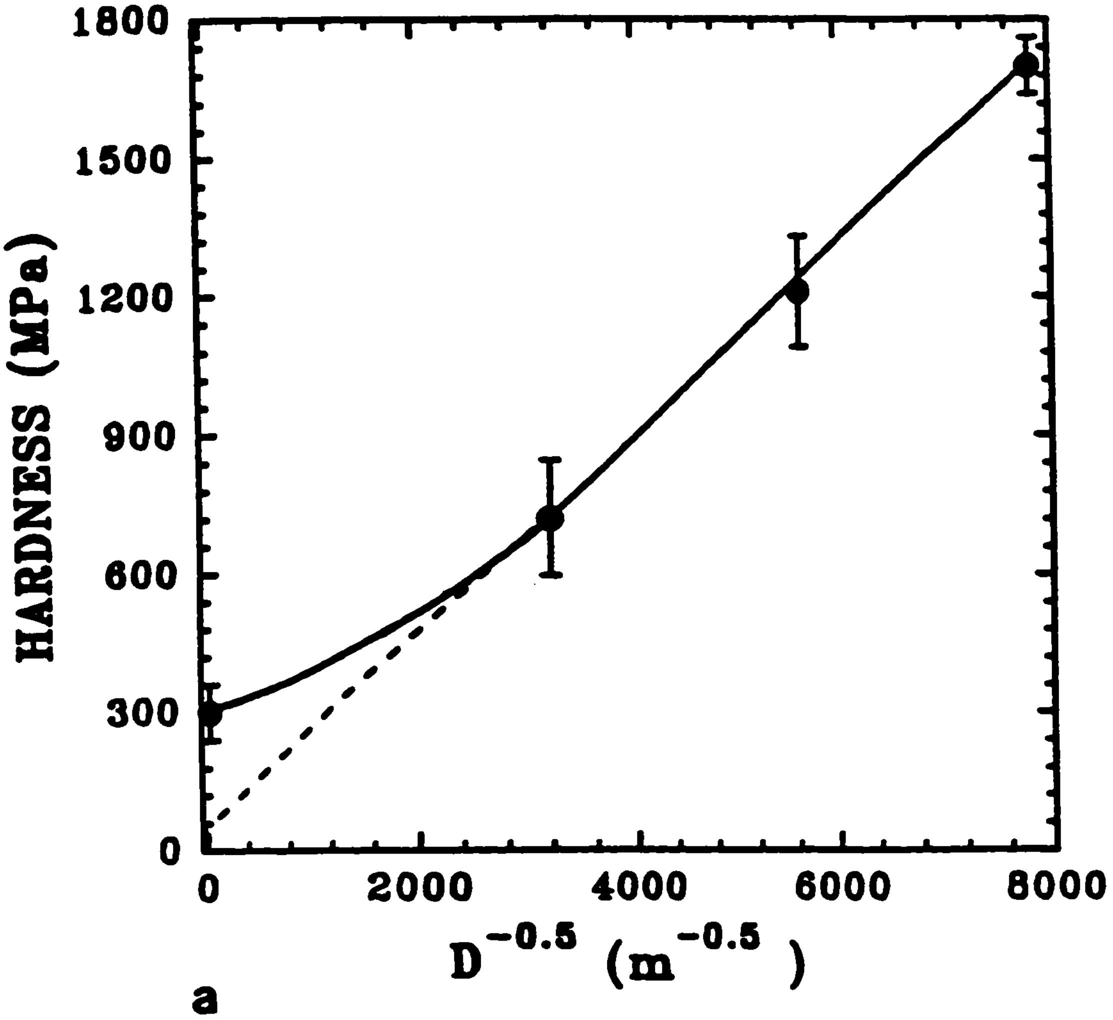

4.9. Hall-Petch plot: (a) hardness versus $D^{-0.5}$, where D is grain size of nanocrystalline aluminum; hardness versus λ^{-1} and $\lambda^{-0.5}$, where λ is the interlayer spacing for b)Al/Al_2O_3; (c)Ti/TiN;(d)Ti/Cu.

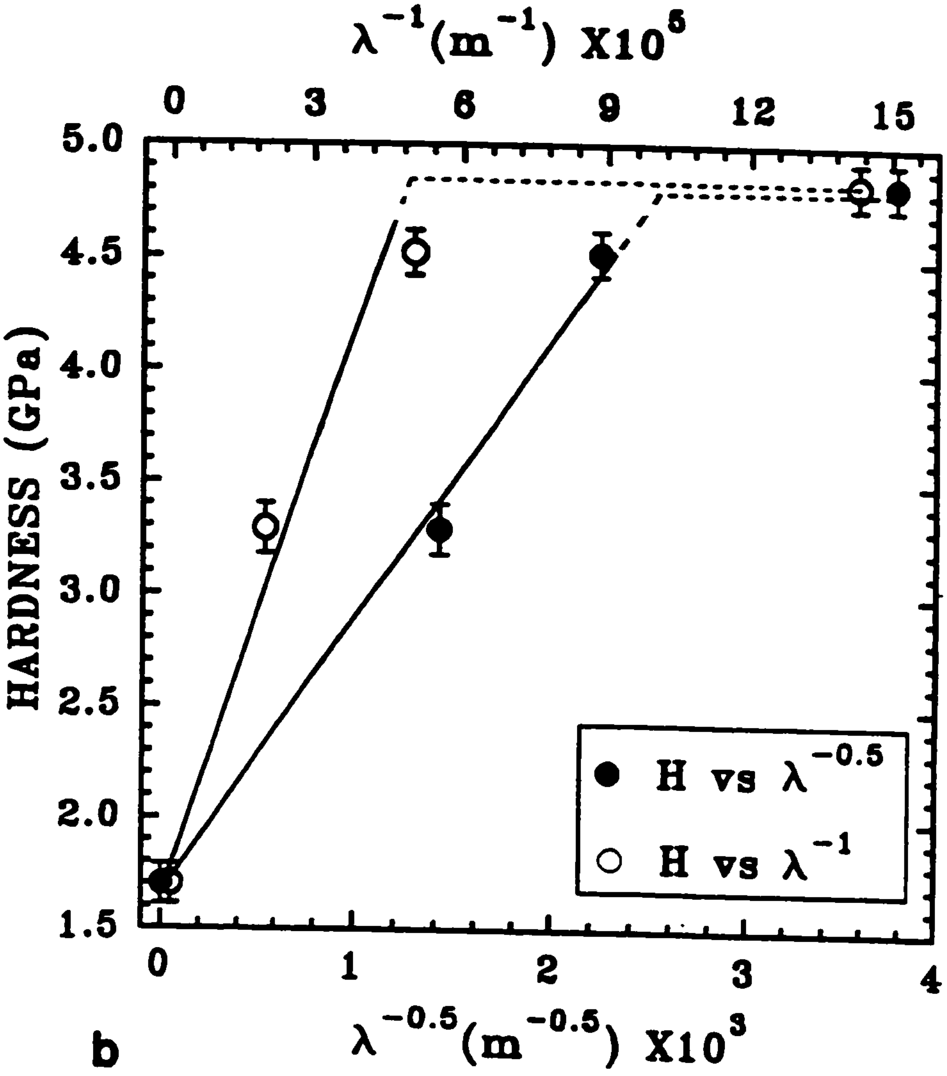

4.9. (continued).

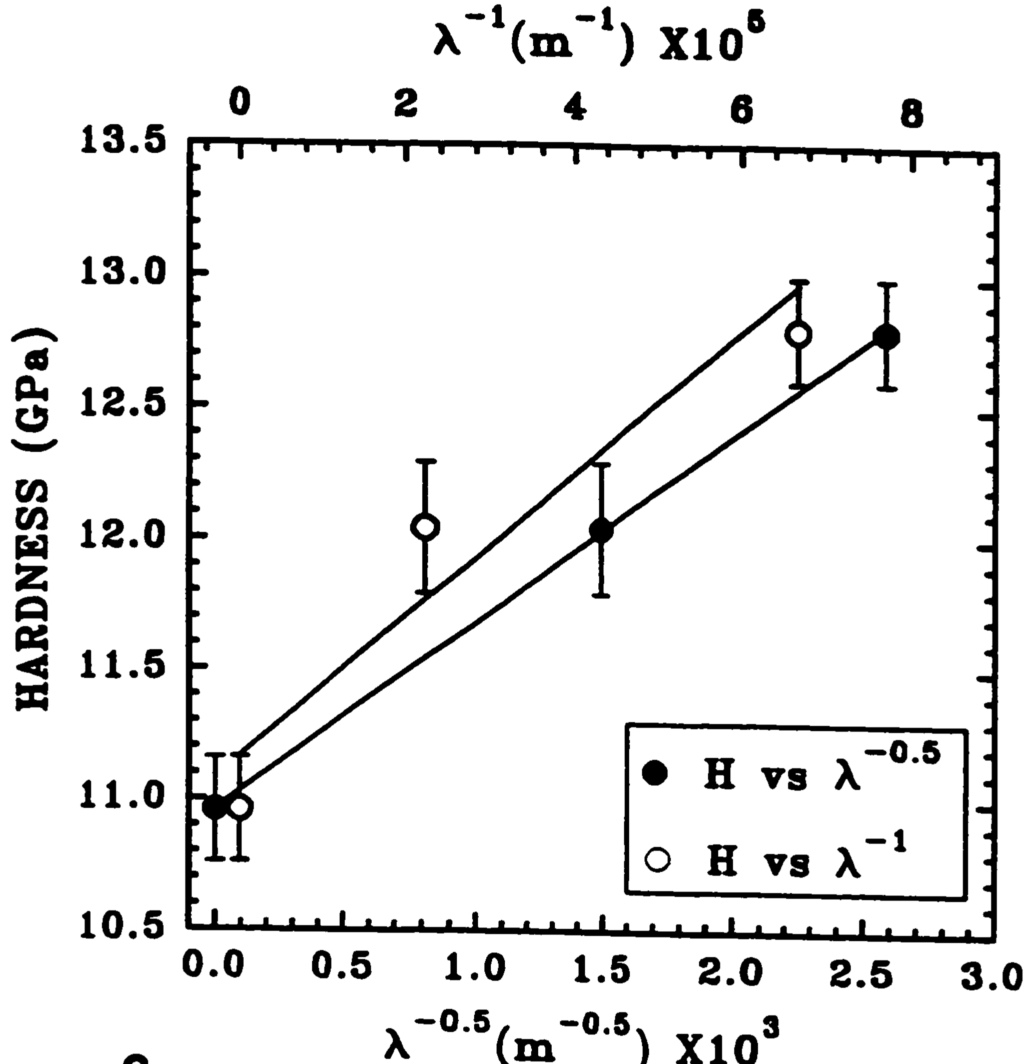

C

4.9. (continued).

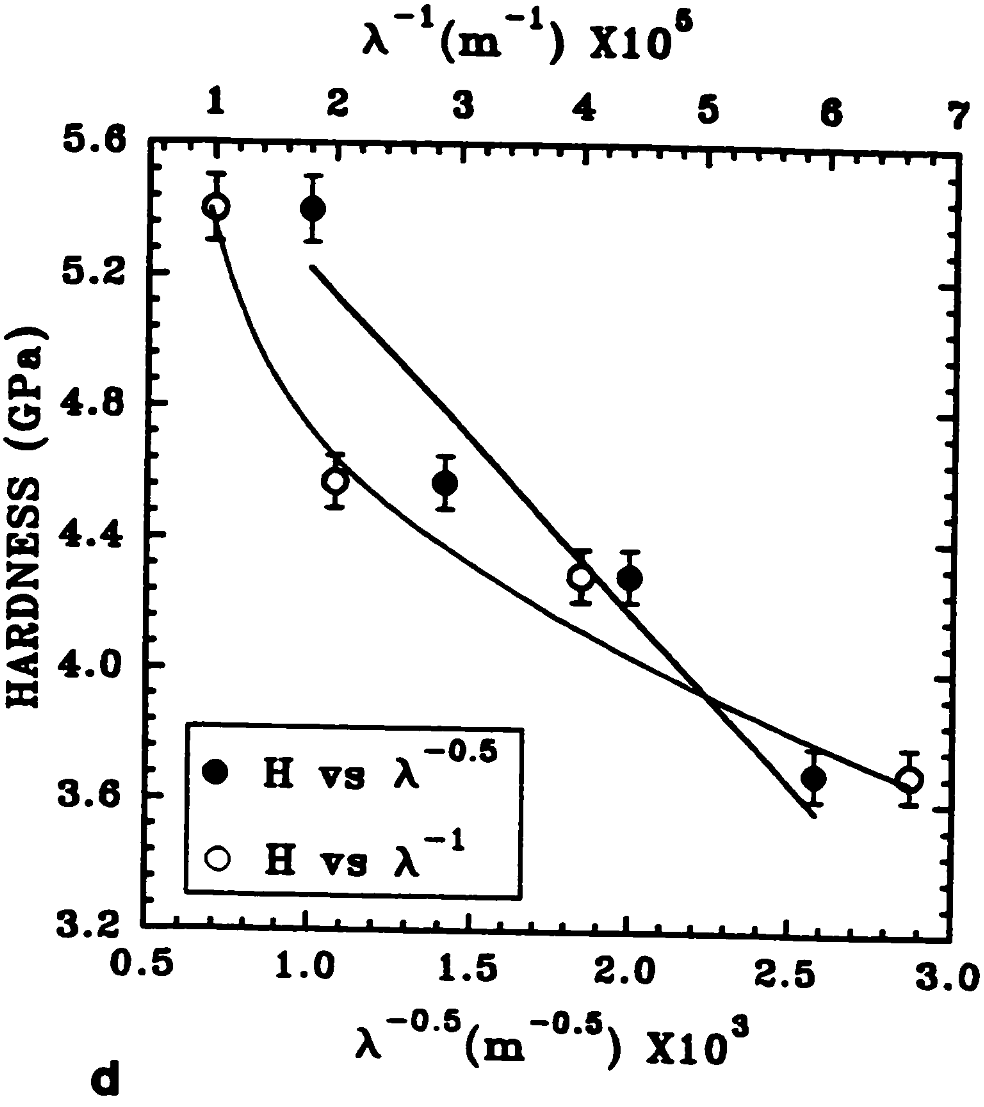

4.9. (continued).

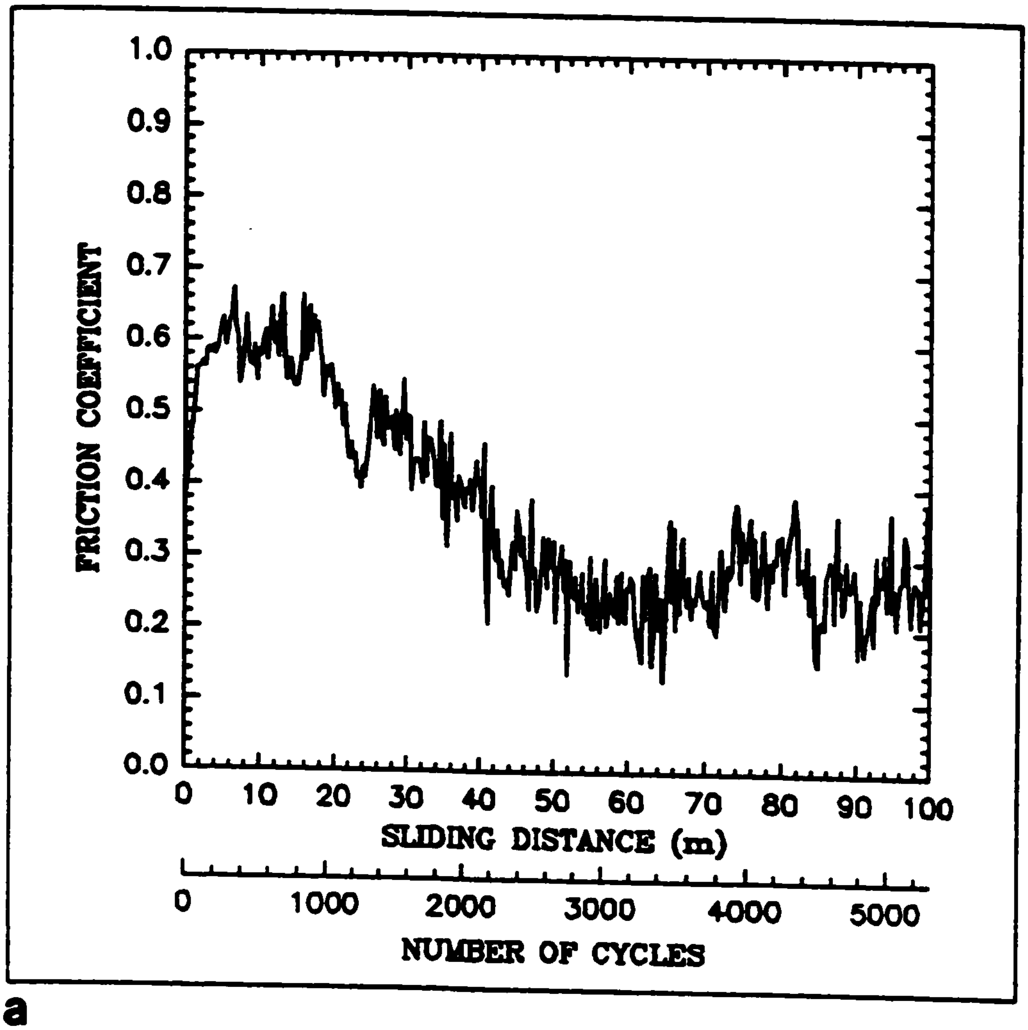

a

4.10. Coefficient of friction versus sliding distance curves, obtained using a normal load of 1.0 N and a sliding speed of $1.3\text{x}10^{-2}$ m.s^{-1} under unlubricated sliding condition, for nanocrystalline aluminum having grain sizes of: (a)16.4 nm; (b)43.1 nm; (c)98.0 nm; (d)10^6 nm; (e) 1100 aluminum alloy used as a substrate material.

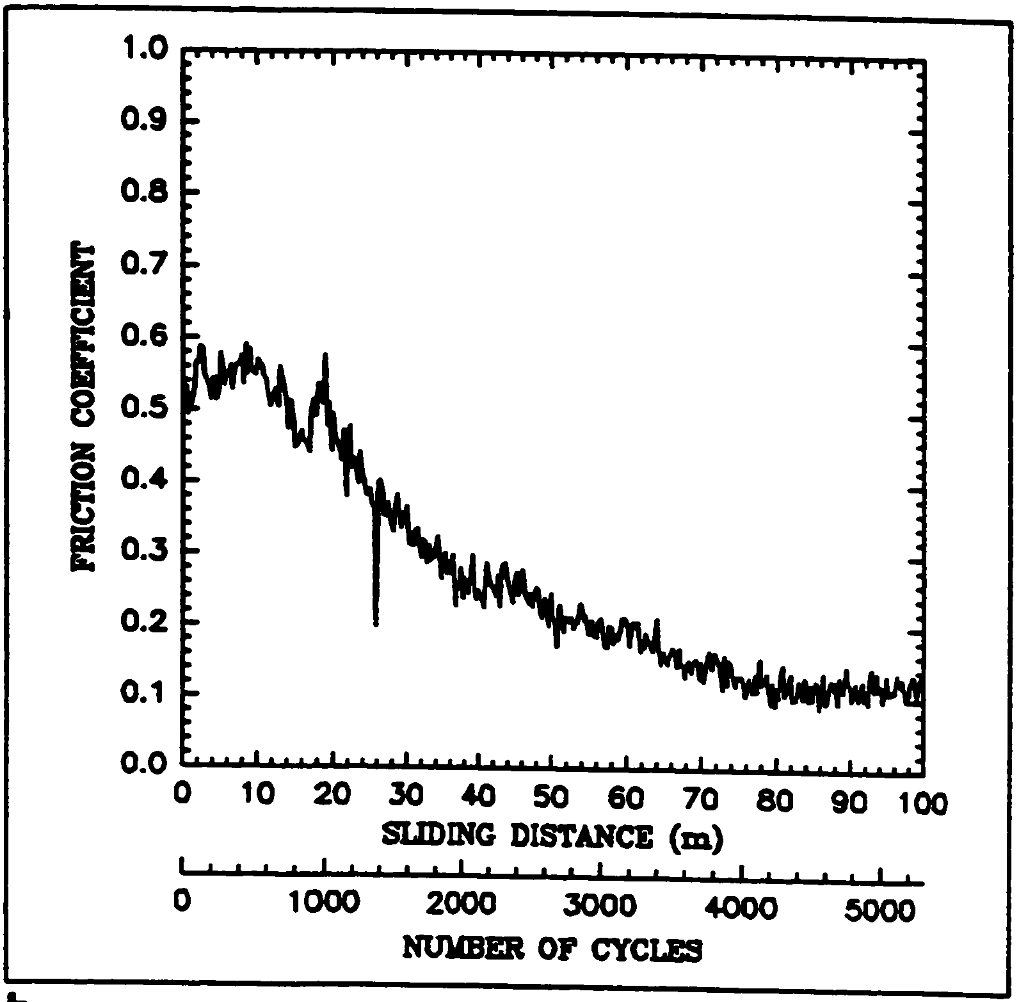

b

4.10. (continued).

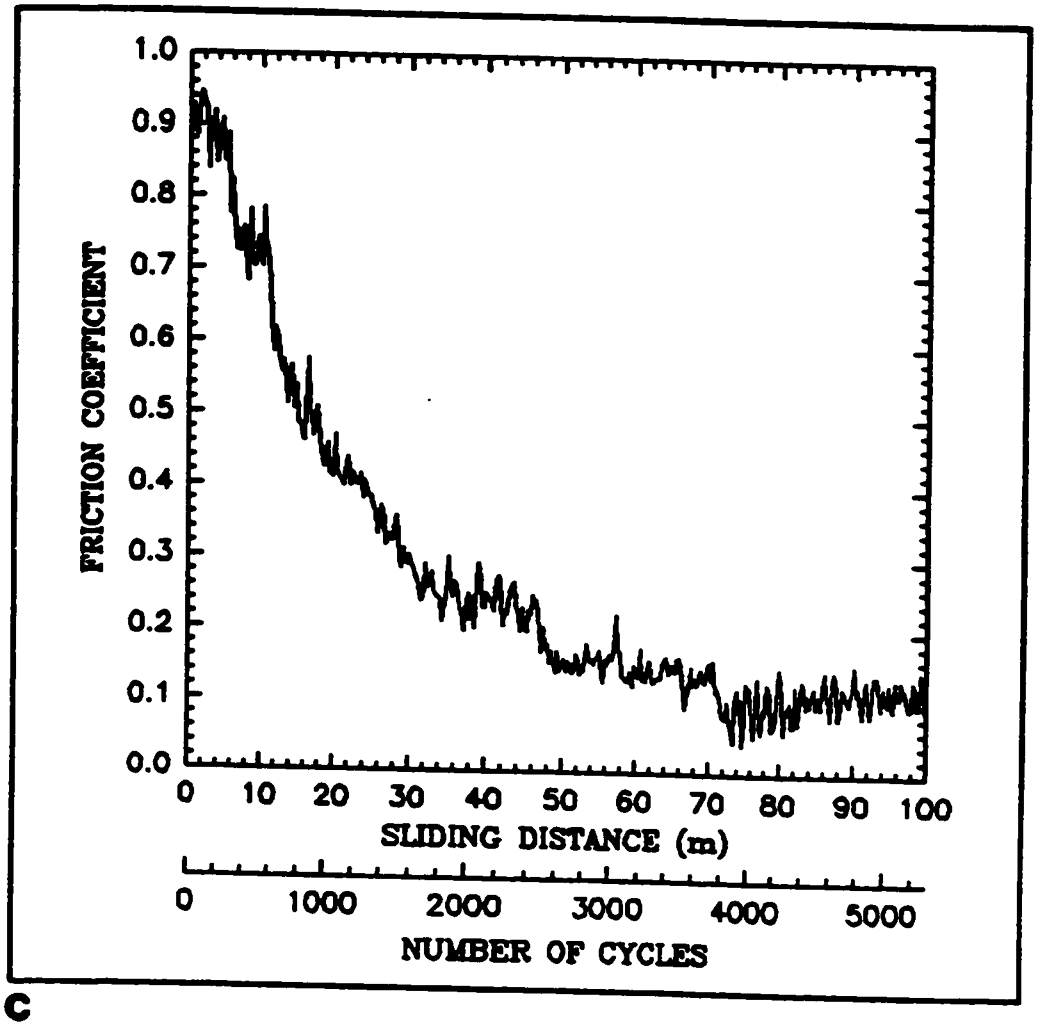

c

4.10. (continued).

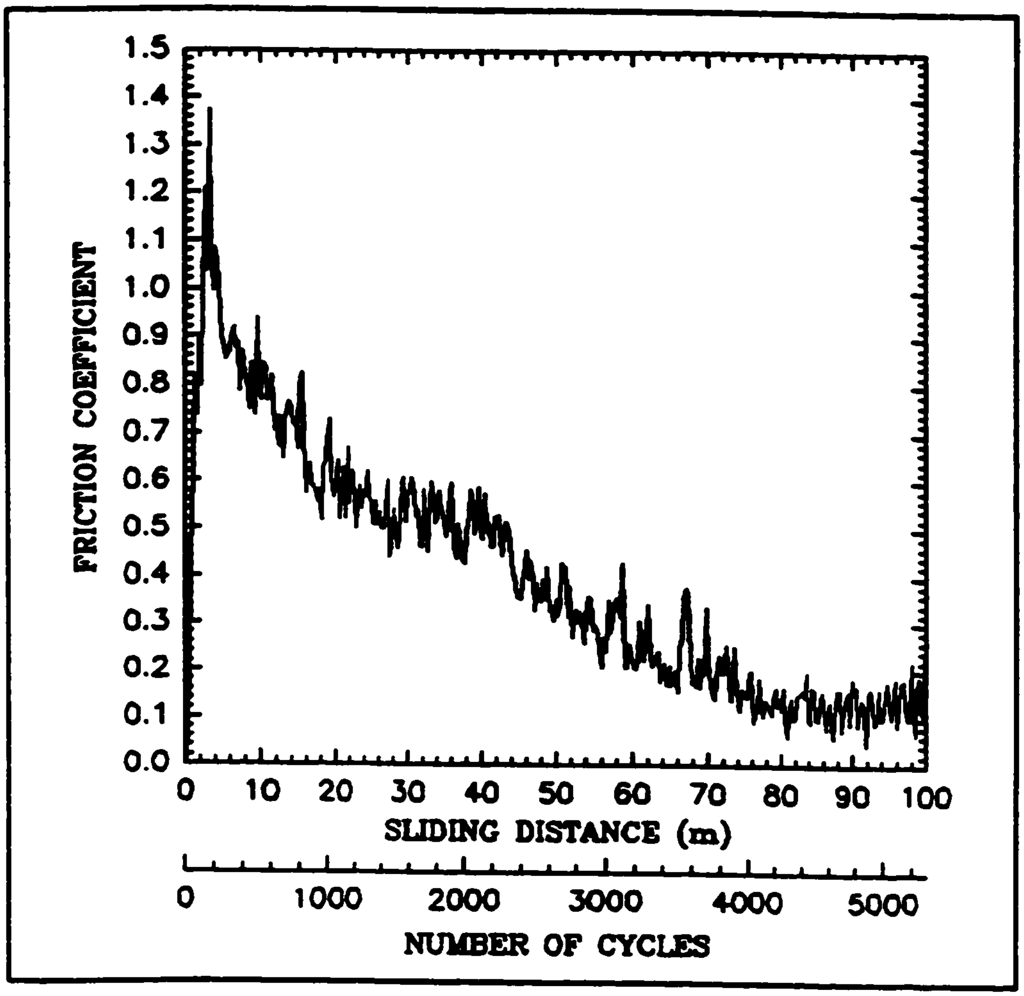

d

4.10. (continued).

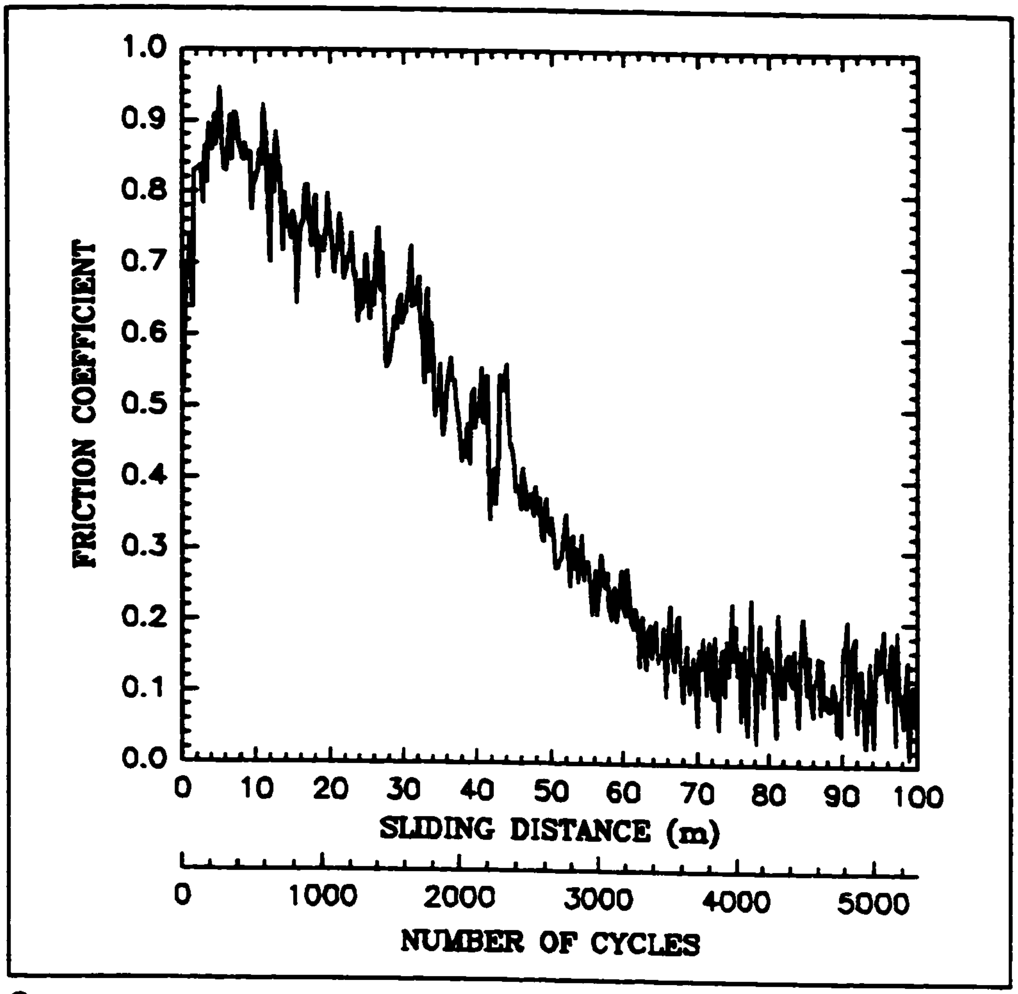

e

4.10. (continued).

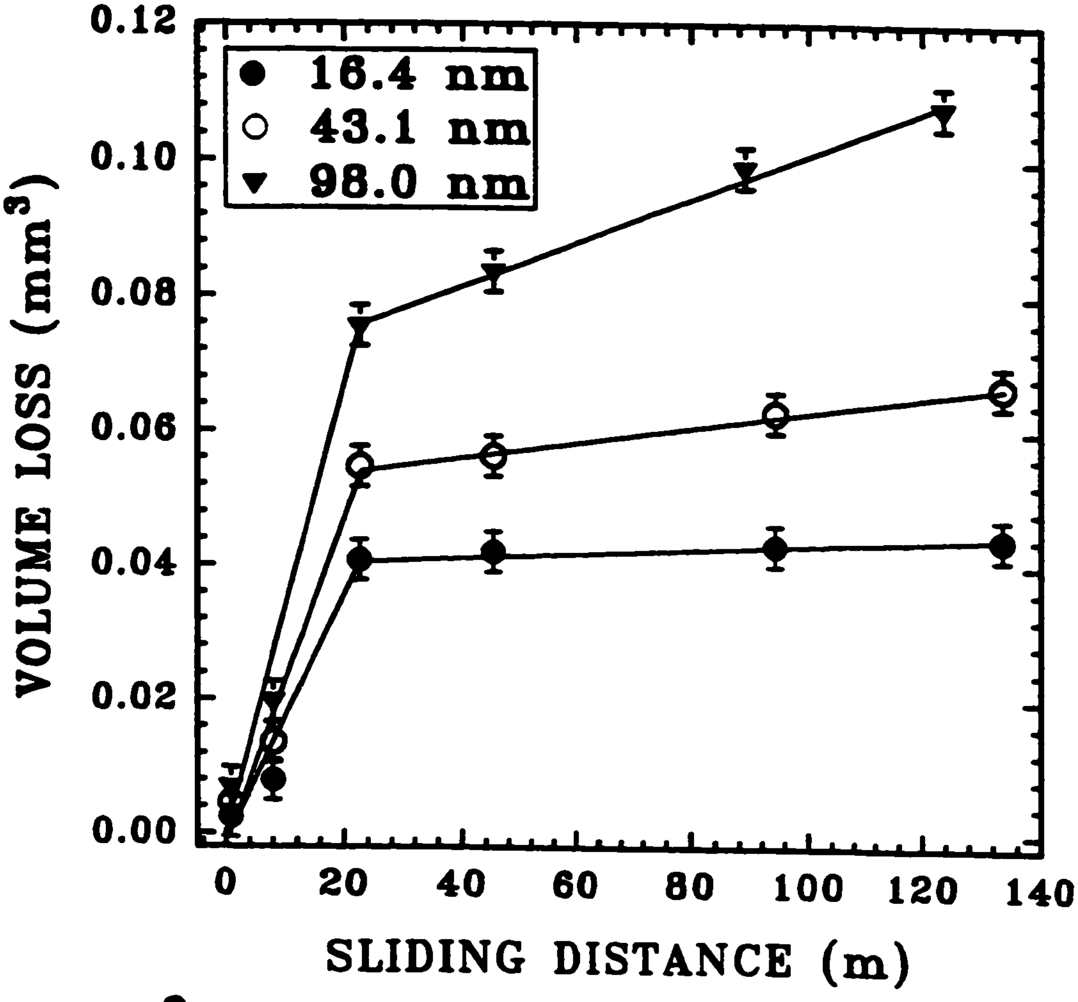

a

4.11. Cumulative volume loss versus sliding distance curves, obtained using a normal load of 1.0 N and a sliding speed of $1.3x10^{-2}$ m.s^{-1} under unlubricated sliding condition, for nanocrystalline aluminum having grain sizes of: (a)16.4 nm, 43.1 nm and 98.0 nm; (b)10^6 nm.

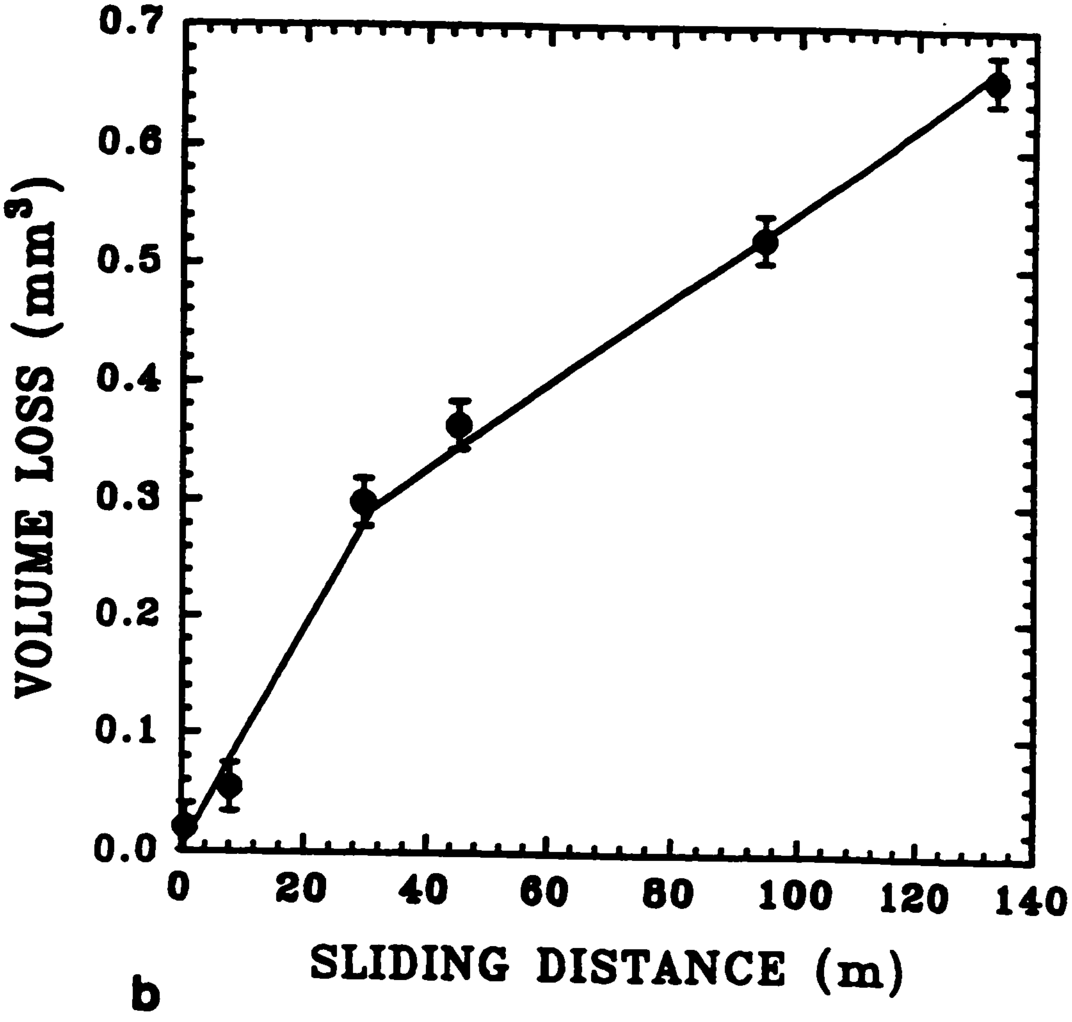

4.11. (continued).

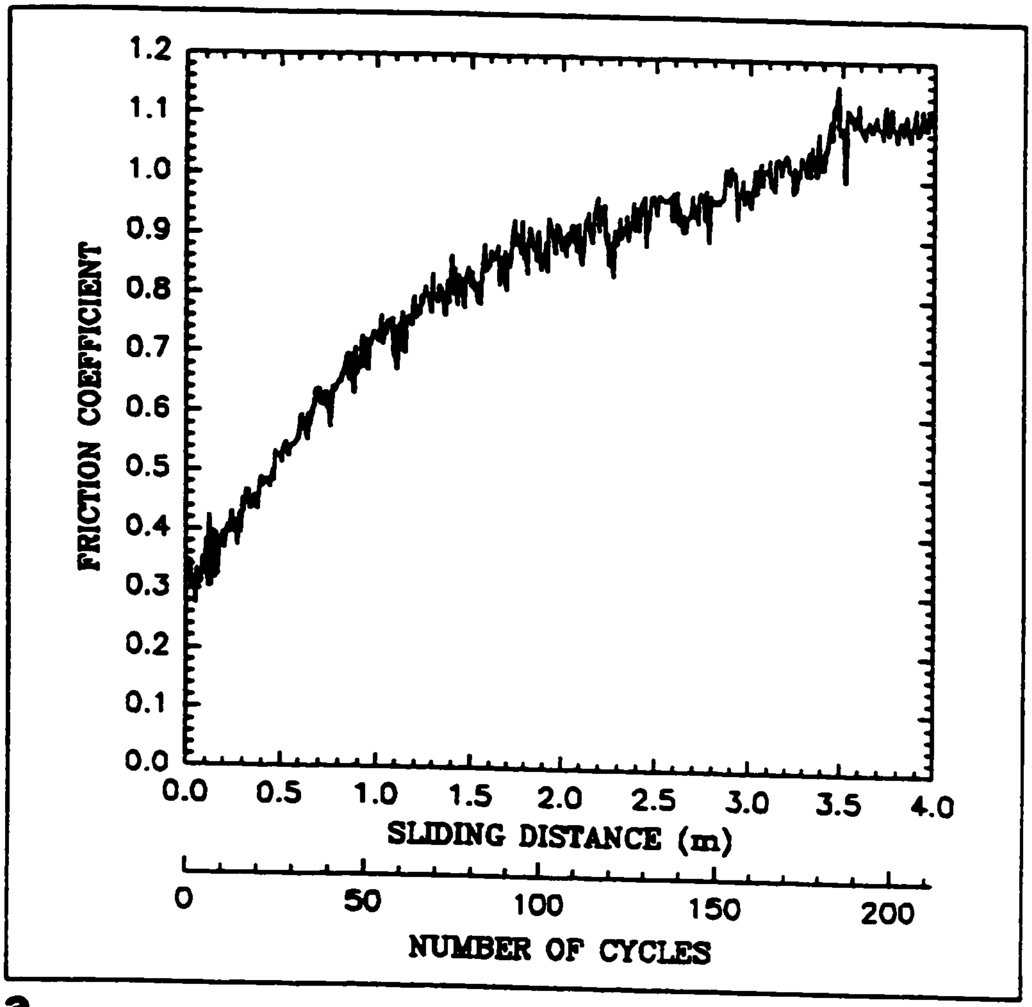

a

4.12. Coefficient of friction versus sliding distance curves performed in vacuum (10^{-6} torr) using a normal load of 1.0 N and a sliding speed of 4.2×10^{-4} m.s^{-1} under unlubricated sliding condition, for nanocrystalline aluminum having grain sizes of: (a)16.4 nm; (b)98.0 nm; (c)10^6 nm.

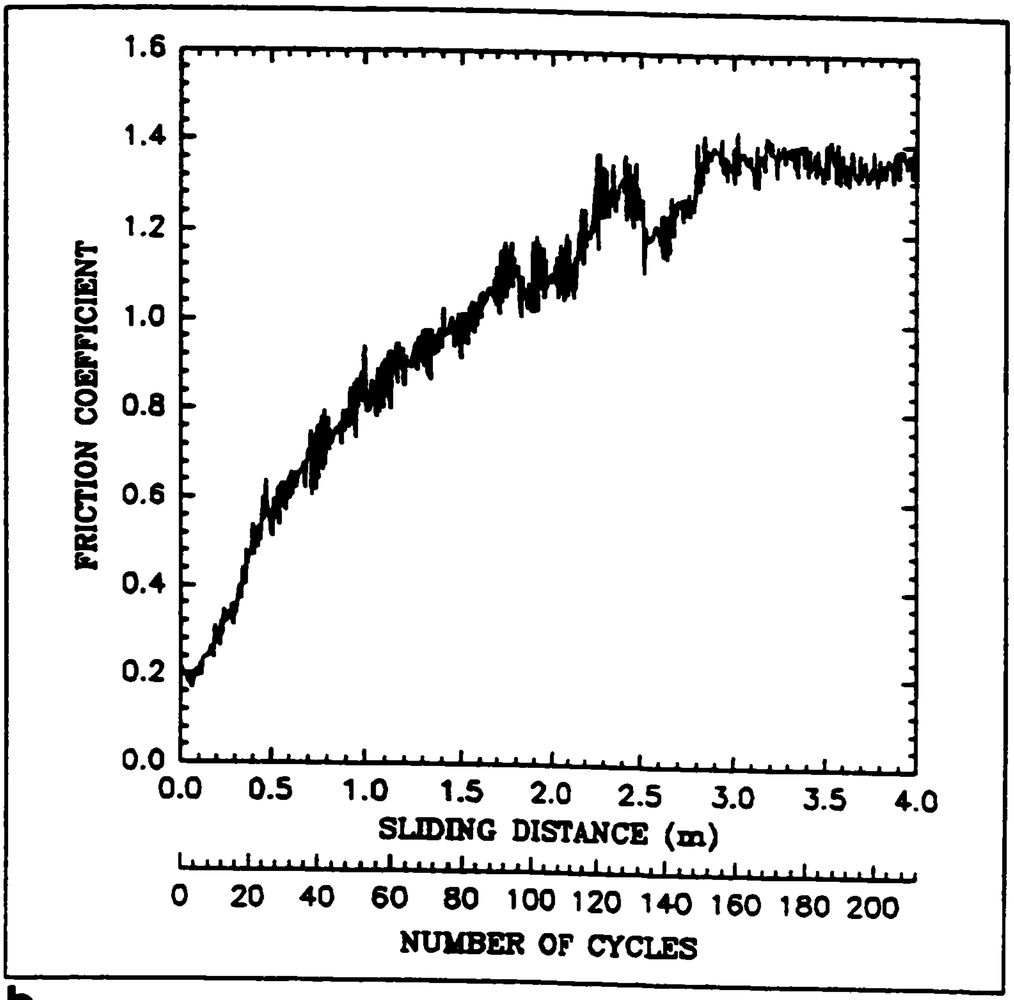

b

4.12. (continued).

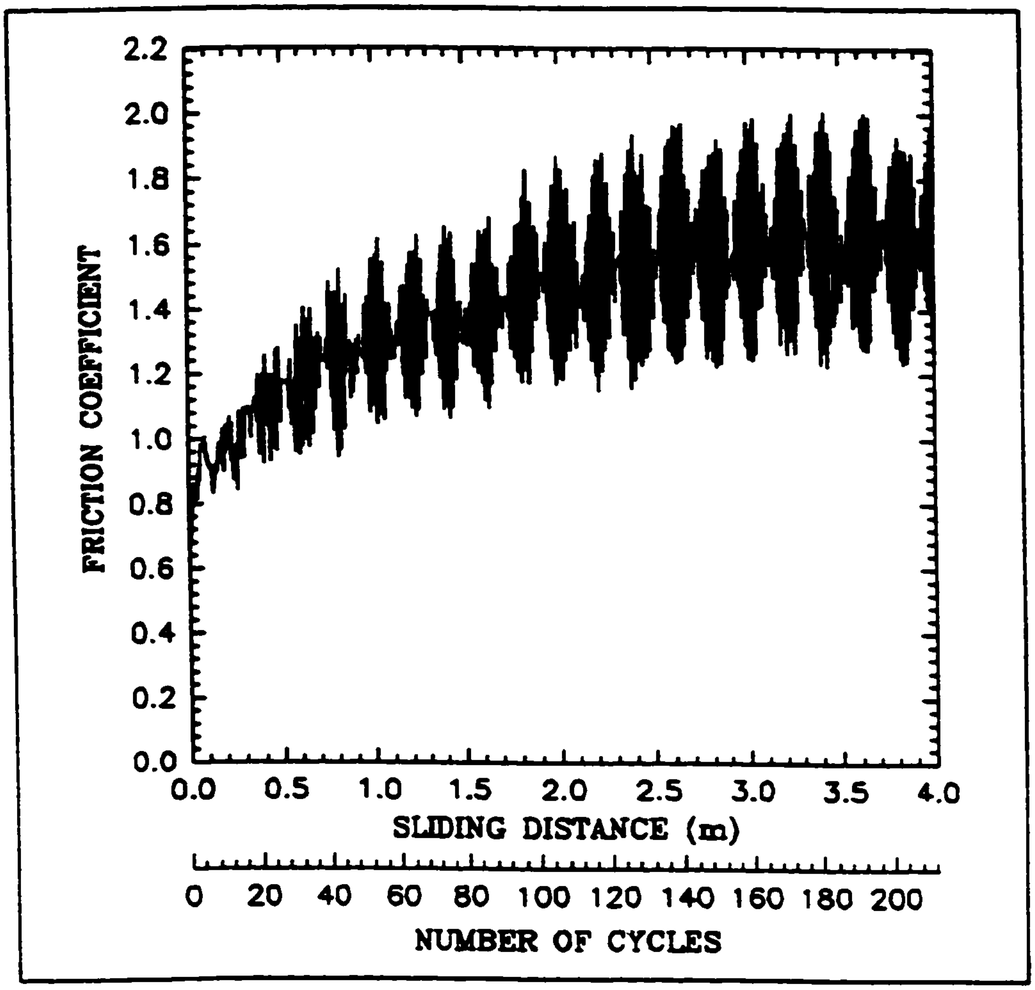

c

4.12. (continued).

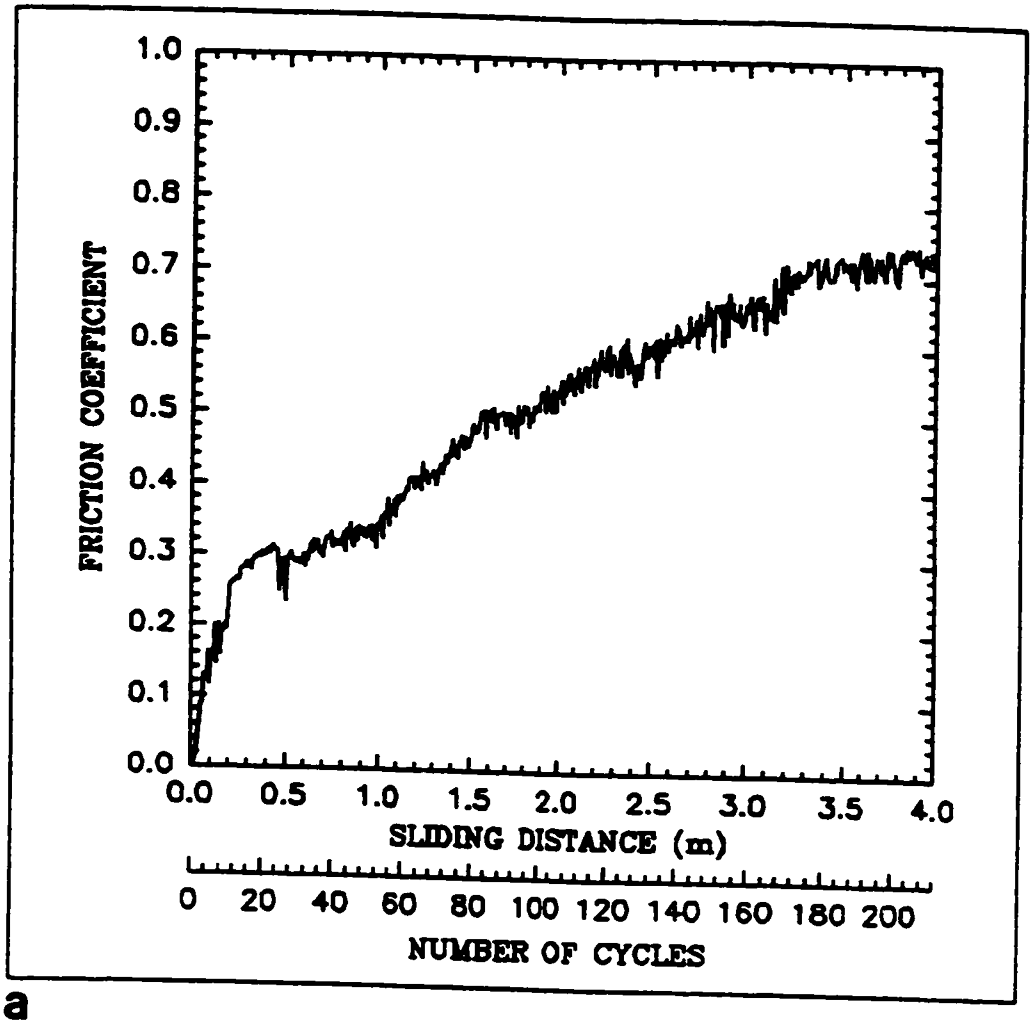

a

4.13. Coefficient of friction versus sliding distance curves performed in air using a normal load of 1.0 N and a sliding speed of $4.2\text{x}10^{-4}$ m.s^{-1} under unlubricated sliding condition, for nanocrystalline aluminum having grain sizes of: (a)16.4 nm; (b)98.0 nm; (c)10^6 nm.

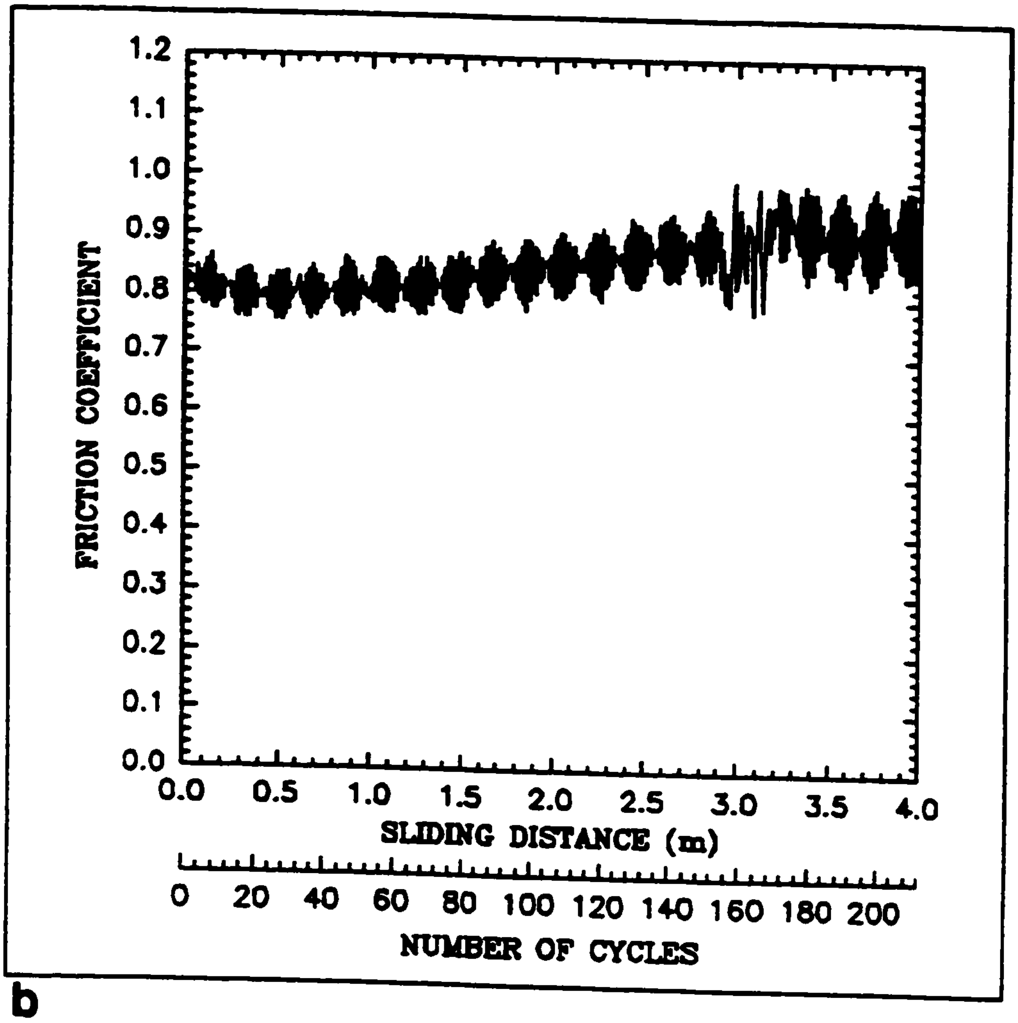

4.13. (continued).

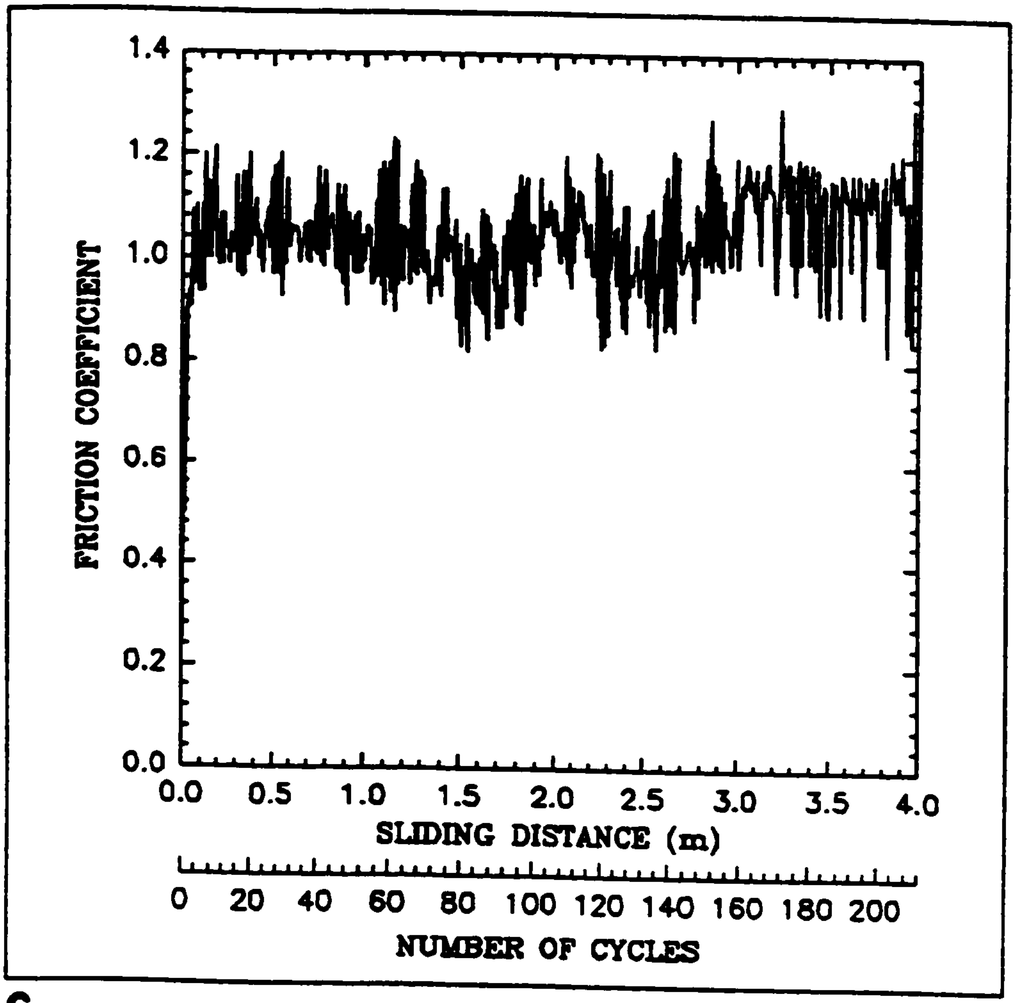

c

4.13. (continued).

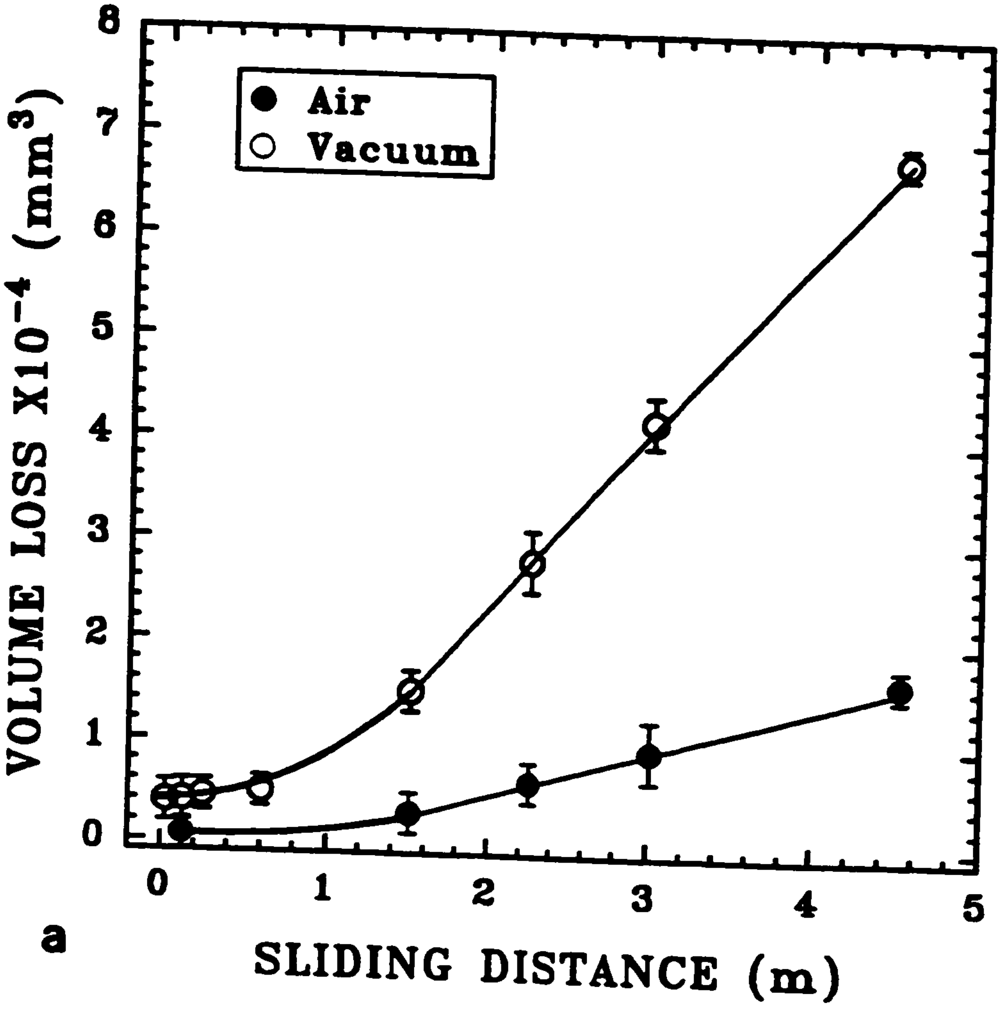

4.14. Cumulative volume loss versus sliding distance curves preformed in vacuum and air using a normal load of 1.0 N and a sliding speed of $4.2x10^{-4}$ $m.s^{-1}$ under unlubricated sliding condition, for nanocrystalline aluminum having grain sizes of:(a)16.4 nm; (b)98.0 nm; (c)10^6 nm.

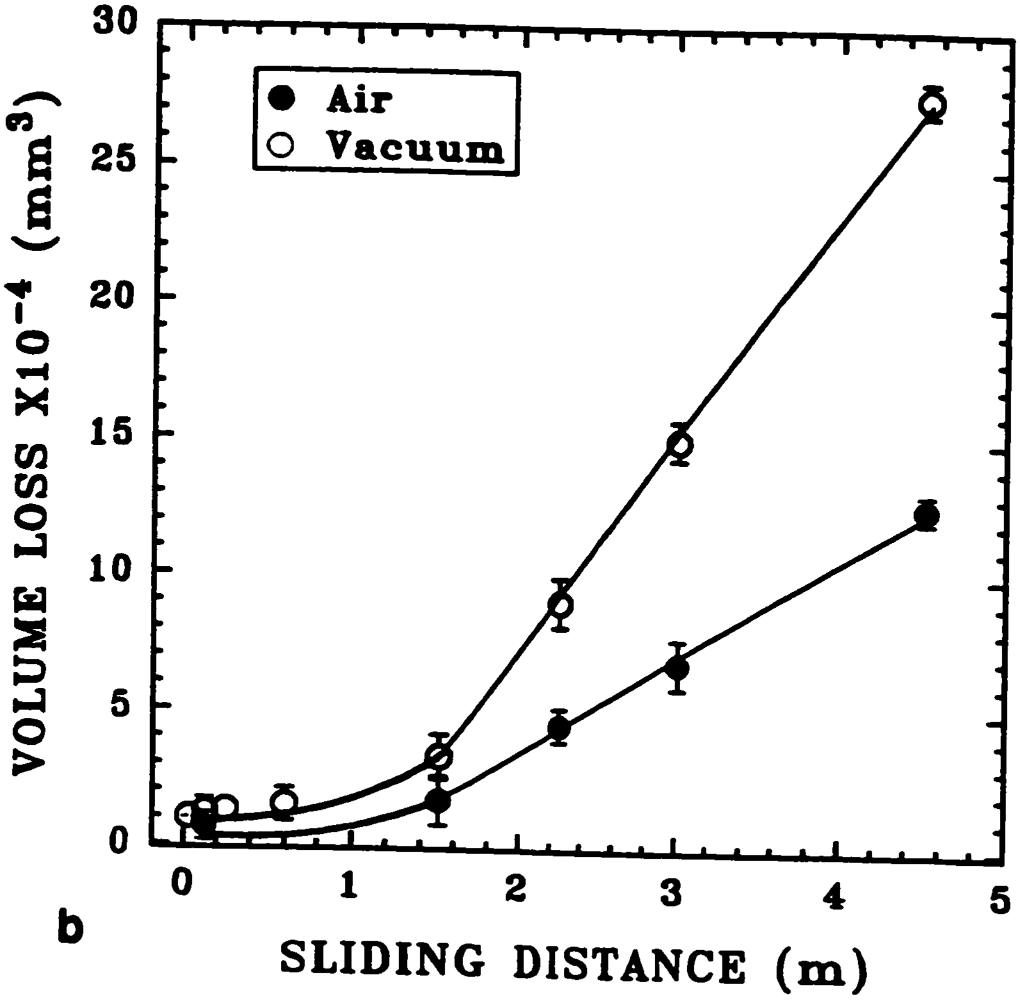

4.14. (continued).

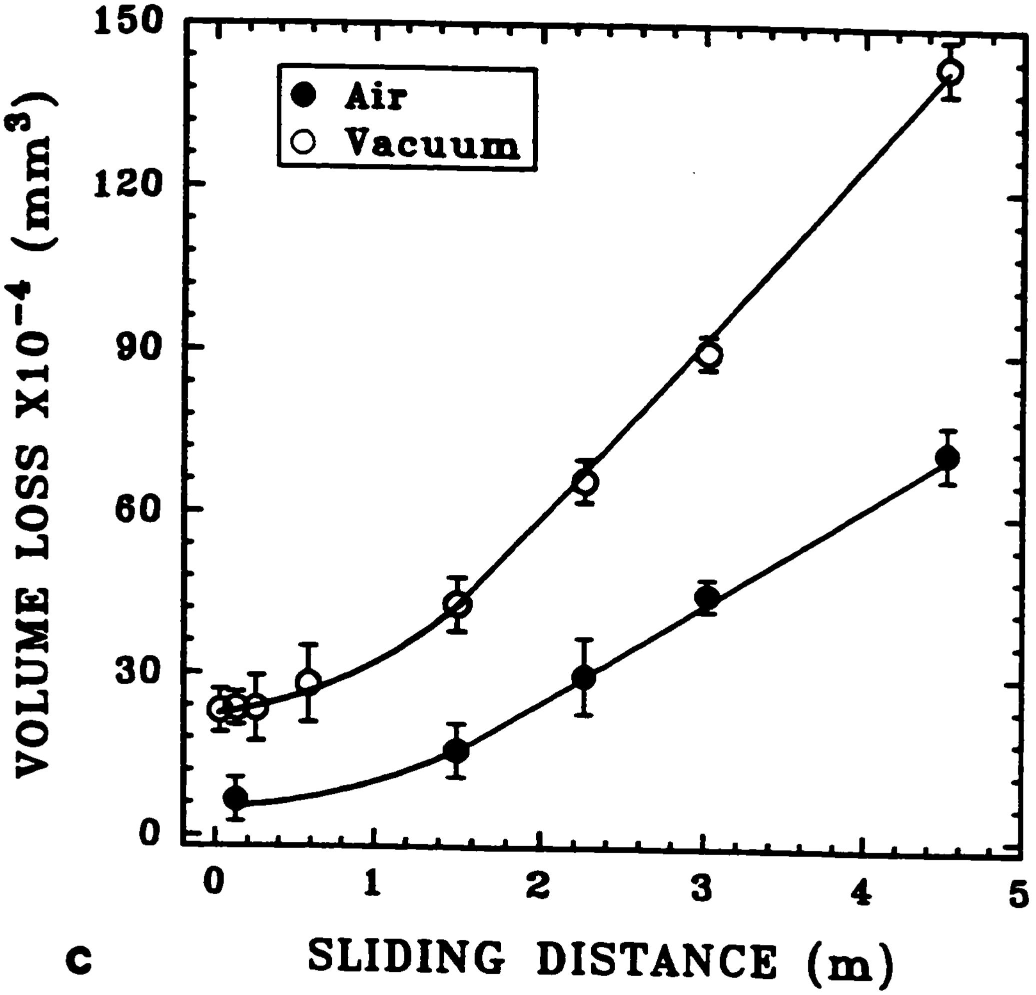

4.14. (continued).

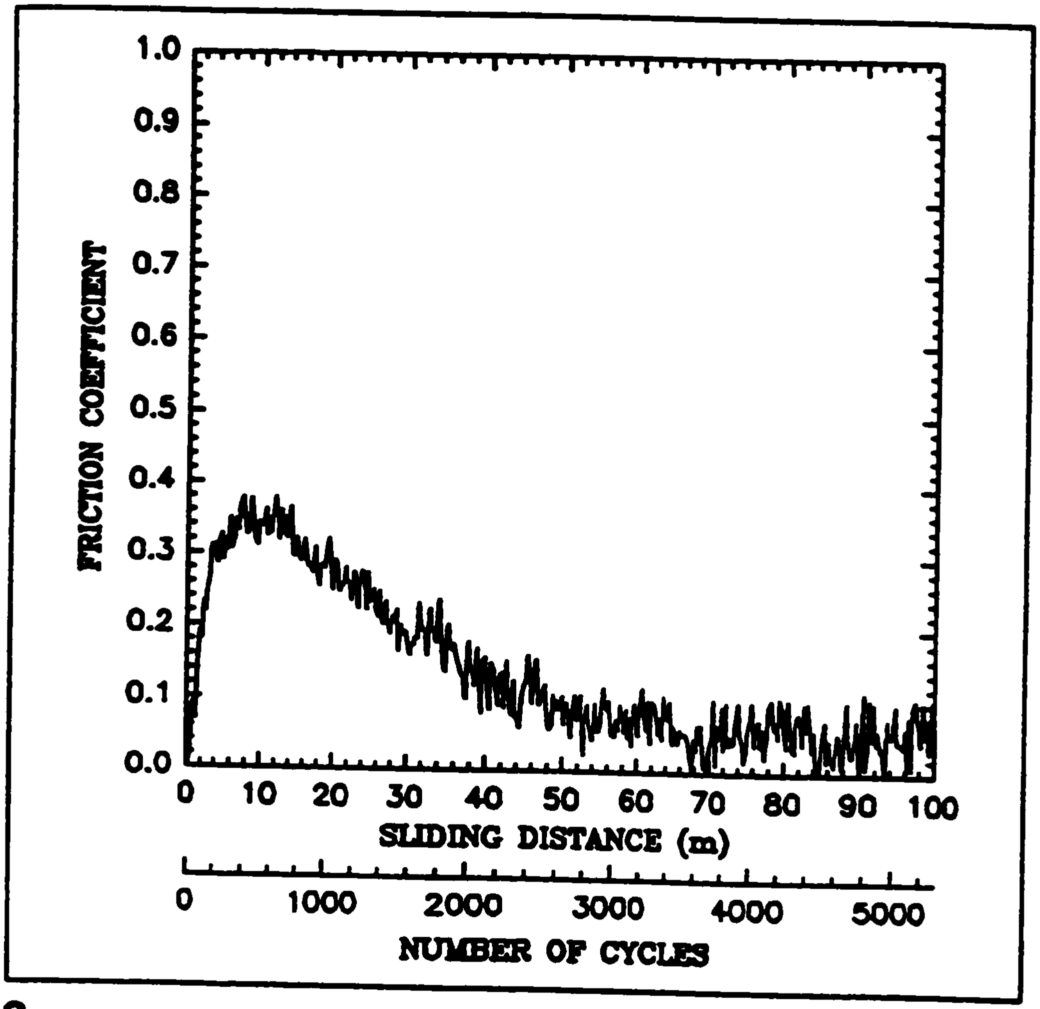

a

4.15. Coefficient of friction versus sliding distance curves, obtained using a normal load of 1.0 N and a sliding speed of 1.3×10^{-2} m.s^{-1} under unlubricated sliding condition, for Al/Al_2O_3 having an average aluminum layer thickness of: (a)200 nm; (b)500 nm.

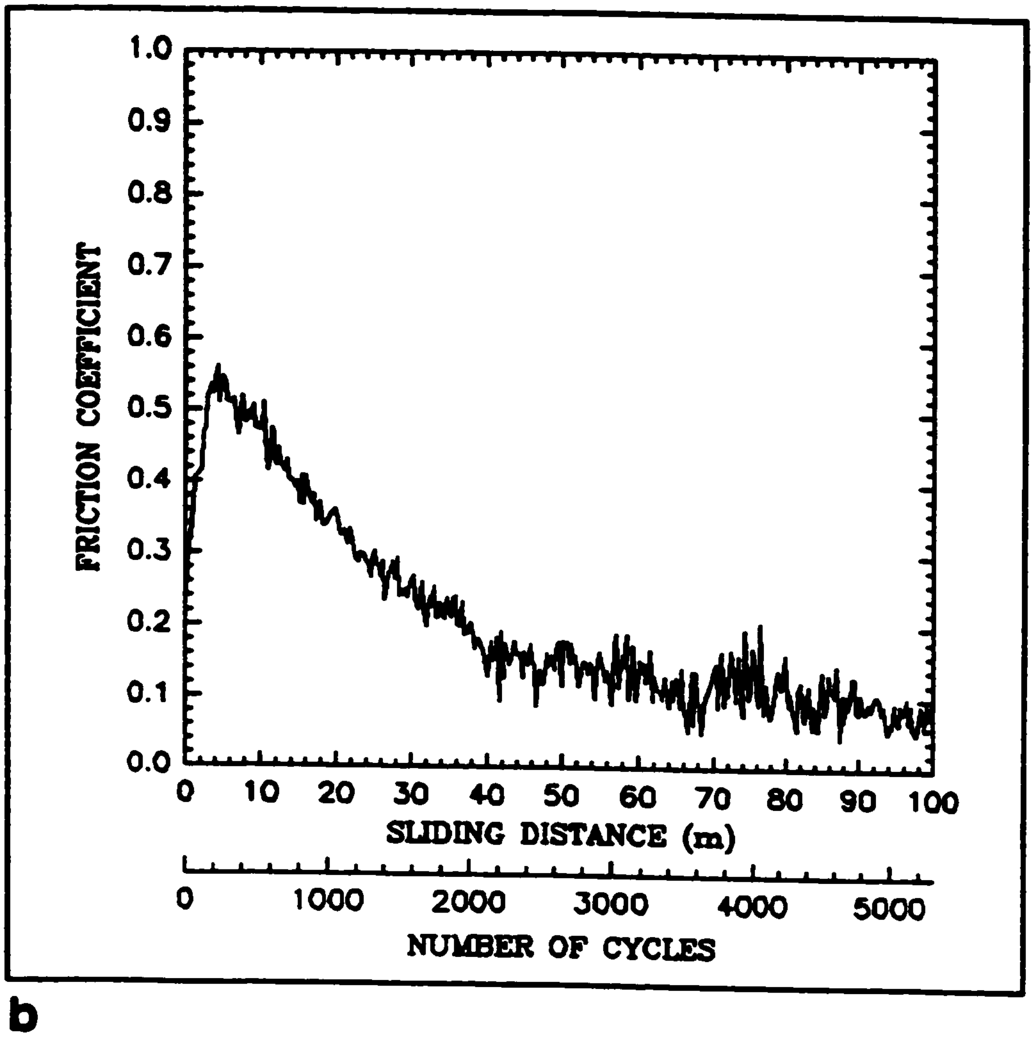

4.15. (continued).

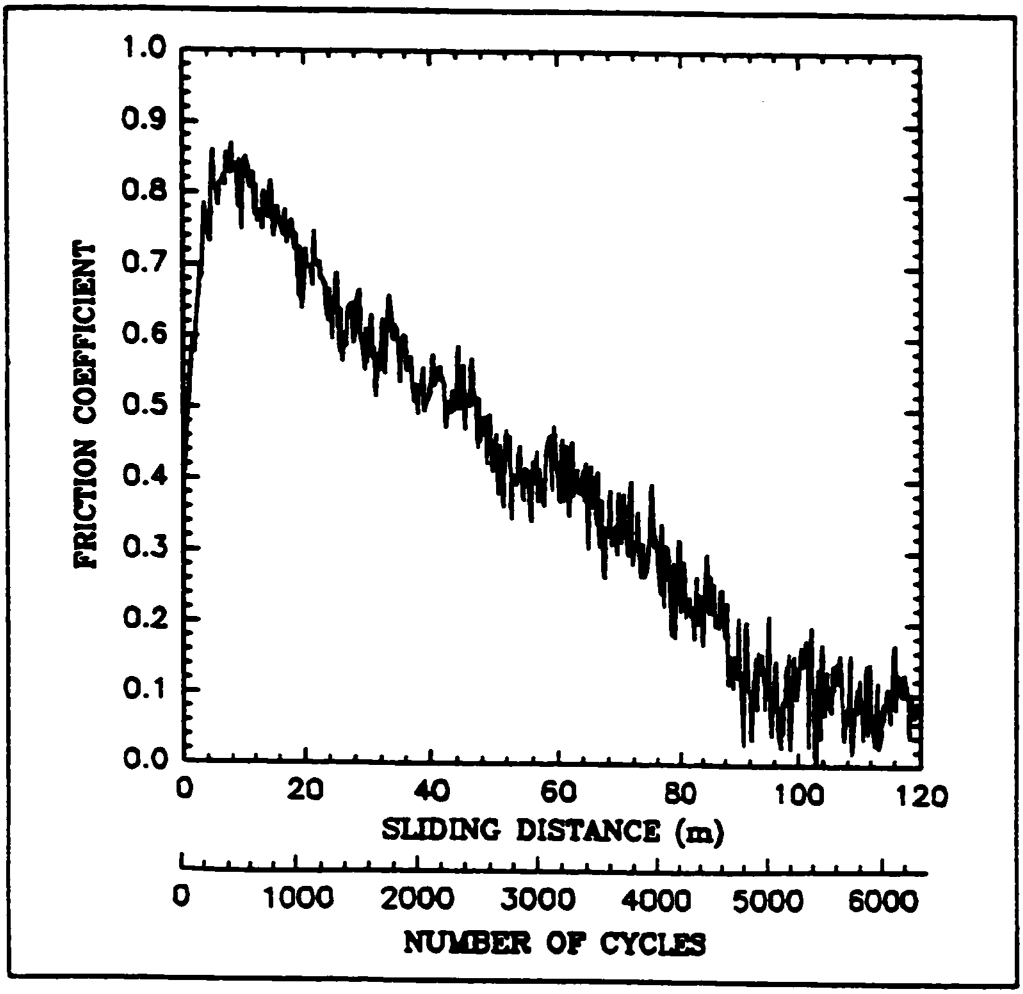

4.16. Coefficient of friction versus sliding distance curve for Al_2O_3 obtained using a normal load of 1.0 N and a sliding speed of 1.3×10^{-2} $m.s^{-1}$ under unlubricated sliding condition.

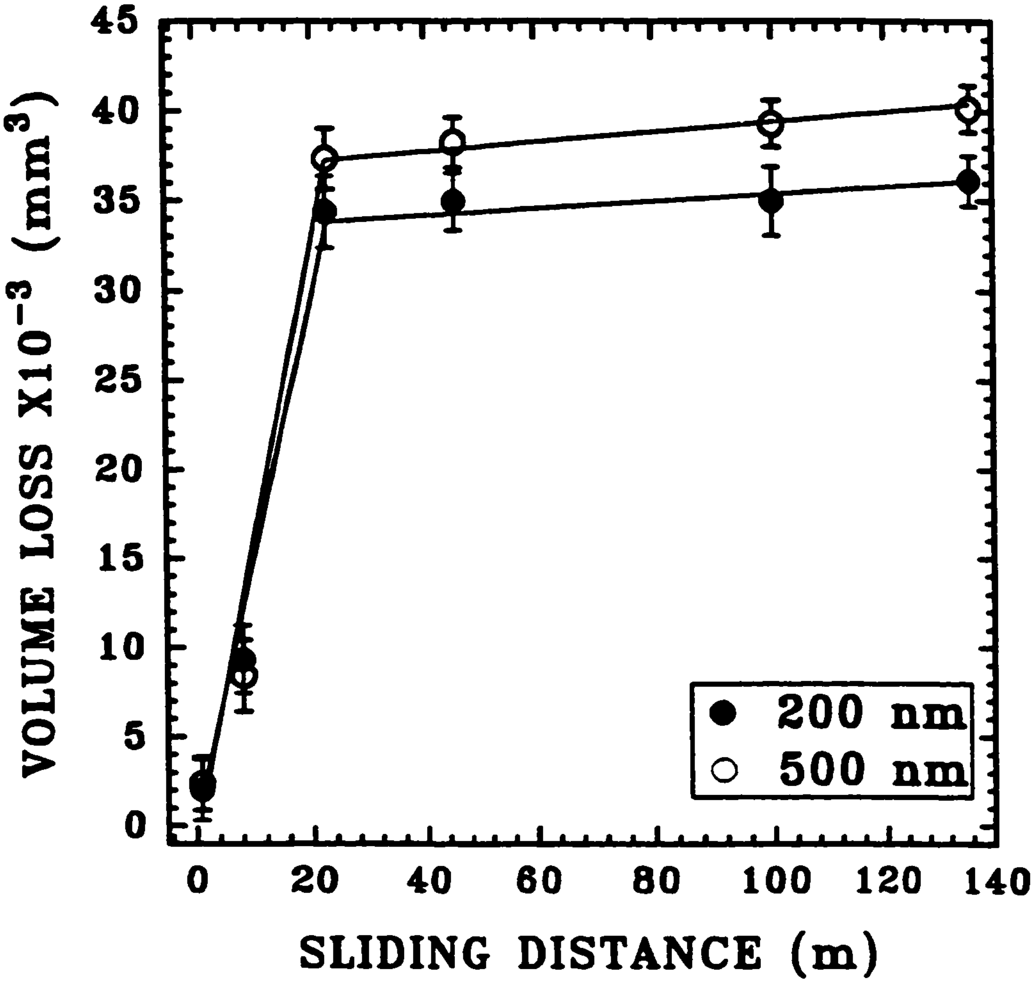

4.17. Cumulative volume loss versus sliding distance curves, obtained using a normal load of 1.0 N and a sliding speed of $1.3\text{x}10^{-2}$ m.s^{-1} under unlubricated sliding condition, for Al/Al_2O_3 having aluminum layer thickness of 200 and 500 nm.

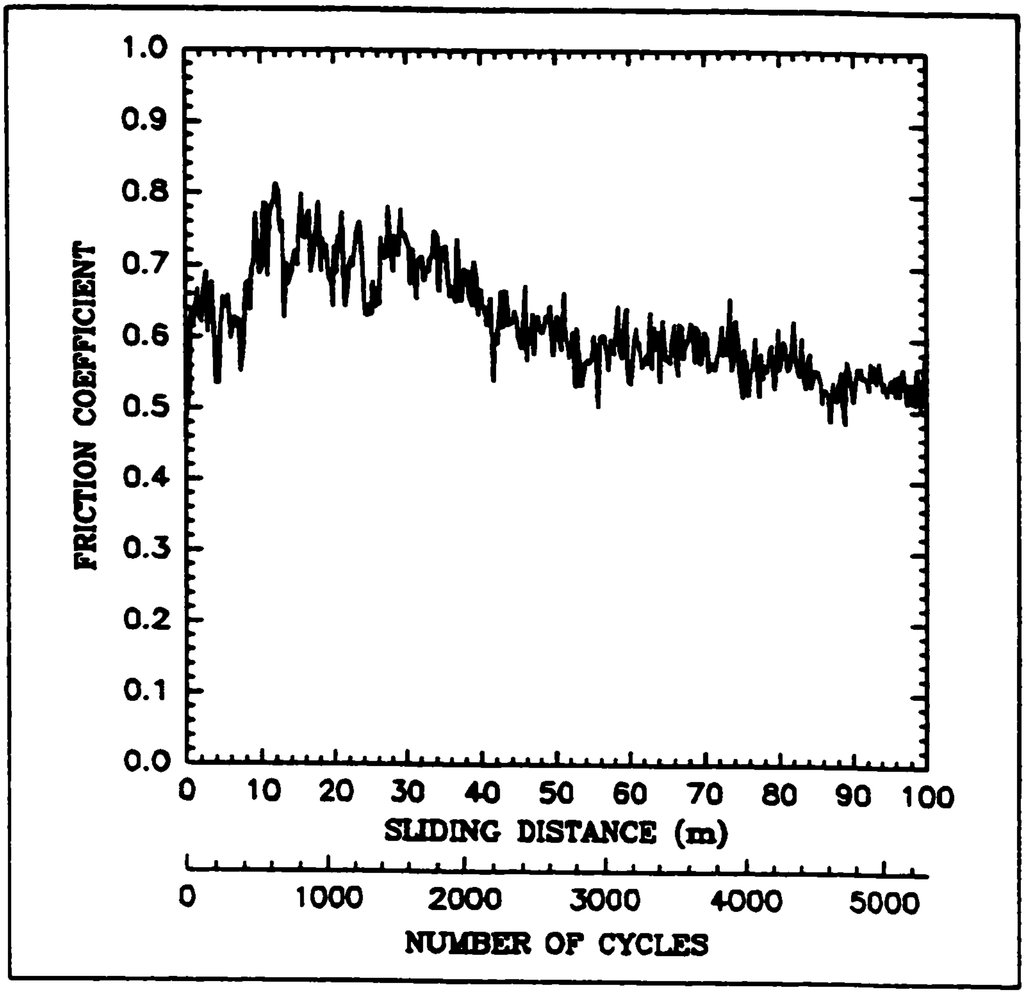

a

4.18. Coefficient of friction versus sliding distance curves, obtained using a normal load of 1.0 N and a sliding speed of 1.3×10^{-2} $m.s^{-1}$ under unlubricated sliding condition, for: (a)as-sputtered titanium; (b)Ti/TiN having 150 nm titanium layer thickness; (c)Ti/TiN having 450 nm titanium layer thickness; (d)monolithic TiN (RIP).

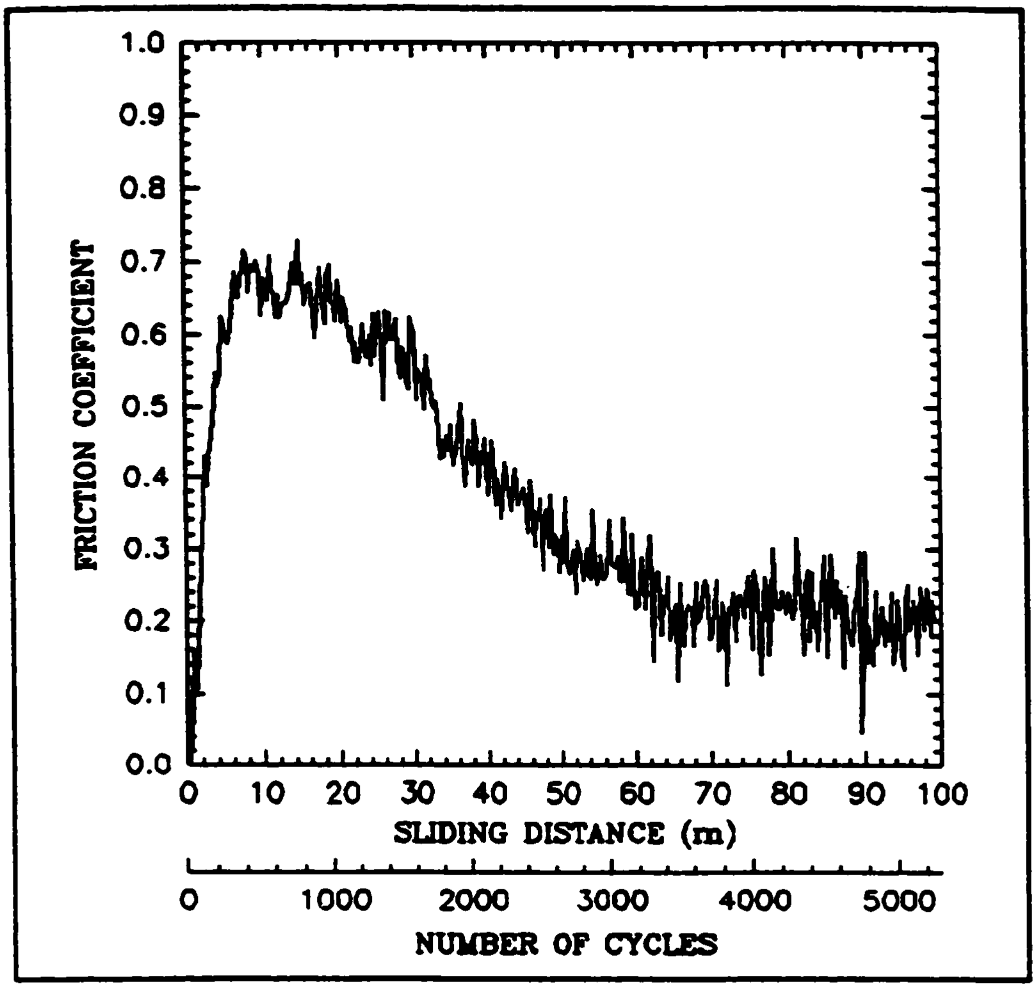

b

4.18. (continued).

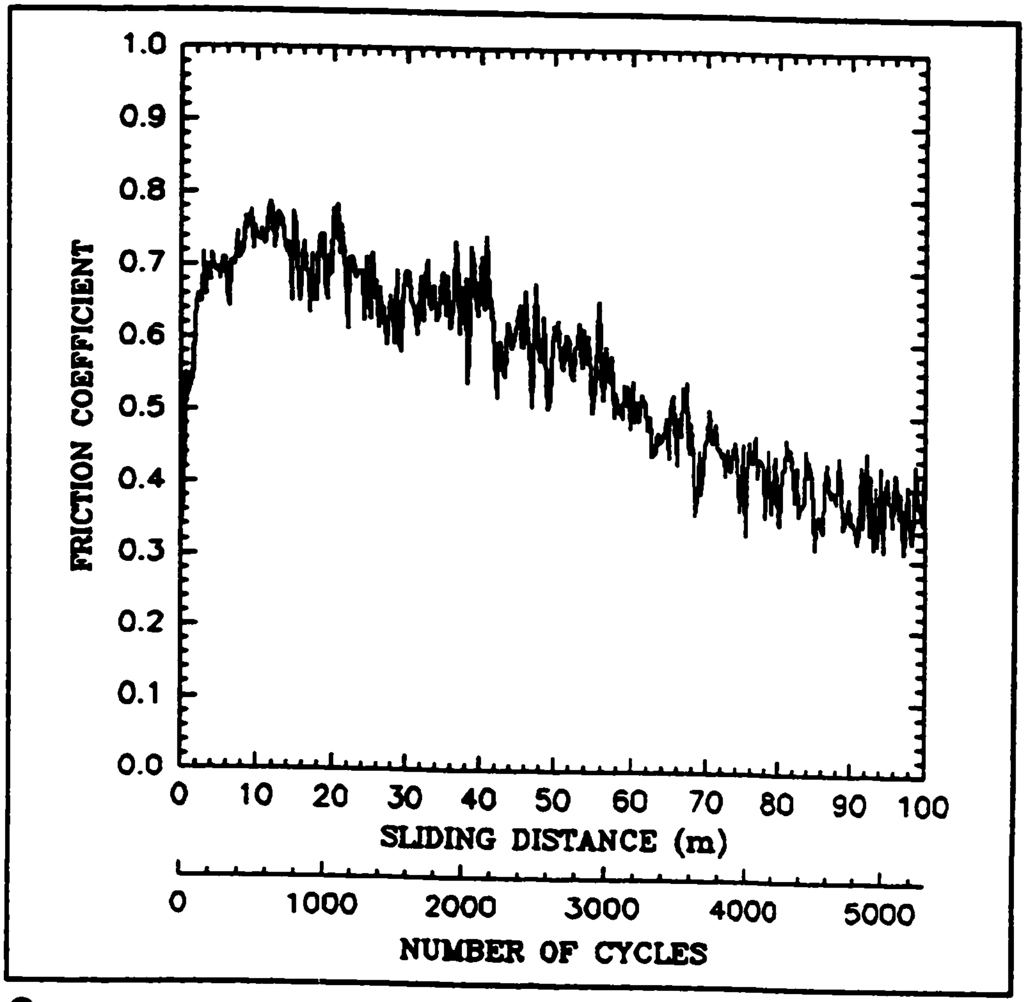

C

4.18. (continued).

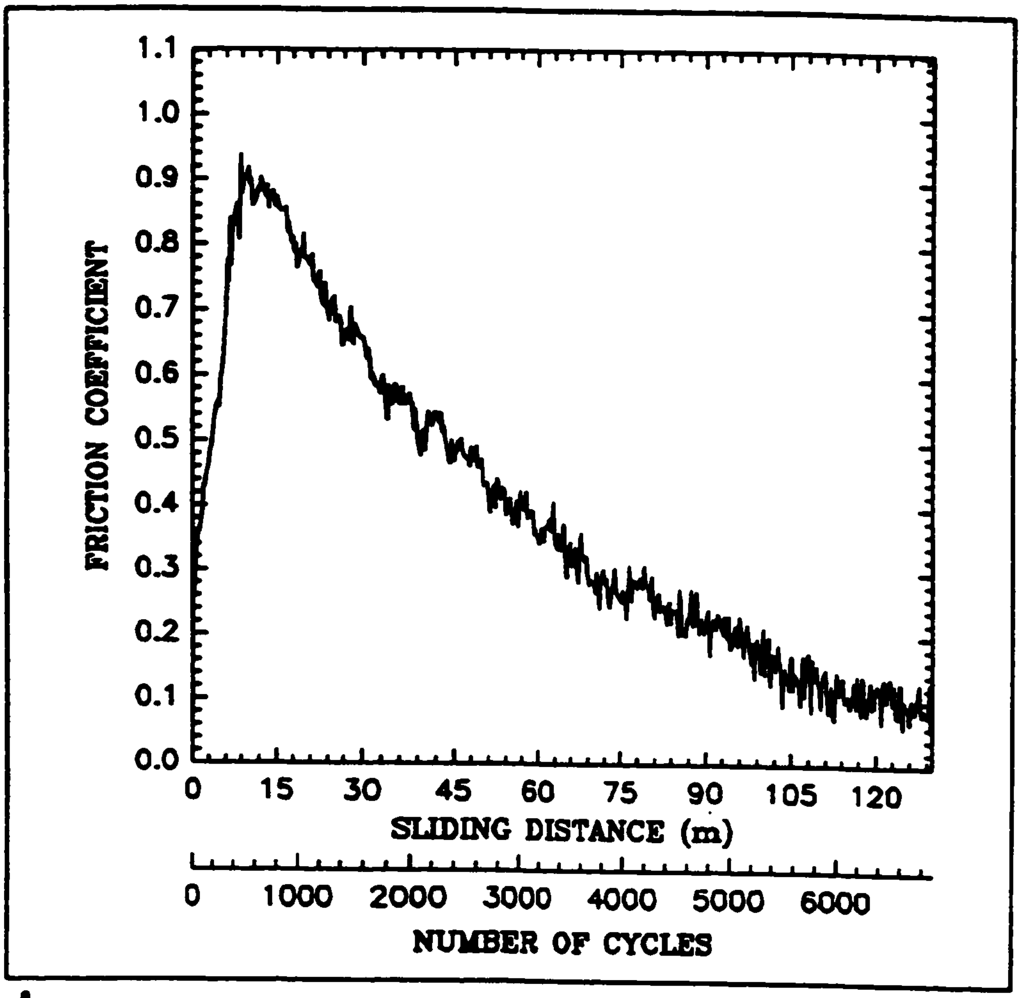

d

4.18. (continued).

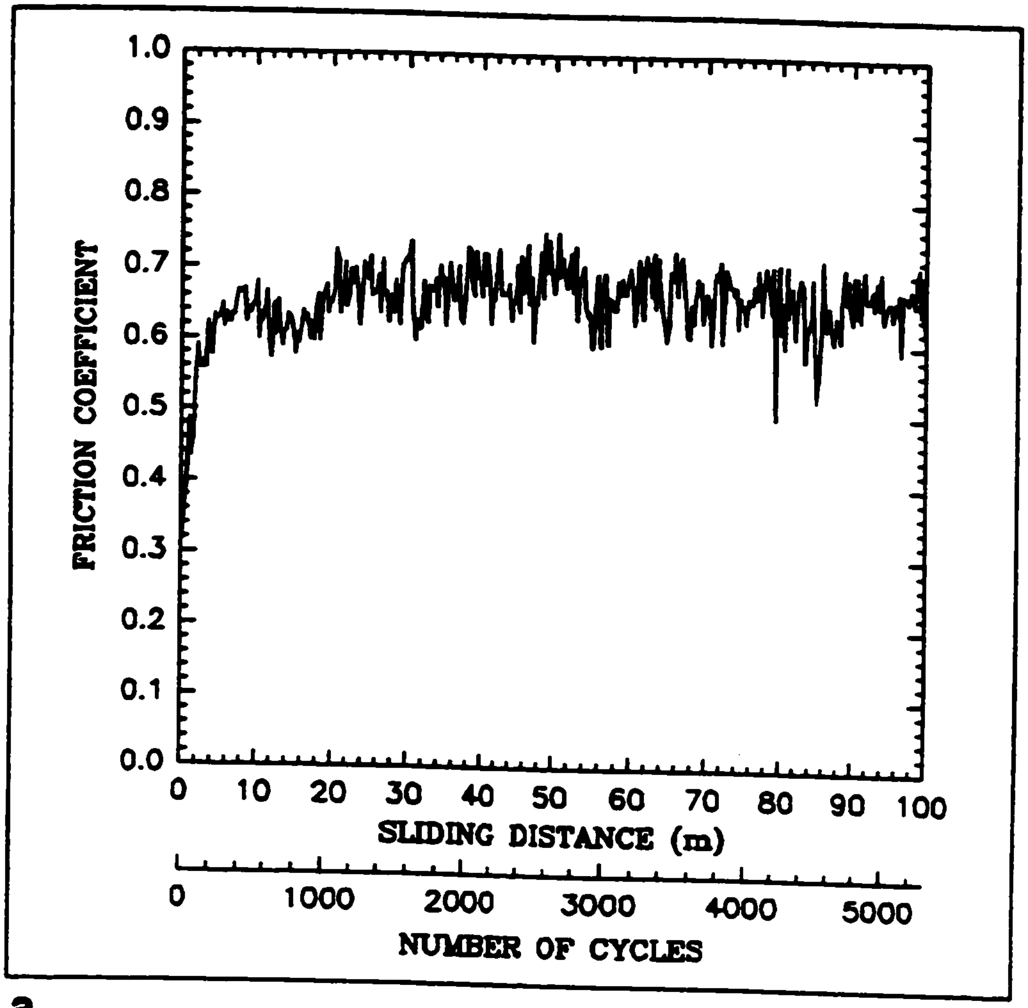

a

4.19. Coefficient of friction versus sliding distance curves, obtained using a normal load of 1.0 N and a sliding speed of 1.3×10^{-2} m.s^{-1} under unlubricated sliding condition, for coarse-grained titanium: (a) normal section; (b) transverse section.

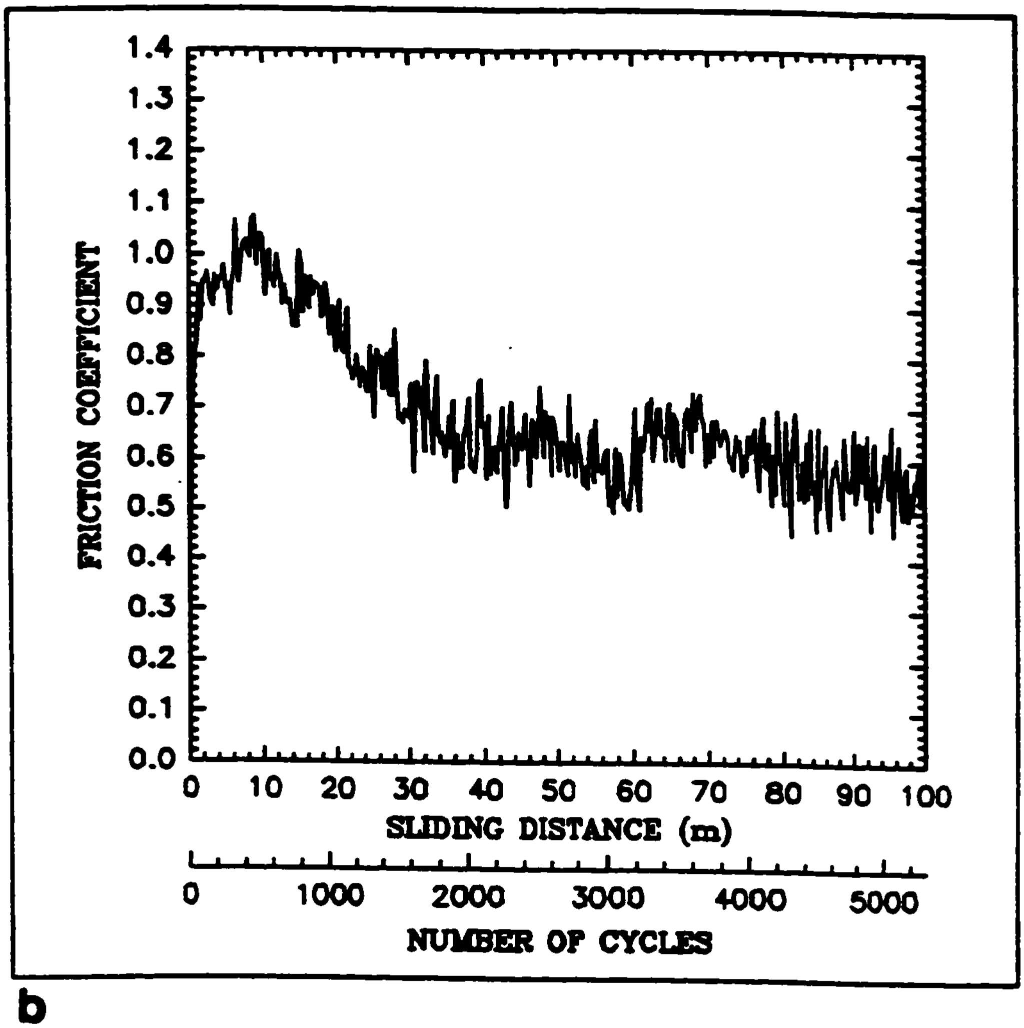

4.19. (continued).

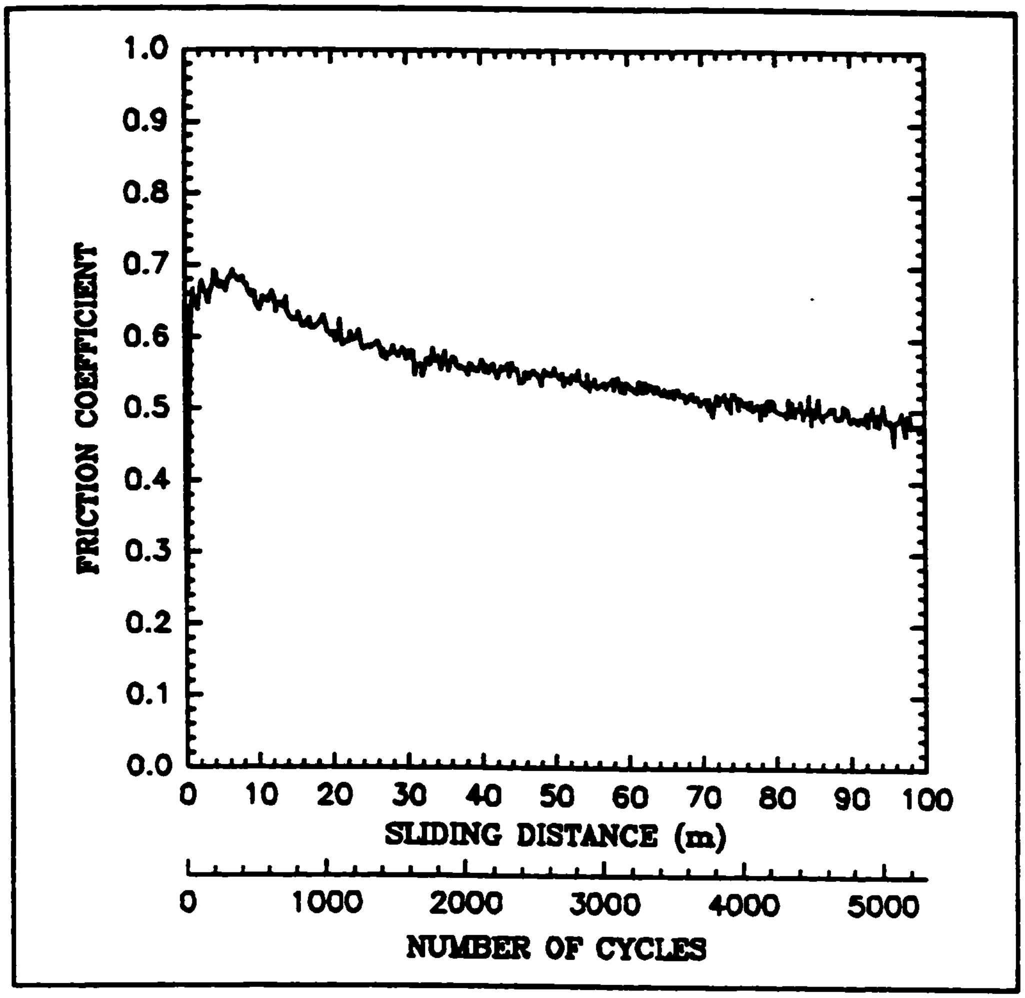

4.20. Coefficient of friction versus sliding distance curve, obtained using a normal load of 1.0 N and a sliding speed of $1.3x10^{-2}$ $m.s^{-1}$ under unlubricated sliding condition, for silica glass.

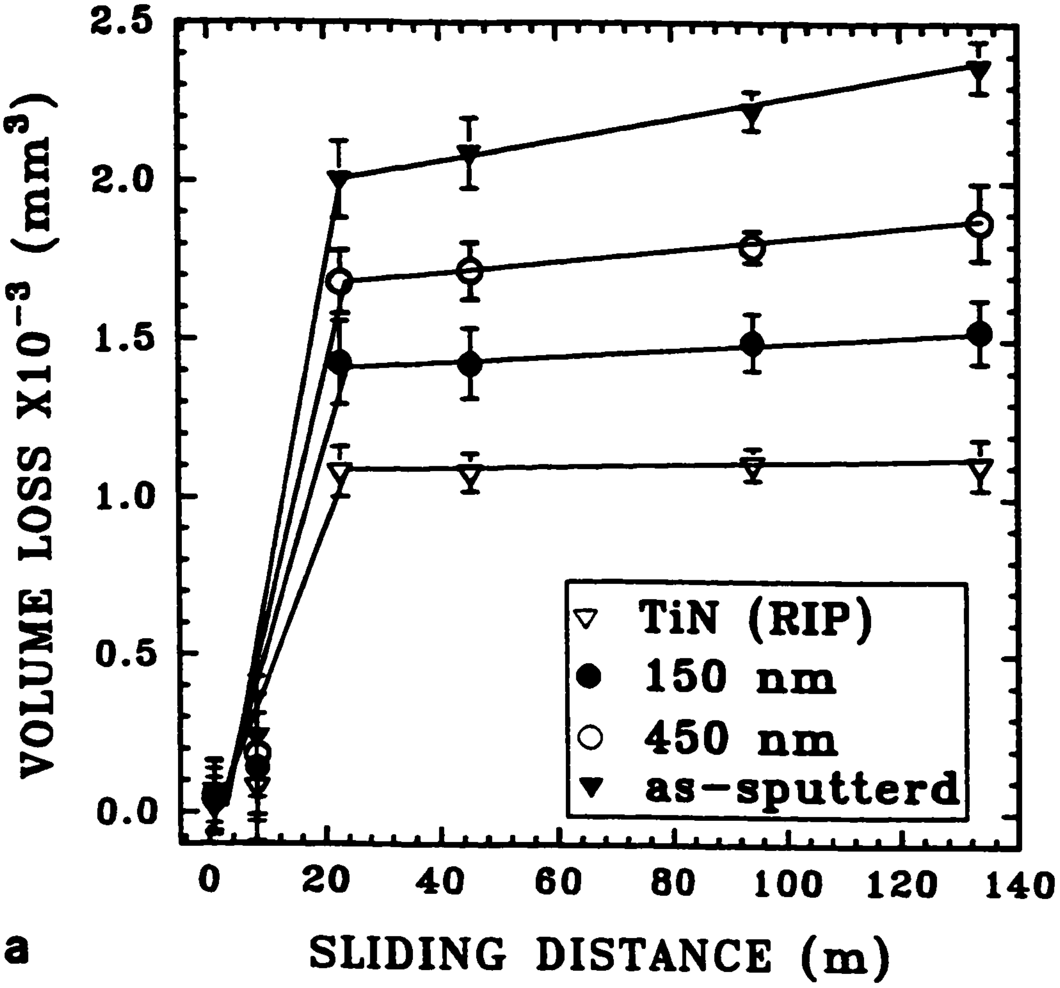

4.21. Cumulative volume loss versus sliding distance curves, obtained using a normal load of 1.0 N and a sliding speed of 1.3x10^{-2} m.s^{-1} under unlubricated sliding condition, for: (a)as-sputtered titanium, T/TiN having 150 and 450 nm titanium layer thickness and monolithic TiN (RIP); (b)coarse-grained titanium (normal section).

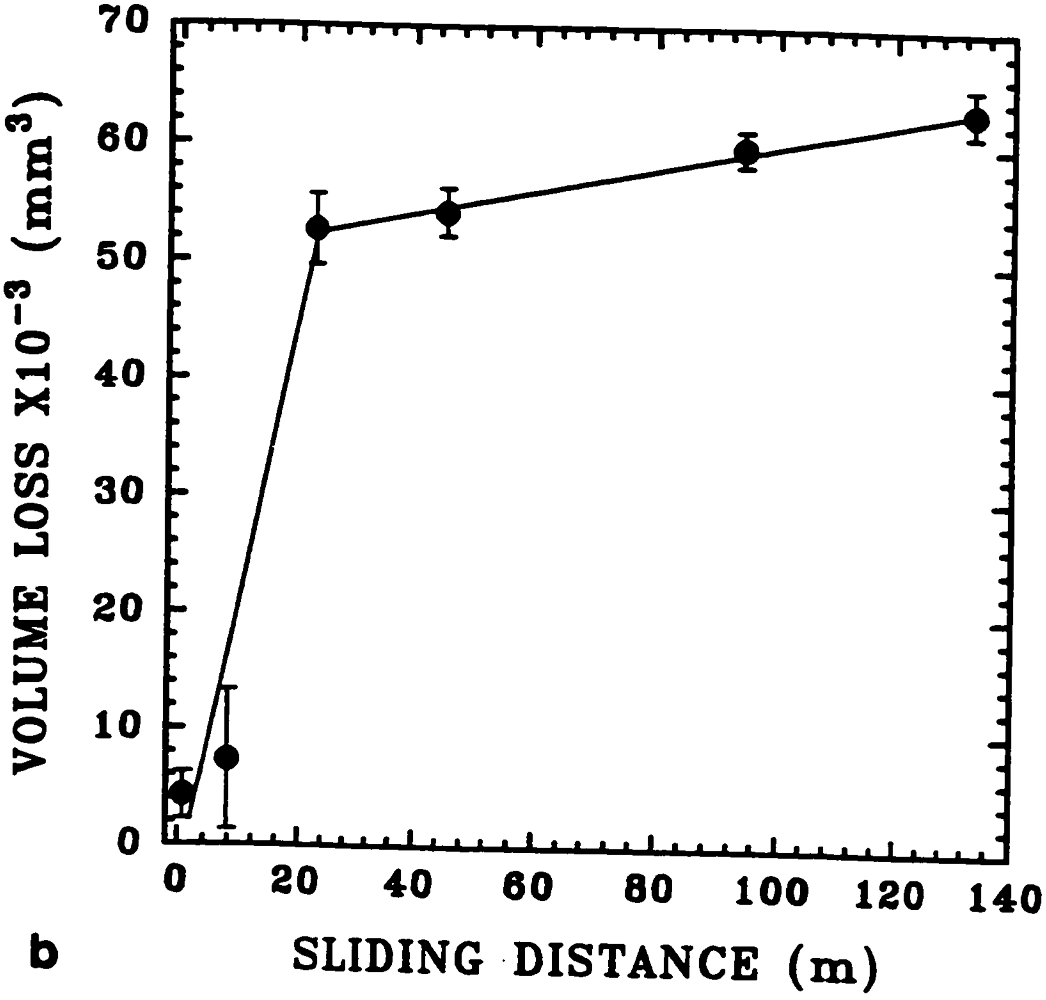

4.21. (continued).

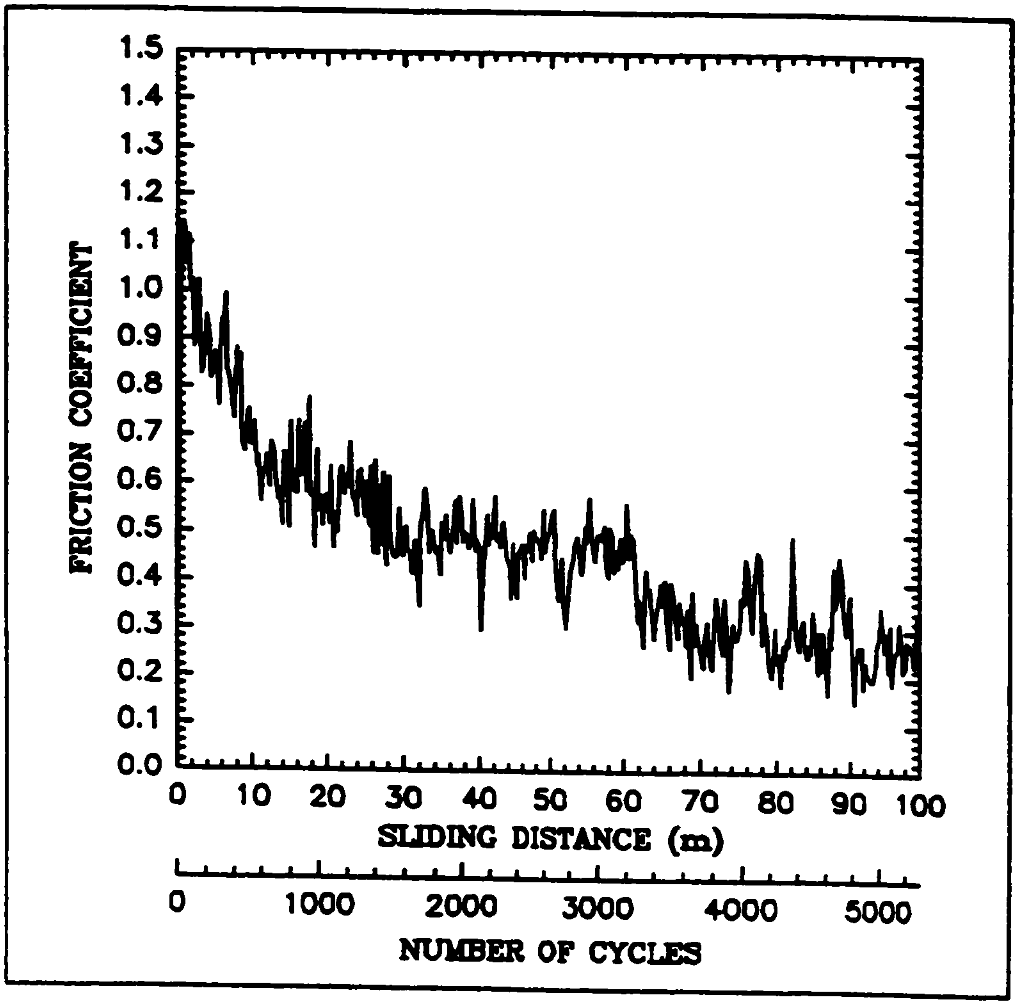

a

4.22. Coefficient of friction versus sliding distance curves, obtained using a normal load of 1.0 N and a sliding speed of $1.3x10^{-2}$ $m.s^{-1}$ under unlubricated sliding condition, for:(a) coarse-grained Cu; (b)Ti/Cu having 150 nm Ti layer thickness.

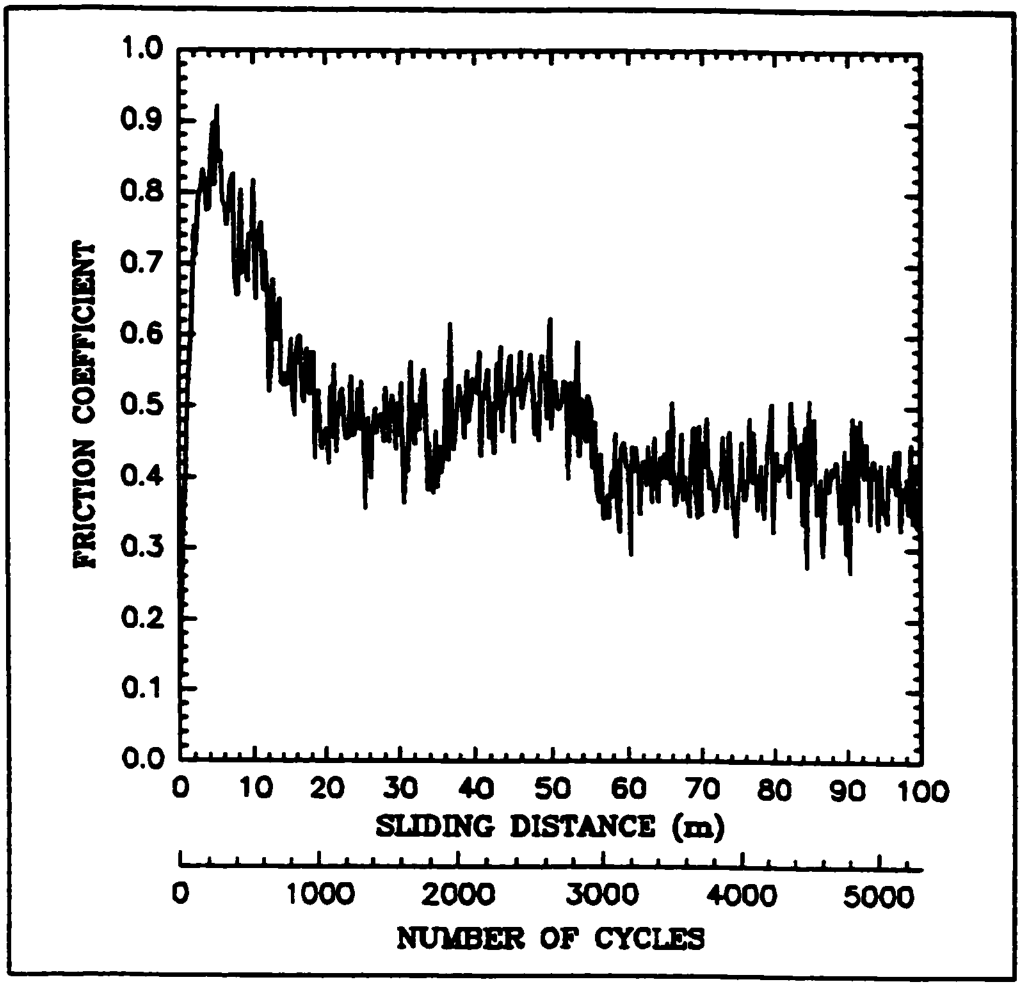

b

4.22. (continued).

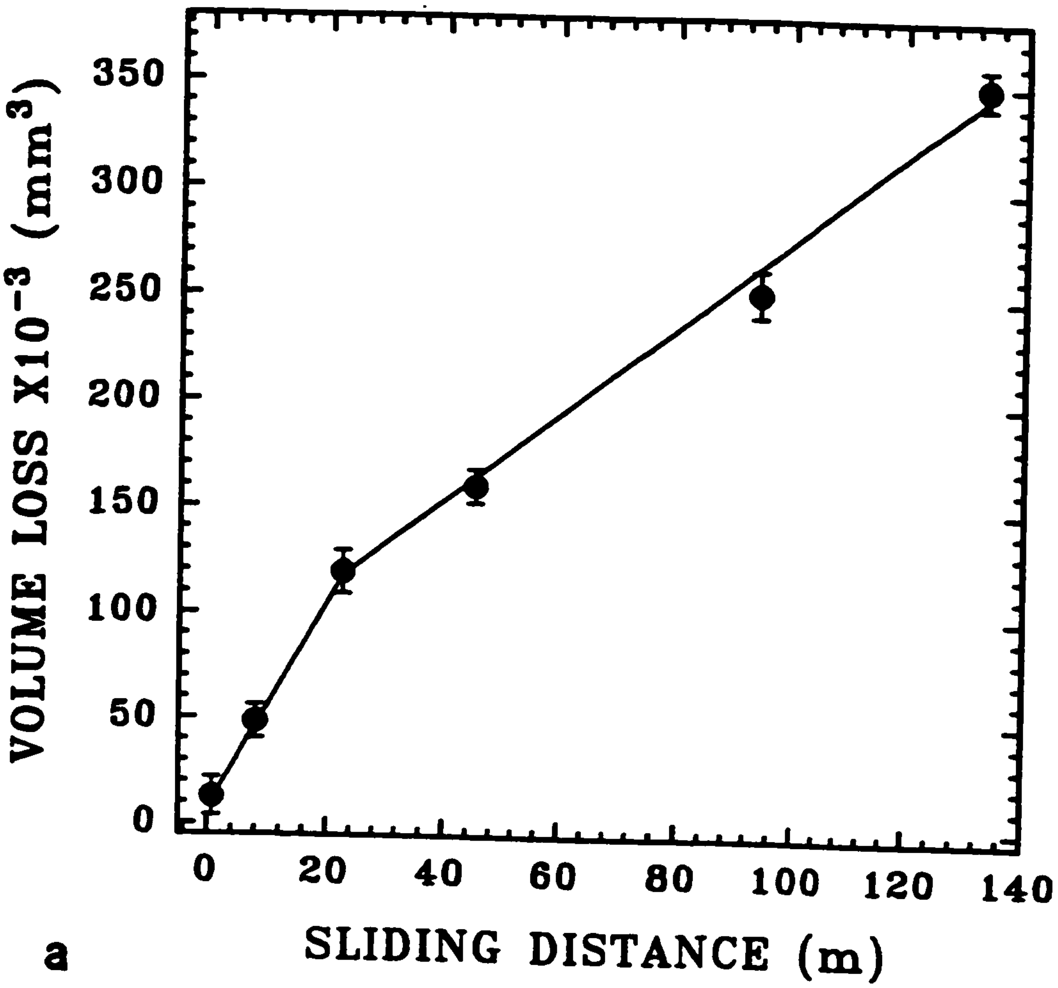

4.23. Cumulative volume loss versus sliding distance curves, obtained using a normal load of 1.0 N and a sliding speed of 1.3×10^{-2} m.s^{-1} under unlubricated sliding condition, for:(a)coarse-grained Cu; (b)Ti/Cu having 150 nm Ti layer thickness.

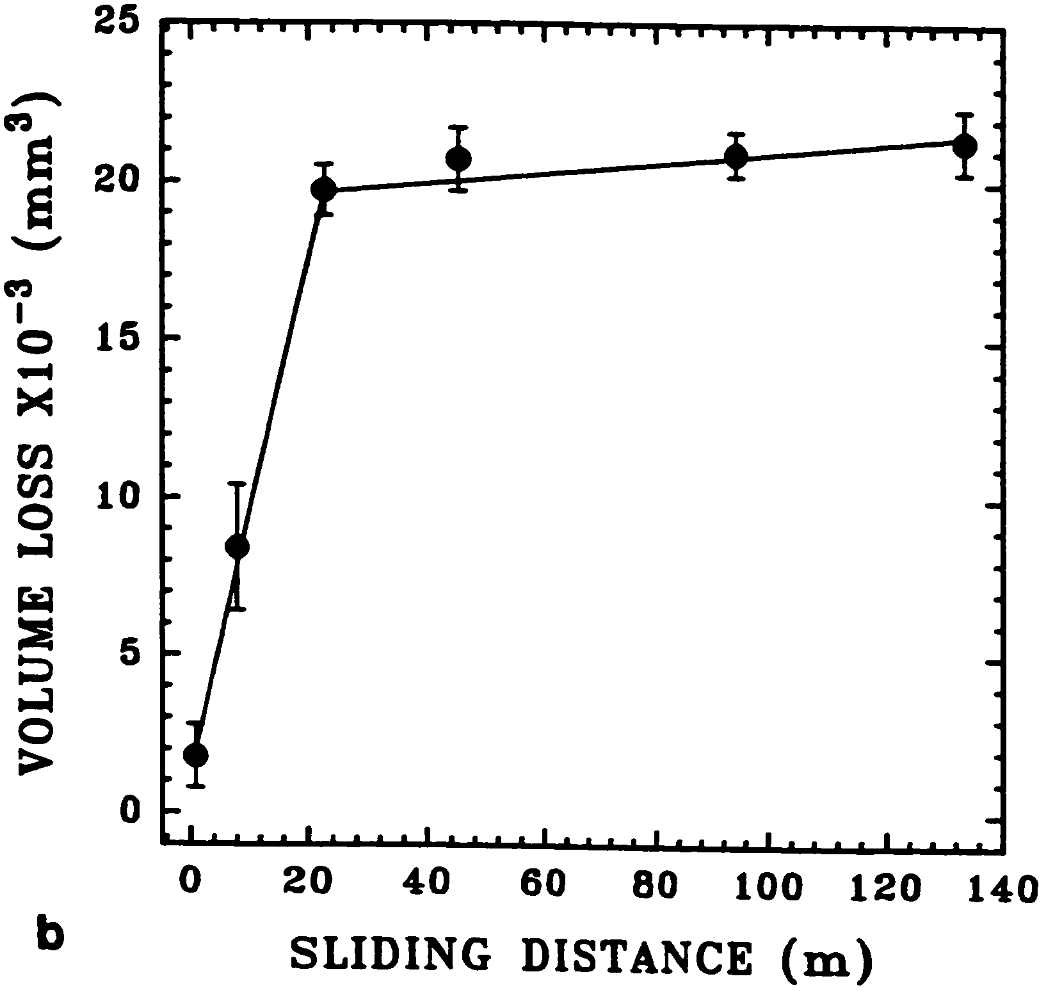

4.23. (continued).

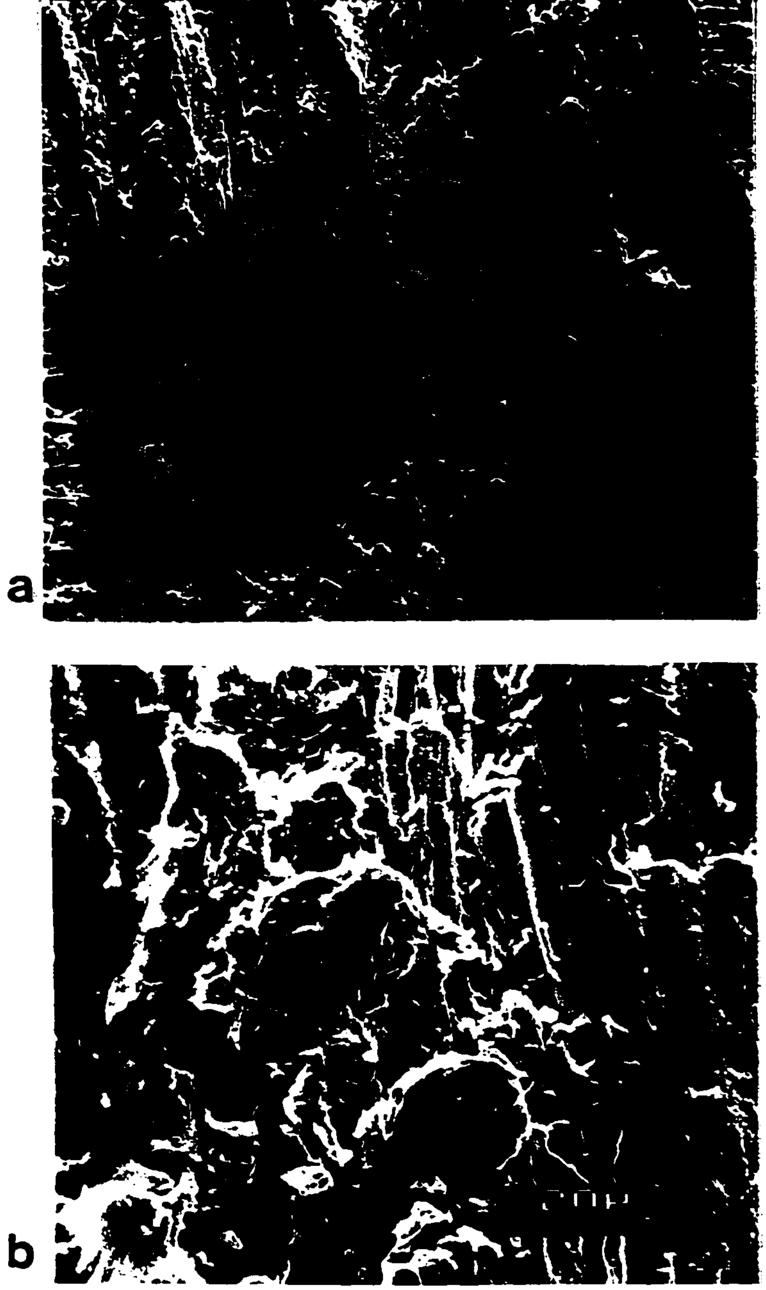

4.24. SEM micrograph of worn surface of coarse-grained aluminum at 12 m sliding distance showing: (a)general topography; (b)microcracking; (c)debris particles adhering on worn surface; (d)microcutting (optical); (e)shear flow of material; (f)separation of large wear debris from worn surface; (g)fragmentation of large debris.

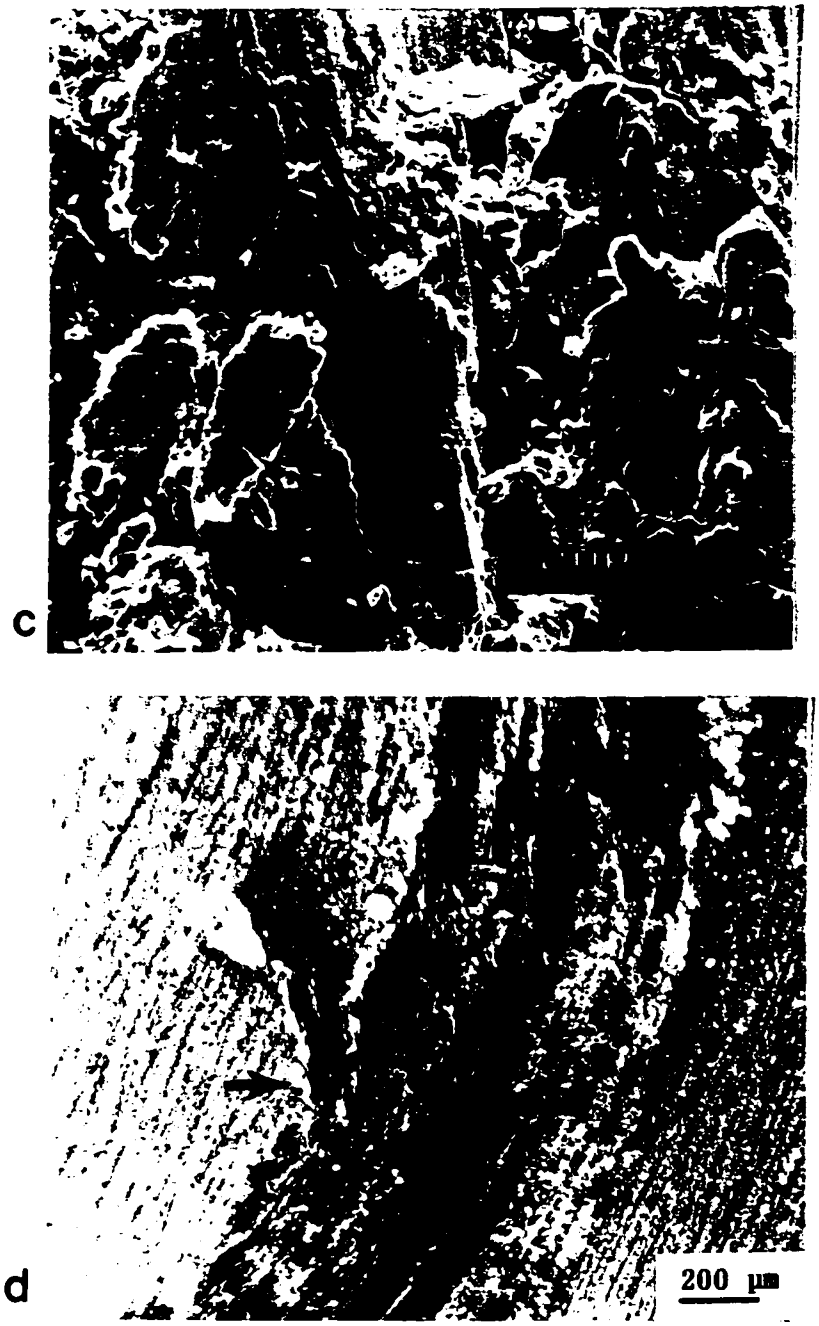

4.24. (continued)

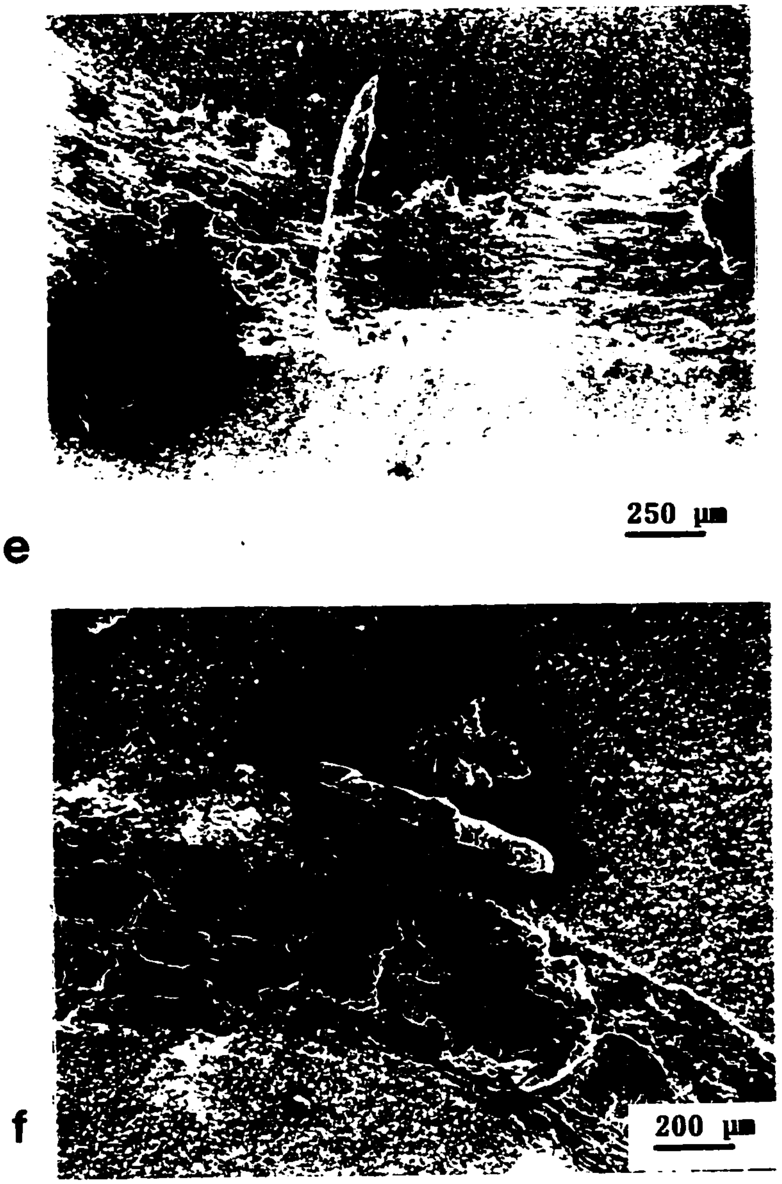

4.24. (continued).

g

4.24. (continued).

4.25. SEM micrograph of worn surface of 16.4 nm grain size aluminum, sliding distance = 12 m, showing shallow grooves and scratch marks.

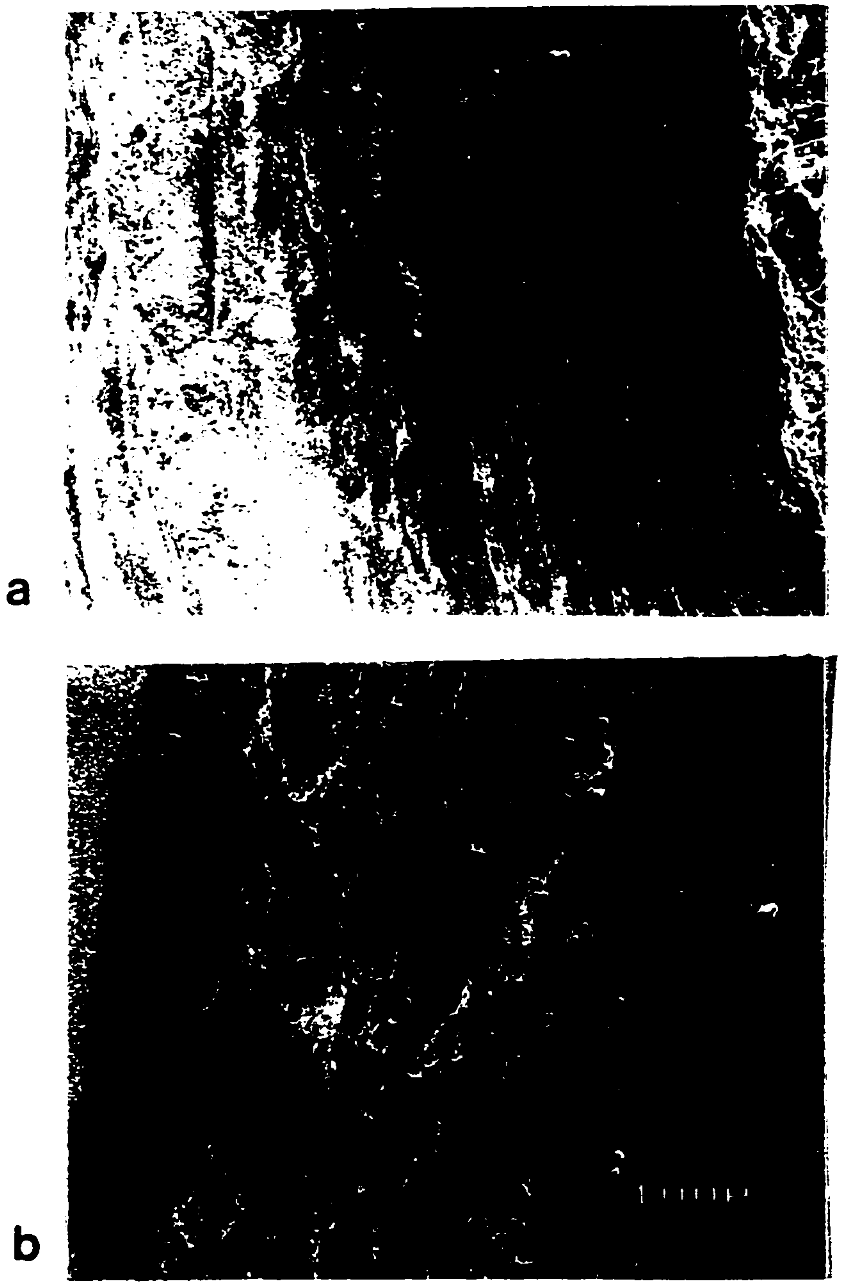

4.26. SEM micrograph of worn surface of aluminum (sliding distance=90 m) having grain sizes of: (a)10^6 nm; (b)16.4 nm. Both images show a smooth wear track.

4.27. SEM micrograph of the contact surface of the stainless steel pin after sliding on aluminum to sliding distance of 90 m. The pin shows no evidence of damage or wear.

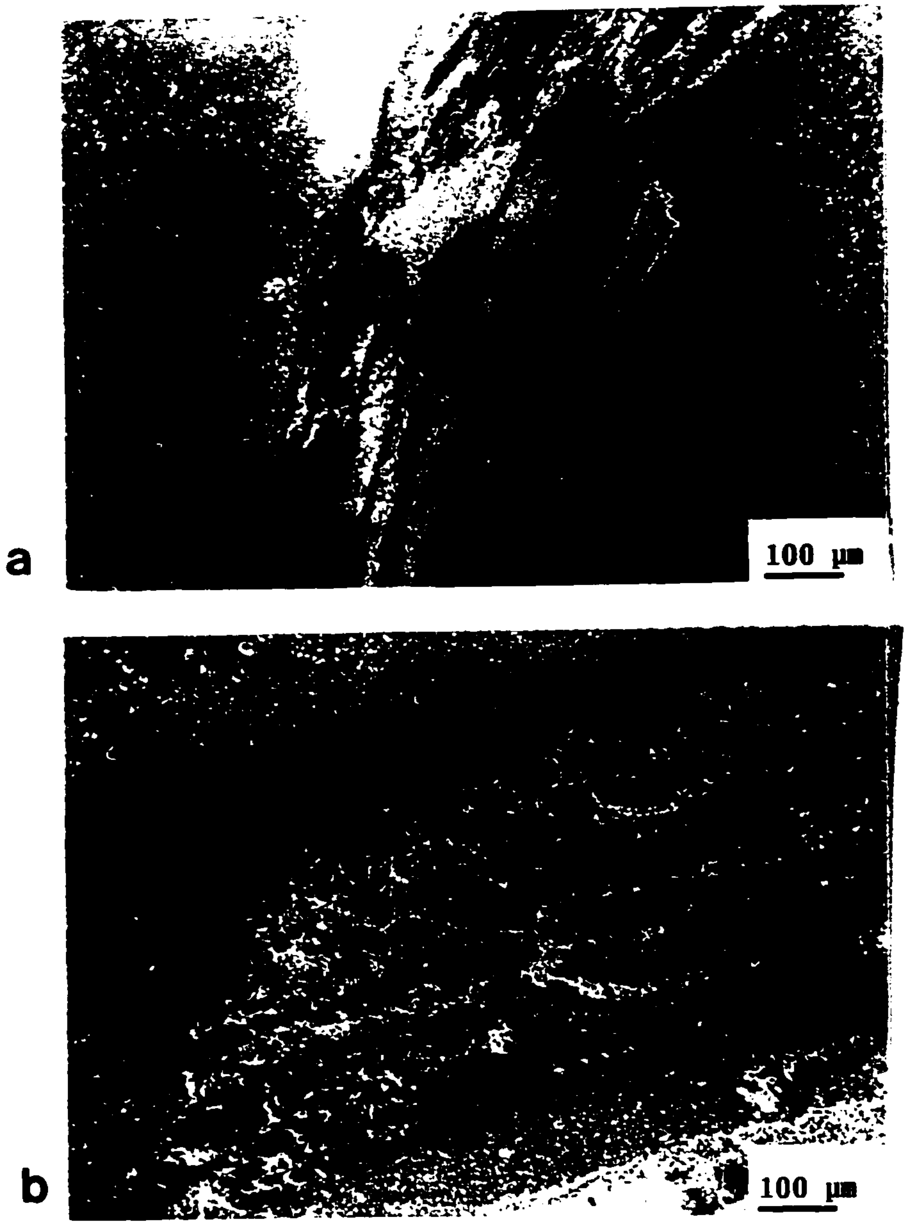

4.28. SEM micrograph of worn surface of Al/Al_2O_3 having 200 nm aluminum layer thickness at sliding distances of: (a)12 m; (b)90 m.

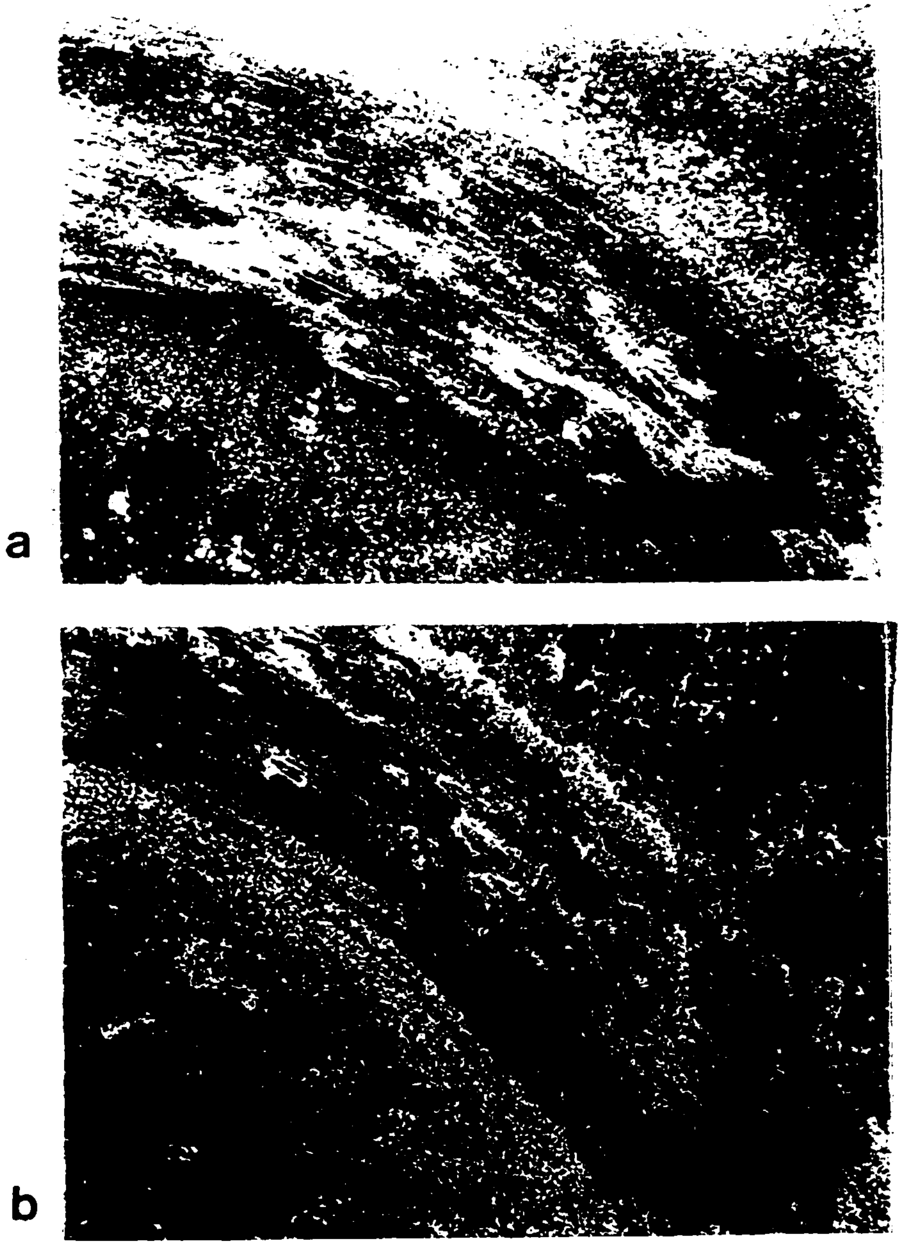

4.29. SEM micrograph of worn surface of coarse-grained titanium at a sliding distance of: (a)12 m; (b)90 m.

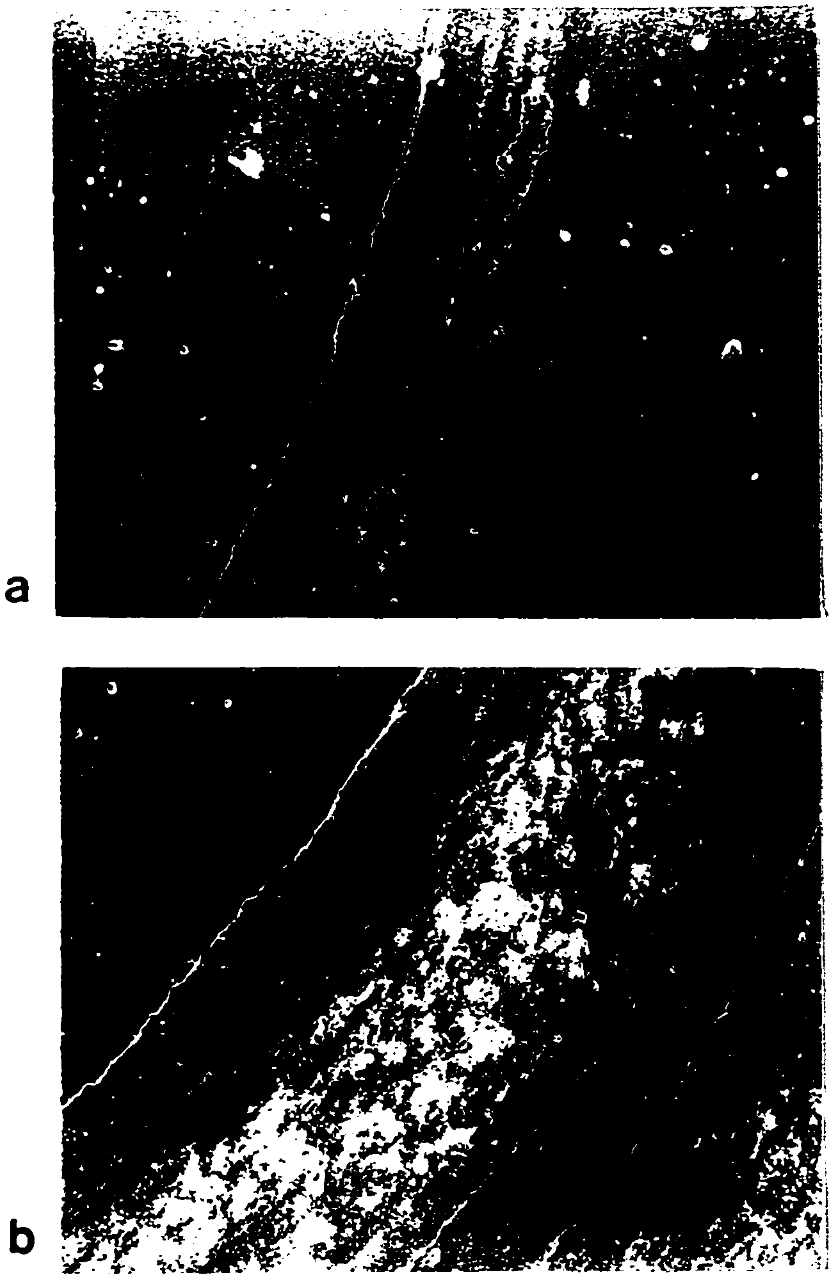

4.30. SEM micrograph of worn surface of Ti/TiN (having titanium layer thickness of 150 nm) at sliding distances of: (a)12 m; (b)90 m.

4.31. SEM micrograph of worn surface of Ti/Cu (having titanium layer thickness of 150 nm) at a sliding distance of 12 m.

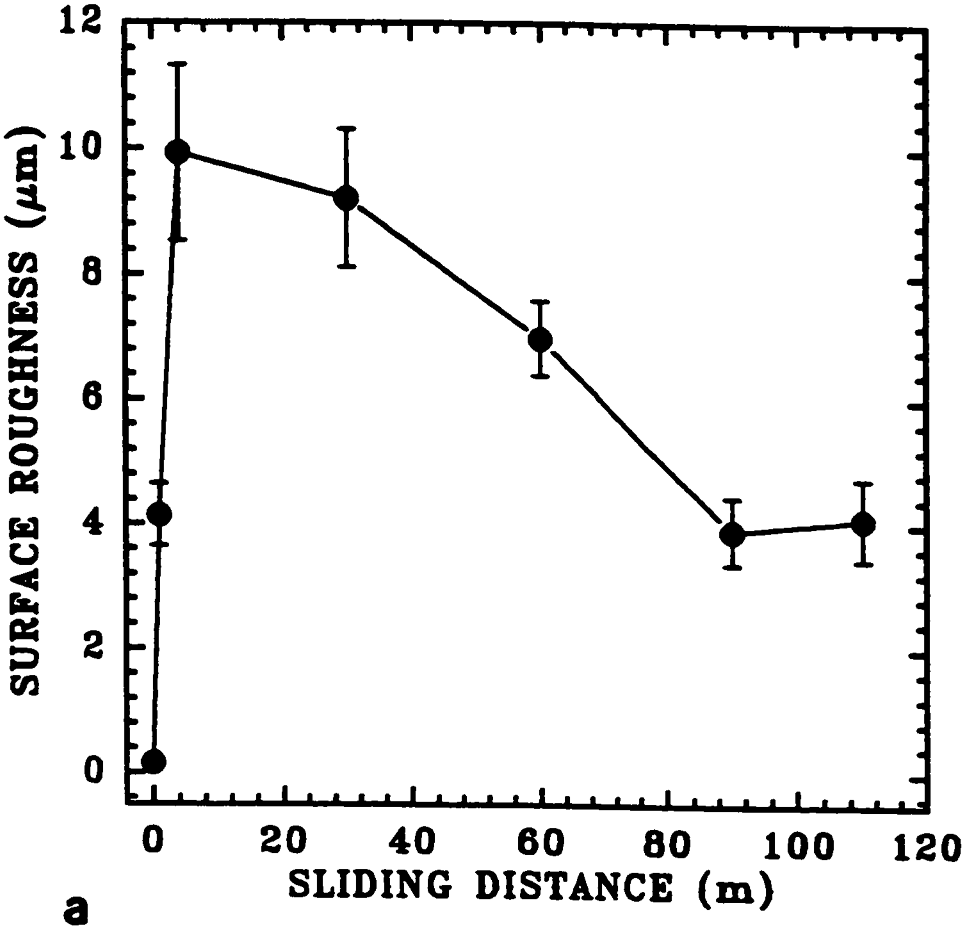

4.32. Roughness of worn surface as a function of sliding distance for: (a)coarse-grained aluminum; (b)coarse-grained titanium.

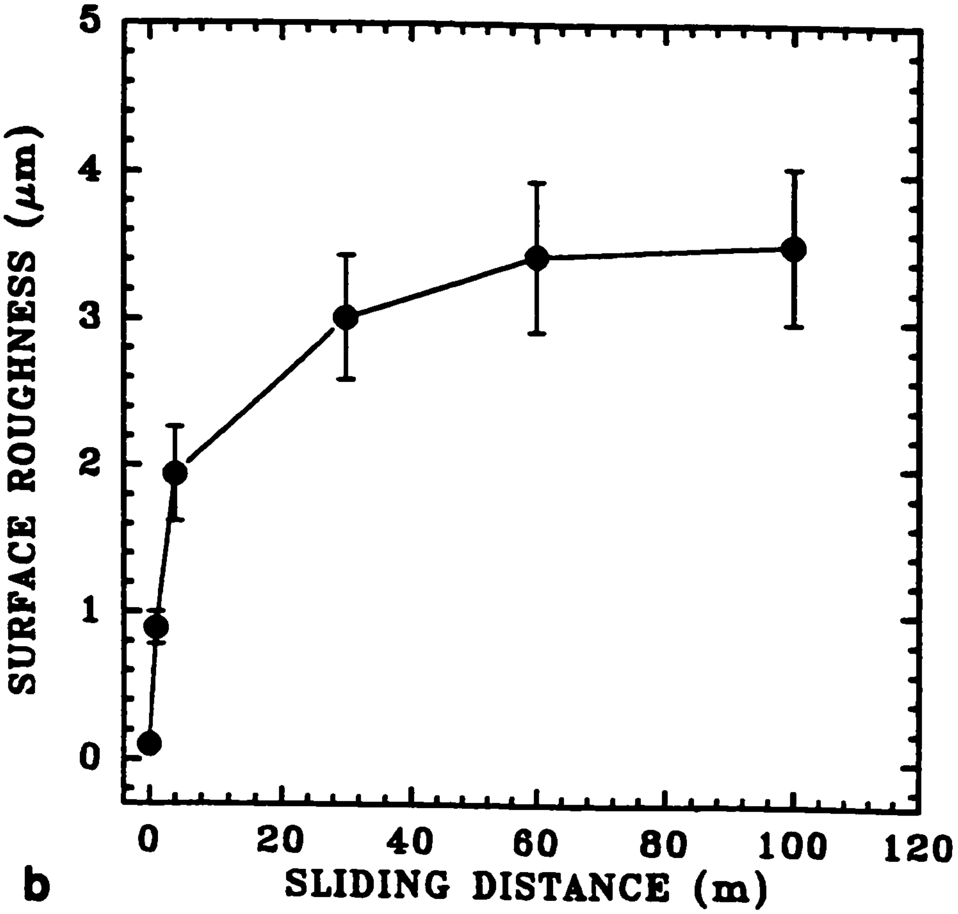

4.32. (continued).

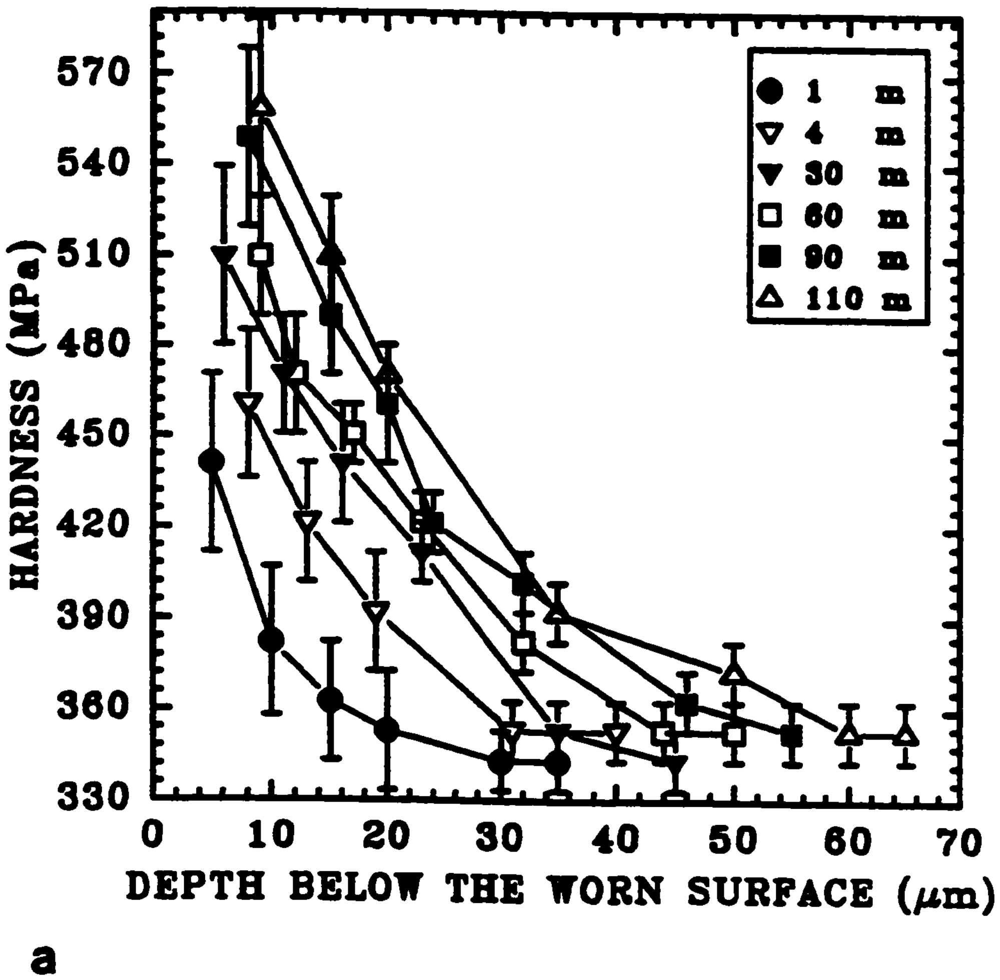

4.33. Knoop microhardness versus depth below worn surface for: (a)coarse-grained aluminum; (b)coarse-grained titanium.

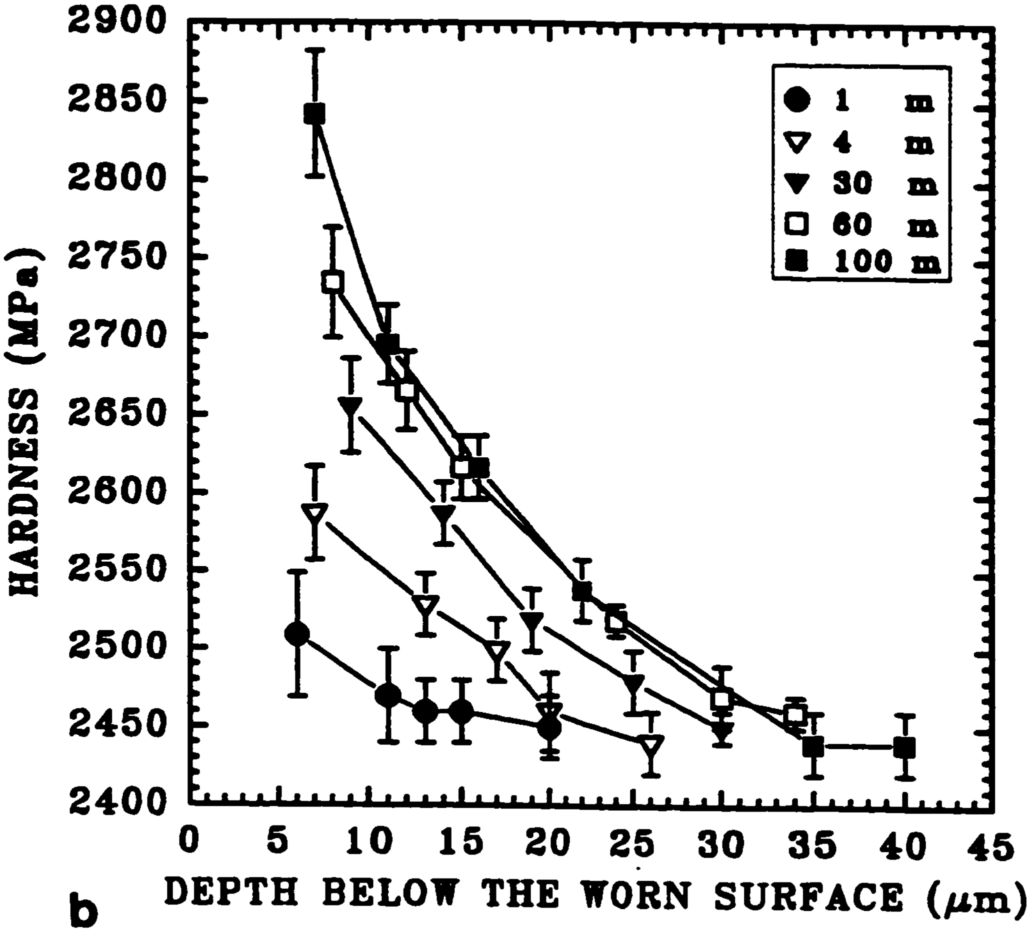

4.33. (continued).

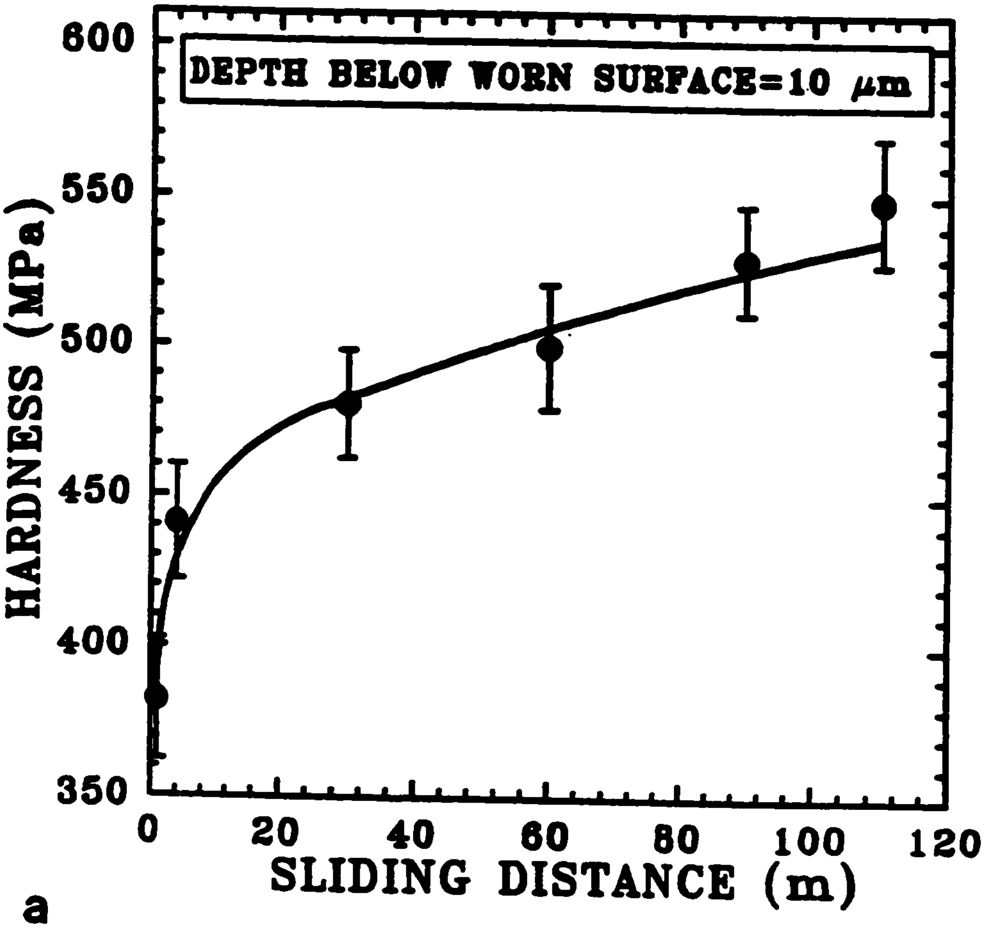

a

4.34. Knoop microhardness below worn surface versus sliding distance for: (a)coarse-grained aluminum; (b)coarse-grained titanium.

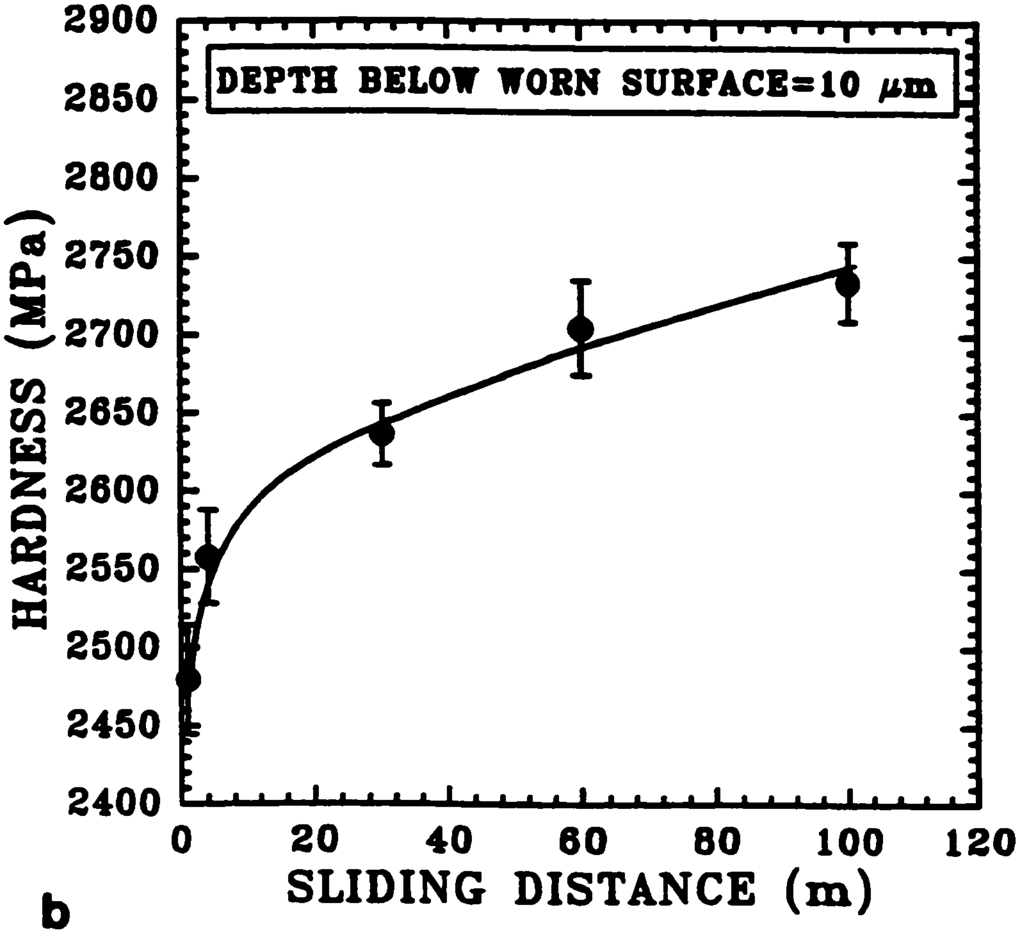

4.34. (continued).

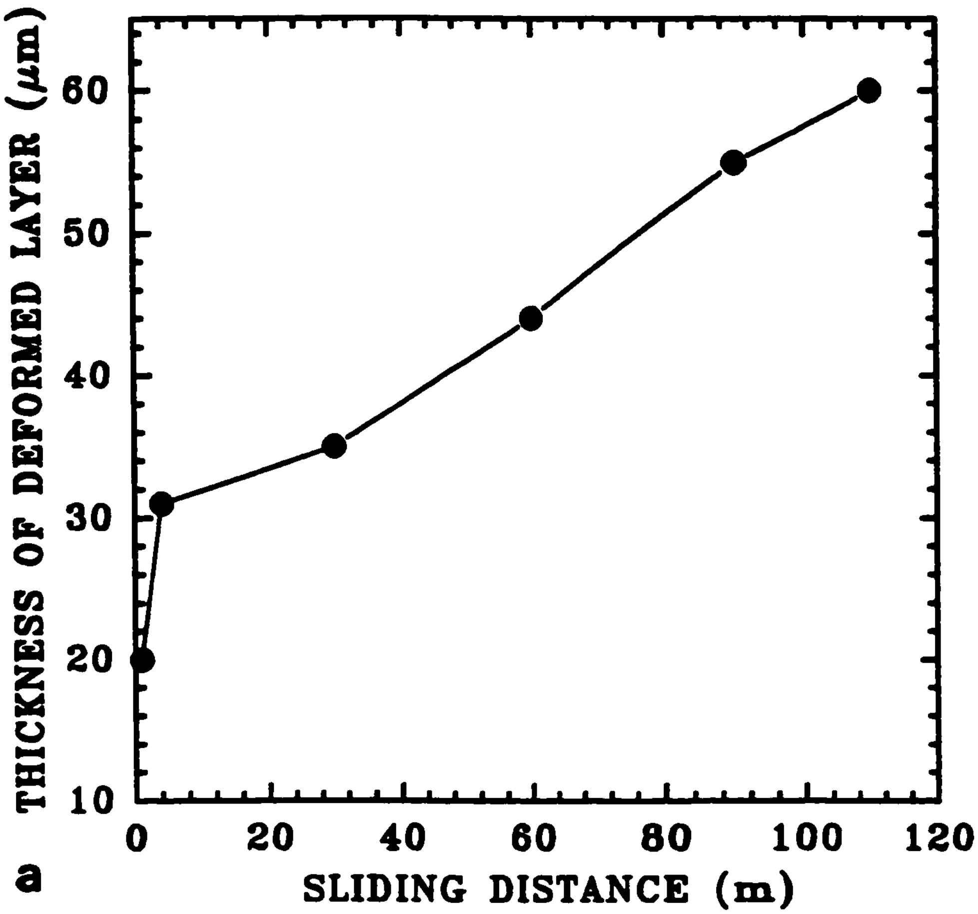

4.35. Thickness of plastically deformed layer versus sliding distance for: (a)coarse-grained aluminum; (b)coarse-grained titanium.

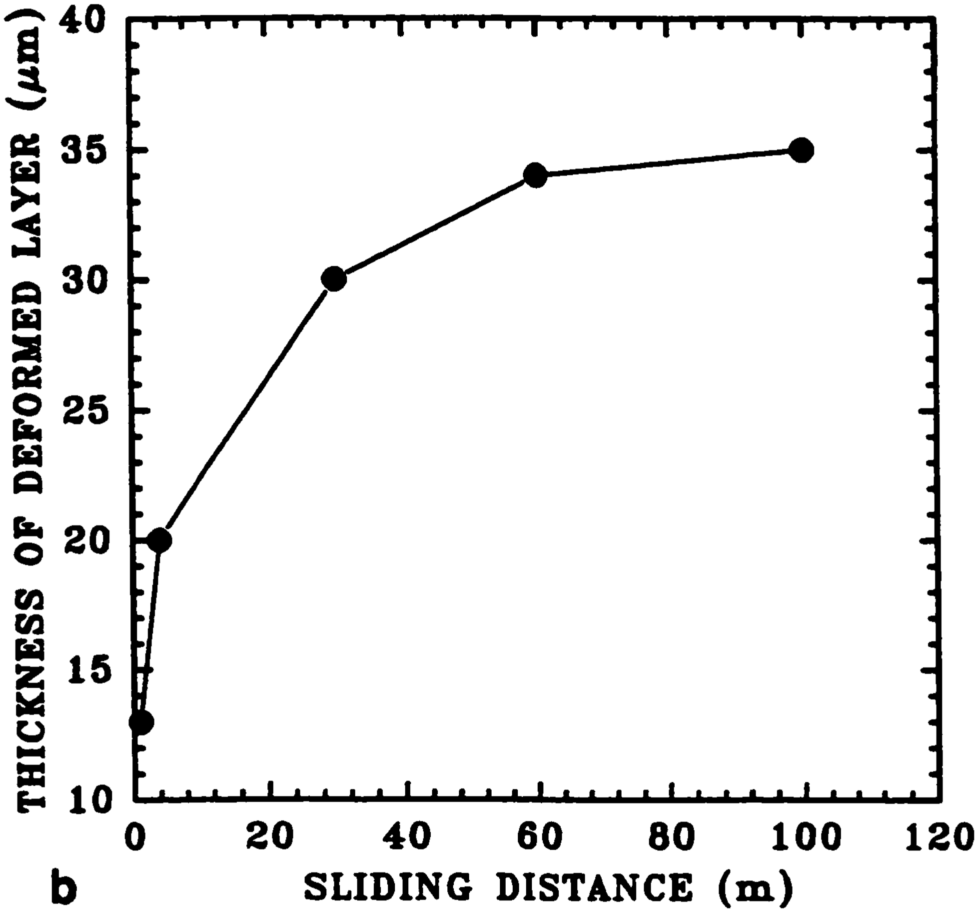

4.35. (continued).

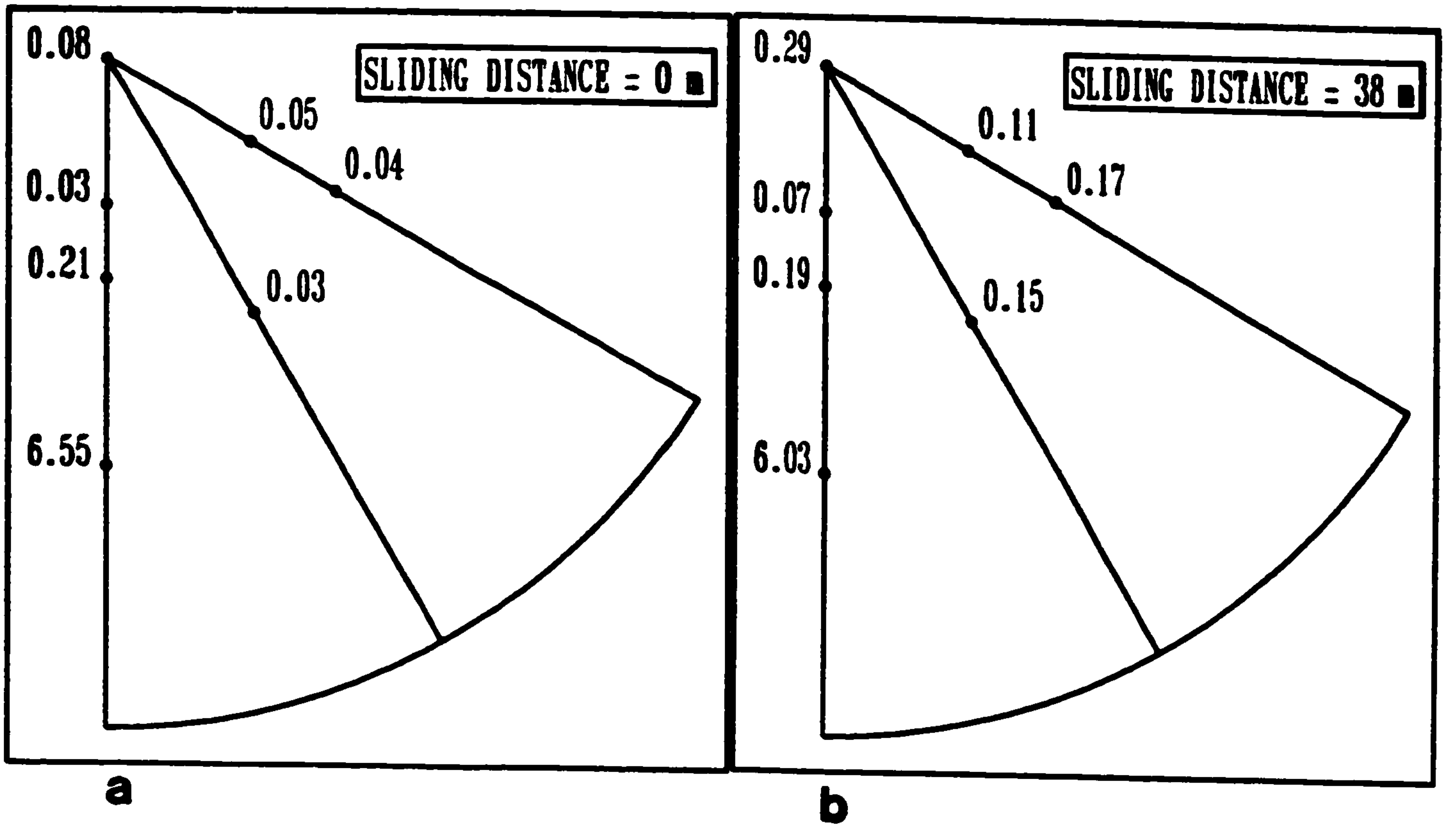

4.36. (111) inverse pole figure for coarse-grained aluminum at sliding distances of: (a)0 m; (b)38 m; (c)302 m; (d)603 m; (e)905 m; (f)2714 m; (g)4524 m.

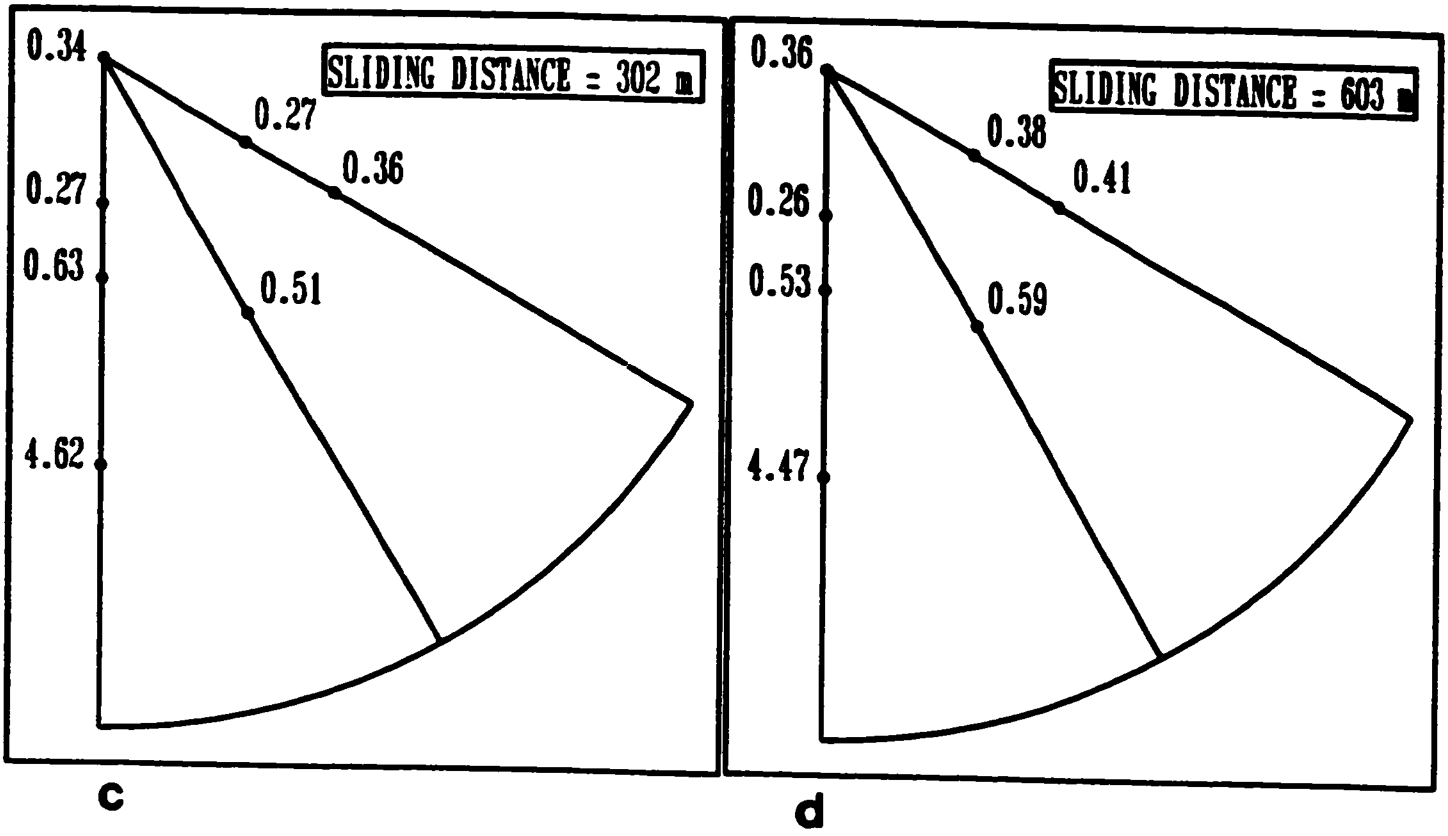

4.36. (continued).

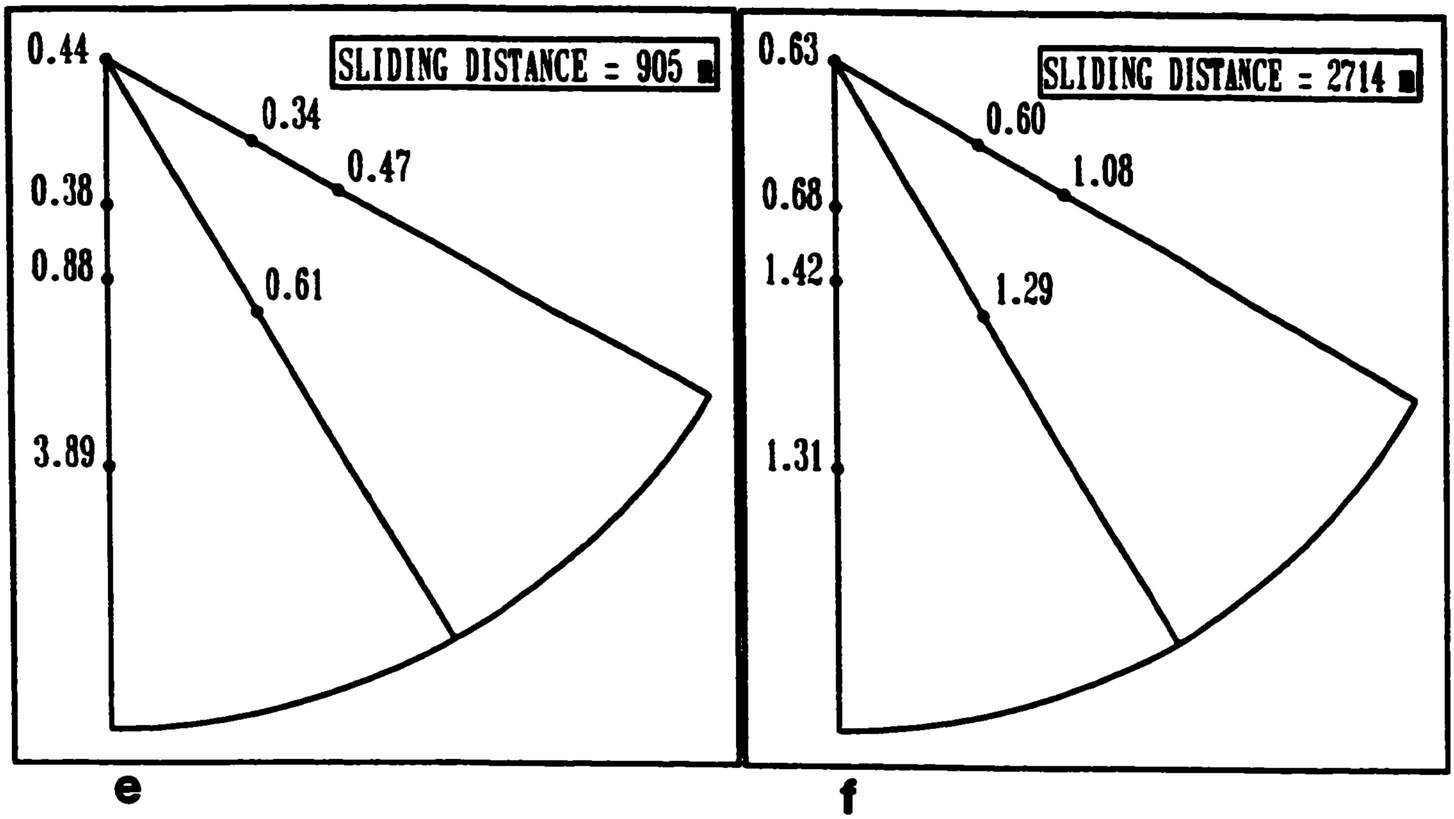

4.36. (continued)

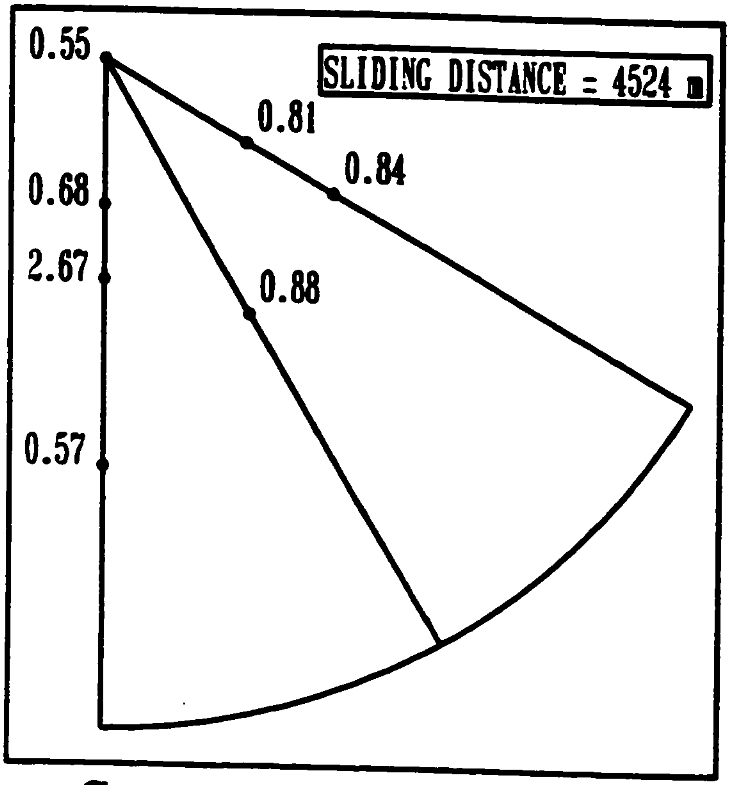

g

4.36. (continued).

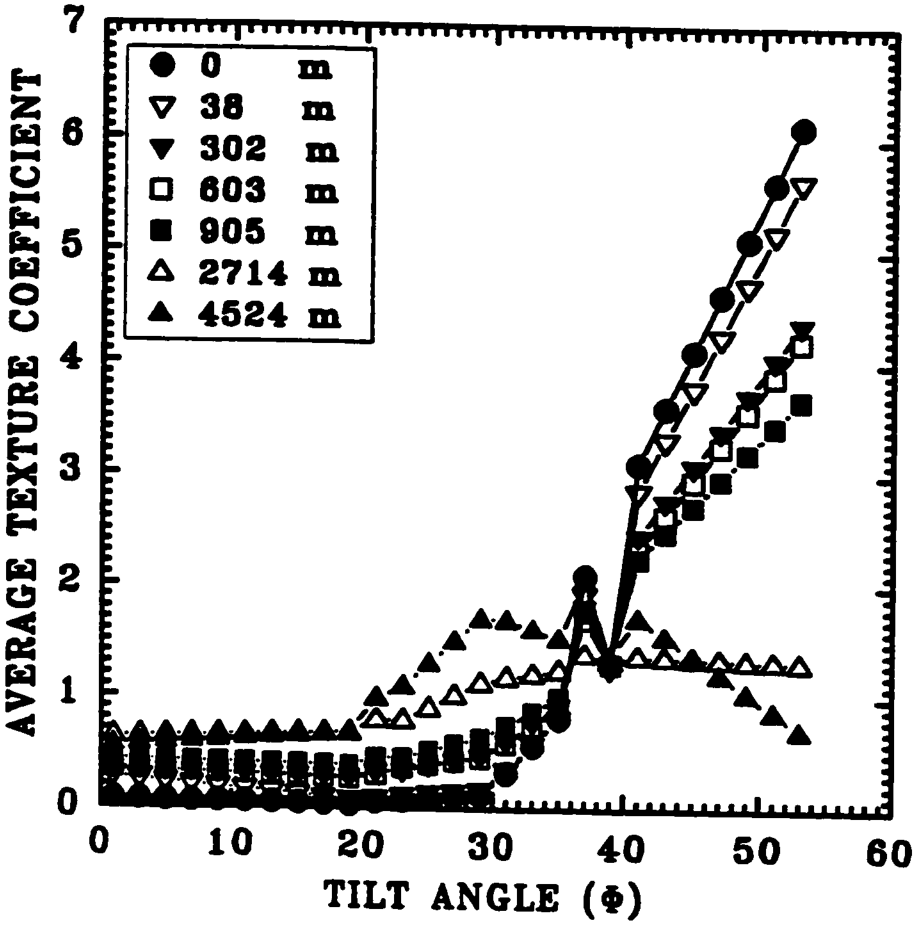

4.37. Average texture coefficient versus tilt angle from the reference direction (normal to the worn surface) for coarse-grained aluminum.

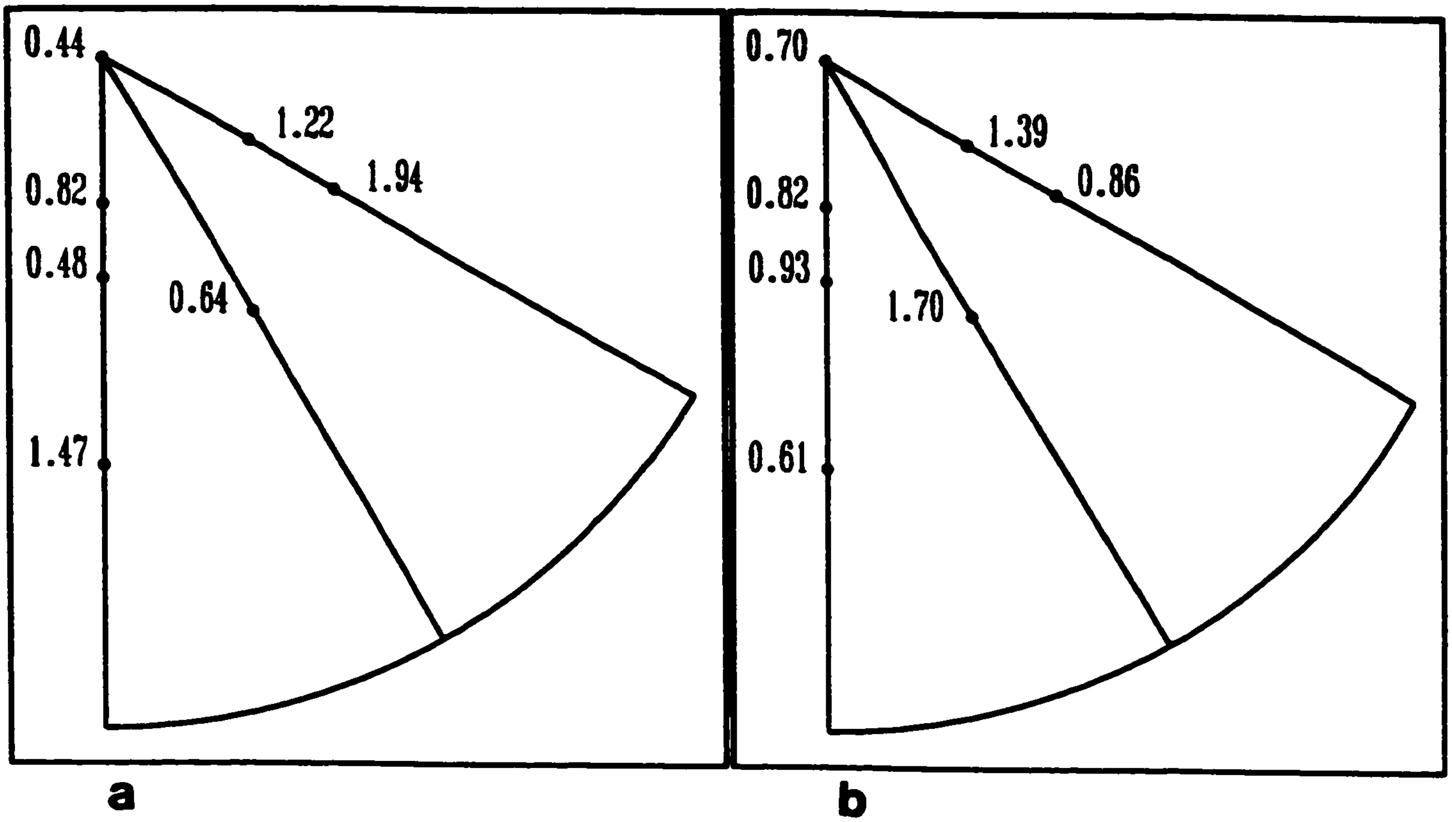

4.38. (111) inverse pole figure at 0 m sliding distance for nanocrystalline aluminum having grain sizes of: (a)16.4 nm; (b)43.1 nm.

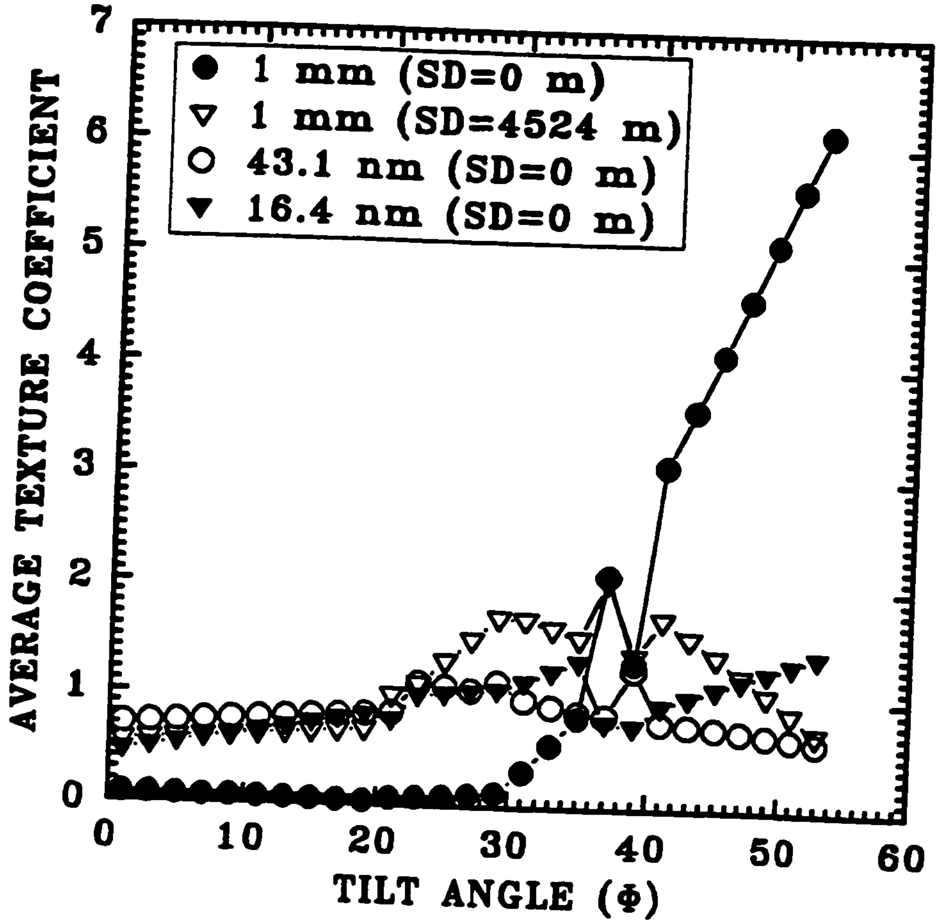

4.39. Average texture coefficient versus tilt angle from the reference direction (normal to the worn surface) for nanocrystalline aluminum.

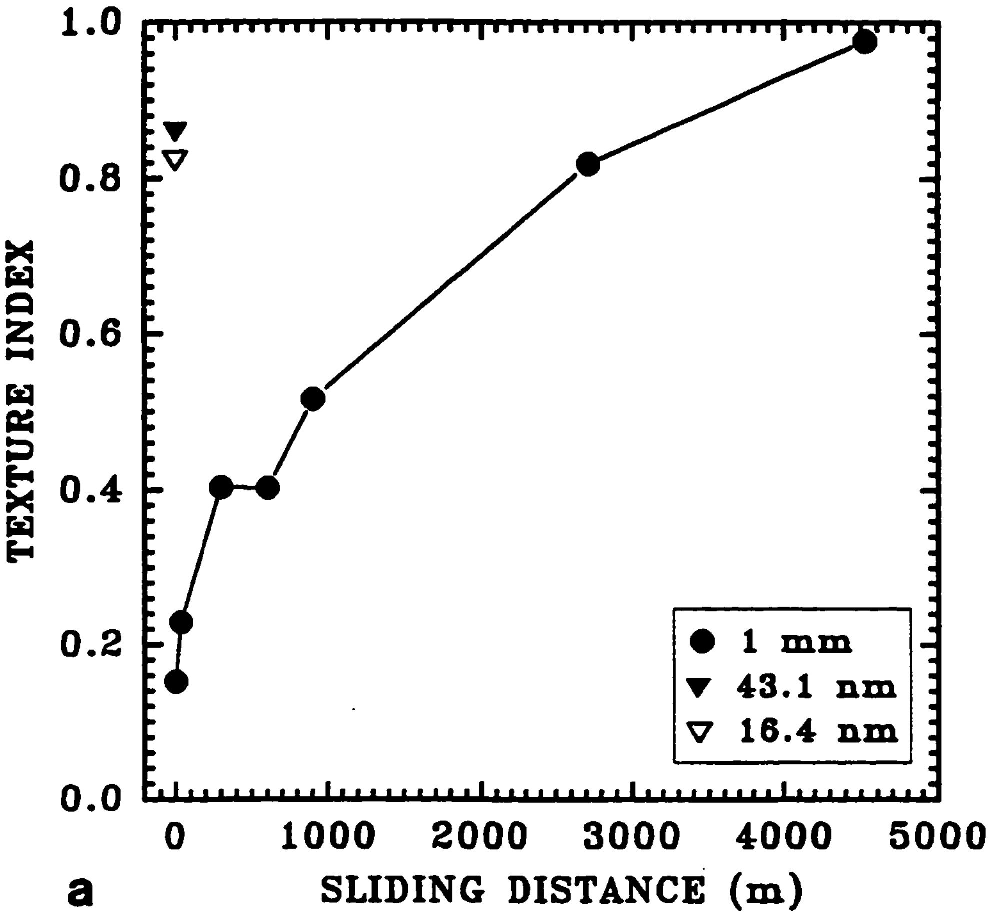

4.40. Texture index versus sliding distance of coarse-grained aluminum for: (a)0≤Φ≤35°; (b)40°≤Φ≤<90°.

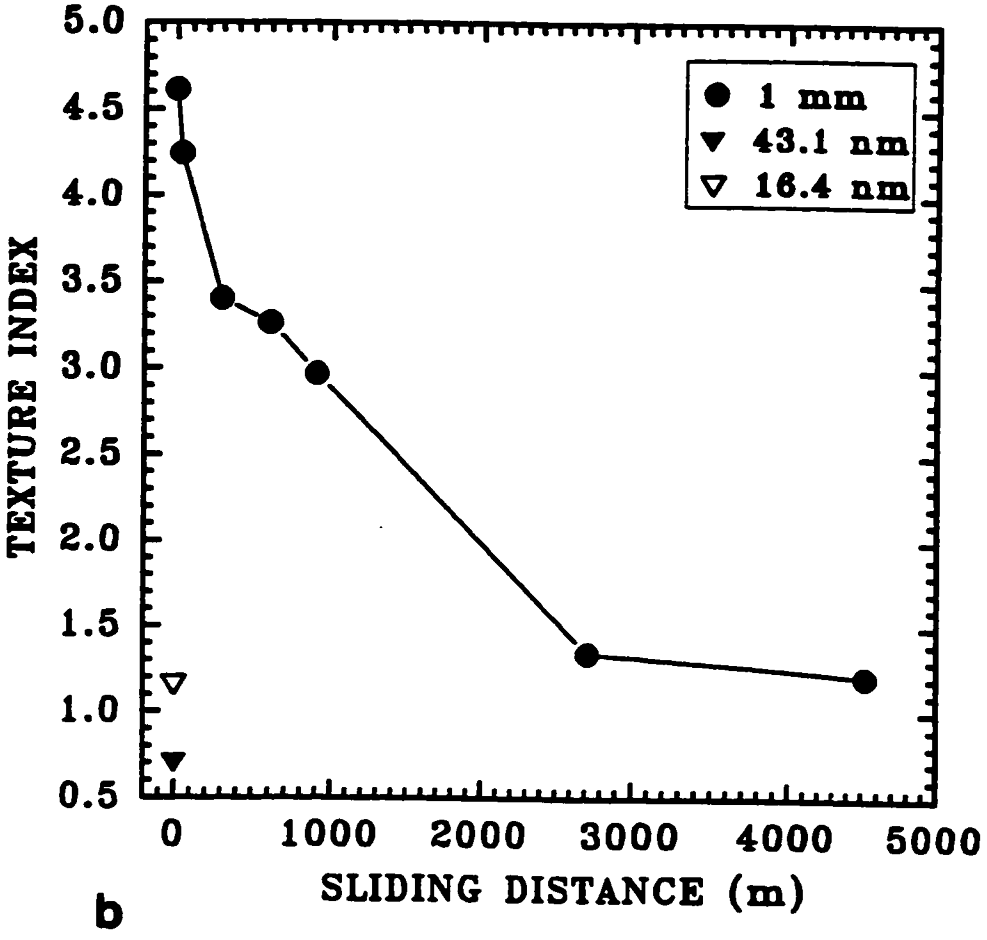

4.40. (continued).

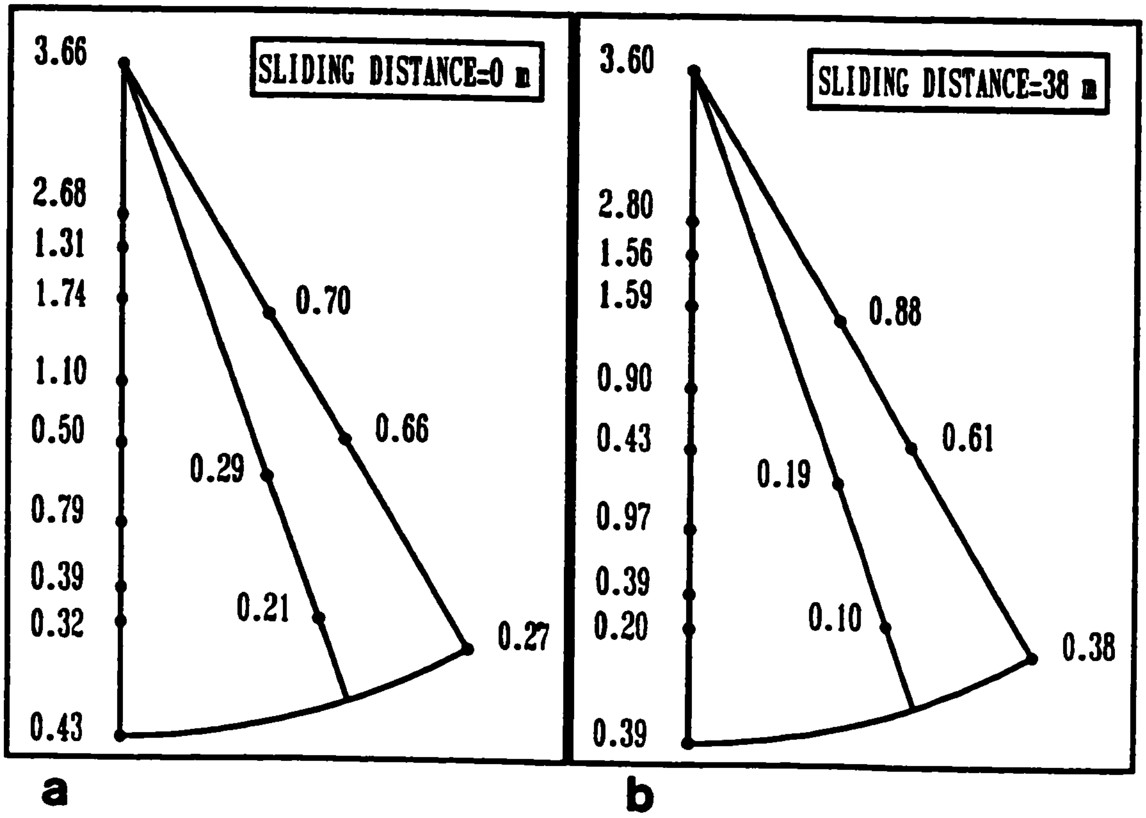

4.41. (0001) inverse pole figure for coarse-grained titanium at sliding distances of: (a)0 m; (b)38 m; (c)603 m; (d)2413 m; (e)4524 m; (f)7540 m.

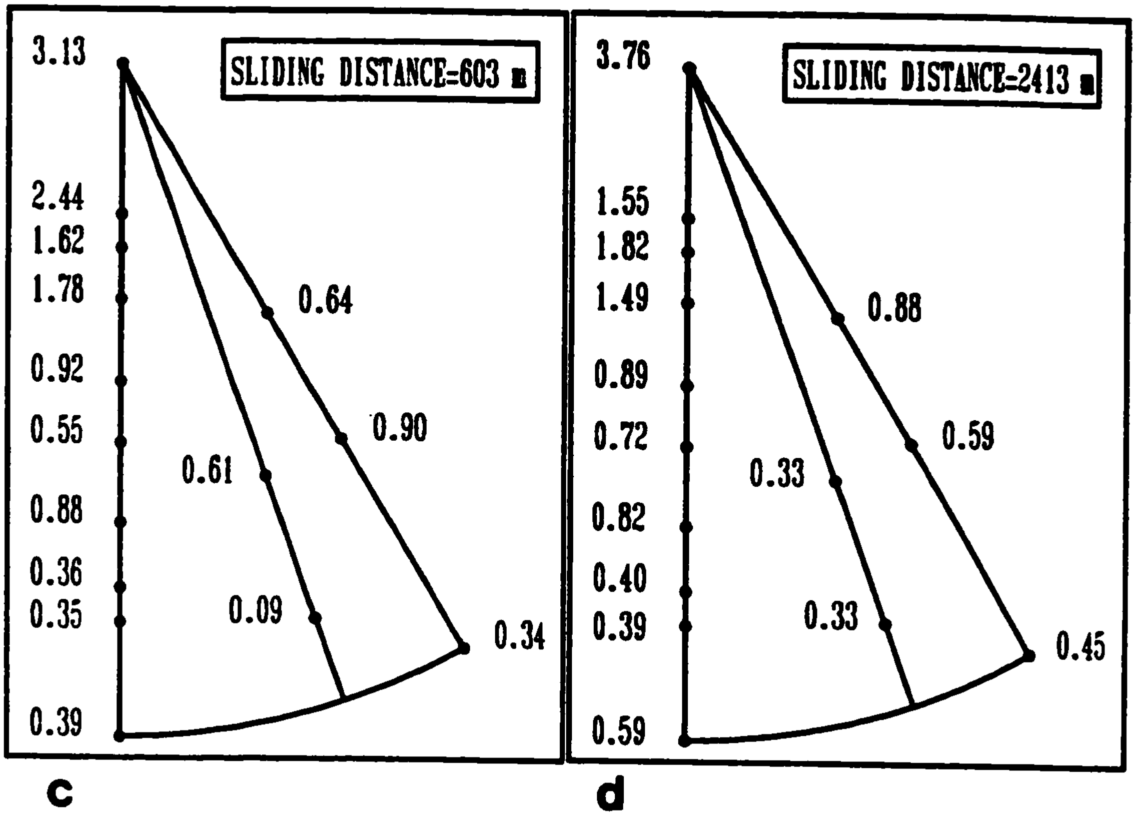

4.41. (continued).

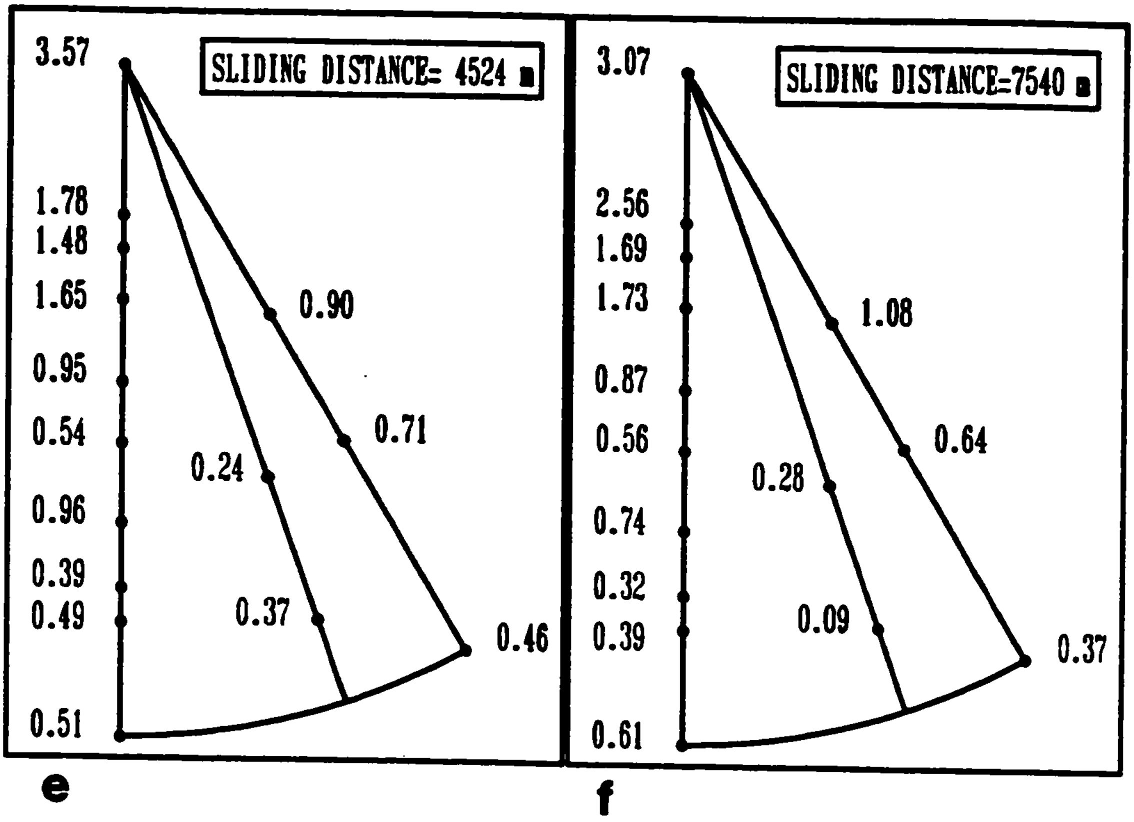

4.41. (continued).

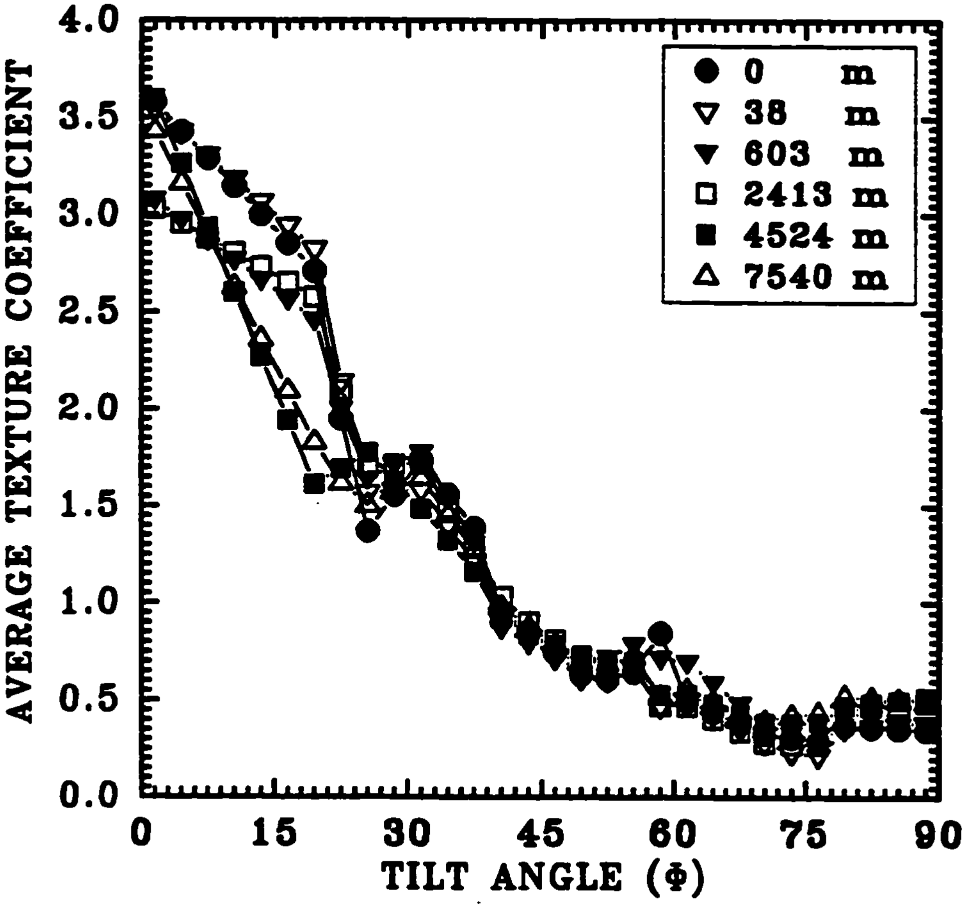

4.42. Average texture coefficient versus tilt angle from the reference direction (normal to the worn surface) for coarse-grained titanium.

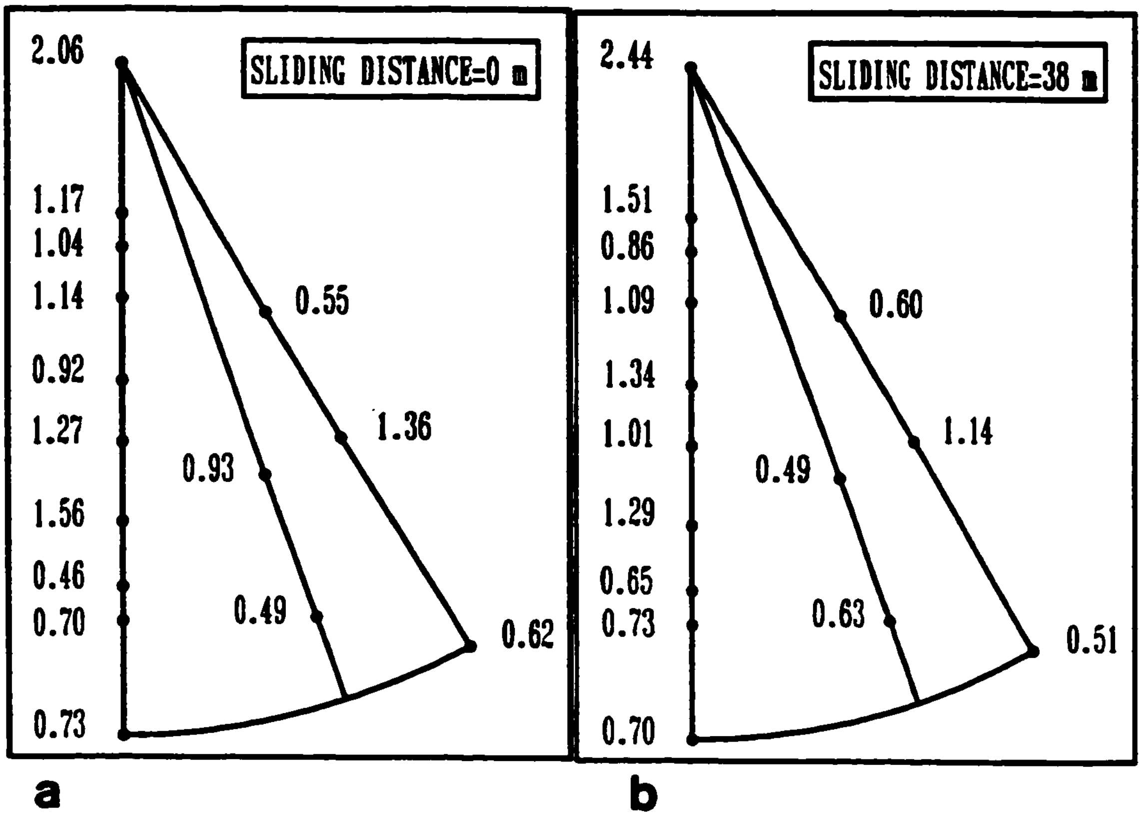

4.43. (0001) inverse pole figure for a transverse section of coarse-grained titanium at sliding distances of: (a)0 m; (b)38 m; (c)603 m; (d)2413 m; (e)4524 m.

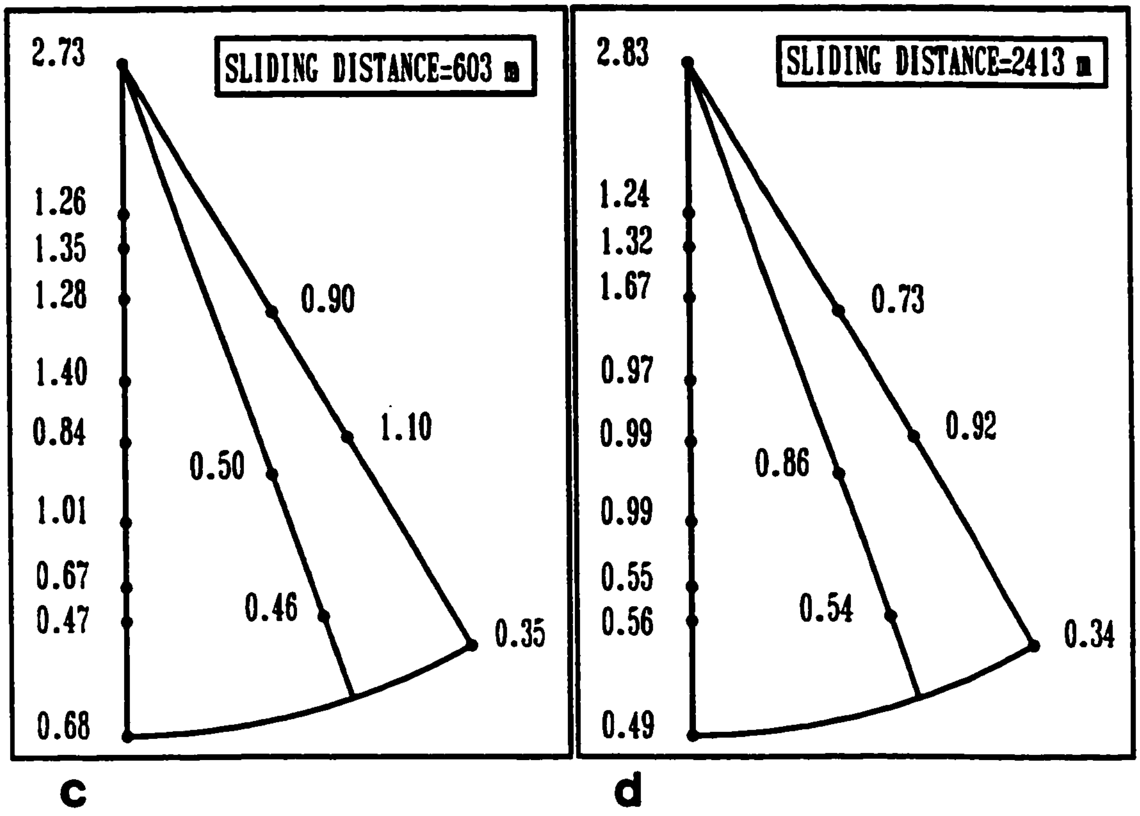

4.43. (continued).

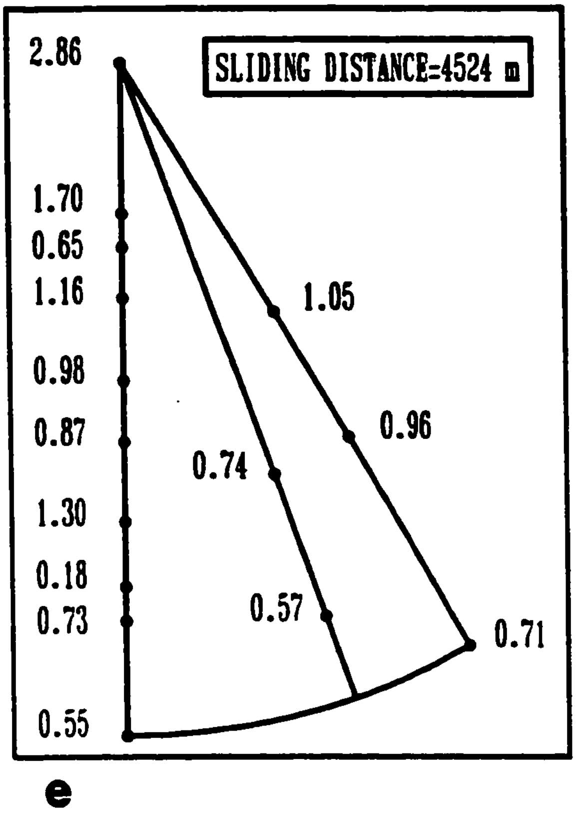

4.43. (continued).

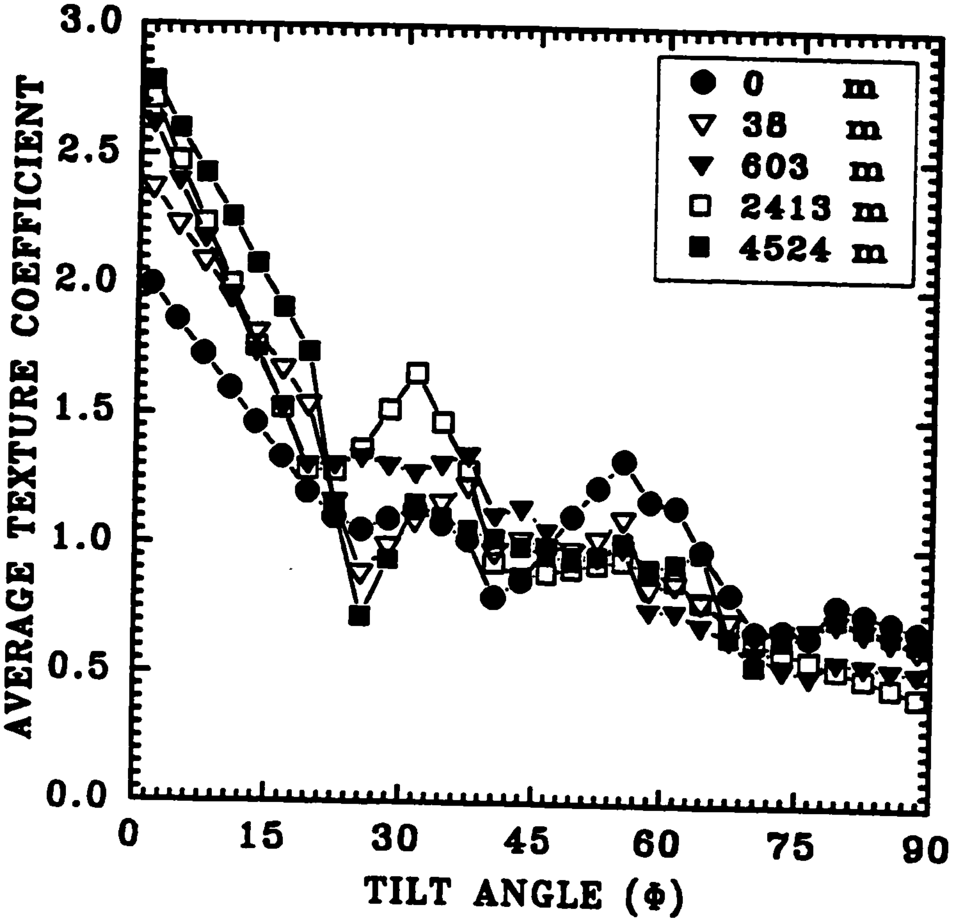

4.44. Average texture coefficient versus tilt angle from the reference direction (normal to the worn surface) for a transverse section of coarse-grained titanium.

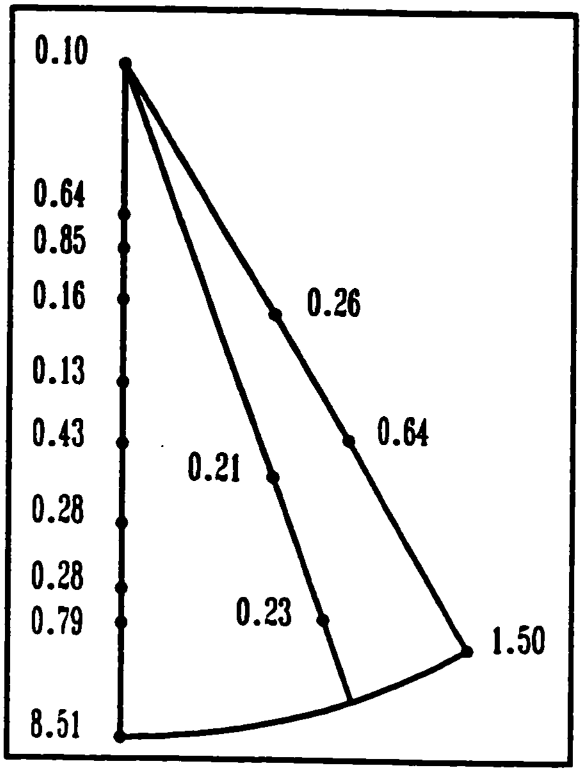

4.45. (0001) inverse pole figure at 0 m sliding distance for as-sputtered titanium.

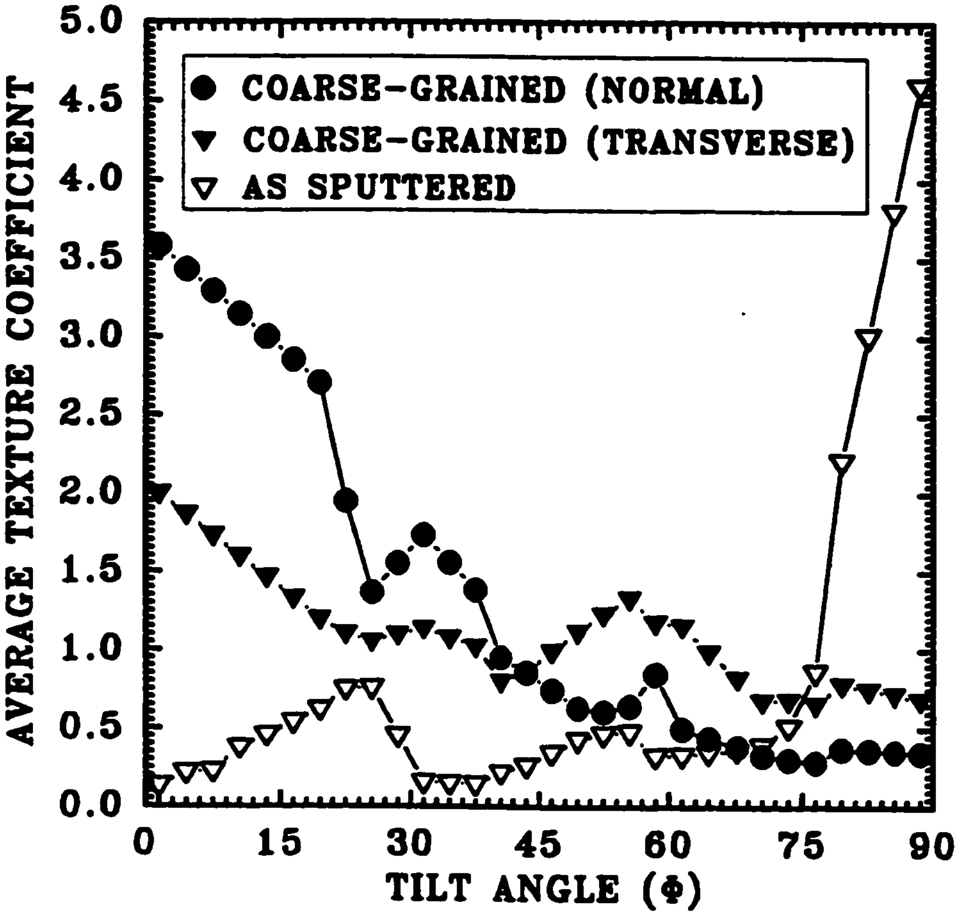

4.46. Average texture coefficient versus tilt angle from the reference direction (normal to the worn surface) for titanium.

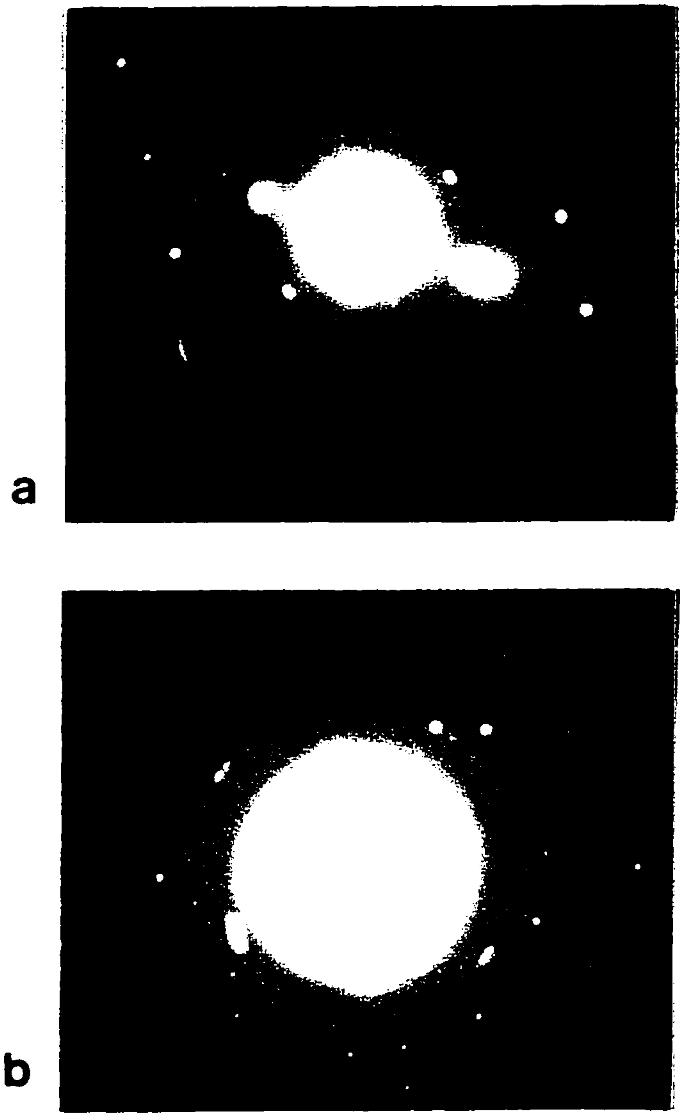

4.47. Selected area electron diffraction (SAED) patterns for coarse-grained aluminum for: (a)surface prior to wear testing; (b) after 4524 m sliding distance.

CHAPTER 5

DISCUSSION

5.1. Mechanical Properties of Nanoscale Materials

The objective of this section is to examine the effect of structural refinement in the nanometer scale on the strength of nanocrystalline and nanolaminated composites. It is also attempted to clarify possible strengthening mechanisms operating in these structures.

5.1.1. Effect of Grain Size on the Strength of Nanocrystalline Aluminum

It is appropriate to first comment on the applicability of the Hall-Petch equation to the nanocrystalline grain size range. The hardness versus grain size data for aluminum depicted in Figure 4.9(a) covers a grain size range 15-100 nm which has not been explored previously. The highest level of hardness obtained was 1.70±0.06 GPa (in the specimen with 16.4 nm grain size). This corresponds to an increase of about 130% by comparison to a grain size of 98 nm and an increase of about 450% with respect to that of aluminum having a grain size of 1 mm.

Data in Figure 4.9(a) also shows that the extrapolation of the Hall-Petch plot to the coarse grain range underestimates the measured hardness. However, caution must be exerted in comparing hardness results over a broad range of grain sizes because when a load of 20 mN is applied the indentation impression covers approximately 5-50 grains for the nanocrystalline material which is clearly not the case for the material with a grain size of 1 mm. When the hardness versus $d^{-0.5}$ is plotted over a wide grain size range, a deviation in the Hall-Petch plot towards the large grains range is expected and is reported by many authors (32,33,35,40-44). This behaviour was attributed to the fact that deformation in the large grain size specimen will not be effected by the grain boundary and increasing the grain size any further will not show any significant increase in hardness. Hence, a curve with a decreasing slope, towards the large grain size range, in the Hall-Petch plot is observed. The differences in the frictional stresses (σ_o) between the nanocrystalline and the large grain size is rationalized (35,40,43,44) in terms of differences in the subgrain structure, such as, dislocation cells, twins, dislocation density and work hardening effects, that actually control the value of the σ_o.

The elastic modulus, E, of the aluminum, which is a microstructure insensitive property, measured from the slope of unloading parts of curves in Figure 4.8(a) using equations 3.7 and 3.8 did not vary significantly with the grain size and has a mean value of 61 GPa.

As a first approximation, assuming that the hardness H is related to the yield strength, σ, by $H = 3\sigma$, the Hall-Petch parameters for nanocrystalline aluminum deduced from equation 4.1 (σ_o = 11.3 MPa, k = 0.07 MPa.m$^{0.5}$) can be compared with the published results on aluminum with coarser grain sizes (Table 5.1). Both the intercept strength and the Hall-Petch slope (equation 4.1) of nanocrystalline aluminum are in agreement with those reported for a grain size range of 1-200 μm (36-40). This suggests that the grain boundaries may be continuing to provide strengthening to aluminum down to grain sizes as small as 15 nm. However, this comparison is rather simplistic and does not take into account for example the possibility of smaller work hardening rates expected in the specimens with ultrafine grain size. There is currently a controversy on the applicability of the Hall-Petch equation to the nanocrystalline materials. Based on a survey of existing literature on grain size and hardness data of nanocrystalline materials, Fougere et al (19) suggested that an inverse Hall-Petch behaviour (e.g., softening with decreasing grain size) should be expected in nanoscale materials for which the grain size is increased by annealing. The present results disagree with this suggestion. One important difference between the materials that have reported to exhibit inverse Hall-Petch behaviour and nanocrystalline aluminum studied here is that the present materials produced by rf sputtering were effectively porosity free and were less susceptible to complications such as shrinkage and internal necking that occurs during subsequent heat-treatment in material produced in powder form.

5.1.2. Effect of Titanium Layers on the Modulus and Strength of Ti/TiN Composites

It was observed that both elastic modulus and hardness of Ti/TiN composites increased with decreasing layer thickness (Table 4.4). It is clear that compared to as-sputtered monolithic titanium films, nanolaminated composites incorporating TiN layers exhibit higher hardnesses and elastic moduli. For example, a 16% increase in hardness and a slight increase (6%) in elastic modulus is observed in laminates (of 150 nm thick titanium and 20 nm TiN) relative to monolithic titanium films with an average grain size of 30 nm.

The elastic moduli of the laminated composites consistently increase with decreasing the metal layer thickness. Since indentations were made perpendicular to the plane of the layers, it can be argued that isostress conditions should prevail in the layers and thus the modulus of the laminates would be:

$$E_{Ti/TiN} = 1 / [(f_{Ti} / E_{Ti}) + (f_{TiN} / E_{TiN})] \qquad 5.1(a)$$

where

$$f_{Ti} = \lambda_{Ti} / (\lambda_{Ti} + \lambda_{TiN}) \quad \text{and} \quad f_{TiN} = \lambda_{TiN} / (\lambda_{Ti} + \lambda_{TiN}) \qquad 5.1(b)$$

in equation 5.1, $\lambda_{Ti,TiN}$ are the layer thicknesses and $f_{Ti,TiN}$ are the corresponding volume fractions. To predict the elastic moduli of the laminates the experimentally determined values of the elastic moduli of monolithic Ti and TiN were used (i.e., E_{Ti} = 113 GPa, E_{TiN} = 299 GPa, from Table 4.4). The elastic moduli of Ti(450 nm)/TiN(40 nm) and Ti(150 nm)/TiN(20 nm) composite films, calculated using equation 5.1, are given in Table 5.2. There is a reasonable agreement between the measured value of the elastic modulus of laminate (see Table 4.4) and prediction based on the rule of mixtures. Thus, it can be suggested that, the elastic modulus is controlled by the volume fractions of the phases and since isostress conditions prevail, then the contribution of the nitride layers at relatively low volume fractions to the elastic moduli of the composites is relatively small.

The introduction of continuous TiN layers clearly increases the strength of titanium. The dependence of hardness, and thus flow strength on the Ti layer thickness is more complex and can not be successfully predicted using an equation similar to equation 5.1. The rule of mixtures underestimates the hardness of the Ti/TiN composite (Table 5.2) compared to the measured values (given in Table 4.4). Thus, the role of the nitride layers is not limited to supporting the applied load. In these fine structures, the layers could therefore play additional role in restricting plastic deformation by restricting slip transfer across adjacent metallic layers. It appears that the titanium layer thickness controls the hardness (or strength) of the laminates according to Hall-Petch relationship (Fig. 4.9 (c)). Also, Ti/TiN interface may have an epitaxial structure which would influence the dislocation movement and then influence the strength (or hardness) as has demonstrated by Kung et al (59).

Since the elastic and shear moduli of TiN are much larger than those of Ti it is possible that, below a critical thickness, a Koehler strengthening mechanism could be operative in Ti/TiN nanolaminated composites. However, based upon the data given in Table 4.4 and ref. (172), equation 2.14 predicts that the strength of Ti(150nm)/TiN(20nm) would be 5.34 GPa which overestimates the measured value of 4.3 GPa (calculated using $\sigma_Y \approx H/3$). Thus, a Koehler strengthening mechanism is not expected to be operative in the Ti/TiN specimens tested.

5.1.3. Effect of Aluminum Layer Thickness on the Strength of Nanolaminated Al/Al_2O_3 Composites

It is immediately noticeable that compared to monolithic aluminum film (16 nm grain size), nanolaminated composite incorporating Al_2O_3 layers exhibit higher hardness and elastic modulus (Table 4.4). For instance, 180% increase in hardness and 39% increase in elastic modulus is observed in laminates consisting of 70 nm thick aluminum layers with 10 nm thick Al_2O_3 layers, relative to the monolithic aluminum film (with grain size = 16 nm). Table 4.4 indicates that the elastic moduli of the laminated composites consistently increase with decreasing aluminum layer thickness. Since indentations were made perpendicular to the plane of the layers, the isostress conditions should dominate in the layers and thus the moduli of Al/Al_2O_3 laminates can be expressed by an equation similar to equation 5.1. To predict the elastic moduli of the laminates we have used the measured moduli of monolithic aluminum film (E_{Al}=61 GPa) and aluminum oxide (E_{Al2O3}=320 GPa) (172) and equation 5.1. The agreement between the measured and calculated values of E is excellent (Table 5.3) except for the highest value of f_{Al2O3} where the measured elastic modulus is significantly higher than the calculated one. The highest value of f_{Al2O3} corresponds to the smallest value of λ (metal layer thickness or Al_2O_3 layer spacing) which is where a deviation from a Hall-Petch relationship in Figure 4.9(b) occurs.

As in the case of nanolaminated Ti/TiN composites,the hardness dependence on the layer thickness can not be successfully predicted using a rule of mixtures, an equation similar to equation 5.1. This is shown in Table 5.3 where the rule of mixtures underestimates the hardness of composites compared to the measured values (Table 4.4). In these calculations the hardness of monolithic aluminum film (H=1.70 GPa) and that of bulk alumina (VH=6.0 GPa) were used. The hardness data (Fig. 4.9(b)) varies as $\lambda^{-0.5}$ down to an aluminum layer thickness of 200 nm. This effect agrees with a Hall-Petch strengthening. Figure 4.9(b) also shows that there is no significant further increase in hardness of the Al/Al_2O_3 laminates for very thin aluminum layers ($\lambda_{Al}<200$ nm).

Due to the large elastic moduli difference between the Al (E=61 GPa) and the Al_2O_3 (E=320 GPa) layers, it can be expected that below a critical thickness Koehler strengthening becomes operative. The maximum strength achieved in Al/Al_2O_3 can be rationalized by considering both the scale of the multilayers and the elastic modulus difference of the constituents. The strengthening mechanism proposed by Koehler predicted that strengthening in multilayered structures arises from the elastic modulus difference between the constituents such that, below a critical layer thickness, a large externally applied force is required to move dislocations from a layer with low shear modulus into a layer with higher one.

The deviation from the Hall-Petch behaviour for laminates (with a layer thickness of 70 nm) is possibly due to a Koehler strengthening effect. Because of the large difference in the shear moduli between the aluminum and the aluminum oxide layers, Koehler strengthening mechanism might be a contributing factor to the strength of Al/Al_2O_3 laminates with the smallest Al layer thickness (λ_{Al}=70 nm). Using data in Table 4.4 and ref. (172), the Koehler approach (equation 2.14) predicts a strength for the Al/Al_2O_3 with 70 nm Al layer thickness of 1.80 GPa. The predicted strength is in reasonable agreement with the measured value of 1.61 GPa (obtained assuming $\sigma_y \approx H/3$).

Additional strengthening in nanocomposites can be provided by decreasing the grain size of metallic layers. This is shown in the case of Al/Al_2O_3 of which the strength of unreinforced monolithic aluminum can be described by equation 4.1. Thus, a modified Hall-Petch equation is proposed to describe the dependence of the strength of laminates on both the grain size (D) of the metallic layers and the spacing between non-metallic layers (λ), hence,

$$\sigma_{Al/Al2O3} = (\sigma_{o\,Al} + k_{Al} \cdot D^{-0.5}{}_{Al}) + k_{Al/Al2O3} \cdot \lambda^{-0.5}{}_{Al} \qquad 5.2$$

5.1.4. Effect of Varying the Ti and Cu Layer Thicknesses on the Strength of Nanolaminated Ti/Cu Composites

Hardness data for multilayers of Ti/Cu (Fig. 4.9(d)) exhibit a decrease in hardness with decreasing titanium layer thickness while the volume fractions of titanium and copper phases are constant, in contradiction to the rule of mixtures. Ti/TiN composite show higher strength than Ti/Cu having the same layer thickness. For example, Ti(150 nm)/TiN(20 nm) has a hardness of 12.8 while the hardness for Ti(150 nm)/Cu(20 nm) is 3.69 GPa.

Koehler analysis does not hold for Ti/Cu type laminate. For example, the predicted value of the yield strength (equation 2.14) for Ti(150 nm)/Cu(20 nm) is 3.61 GPa is almost three times larger than the measure value (e.g. 1.23 GPa). The observed softening in the Ti/Cu composite as the Ti layer thickness is decreased implies that deformation and damage mechanisms other than Hall-Petch type mechanisms are occurring during indentation.

Figure 5.1 shows the energy expended during the penetration of the indenter which is calculated as the difference between the total energy consumed during a full loading-unloading cycle (W_t) and the elastic energy expended during the unloading (W_e) using the areas under the load-displacement curves in Figure 4.8(d). As indicated in Figure 5.1, larger amounts of energy are expended during the indentation process as the Ti layer thickness in Ti/Cu composites becomes smaller. A typical indenter penetrates normally to a depth of about 400 nm and initiates deformation processes in Ti. Once the dislocation glide process is initiated inside the Ti layer dislocations propagate through the softer Cu layer by a shearing deformation mechanism. However, the above analysis indicates that the Cu layer does not act as an effective barrier to dislocation motion. In addition, as observed by cross-sectional metallography (Fig. 5.2), Cu/Ti interfaces are susceptible to delamination during the indentation process indicating a weak Ti/Cu interface. The shearing and decohesion occurring at the Cu/Ti interfaces are schematically shown in Figure 5.3 for the laminates with fine and coarse structures. For smaller Ti layer thickness, a large number of "weak" interfaces cause increased shearing and delamination (consuming large amount of energy) across the Ti/Cu interfaces which leads to premature failure.

5.2. Tribological Behaviour

The objective of this section is to discuss the time-dependent features of the friction curves in conjunction with the wear transitions (severe to mild). Morphological and microstructural observations, subsurface work-hardening and crystallographic texturing will be considered. The friction and wear behaviour of the nanocrystalline aluminum and nanolaminated Al/Al_2O_3, Ti/TiN and Ti/Cu composites will be discussed in terms of structural refinement.

5.2.1. Factors Determining Friction and Wear Transitions

The shape of the friction and wear curves (e.g. Fig. 4.10 and Fig. 4.11, respectively) are not particular to one type of material, but rather are observed in many tribological systems and are attributed to the changes occurring near the contact surface during sliding wear.

a) Morphology and microstructure of wear track

Considering the behaviour of aluminum first, surface deformation starts as soon as the sliding process commences. The surface of coarse grained aluminum exhibits signs of heavy damage resulting from severe plastic deformation and ploughing (Fig. 4.24), and the roughness of the worn surface rises to a maximum value of $Ra \approx 10\ \mu m$ (Fig. 4.32(a)). These processes would increase the magnitude of the coefficient of friction up to a peak value (μ_p) due to increase in the deformation (μ_d) and ploughing (μ_{pl}) components of friction and hence the overall value of the coefficient of friction will increase (i.e., equation 2.24). In this region, the material undergoes severe wear (Fig. 4.11) as a result of heavy plastic deformation and consequently large amounts of material are ploughed off the surface and removed.

As sliding proceeds, a smoothing of the specimen surface occur, that is, polishing out of surface asperities by plastic deformation, represented by a decrease in the magnitude of the surface roughness and levelling off at a low value at $Ra \approx 4\ \mu m$. This transition in surface topography is also evident in the SEM micrographs of the wear track (Figs. 4.24-4.26). This leads to a low coefficient of friction (steady state coefficient of friction). Because of little deformation and material removal during steady state the wear rates are also low (mild wear).

It should be mentioned here that the grain size at the steady state (i.e., mild wear region) becomes smaller. This is evident in the SAED pattern in Figures 4.47. The SAED pattern of the surface before wear shows spots characteristic of single crystal, while the SAED pattern of the wear track at the steady state shows spotty rings which indicate that the grains broke up during wear and formed smaller grains.

For coarse-grained titanium, the coefficient of friction increases rapidly as a result of an increase in the ploughing and the deformation components of overall coefficient of friction. The roughness of the worn surface increases rapidly at the initial stages of sliding to maximum value of 3.5μm and increases at a lower rate afterwards (Fig. 4.32(b)). A somewhat similar surface roughness has also been confirmed by SEM observations after 12 and 90 m sliding distances (Fig. 4.29). The shape of the surface roughness versus sliding distance curve is reflected in the time-dependent friction curve, i.e., there is no change in the surface roughness profile at large sliding distances, hence, no drop in the coefficient of friction.

Attention should also be given to the role of surface films on the coefficient of friction. Experiments performed in vacuum clearly indicate that the coefficient of friction and the wear rate are higher than those performed in air (Table 4.6). A possible interpretation of this effect is that when the surfaces are clean and free of oxides, such as aluminum and iron oxides, the resistance to plastic deformation is low. Hence, the extent of ploughing of the clean surface increases, resulting in a higher coefficient of friction and a higher wear rate. In air, oxides continuously form on the worn surface as the fresh metal becomes exposed to air during sliding (60,62). Due to the high hardness of these oxides they provide a solid lubrication action.

Nanocrystalline and coarse-grained aluminum tested in vacuum and air at a sliding speed of $4.2X10^{-4}$ $m.s^{-1}$ (Fig. 4.14) reveal that at the early stages of sliding very mild wear "or better be described as an incubation period" occurs prior to severe wear. A possible cause for this behaviour is that under the current sliding conditions (i.e., low speed) a surface layer of contamination on the specimen surface may provide protection to the specimen by acting as a lubricant, hence, an incubation stage is observed. As the sliding distance increases this contamination layer breaks and wearing of the specimen occurs more readily, thus, severe wear. For tests performed using higher speed ($1.3x10^{-2}$ $m.s^{-1}$) the surface contamination layer breaks fast enough that this "incubation period" is not detectable.

b) Work-hardening

The stress-strain distribution in the material adjacent to the contact surfaces changes during the wear process. The hardness of the subsurface region, for aluminum, continuously increases (Figs. 4.33(a),4.34(a)) first at a high rate then steadily from 370 to 550 MPa. The work hardening effect during sliding is also evident by the changes in the subsurface hardness of titanium (Fig. 4.33(b)). This increase in the subsurface hardness causes plastic deformation and associated surface damage processes become progressively more difficult to operate which in turn translate to a drop in the coefficient of friction and an increase in the wear resistance. Therefore, at the later stages of sliding, the damage processes depend largely on the properties of the material within the deformed subsurface zone rather than the initial material properties before the test. This trend, i.e., the stronger dependence of the μ_p to the (bulk) hardness is shown in Figure 5.4.

The increase in subsurface hardness, for titanium, is around 10% at 100 m sliding distance in comparison to aluminum which exhibits 60% increase at the same sliding distance (Fig. 5.5). Furthermore, the thickness of the deformed zone (Fig. 4.35) for titanium is half that of aluminum. A large surface hardening effect, for aluminum, is translated to larger difference between μ_p and μ_{ss}.

c) Crystallographic texture evolution

A preferred crystallographic orientation evolves near the worn surfaces during the wear process. A strong (111) texture progressively develops in the coarse-grained aluminum in the material adjacent to the contact surface (Fig. 4.37). The number of the (111) planes parallel (or nearly parallel) to the worn surface, are represented by a texture index (Fig. 4.40(a)) which increases rapidly at the initial stages of sliding and steadily afterwards. The texture index ranges from 0.15 (prior to wear) to 0.80 (at a sliding distance of about 4500 m). While the number of the (111) planes making large angles with the contact surface decreases rapidly with increasing sliding distance (Fig. 4.40(b)).

Formation of a (111) texture parallel to the worn surface reduces the resistance to the sliding motion since the (111) plane is a slip plane in the fcc aluminum crystal and deformation occurs by shearing of surface layers. In turn, this causes the coefficient of friction to drop.

A (111) texture parallel to the worn surface is in aluminum with grain sizes of 16.4 and 43.1 nm even prior to wear (Fig. 4.39). In fact, the initial texture of nanocrystalline aluminum resembles that of the 1 mm grain size aluminum at a sliding distances > 4000 m (Fig. 4.40). Consequently, the transition in the coefficient of friction ($\Delta \mu_p$ in Table 4.5) of nanocrystalline aluminum is smaller than that of coarse-grained aluminum.

On the other hand, there is no significant textural changes during wear for coarse-grained titanium. This is expected in light of the fact that prior to wear, the "normal" section of the titanium disc has a strong (0001) texture (Fig. 4.42). The (0001) planes, being slip planes in the hcp titanium crystal, are parallel to the worn surface and remain at this orientation throughout the wear process. This, in part, explains the constant coefficient of friction ($\Delta \mu_p=0$, see Table 4.8) exhibited during sliding. On the other hand, sliding wear experiments performed on the "transverse" section of the titanium disc indicate a development of a (0001) texture as sliding progresses (Fig. 4.44). The texture index ($0 \leq \Phi \leq 35°$) reveals that the texture of the normal section remains essentially constant while the transverse section (which initially has no (0001) texture) has undergone a 30% increase (Fig. 5.6). Hence, there is a drop in the coefficient of friction ($\Delta \mu_p$=0.4) of the transverse section (Fig. 4.19(b)) as a consequence of the (0001) planes becoming parallel to the contact surface, which in turn, reduces the resistance to sliding. The increase in the texture index for coarse grained aluminum is about 550% (Fig. 5.6) this is accompanied by a larger drop in the coefficient of friction, $\Delta \mu_p$=1.22, in comparison to coarse-grained titanium.

The initial texture of the as-sputtered titanium (prior to wear) is characterised by a large number of [0001] poles oriented at 90° from the contact surface as opposed to the normal section of coarse-grained titanium. Therefore, as expected, it shows a corresponding drop in the coefficient of friction ($\Delta \mu_p$=0.21) at large sliding distances (Table 4.8).

5.2.2. Effect of Grain Size on Friction and Wear of Nanocrystalline Aluminum

Experimental results indicate that the basic shape of friction curve for the polycrystalline aluminum (worn against a stainless steel slider) remains relatively unchanged within the broad range of grain sizes. The peak value of the coefficient of friction and the rate of wear (severe wear) at the initial stages of sliding decrease with decreasing the grain size. The large improvement in the wear resistance (severe and mild) indicates that nanocrystalline structures may be of value in certain tribological applications. However, the wear rates at the later stages of sliding (mild wear) and the steady-state value of coefficient of friction are less sensitive to the initial grain size (and hence to the bulk hardness of samples). This is due to the work hardening of the material adjacent to the worn surface and also the grain size becomes smaller with increasing sliding distance. In the nanocrystalline samples with surface hardness about six times larger than the coarse grained aluminum deformation, microploughing cannot occur as readily (Fig. 4.25) resulting in a smaller μ_p and lower wear rates.

In the early stages of sliding, the bulk hardness of nanocrystalline aluminum appears to be a good index of the wear resistance. Figure 5.7 shows the variation of the wear rates within the 15-100 nm grain size range with the hardness. A simple linear regression analysis of the data in Figure 5.7 indicates that the rate of wear in the severe wear regime (W_s) obeys the following expression.

$$W_s = 8.5 \times 10^{-4} + (1.73 \times 10^{-3}) \cdot H^{-1} \qquad 5.3(a)$$

The mild wear rates are less sensitive to the initial bulk hardness. The mild wear rate (W_m) versus H^{-1} plot can be described as follows

$$W_m = -1.9 \times 10^{-4} + (3.7 \times 10^{-4}) \cdot H^{-1} \qquad 5.3(b)$$

We can also establish a relationship between the grain size and wear rates, i.e., for the severe wear

$W_s = 8.5 \times 10^{-4} + (2.44 \times 10^{-4}) \,.\, D^{1/2}$ 5.4(a)

and for the mild wear

$W_m = -1.9 \times 10^{-4} + (5.1 \times 10^{-5}) \,.\, D^{1/2}$ 5.4(b)

The linear relationship between W_s, W_m and the grain size is shown in Figure 5.8.

Equation 5.3 relating the volume of the material worn per unit sliding distance, W, to the hardness H of the nanocrystalline material is an Archard type wear (Equation (2.20)). According to Equation 5.3, under the ambient conditions the wear coefficients of the nanocrystalline aluminum are 1.73×10^{-3} and 3.7×10^{-4} for severe and mild wear regimes respectively (note that here the applied load, F_N, in Archard's law is equal to 1.0 N). Combining equations 5.3 and 5.4, Archard's wear law can be re-expressed in the formalism of the Hall-Petch relationship, i.e.

$W = W_o + K\ [F_N / (H_o + kD^{-0.5})]$ 5.5

The term W_o represents a grain size independent component for 15-100 grain size range, the constant K is termed wear coefficient and is related to the severity of the sliding wear process. Equation 5.5 describes the effect of grain size refinement on the wear rates.

5.2.3. Effect of Layer Thickness of Al/Al_2O_3, Ti/TiN and Ti/Cu Nanolaminated Composites on Friction and Wear

Experimental data on Ti-based materials (Fig. 5.9) indicate a decrease in the steady state coefficient of friction for the as-sputtered titanium film (D=30 nm) as compared to coarse-grained titanium (D=50 μm). Further reduction is achieved by incorporating TiN layers and reducing the spacing between them. Comparison of the coefficient of friction of Ti/TiN with the finest titanium interlayer spacing with monolithic TiN and Ti films indicates that the laminated composite may provide "optimum" combinations of friction properties for certain surface coatings owing to a smaller peak coefficient of friction than its monolithic ceramic component (and lower steady state coefficient of friction than monolithic titanium) as well as a shortest time to steady-state. However, the wear rates (severe and mild) of the monolithic TiN are 1.5 and 3.3 times, respectively, smaller compared to Ti(150 nm)/TiN(20 nm).

In the sliding wear experiments of Ti-based films, the hardness of the films is higher (Table 4.4) than that of the stainless steel slider (VH=4.5 GPa). In this case the wear process becomes more complex and the hardness of the counterface must also be taken into consideration. In this situation, both the TiN and the stainless steel slider, undergo plastic deformation. Unlike sliding wear of aluminum, TiN inflicts a heavy damage on the stainless steel slider (Fig. 5.10), resulting in heavy plastic deformation and ploughing on the slider surface. This translates into a higher peak coefficient of friction between the contacting bodies.

The coefficient of friction, sliding distance to steady state and wear rates of the nanolaminated composites are reduced by reducing the interlayer spacing between non-metallic layers (Table 4.7). For example, a 42% decrease in the peak coefficient of friction of Al(200 nm)/Al_2O_3(20 nm) is achieved over monolithic nanocrystalline film with a grain size of 16.4 nm. At the beginning of sliding, the worn surface of the Al/Al_2O_3 laminates exhibits some degree of plastic deformation as depicted by Figure 4.28(a). This would give rise to an increase in the coefficient of friction as a consequence of microploughing of the surface and deformation of surface asperities. However, the surface damage and plastic deformation are milder in comparison to that of coarse-grained aluminum (Fig. 4.24). A possible role that the Al_2O_3 or TiN layers may play is to reduce the subsurface damage accumulation by preventing slip transfer between the metallic layers. This translates to less energy consumption during wear, hence resulting in a low coefficient of friction.

On the other hand, Ti/Cu laminates (Fig. 4.31) exhibit delamination of the titanium and copper layers during wear. The delamination in Ti/Cu laminate translates into higher wear rates than Ti/TiN composites. The worn surface also exhibits zigzagged and fractured edges of the wear track, which are an indication of the brittle nature of the laminate (Fig. 4.31).

The wear rates of nanolaminated Ti/TiN composites were analyzed to determine the role of hardness and interlayer spacing, and the results of the analysis are summarised in Figures 5.11 and 5.12 . Figure 5.11 suggests that there is a linear relationship between the wear rate and the inverse of the material hardness, in agreement with Archard's law of wear. Best fit to data in Figure 5.11 gives

$W_s = -4.6 \times 10^{-5} + (1.5 \times 10^{-3}) \cdot H^{-1}$ 5.6(a)

and

$W_m = -1.2 \times 10^{-5} + (1.7 \times 10^{-4}) \cdot H^{-1}$ 5.6(b)

The severe (W_s) and mild (W_m) wear rates of laminated Ti/TiN composites are plotted as a function of the square-root of the titanium layer thickness in Figure 5.12. A linear regression analysis gives for the severe wear

$W_s = 7.0 \times 10^{-5} + (2.9 \times 10^{-7}) \cdot \lambda^{0.5}_{Ti}$ 5.7(a)

and for the mild wear

$W_m = 8.0 \times 10^{-7} + (3.0 \times 10^{-8}) \cdot \lambda^{0.5}_{Ti}$ 5.7(b)

Where the units of W and λ are mm^3/m and nm, respectively.

The effect of the hardness (H) and the interlayer spacing (λ) on the mild and severe wear rates, for nanolaminated Al/Al_2O_3, are illustrated in Figures 5.13-5.14, respectively. Linear regression analysis of the hardness versus wear rates gives

$W_s = 1.2 \times 10^{-3} + (8.5 \times 10^{-4}) \cdot H^{-1}$ 5.8(a)

$W_m = 1.5 \times 10^{-5} + (1.7 \times 10^{-5}) \cdot H^{-1}$ 5.8(b)

Similar analysis between the aluminum layer thickness and wear rates yields

$W_s = 1.2 \times 10^{-3} + (8.5 \times 10^{-6}) \cdot \lambda^{0.5}_{Al}$ 5.9(a)

$W_m = 1.6 \times 10^{-5} + (1.7 \times 10^{-7}) \cdot \lambda^{0.5}_{Al}$ 5.9(b)

Considering the inverse relationship between the layer thickness and the hardness, it can be shown that equations 5.6-5.9 provide a useful way to design wear resistant layered structures on the basis of Archard's law of wear by introducing the role of microstructure. A modified Archard's law, similar to that derived for the grain size (equation 5.5) also applies here by replacing the grain size D by the interlayer spacing λ.

5.2.4. Comparison of Friction and Wear Behaviour of Nanoscale Materials

The peak coefficient of friction is found to correlate with the normalized hardness of the material, i.e., the hardness ratio of the specimen to that of the slider (H_{sp}/H_{sl}), as given in Figure 5.15 .The trend in Figure 5.15 indicates that the peak coefficient of friction, as a function of large range of normalized hardness, increases as the hardness difference between the specimen and the slider increases and is minimum when the harness ratio is approximately equal to unity (i.e., the specimen and the slider have similar hardness).

The severe and mild wear rates vary exponentially as the H_{sp}/H_{sl} ratio (Figs. 5.16(a,b)). Wear rates decrease rapidly as the hardness of the specimen and the slider become very similar (when H_{sp}/H_{sl} approaches unity) and decreases at a lower rate afterwards. For a soft material where $H_{sp}<H_{sl}$, as in the case of coarse-grained aluminum, the specimen undergoes high wear while the slider exhibits no significant wear. In the case of very hard specimen (e.g., TiN) where $H_{sp}>H_{sl}$ the sample wear rates are very low, but the counterface (slider) undergoes severe wear. Minimal wear rates are achieved on both the specimen and the slider when their hardness are equal.

The diagrams in Figures 5.8, 5.12 and 5.14 as well as equation 5.5 provide guidelines for material selection for a given tribological application. Depending on the wear rate specified for the application, a monolithic or layered film can be selected. It is noted that the wear resistance achieved by Al/Al_2O_3 nanolaminated composites is higher than those of monolithic aluminum films. The superior wear resistance of Ti/TiN nanolaminated composites, however, is clearly seen. The diagrams also highlight the fact that in unreinforced nanocrystalline films, grain growth, which might result during wear in high temperature environments, would reduce the wear resistance. Therefore, under these conditions, nanolaminated materials are preferred for surface coating applications.

Table 5.1. Comparison of Hall-Petch parameters of aluminum.

Material	σ_o (MPa)	k (MPa.m$^{0.5}$)	Grain Size (μm)	Ref.
99.97 %Al	15.0	0.07	20-150	(36)
99.999%Al	15.5	0.04	150-250	(37)
99.99 %Al	22.4	0.07	30-100	(38)
1100 Al	14.3	0.07	20-200	(39)
Al-6%Ni	11.0	0.14	0.5-20	(40)
99.99%Al	11.3	0.07	0.015-0.1	*

* this work.

Table 5.2. Elastic moduli and hardness calculated using the rule of mixtures for Ti/TiN nanolayered composites.

λ_{Ti}(nm)	λ_{TiN}(nm)	f_{Ti}	f_{TiN}	E(GPa)	H(GPa)
450	40	0.92	0.08	119	11.59
150	20	0.88	0.12	122	11.93

Table 5.3. Elastic moduli and hardness calculated using the rule of mixtures for Al/Al_2O_3 nanolayered composites.

λ_{Al}(nm)	λ_{Al2O3}(nm)	f_{Al}	f_{Al2O3}	E(GPa)	H(GPa)
500	20	0.96	0.04	63	1.75
200	20	0.91	0.09	66	1.82
70	10	0.88	0.12	67	1.86

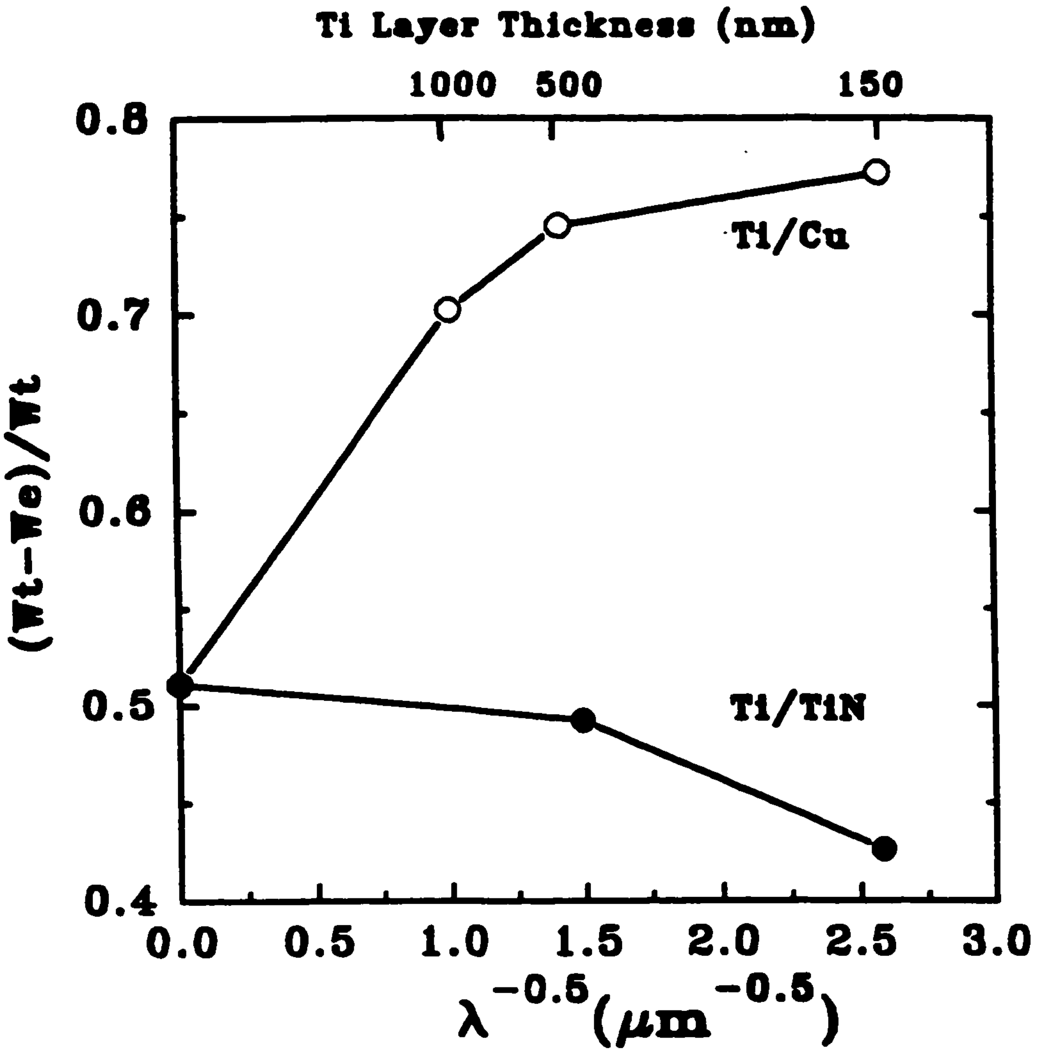

5.1. The relationship between the energy expended during indentation and the Ti layer thickness in Ti/Cu and Ti/TiN laminated composites.

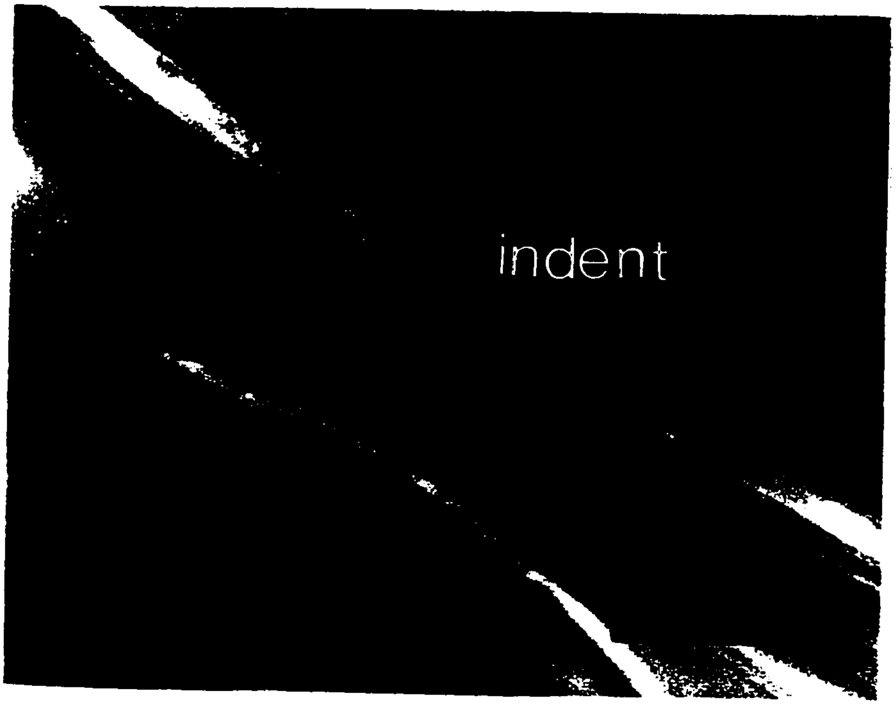

5.2. SEM micrograph of cross-section below Vickers indenter impression (using a load of 0.1 N) for Ti(150 nm)/Cu(20 nm) laminated composite.

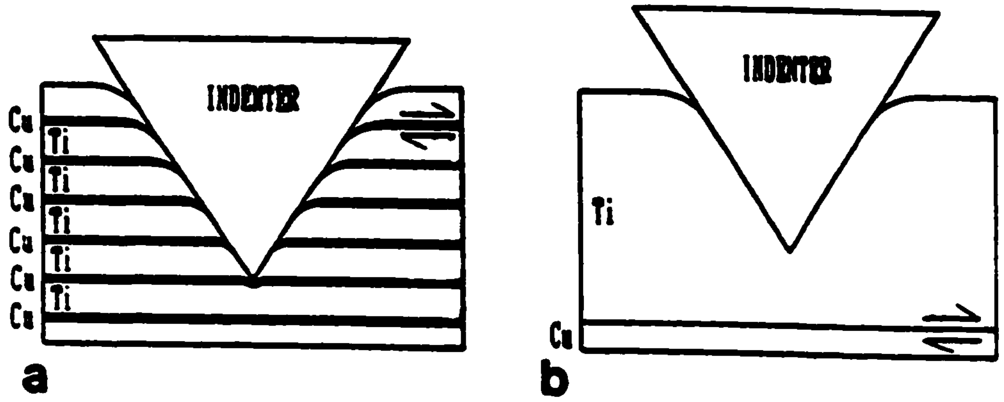

5.3. Schematic diagram of Ti/Cu composites showing delamination between Ti and Cu layers below the indentation impression. (a) fine structure, e.g., Ti (150 nm)/Cu (20 nm); (b) coarse structure, e.g., Ti (1000 nm)/Cu(120 nm). Figures drawn to scale. Shear stress pattern near the interface is omitted. Indentation penetrates deeper and more energy expended in the fine structure.

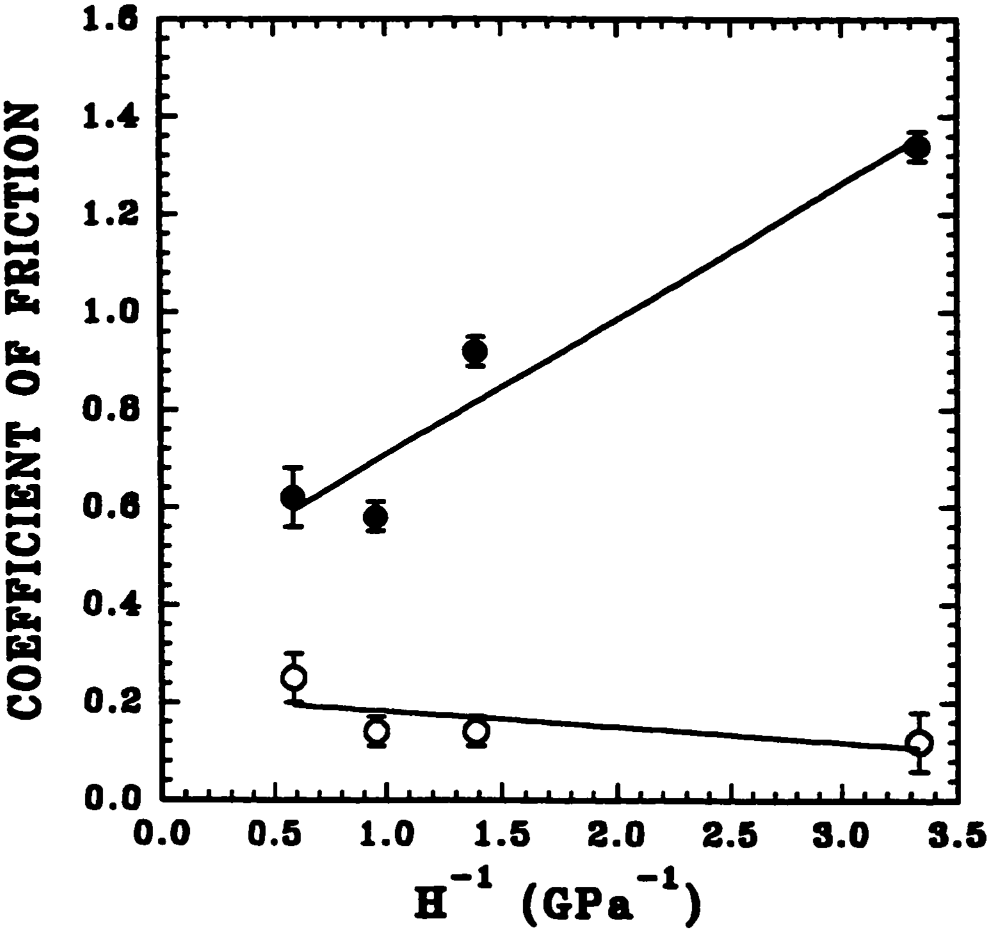

5.4. Peak (closed symbols) and steady state (open symbols) coefficients of friction as a function of the hardness of aluminum.

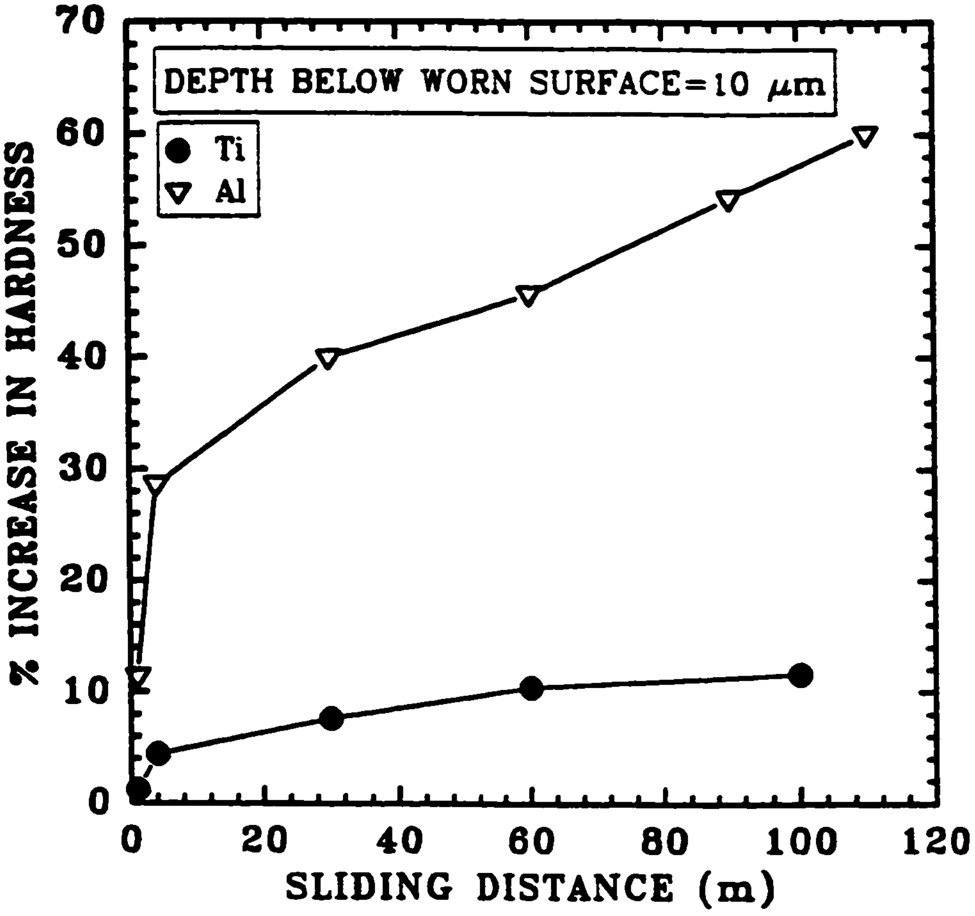

5.5. The increase in subsurface hardness versus sliding distance for aluminum and titanium.

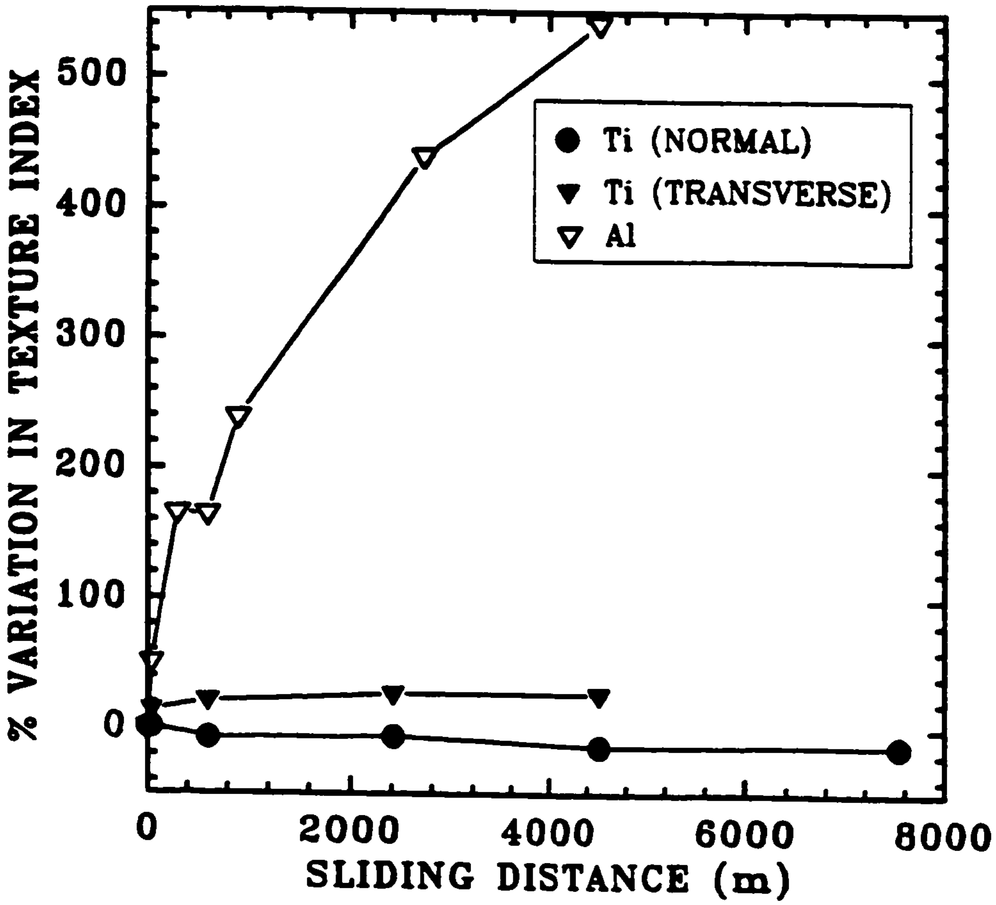

5.6. Texture evolution during the wear process as a function of sliding distance.

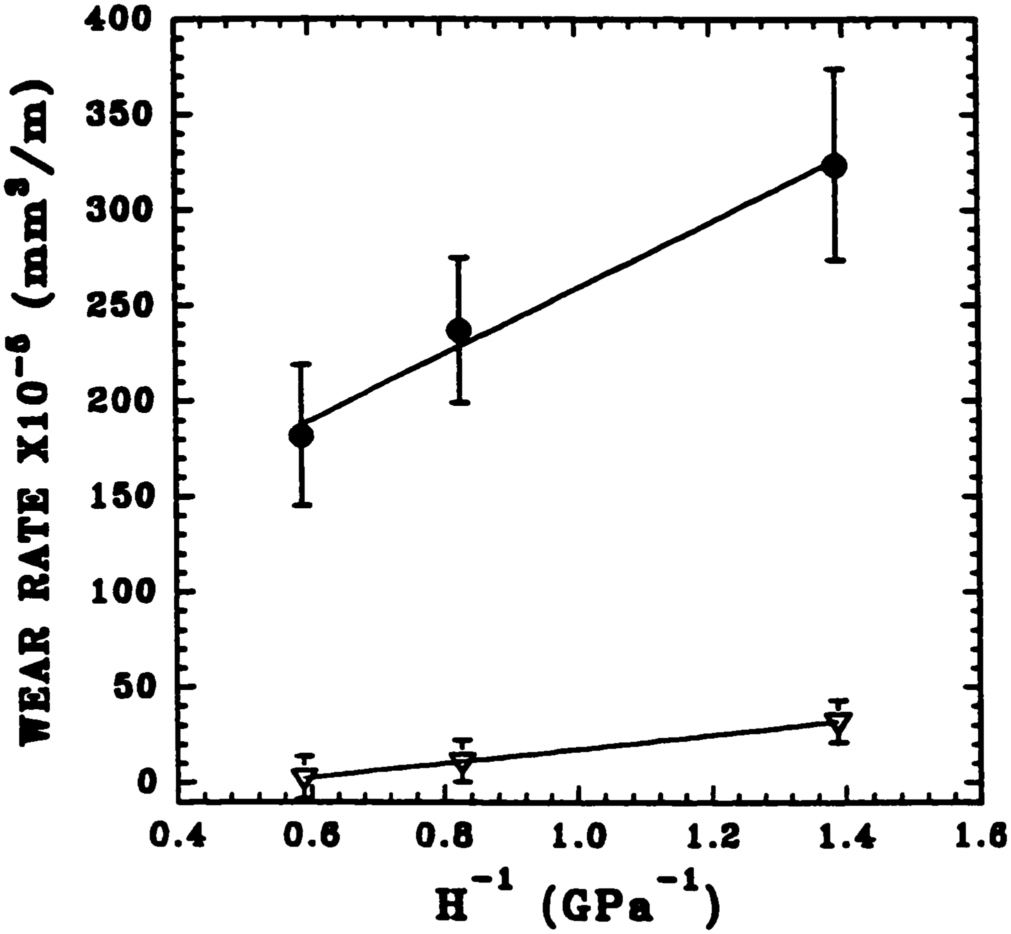

5.7. Severe (closed symbols) and mild (open symbols) wear rates as a function of hardness of aluminum.

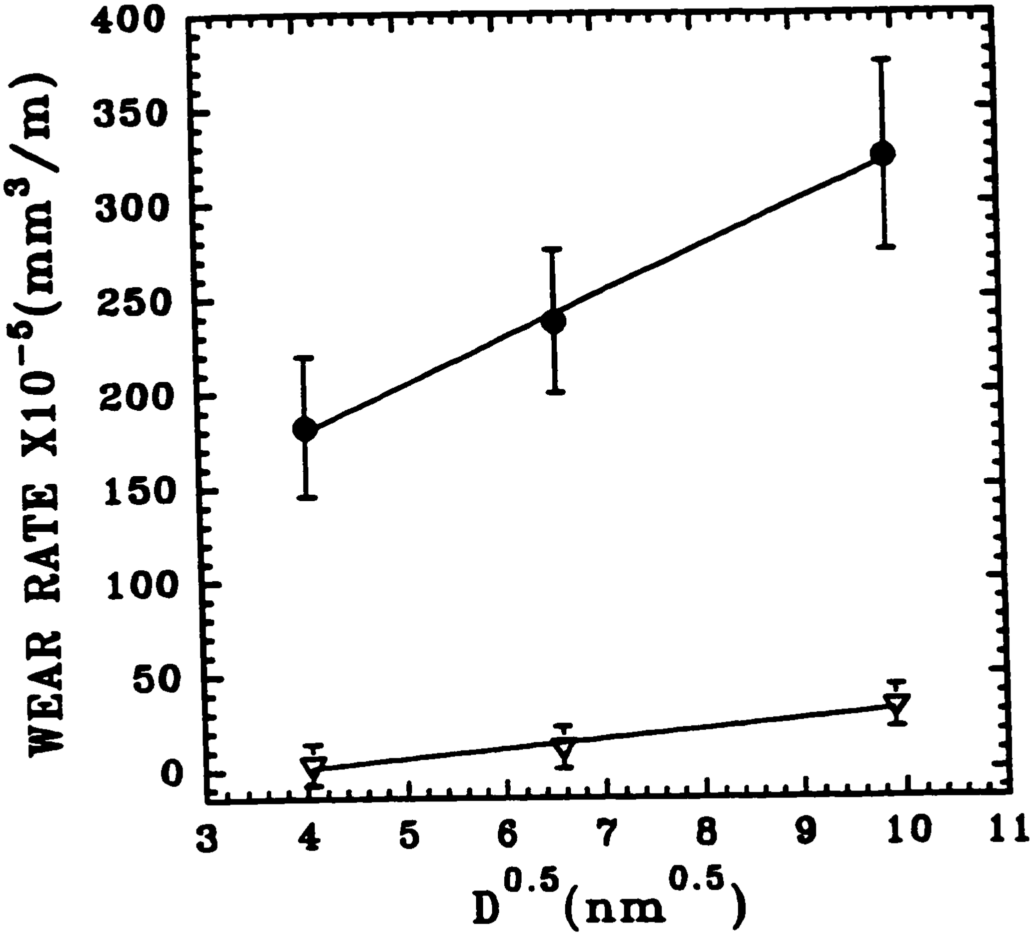

5.8. Severe (closed symbols) and mild (open symbols) wear rates as a function of aluminum grain size.

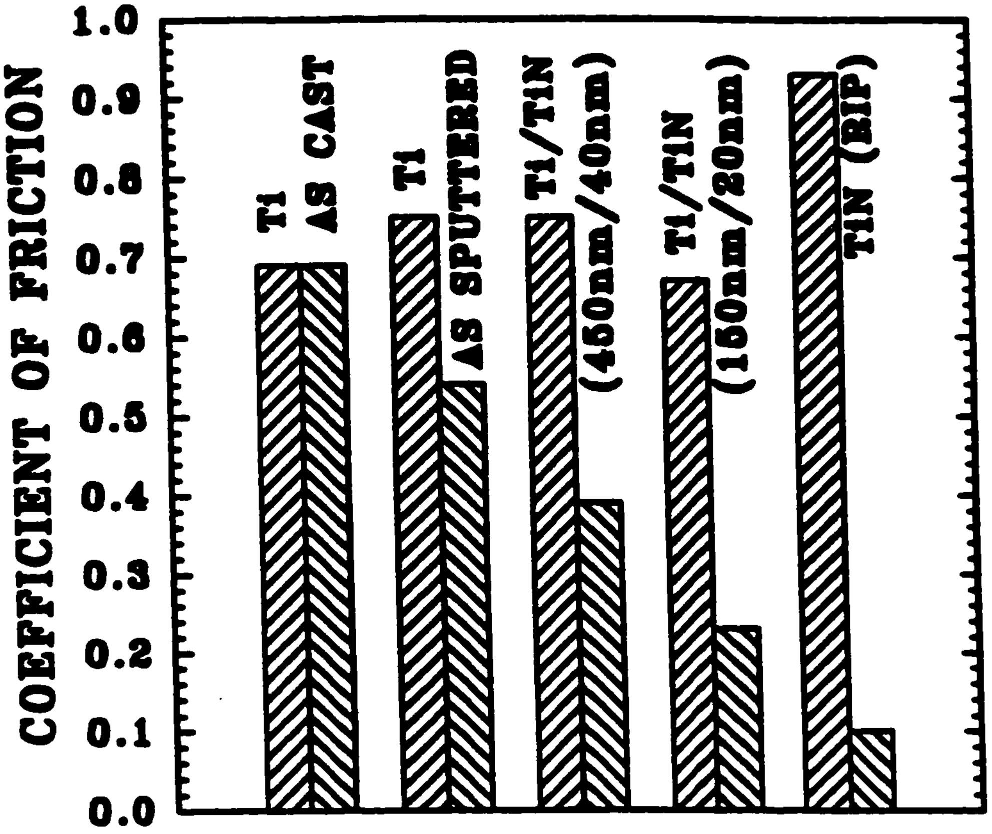

5.9. Peak ▨ and steady state ▧ coefficients of friction for titanium-based coatings.

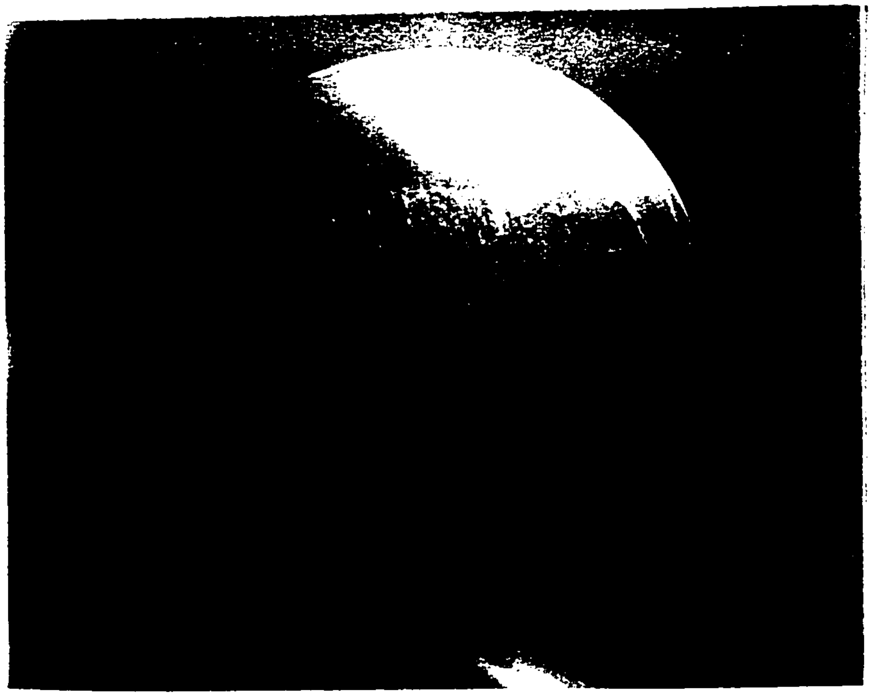

5.10. SEM micrograph of the stainless steel pin slid against monolithic TiN at 90 m sliding distance.

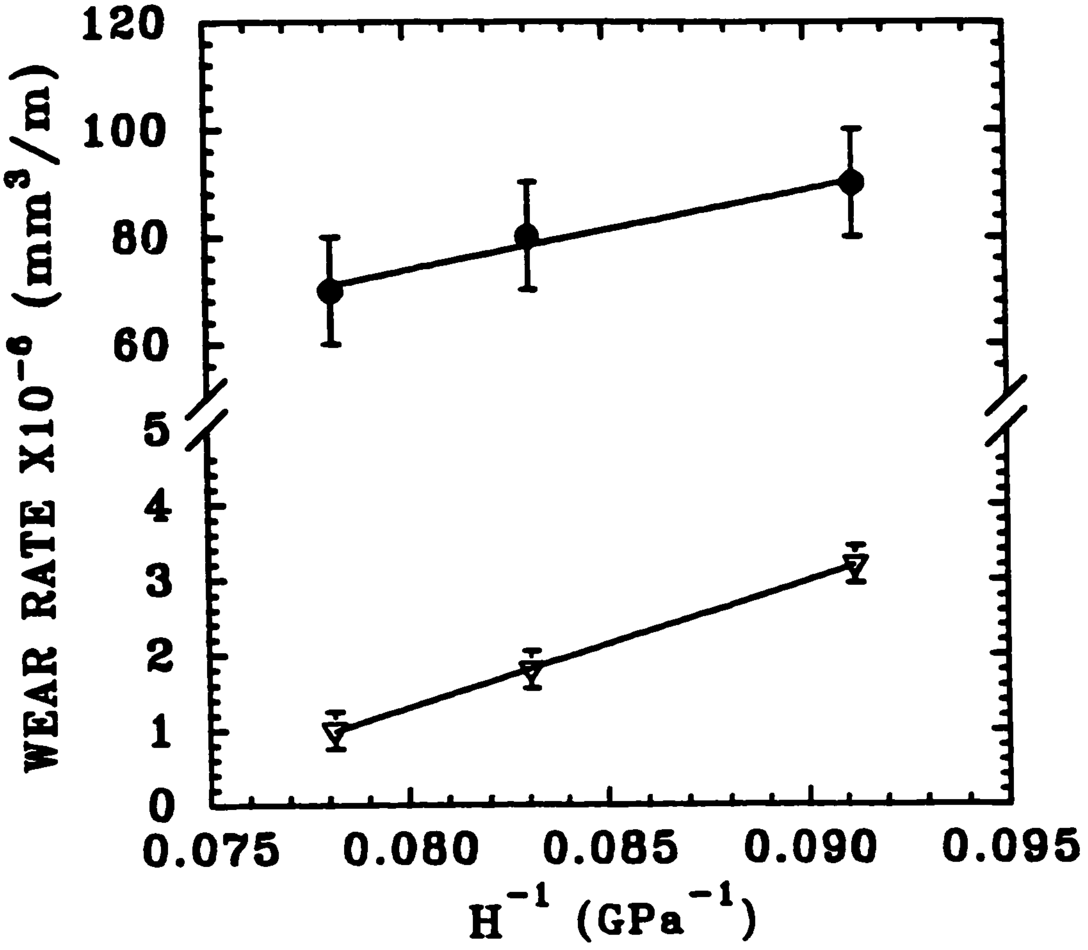

5.11. Severe (closed symbols) and mild (open symbols) wear rates as a function of hardness of Ti/TiN laminated composites.

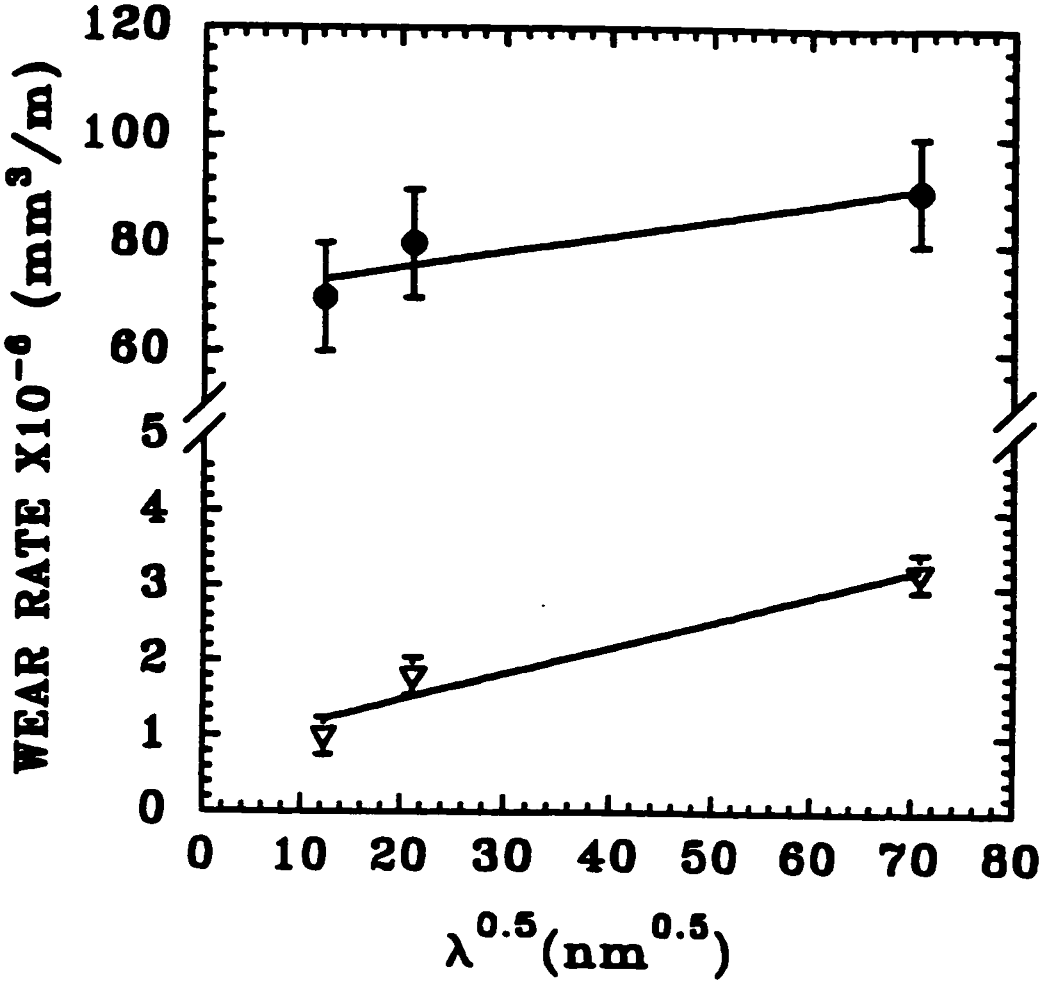

5.12. Severe (closed symbols) and mild (open symbols)wear rates as a function of Ti layer thickness in Ti/TiN laminated composites.

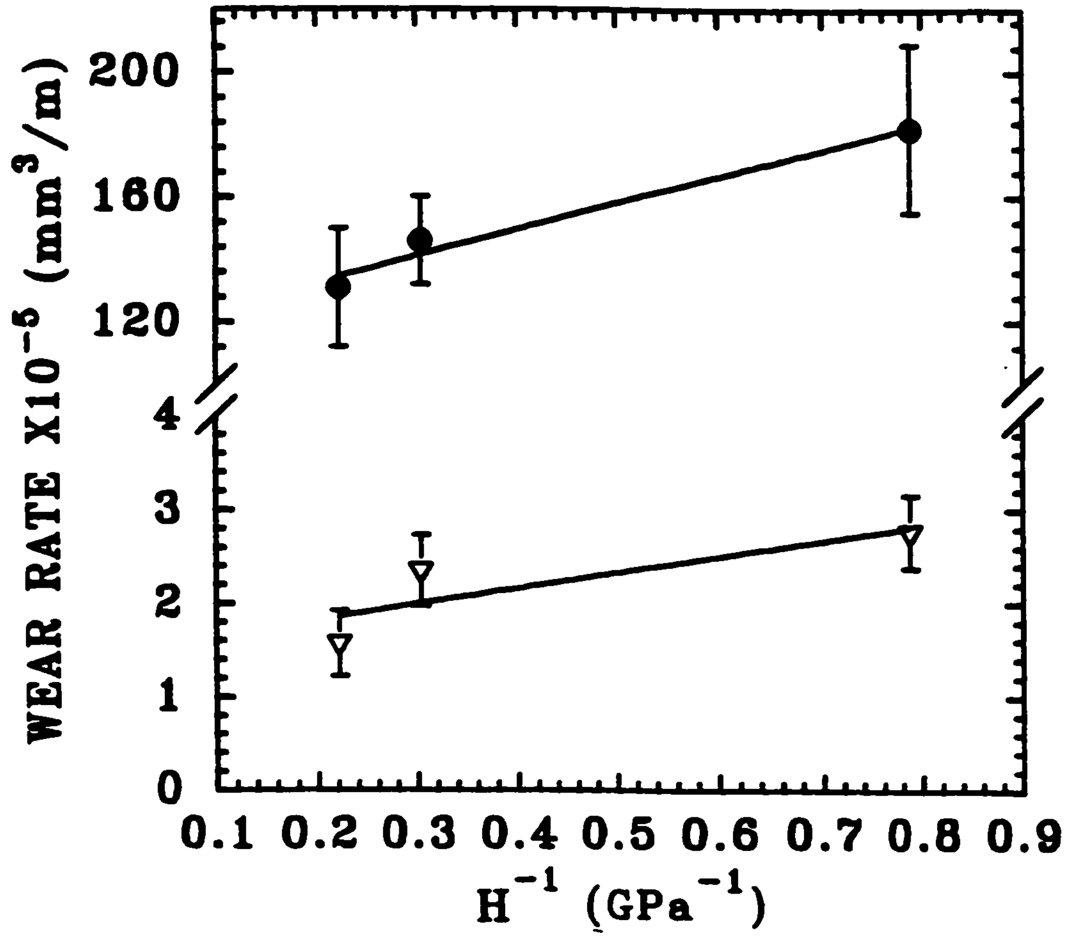

5.13. Severe (closed symbols) and mild (open symbols) wear rates as a function of hardness of Al/Al_2O_3 laminated composites.

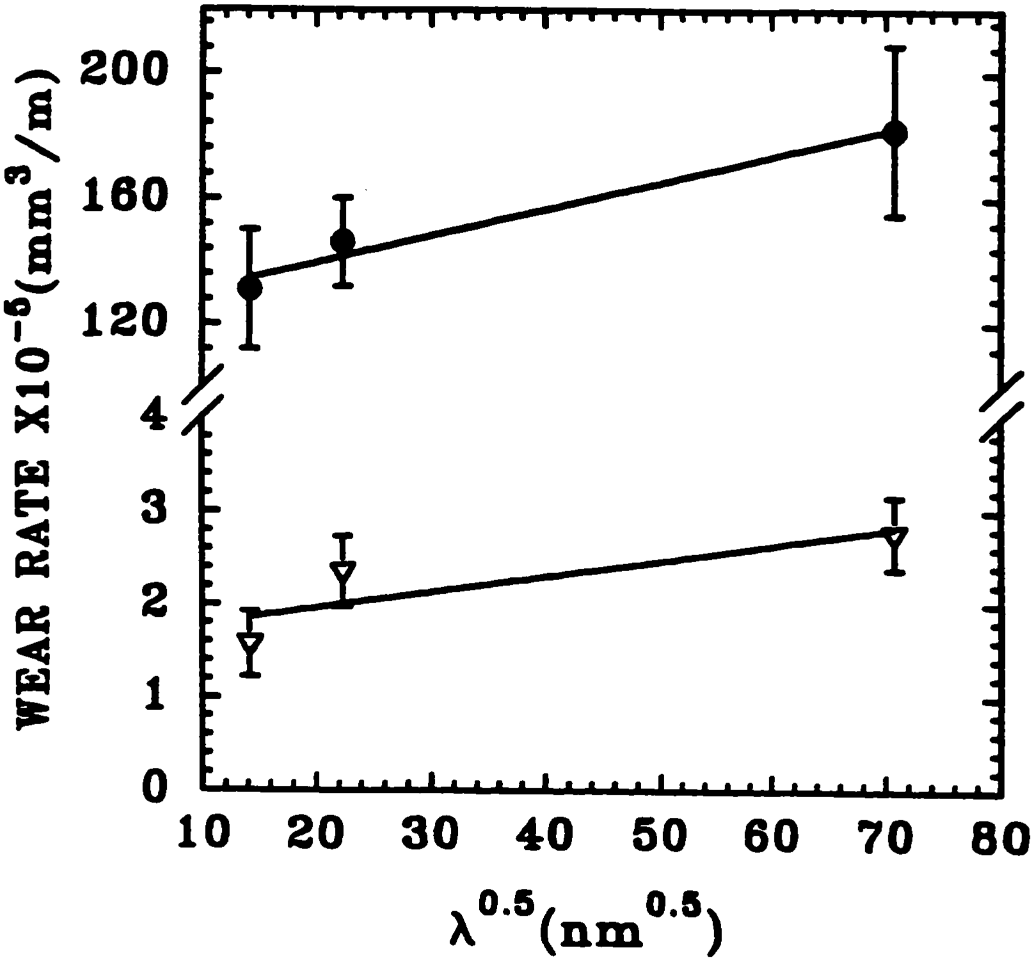

5.14. Severe (closed symbols) and mild (open symbols) wear rates as a function of Al layer thickness in Al/Al_2O_3 laminated composites.

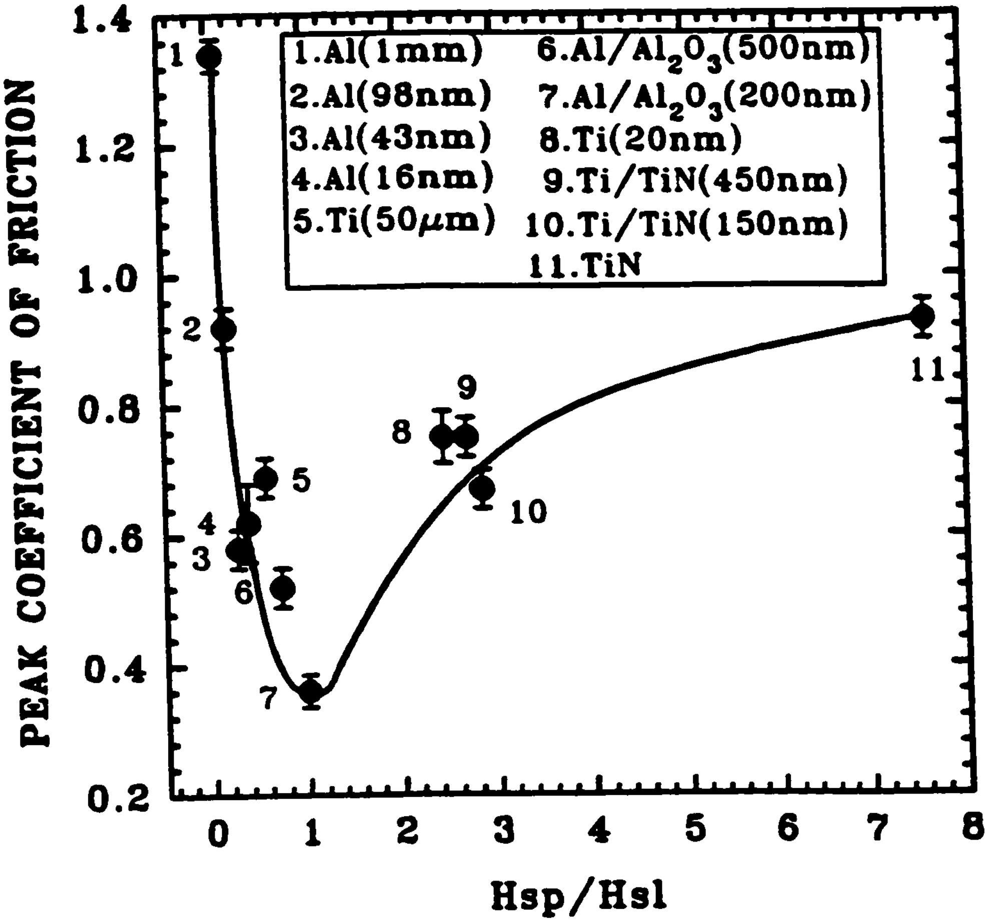

5.15. The relationship between the peak coefficient of friction and the normalized hardness for different coatings.

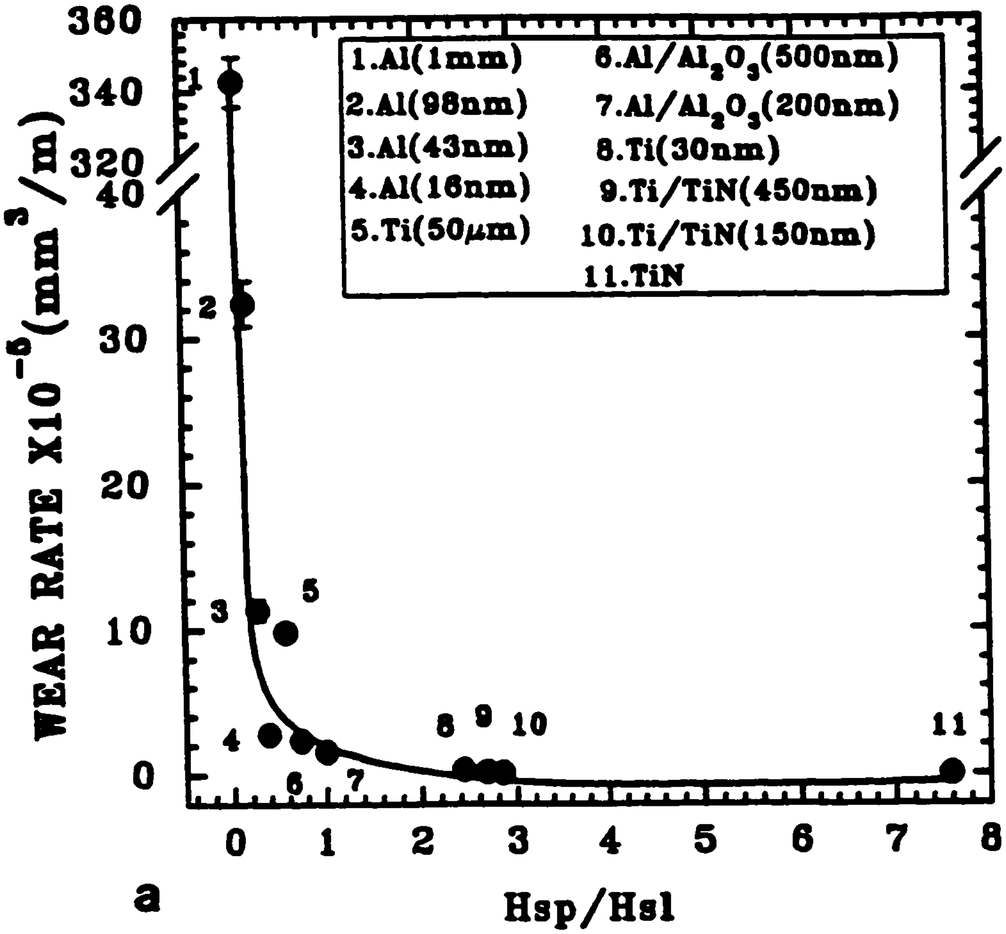

5.16. Wear rate of specimens as a function of normalized hardness of specimens with respect to the slider hardness; (a)sever wear; (b)mild wear.

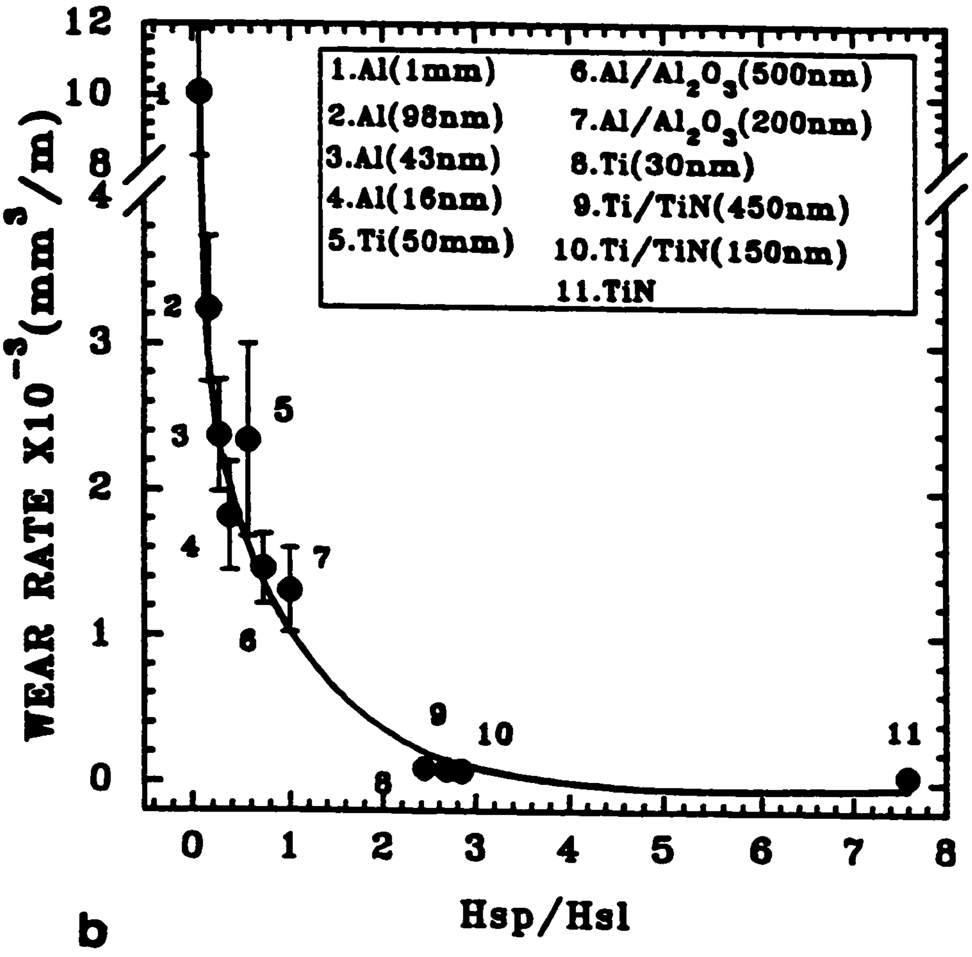

5.16. (continued).

CHAPTER 6

CONCLUSIONS

6.1. Conclusions

1. Friction and wear properties of nanocrystalline aluminum and nanolaminated Al/Al_2O_3, Ti/TiN and Ti/Cu composite films sliding against stainless steel were studied. The aluminum grain size varied between 15 and 10^6 nm. In Al/Al_2O_3 and Ti/TiN composites, the Al and Ti layer thicknesses ranged from 70 to 500 nm and from 150 to 450 nm, respectively.

2. Within the grain size range of 15-100 nm, the hardness of aluminum is inversely dependent on the square root of grain size, i.e., it follows a Hall-Petch type relationship.

3. The hardness of Ti/TiN and Al/Al_2O_3 films increases as $\lambda^{-0.5}$ of Ti and Al layer thickness in agreement with the Hall-Petch formalism. Young's modulus of the composites is comparable with those predicted by the rule of mixtures.

4. The Ti/Cu composites show a softening effect with decreasing Ti layer thickness due to delamination of the layers under the hardness indenter.

5. The coefficient of friction is time-dependent. The shape of the coefficient of friction curve is strongly influenced by strain hardening of the subsurface layer, crystallographic texture formation in these layers, and the change in roughness of

the wear track which occur simultaneously but at different rates.

6. The severity of wear damage, i.e., plastic deformation, microploughing and microfracture decreases during sliding as the subsurface material undergoes hardening. Consequently, mild wear rates and values of the steady-state coefficient of friction become less sensitive to the initial bulk hardness. The severe wear (and μ_p) are sensitive to both the scale of the microstructure and the bulk hardness of the material.

7. (0001) and (111) textures develop parallel to the worn surface during the sliding wear of titanium and aluminum, respectively. The development of these textures provides easy sliding. Consequently, they contribute to the transition from peak to steady state coefficient of friction.

8. The peak coefficient of friction and severe and mild wear are sensitive functions of the normalized hardness (i.e., H_{sp}/H_{sl}) of the material.

9. The peak coefficient of friction is minimum when the ratio $H_{sp}/H_{sl}=1$ and increases as the ratio H_{sp}/H_{sl} departs from unity. The severe and mild wear rates decrease exponentially as H_{sp}/H_{sl} approaches unity.

10. In general, the coefficient of friction rises to a peak value (μ_p) after a short sliding distance then settles down to a steady-state ($\mu_{s.s}$). Similarly, the wear rate versus sliding distance curves reveal a transitional behaviour from severe wear to mild wear above a critical sliding distance corresponding to the transition from μ_p to $\mu_{s.s}$.

11. The peak coefficient of friction (μ_p) of aluminum decreases about 55% with decreasing the grain size from 10^6 nm to 16.5 nm. Coefficients of friction become higher when the sliding tests are performed in vacuum (10^{-6} torr). The severe and mild wear rates decrease by one and two orders of magnitude, respectively, when reducing the grain size from 10^6 to 16.4 nm.

12. The coefficient of friction and wear rate, for nanolaminated Ti/TiN and Al/Al_2O_3 composites are consistently reduced as the metal layer thickness is reduced.

13. Laminates exhibit higher wear resistance than monolithic metallic films. The coefficient of friction of Al/Al_2O_3 is 70% lower than that for monolithic aluminum. A 60% decrease in the steady state coefficient of friction is observed in Ti/TiN with respect to monolithic titanium.

14. Based on the experimental evidence, a modified Archard type equation which incorporates the effect of grain size and metallic layer thickness is proposed in order to describe the wear rates of nanocrystalline aluminum and laminated Al/Al_2O_3 and Ti/TiN composites. This relates the wear rate to structure refinement and can be used as a guideline for material selection for certain wear resistant coating applications.

6.2. Recommendations For Future Work

1. In order to get a better understanding of the wear process the nanoscale

materials should be tested under different loads, sliding speeds and counterface materials and wear maps should then be constructed.

2. Investigate the work-hardening behaviour of the coatings by performing nanohardness measurements below worn surfaces of the films.

3. Measure the subsurface strain gradient as a function of sliding distance in order to study the stress/strain behaviour of the films.

4. Determine the films crystallographic textures as a function of sliding distance and relate them to friction and wear properties.

5. Study the size and shape of the asperities of the hard counterface and its effect on friction and wear.

6. Model mathematical modelling the time-dependent coefficient of friction in terms of work hardening, crystallographic texturing and smoothening of the worn surface.

7. Examine grain structure and monitor changes occurring during deformation of nanocrystalline materials in order to understand the strengthening (or softening) mechanism(s) that takes place in these structures.

6.3. Original Contributions in this Dissertation

1. Design and construction of a tribometer for measuring coefficient of friction and wear of thin films. The test can be conducted either in air or inside an SEM

vacuum chamber.

2. Establishing a Hall-Petch behaviour in nanocrystalline aluminum and laminated composites.

3. Studying the coefficients of friction and wear rates (severe and mild) of nanocrystalline aluminum in air as well as vacuum (inside an SEM vacuum chamber) and relating it to grain size. It was shown that the peak coefficient of friction decreases by reducing aluminum the grain size. It was also found that the wear rate (severe and mild) increases as the square-root of the grain size.

4. Relating the coefficients of friction and wear rates (severe and mild) of laminated Al/Al_2O_3 and Ti/TiN composites to their metallic layer thicknesses.

5. It was demonstrated that the layered composites show better coefficient of friction and wear properties than monolithic materials.

6. Establishing a relationship, based on Archard's law of wear, between wear rates (severe and mild) and structure refinement "a modified Archard's law". It has been established that wear resistance increases as the scale of the microstructure is decreased.

7. Relating surface hardening, texture evolution and microstructural changes to the time dependent coefficient of friction and wear transitions for aluminum and titanium. It is shown that near-surface work-hardening and texturing contribute to the transition from peak to steady-state coefficient of friction and from severe to mild wear.

8. Relating the peak coefficient of friction to the hardness of both the specimen and the slider by the ratio H_{sp}/H_{sl}. The peak coefficient of friction was found to be a minimum when the hardness of both the specimen and the slider are similar.

REFERENCES

1. T. Chou, D. Adamson, J. Mardinly and T. Nieh, Thin Solid Films, 205(1991)131.
2. A. Chokshi, A. Rosen, J. Karch and H. Gleiter, Scripta Met., 23 (1989)1679.
3. J. Karch, R. Birringer and H. Gleiter, Nature, 330(1987)556.
4. J. Horvath, R. Birringer and H. Gleiter, Solid State Communications, 62(1987)319.
5. S. Schuncher, R. Birringer, R. Straub and H. Gleiter, Acta Metall., 37(1989)2485.
6. C. G. Granquist and R. A. Buhrman, J. Appl. Phys., 47(1976)2200.
7. R. W. Springer and D. S. Catleh, Thin Solid Films, 54(1978)192.
8. T. R. Jervis and L. R. Newkirk, J. Mater. Res., 1(1986)420.
9. E. Arzt and L. Schultz, New Materials by Mechanical Alloying Techniques Deutsche Gesellschaft for Metallkunde, Oberursel, Germany, 1989.
10. B. A. Joyce, Rep. Prog. Phys., 48(1985)1637.
11. X. D. Liu, J. T. Wang and B. Z. Ding, Scripta Metall., 28(1993)59.
12. G. Hughes, S. Smith, C. Pande, H. Johnson and R. Armstrong, Scripta Met., 20(1986)93.
13. G. Nieman and J. Weertman, Scripta Met., 23(1989)2013.

14. J. Jang and C. Koch, Scripta Met., 24(1990)1599.

15. R. Valiev, F. Chmelik, F. Bodeaux, G. Kapelski and B. Baudelet, Scripta Met., 27(1992)855.

16. X. Liu, J. Wang and B. Ding, Scripta Metall., 28(1993)59.

17. K. Lu, W. Wei and J. Wang, Scripta Met., 24(1990)2319.

18. A. El-Sherik, U. Erb, G. Palumbo and K. Aust, Scripta Metall., 27(1992)1185.

19. G. Fougere, J. Weertman, R. Siegel and S. Kim, Scripta Met., 26(1992)1879.

20. G. Palumbo, S. Thorpe and K. Aust, Scripta Met., 24(1990)1347.

21. N. Wang, Z. Wang, K. T. Aust and U. Erb, Acta Metall., 43(1995)519.

22. R. Z. Valiev, N. A. Krasilnikov and N. K. Tsenev, Mat. Sci. and Eng., A137(1991)35.

23. Z. Fan, Mat. Sci. and Eng., A191(1995)73.

24. R. W. Siegel, Mat. Sci. and Eng., B19(1993)37.

25. E. O. Hall, Proc. Phys. Soc. London, B64(1951)747.

26. N. J. Petch, J. Iron Steel Inst., 174(1955)25.

27. J. D. Eshelby, F. Frank and F. Nabarro, Phill. Mag., 42(1951)351.

28. A. H. Cottrell, Trans. TMS-AIME, 212(1958)192.

29. J. C. Li, Trans. TMS-AIME, 227(1963)239.

30. H. Conrad, Acta Metall., 11(1963)75.

31. R. W. Armstrong, Y. T. Chou, R. M. Fisher and N. Louat., Phill. Mag., 14(1966)943.

32. E. Anderson, D. W. King and J. S. Spreadborough, Trans. TMS-AIME, 242(1968)115.

33. R. W. Armstrong in: Yield Flow and Fracture of Polycrystals, ed. by T. N. Baker, Applied Science, London, (1983)3.

34. J. P. Hirth, Metall. Trans., 3(1972)3047.

35. J. D. Embury in: Strengthening Methods in Crystals, ed. by A. Kelly and R. B. Nicolson, Elsevier, (1971)331.

36. P. R. Carreker and W. R. Hibbard, Trans. Met. Soc., AIME, 209(1957)863.

37. N. Hansen, Acta Metall., 25(1977)863.

38. H. Fujita and T. Tabata, Acta Metall., 21(1973)335.

39. A. W. Thompson and M. I. Baskes, Phill. Mag., 28(1973)301.

40. D. J. Lloyd, Metal Science, May(1980)193.

41. R. W. Armstrong, Metall. Trans., 1(1970)1169.

42. A. Lasalmonie and J. L. Strudel, J. Mat. Sci., 21(1986)1837.

43. A. W. Thompson, Acta Metall., 23(1975)1337.

44. H. J. McQueen, Metall. Trans., 8A(1977)807.

45. D. J. Abson and J. J. Jonas, Met. Sci. J., 4(1970)24.

46. J. S. Koehler, Phys. Rev., B2(1970)547.

47. S. L. Lehoczky, J. Appl. Phys., 49(1978)5479.

48. S. L. Lehoczky, Phys. Rev. Lett., 41(1978)1814.

49. A. Kelly, Phill. Trans. R. Soc. Lond., A322(1987)409.

50. R. Springer and D. Catlett, Thin Solid Films, 54(1978)197.

51. R. Bunshah, R. Nimmagada and H. Doerr, B. Movchan, N. Grechanuk and E. Dabrzha, Thin Solid Films, 72(1980)61.

52. R. Bunshah, C. Sans, C. Deshpandey, H. Doerr, B. Movchan, A. Demchishin and G. Badilenko, Thin Solid Films, 96(1982)59.

53. K. Yoshi, H. Takaji, M. Umeno and H. Kawabe, Metall. Trans. A, 15A(1984)2034.

54. D. Tench and J. White, Metall. Trans. A, 15A(1984)2039.

55. A. Alpas and J. Embury, Scripta Metall., 22(1988)265.

56. A. Alpas, J. Embury, D. Hardwick and R. Springer, J. of Mat. Sci., 25(1990)1603.

57. T. Foeck and D. Lashmore, Scripta Metall., 27(1992)651.

58. T. Weihs, T. Barbee and M. Wall in: Thin Films, Stress and Mechanical Properties IV, Mat. Res. Soc. Sym. Proc., eds., P. H. Townsend, T. P. Weihs and J. E. Sanchez, Pittsburgh, 308(1993)753.

59. H. Kung, M. Nastasi, T. R. Jervis, K. M. Hubbard, R. M. Messner, T. E. Mitchell and J. D. Embury in: Thin Films, Stress and

Mechanical Properties IV, Mat. Res. Soc. Sym. Proc., eds., P. H. Townsend, T. P. Weihs and J. E. Sanchez, Pittsburgh, 308(1993)747.

60. K. Kato, Plastic Deformation and Fracture of Materials, in Materials Science and Technology Vol. 6, eds., R. W . Chaba, P. Hassen and E. J. Kramer, VCH Publishing, U.S.A., (1994)635.

61. B. J. Briscoe and T. A. Stolarski, Characterization of Tribological Materials, eds., W. A. Glaeser, Manning Publications Inc., U.S.A., (1993)30.

62. K. Zum-Gahr, Microstructure and Wear of Materials, Elsevier, Amsterdam, 1987.

63. S. C. Lim, M. F. Ashby and J. H. Brunton, Acta. Metall., 35(1987)1.

64. J. F. Archard, J. Appl. Phys., 24(1953)981.

65. H. Kato, T. Eyre and B. Ralph, Acta Metall., 42(1994)1703.

66. P. J. Blau, Friction and Wear Transitions of Materials, Noyes Publishing, New Jersey, 1989.

67. W. A. Glaeser, Wear, 73(1981)371.

68. S. C. Lim and J. H. Brunton, Wear, 101(1985)81.

69. K. Iwata and K. Ueda, Wear, 60(1980)329.

70. K. Kato, H. Furuyama and M. Mizumoto, in Proc. Japan, Int. Tribo. Conf., Japanese Society of Tribologists, Nagoya, (1990)261.

71. T. Akagaki and D. A. Rigney, in Wear of Materials, eds., K. C. Ludema and R. G. Bayer, ASME, New York, (1991)265.

72. W. Wang and S. Wen, Wear, 171(1994)19.

73. E. Rabinowicz, Friction and Wear of Materials, Wiley, U.S.A., 1965.

74. R. M. Bentley and D. J. Duquette, in Fundamentals of Friction and Wear of Materials, ed., D. A. Rigney, ASM, Metals Park Ohio, (1980)291.

75. N. C. Welsh, Phil. Trans. Roy. Soc. London, A257(1965)31.

76. F. P. Bowden and D. Tabor, Friction and Lubrication of Solids, Part II, Clarendon, Press, Oxford, England, 1964.

77. F. H. Scott, D. S. Lin, G. C. Wood and C. W. Stevenson, Wear, 36(1976)147.

78. D. A. Rigney, Ann. Rev. Mater. Sci., 18(1988)141.

79. S. Jahanmir, Fundamentals of Tribology, eds., N. P. Suh and N. Saka, MIT Press, U.S.A., (1980)455.

80. D. E. Kim and N. P. Suh, in Wear of Materials, eds., K. C. Ludema and R. G. Bayer, ASME, New York, (1991)475.

81. M. F. Ashby and S. C. Lim, Scripta Metall., 24(1990)805.

82. S. L. Rice, in Fundamentals of Tribology, eds., N. P. Suh and N. Saka, MIT Press, U.S.A., (1980)469.

83. J. T. Burwell and C. D. Strang, J. Appl. Phys., 23(1952)18.

84. B. Bhushan and B. K. Gupta, Handbook of Tribology, McGraw-Hill, 1991.

85. M. A. Moore, in Fundamentals of Friction and Wear of Materials, ed.,

D. A. Rigney, ASM, Metals Park Ohio, (1980)73.

86. T. O. Mulhearn and L. E. Samuels, wear, 5(1962)478.

87. A. J. Sedriks and T. O. Mulhearn, Wear, 6(1963)457.

88. N. P. Suh, H. C. Sin and N. Saka, in Fundamentals of Tribology, eds., N. P. Suh and N. Saka, MIT Press, U.S.A., (1980)493.

89. E. Rabinowicz, L. A. Dunn and P. G. Russell, Wear, 4(1961)345.

90. N. P. Suh, Tribophysics, Prentice-Hall, New Jersey, 1986.

91. M. M. Kruschov, in Eng. Conf. Lubr. Wear, London, (1957)655.

92. D. G. Teer and R. D. Arnell, in Principles Of Tribology, ed., J. Halling, Macmillan, New York, (1975)102.

93. S. Bian, S. Maj and D. W. Borland, Wear, 166(1993)1.

94. R. C. Richardson, Wear, 11(1968)245.

95. F. P. Bowden and D. Tabor, Friction and Lubrication of Solids, Part I, Clarendon, Press, Oxford, England, 1950.

96. D. Tabor, J. Lubr. Tech., 103(1981)169.

97. E. F. Finkin, Wear, 47(1978)107.

98. T. A. Stolarski, Wear, 171(1994)203.

99. N. P. Suh, Wear, 25(1973)111.

100. S. Jahanmir and N. P. Suh, Wear, 44(1977)17.

101. J. R. Fleming and N. P. Suh, Wear, 44(1977)39.

102. S. Jahanmir, J. W. Dally and Y. M. Chen, in Proc. Japan, Int. Tribo.

Conf., Japanese Society of Tribologists, Nagoya, (1990)581.

103. J. P. Hirth and D. A. Rigney, Wear, 39(1976)133.

104. J. Zhang and A. T. Alpas, Mat. Sci. and Eng., A160(1993)25.

105. P. Heilmann and D. A. Rigney, Wear, 72(1981)195.

106. H. C. Sin, N. Saka and N. P. Suh, Wear, 55(1979)163.

107. N. Alereyev and S. Jahanmir, Wear, 166(1993)41.

108. J. Zhang, F. A. Moslehy and S. L. Rice, in Wear of Materials, eds., K. C. Ludema and R. G. Bayer, ASME, New York, (1991)215.

109. J. Zhang, F. A. Moslehy and S. L. Rice, in Wear of Materials, eds., K. C. Ludema and R. G. Bayer, ASME, New York, (1991)207.

110. M. Hirano and K. Shinjo, in Proc. Japan, Int. Tribo. Conf., Japanese Society of Tribologists, Nagoya, (1990)1207.

111. Y. Tsuchida, Proc. in Japan, Int. Tribo. Conf., Japanese Society of Tribologists, Nagoya, (1990)1219.

112. N. Alexeyev and S. Jahanmir, Wear, 166(1993)49.

113. R. D. Arnell, P. B. Dadis, J. Halling and T. L. Whomes, Tribology: Principles and Design Applications, Macmillan, U.S.A., (1991)43.

114. A. Wang and H. J. Rack, Mat. Sci. and Eng., A147(1991)211.

115. Y. L. Su and J. S. Lin, Wear, 166(1993)27.

116. T. E. Levine, P. Revesz, W. Mayer and E. P. Giannelis in: Thin Films, Stress and Mechanical Properties IV, Mat. Res. Soc. Sym. Proc., eds., P. H.

Townsend, T. P. Weihs and J. E. Sanchez, Pittsburgh, 308(1993)635.

117. P. J. Blau, J of Tribology, 109(1987)537.

118. D. A. Rigney and J. P. Hirth, Wear, 53(1979)345.

119. D. Kuhlmann-Wilsdorf, in Fundamentals of Friction and Wear of Materials, ed., D. A. Rigney, ASM, Metals Park Ohio, (1980)119.

120. N. P. Suh, in Fundamentals of Friction and Wear of Materials, ed., D. A. Rigney, ASM, Metals Park Ohio, (1980)43.

121. J. P. Hirth and D. A. Rigney, in Dislocations in Solids Vol. 6, ed., F. R. Nabarro, North-Holland Publishing, Amsterdam, (1983)10.

122. R. W. K. Honeycomb, The Plastic Deformation of Metals, 2nd eds., Edward Arnold Ltd., U.K., (1984)326.

123. D. R. Wheeler and D. H. Buckley, Wear, 33(1975)65.

124. S. L. Semiatin and J. J. Jonas, in Formability and Workability of Metals: Plastic Instability and Flow Localization, ASM, Metals Park Ohio, (1984)100.

125. J. G. Sevillano, P. V. Houtte and E. Aernoudt, in Progress in Materials Science, 25(1980)69.

126. S. S. Hecker and M. G. Stout, in Deformation, Processing and Structure, eds., G. Krauss, ASM, Metals Park Ohio, (1982)14.

127. V. D. Scott and H. Wilman, Proc. Roy Soc. London, A247(1958)353.

128. J. Goddard, H. J. Hacker and H. Wilman, Proc. Phys. Soc.,

80(1962)77.

129. L. D. Dyer, Acta Metall., 9(1961)928.

130. A. T. Gwathmey and H. Leidheiser and G. P. Smith, Proc. Roy. Soc., A212(1952)464.

131. M. A. Moore and R. M. Douthwaite, Metall. Trans., 7A(1976)1833.

132. D. A. Rigney and W. A. Glaeser, Wear, 46(1978)241.

133. M. A. Moore, R. C. D. Richardson and D. G. Attwood, Metall. Trans., 3(11972)2485.

134. S. M. Kuo and D. A. Rigney, Mat. Sci. and Eng., A157(1992)131.

135. A. H. Cottrell, Theory of Crystal Dislocations, Gordon and Beach, New York, (1964)84.

136. I. M. Hutchings, Tribology: Friction and Wear of Engineering Materials, CRC Press, U.S.A., (1992)102.

137. F. E. Kennedy, The Role of Subsurface Zones in The Wear of Materials, ed., Roman Solecki, Trans. Tech., Switzerland, (1988)35.

138. S. K. Ganapathi and D. A. Rigney, Scripta Metall., 24(1990)1675.

139. H. Hiratuska, A. Enomoto and T. Sasada, eds., K. C. Ludema and R. G. Bayer, ASME, New York, (1991)375.

140. S. Jahanmir, Friction and Wear of Ceramics, Marcel Dekker, (1994)3.

141. P. Gautier and K. Kato, Wear, 162-164(1993)305.

142. S. K. Yick and H. M. Hawthorne, NRC, Institute for Machinery

Research, Technical Report, IMR-T&M-TR003, 1994.

143. E. Vancoille, J. P. Celis and R. Roos, Wear, 165(1993)41.

144. A. Blomberg, M. Olsson and S. Hogmark, Wear, 171(1994)77.

145. V. R. Parameswaran, J. P. Immarigeon and D. R. Nagy, Surface and Coatings Technology, 52(1992)251.

146. D. Chuanxian, R. Zatorski, H. Herman and D. Ott, Thin Solid Films 118(1984)467.

147. D. Diao and K. Kato, Thin Solid Films, 245(1994)104.

148. A. G. Evans and D. B. Marshall, Fundamentals of Friction and Wear of Material, ed., D. A. Rigney, ASM, Metals Park Ohio, (1980)439.

149. J. F. Lin and J. H. Horng, Wear, 171(1994)59.

150. T. Sugita and T. Hasegawa, J. Mat. Sci., 13(1978)1471.

151. B. Lawn and T. R. Wilshaw, J. Mat. Sci., 10(1975)1049.

152. M. V. Swain, Proc. Roy. Soc. London, A366(1979)575.

153. C. Subramanian and K. N. Strafford, Wear, 165(1993)85.

154. A. T. Alpas and J. D. Embury, in Wear of Materials, eds., K. C. Ludema and R. G. Bayer, ASME, New York, (1991)159.

155. A. W. Ruff and D. S. Lashmore, Wear, 151(1991)245.

156. E. L. Courtright and J. W. Patten, Office of Naval Research, Battelle, Pacific Northwest Laboratories, Technical Report, Washington, 1982.

157. S. Norose, K. Suzuki and T. Sasada, The 29th Japan Congress on

Materials Research, (1986)93.

158. S. Norose and T. Sasada, Proc. Japan, Int. Tribo. Conf., Japanese Society of Tribologists, Nagoya, (1990)689.

159. L. G. Korshunov, A. M. Polyakova, N. L. Chernenko and V. M. Umova, Phys. Met. Metall., No. 6, 61(1986)160.

160. M. Miranda-Martinez, R. W. Davidge and F. L. Riley, Wear, 172(1994)41.

161. D. Lewis, E. J. Wheeler and D. O. Northwood, Journal of Educational Modules for Materials Science and Engineering, JEMMSE, (1982)665.

162 W. Rachinger, J. Sci Instr., 25(1948)254.

163. C. N. Wagner and E. N. Aqua, Advanc. X-ray Research Anal., 7(1963)46.

164. T. J. Bell, J. S. Field, and M. V. Swain, Mater. Forum, 17(1993)127.

165. J. Mencik and M. V. Swain, Mater. Forum, 18(1994)227.

166. M. F. Doerner and W. D. Nix, J. Mater. Research, 1[4](1986)601.

167. I. N. Sneddon, Int. J. Eng. Sci., 3(1965)47.

168. N. Savides and T. J. Bell, J. Appl. Phys., 72[7](1992)2791.

169. American Society of Testing and Materials, ASTM Standards, G99, ASTM, Philadelphia, 03.02(1990)387.

170. G. B. Harris, Comm. National Phys. Lab, 43(1952)113.

171. J. Kearns, AEC Report, Westinghouse Atomic Power Division-

Technical Memorandum, WAPD-TM-472, (1965).

172. H. J. Frost and M. F. Ashby, Deformation-Mechanism Maps: The Plasticity and Creep of Metals and Ceramics, Pergamon Press, Oxford, (1982)20,43,98.

173. R. W. Armstrong, H. Chin and A. Ruff, Acta Metall., 43(1995)1037.

174. J. B. Pethica, R. Hutchings and W. C. Oliver, Phill. Mag., 48(1983)593.

175. K. Shinohara, K. Yasuda, M. Yamada and C. Kinoshita, Acta Metall., 42(1994)9309.

176. B. L. Hammond and R. W. Armstrong, Pill. Mag. Lett., 57(1988)41.

177. D. L. Joslin and W. C. Oliver, J. Mater. Res., 5(1990)123.

178. H. E. Boyer, Hardness Testing, ASM International, Metals Park, Ohio, 1987.

179. Materials Handbook, ASM, Vol. 3, Metals Park, Ohio, 1980.

APPENDIX

A. Error Analyses

1. Hardness and Elastic Moduli Measurements

i) The mean hardness and elastic moduli values reported in this dissertation (Tables 4.3 and 4.4) were determined using the relationship

$$X_{mean} = (\sum X_i) / n \qquad A.1$$

where X_i is the ith measurement and n is the total number of measurements taken from each specimen (n=15-20).

ii) The scatter in the measured hardness and elastic moduli around the mean was calculated using

$$S = [(\sum X_i - X_{mean})^2) / (n-1)]^{0.5} \qquad A.2$$

where S is the standard deviation of the data and is entered in Tables 4.3 and 4.4 and in Figures 4.9 and 4.33 as error bars.

iii) Vickers hardness (VH) was determined from the relationship,

$$VH = 1.854\ P_V / d^2_V \qquad \text{A.3}$$

where P_V is the applied load in Kg and d_V is the average length of the diagonals of the hardness impression in mm. The estimated error in the Vickers microhardness measurements can be calculated by the use of Taylor's theorem,

$$U_{VH} = [(U_{PV}\ (\partial VH/\partial P_V))^2 + (U_{dV}\ (\partial VH/\partial d_V))^2]^{0.5} \qquad \text{A.4}$$

where U_{PV} and U_{dV} are the uncertainties in the applied load (P_V) and the diagonal length (d_V), respectively. Differentiating A.3 and substituting in A.4 to obtain

$$U_{VH} = [(U_{PV}\ (1.854 / d^2_V))^2 + (U_{dV}\ (-\ 3.708\ P_V / d^3_V))^2]^{0.5} \qquad \text{A.5}$$

Substituting $U_{PV} = \pm 5\text{x}10^{-5}$ Kg, $U_{dV} = \pm 3\text{x}10^{-3}$ mm, $P_V = \pm 2.5\text{x}10^{-2}$ Kg and $d_V = \pm 8.7\text{x}10^{-3}$ mm (smallest d_V value corresponding to the highest VH of all materials tested, i.e., VH(Al_2O_3)= 612.2±20.4 Kg/mm^2, given in Table 3.1) into A.5, yields an estimated error in Vickers hardness measurements (U_{VH}) of ±20.6 Kg/mm^2 or 0.20 GPa. The predicted error in the Vickers hardness is in agreement with the observed experimental deviation. The U_{VH} represents the largest predicted error in VH which is about 3% ((U_{VH} / VH) . 100%).

Similarly, the predicted error in the UMIS nanoindentaion measurements

(U_{NH}) can be calculated by differentiating equation 3.6 ($H = 0.0408\ P / h_p^2$)

$$U_{NM} = [(U_P\ (0.0408 / h_p^2))^2 + (U_{hp}\ (-\ 0.0816\ P / h_p^3))^2]^{0.5} \qquad \text{A.6}$$

The uncertainties in the load (U_P) and depth of penetration (U_{hp}) are 10^{-4} N and 10^{-9} m, respectively. Using the hardness of TiN film (VH=34.09±0.24 GPa, Table 4.4) as an example since it has the highest hardness of all materials tested using UMIS and, hence, it is expected to have the largest error. Substituting 5×10^{-2} N and 2.44×10^{-7} m for P and h_p (Fig. 4.8(c)), respectively, in A.6, one obtains the largest estimated error in the nanohardness measurements (U_{NM}) of 0.29 GPa (1% error).

2. Coefficient of Friction

i) The scatter in the data around a mean coefficient of friction value was taken as the fluctuation in the coefficient of friction versus sliding distance curves. The scatter in the coefficients of friction were given in Tables 4.5-4.9 and represented by error bars in Figures 5.4 and 5.15.

ii) The estimated error in the coefficient of friction measurements (U_μ) due to errors in the tangential (F_T) and normal (F_N) loads can be predicted using the following equation:

$$U_\mu = [(U_{FT}\,(\partial\mu/\partial F_T))^2 + (U_{FN}\,(\partial\mu/\partial F_N))^2]^{0.5} \qquad \text{A.7}$$

Where U_{FT} and U_{FN} are the uncertainties in the tangential and normal load measurements and are equal to ±2 g. Since the coefficient of friction is given by $\mu = F_T/F_N$ (equation 2.23) the error can be determined by differentiating and arranging equation 2.23 according to equation A.7,

$$U_\mu = [(U_{FT}\,(1 / F_N))^2 + (U_{FN}\,(- F_T\ / F^2_N))^2]^{0.5} \qquad \text{A.8}$$

Substituting a normal load of 100 g (which was used for all tests) and taking F_T to be 134 g (the largest of all measured F_T values which is for the coarse-grained aluminum specimen). Equation A.8 yield an estimated error in the coefficient of friction (U_μ) of ±0.03. Thus, the largest estimated error in the calculations of the coefficient of friction (for $\mu=1.34$) is ±0.03 which is about 2% ((U_μ / μ) . 100%). The maximum estimated error in calculating the coefficient of friction is clearly smaller than any measured coefficient of friction value for all materials and in the order of the experimental standard deviation.

3. Wear Measurements

i) The mean and standard deviation of the volume loss measurements were calculated using equations A.1 and A.2. The standard deviations were entered as error bars around the mean in all the volume loss versus sliding distance curves.

ii) The estimated error in the measurements of the volume loss due to errors in the wear track width (U_d), in the wear track radius (U_R) and in the pin tip radius (U_r) was calculated using an equation similar to equation A.4. The equation used for calculating volume loss (equation 3.9) can be rewritten, for simplicity, as (169)

$$V \approx \pi R d^3 / 6r \qquad \text{A.9}$$

Thus, the estimated error in the volume loss, U_V, is

$$U_V = [(U_R\ (\pi d^3 / 6r))^2 + (U_d\ (\pi R d^2 / 2r))^2 + (U_r\ (- \pi R d^3 / 6r^2))^2]^{0.5} \qquad \text{A.10}$$

The uncertainty in the measurements of d, r and R (all measured using low power optical microscope) were 0.003 mm. The wear track width was taken as 0.962 mm (largest d value, obtained for coarse-grained aluminum), r as 2.15 mm and R as 3 mm. Thus, the largest error in calculating the volume loss, U_V, becomes $\pm 6.186 \times 10^{-3}$ mm^3, i.e., about 1% error ((U_V/V) . 100%, where V=0.659 mm^3). The experimental standard divination (±0.02) is higher than the estimated error mainly due to the irregularities in the edges of the wear track encountered when measuring the track width.

iii) The wear rates (Tables 4.5-4.9) were calculated from the slope of the volume loss versus sliding distance curves using the least-square-fit method. Equations for the intercept (A) and slope (B) of the best fit line are given below

$$A = [(\sum Y \,.\, \sum X^2) - (\sum XY \,.\, \sum X)] \,/\, [n \sum Y^2 - (\sum X)^2] \tag{A.11}$$

and

$$B = [n \sum XY - \sum X \,.\, \sum Y] \,/\, [n \sum X^2 - (\sum X)^2] \tag{A.12}$$

The standard deviation in both the intercept and the slope were calculated, respectively, as

$$S_A = S^2_Y \,.\, (\sum X^2) \,/\, [n \sum X^2 - (\sum X)^2] \tag{A.13}$$

and

$$S_B = n\, S^2_Y \,/\, [n \sum X^2 - (\sum X)^2] \tag{A.14}$$

where

$$S_Y = [(1 / n-1) \, . \, (\sum (A + BX - Y)^2]^{0.5} \qquad \text{A.15}$$

The wear rates and their standard deviation calculated using this method are given in Tables 4.5-4.9. Equations A.11 to A.15 were also used to obtain equations 5.3, 5.4 and 5.6-5.9.

B. Comments on Low load indentation

A phenomenon associated with low load indentation testing (using pointed indenters such as Berkovich and Vickers) is that the hardness shows a strong increase above that obtained from higher load measurements of the same bulk material. Armstrong et al (173) observed about a 30 times increase in the hardness of copper when using loads as low as 0.3 g. Pethica et al (174) examined the hardness of Si, Au and Ni at loads as low as 5 g and found a 3-4 folds increase in hardness when compared to conventional hardness tests using a load of 30 Kg. Others (90,175) reported similar increases in the hardness of Cu, Al and Ni at low loads.

Various reasons have been offered for the observed hardness increase at low loads (90,165,173-177). Such reasons include the effect of a thin hard oxide surface layer, surface roughness, dislocations/free surface interactions and bluntness of the indenter tip. However a principal factor that contributed to the observed hardness increase was proposed by Armstrong et al (173). They suggested that because the pointed indenters (Berkovich and Vickers) are not ideally sharp but have a rounded blunt tips, at low loads, the elastic strain would be large compared the plastic strain as opposed to conventional hardness tests using high loads (the plastic strain would be much larger than the elastic strain). In other words, at low loads deformation is mainly elastic and upon unloading the residual plastic depth of penetration (h_p) is very small (vanishes with decreasing load) resulting in high hardness values according to equation 3.6 ($H=P / kh_p^2$).

Hardness results reported in this dissertation were consistently performed using low loads (2-10 g) using either an ultra-microhardness system or Vickers microhardness tester. These tests produced hardness values that were higher than expected from conventional hardness testers using loads in the 100-3000 Kg range and from full tensile tests. For example, the AISI 304 stainless steel hardness was measured by nanohardness (Fig. B.1), Vickers microhardness and Rockwell testers using different loads and compared to published data using conventional methods. These results are given in Table B.1. Table B.1 showed that at low loads (5-10 g) using either Berkovich or Vickers indenters the hardness was about 4.6 GPa which was about 3 times the published hardness using a Rockwell hardness tester with 100 Kg load or a tensile test.

The Vickers hardness dropped down to a value of 2.2 GPa when applying a 1 Kg load and then reduced further when tested under a 100 Kg load using a Rockwell tester. The Rockwell test performed on AISI 304 pin produced a hardness value that was similar to that published in the literature using conventional hardness measurements (high loads).

Table B.1. Hardness of AISI 304 stainless steel pin at various loads.

Test	Load (g)	H (GPa)	Indenter	Comments
Ultra-microhardness	5	4.7	Berkovich (diamond)	Measured
Microhardness	10	4.5	Vickers (diamond)	Measured
Microhardness	1000	2.2	Vickers (diamond)	Measured
Rockwell (B)	100,000	89 HRB*	1/16 " ball (stainless steel)	Measured
Vickers	100,000	1.8	Vickers (diamond)	Converted from '*' using charts (ref. 178)
Rockwell (B)	100,000	88 HRB**	1/16 " ball (stainless steel)	Taken from ref. 179
Vickers	100,000	1.7	Vickers (diamond)	Converted from '**'using charts (ref.178)
Tensile test	0.2 % yield strength	0.530	------------	Taken from ref. 179.

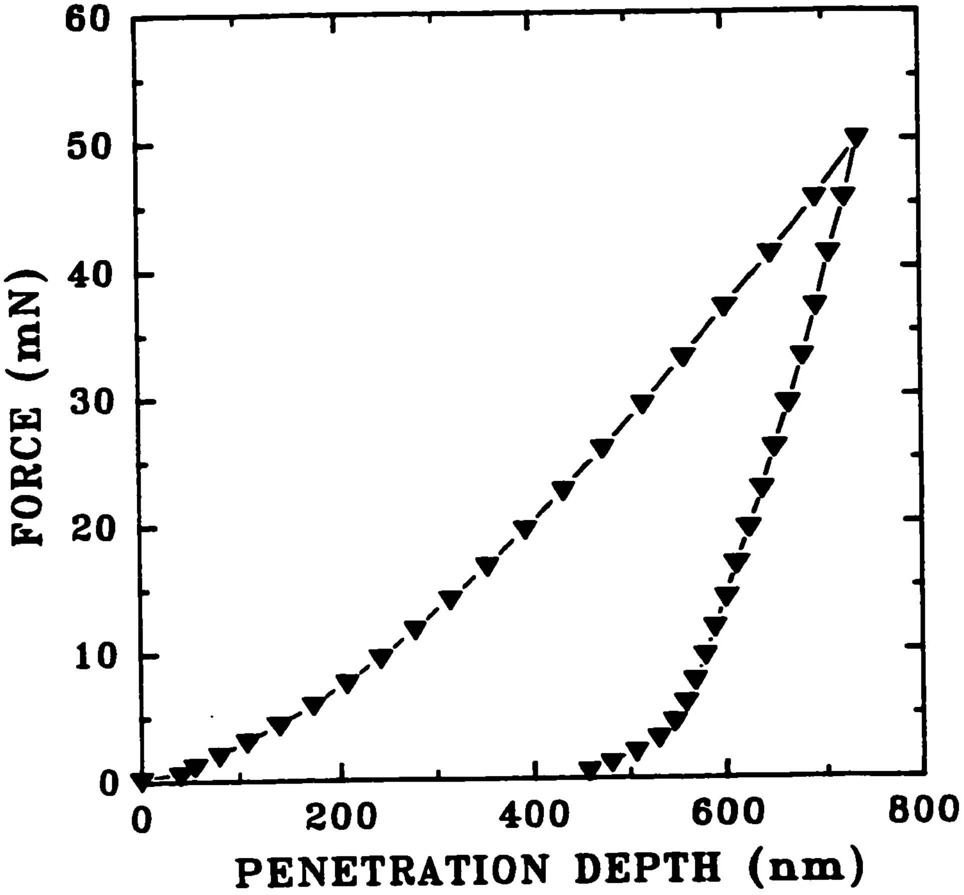

B.1. Force/depth of penetration curve for the AISI 304 stainless steel pin.

C. Total Film Thicknesses versus Penetration Depths

The penetration depth of the sliding pin into the coating was monitored by two methods:

i) Calculating the depth of penetration based on the maximum wear track width (at about 100 m sliding distance) and sliding pin tip geometry and dimensions. It can be shown that the maximum depth of penetration estimated from the consideration of the contact geometry follows equation C.1.

$$\text{depth (max)} = r - (r^2 - (d_{TW}(\text{max}) / 2)^2)^{0.5} \qquad \text{C.1}$$

where depth (max) is the maximum depth reached (near the end of the wear test); r is the pin tip radius; d_{TW}(max) is the maximum track width, i.e., at the maximum sliding distance (~100 m). Table C.1 gives the total film thicknesses and the maximum depth of penetration for the coatings. It should be mentioned that the pin tip radius was purposely machined to a radius of 2.15 mm in order to prevent penetration of the coating by maintaining a relatively flat curvature.

ii) A more reliable method that used to insure that the coatings were not penetrated trough during sliding was by SEM observations of the worn surface at the maximum sliding distance (at end of test). For example, Figure C.1 shows the wear track of monolithic aluminum film (D=98 nm) at a 200 m sliding distance. The micrograph reveals that the film is starting to break exposing the substrate beneath. This film was the softest of all films and, according to table C.1, undergoes the largest depth of penetration. The calculated maximum depth of penetration predicted that the film would be penetrated through at a sliding distance of 100 m. However, SEM observation showed that the film integrity was maintained up to a sliding distance of about 200 m (i.e., double the maximum sliding distance). Equation B.1 overestimates the maximum depth of penetration because of the coatings elastic recovery effect. This effect made the wear track curvature actually larger than the pin curvature upon unloading. Subsequently, the wear track would be shallower than what was predicted by equation C.1.

Based on calculations and SEM observations the pin was always maintained sliding on the coating (throughout the wear test) rather than the substrate.

Table C.1. Total film thicknesses and corresponding maximum depths of penetration.

Material	Total film thickness (μm)	Maximum wear track width (μm)*	Maximum depth (μm)**
Al (D=16.4 nm)	15	389	8.8
Al (D=43.1 nm)	15	441	11.3
Al (D=98.0 nm)	15	513	15.4
Al(200nm)/Al_2O_3	15	363	7.7
Al(500nm)/Al_2O_3	15	376	8.2
TiN	10	115	0.8
Ti(150nm)/TiN	10	128	1.0
Ti(450nm)/TiN	10	137	1.1
Ti (D=30 nm)	10	148	1.3
Ti(150nm)/Cu	10	306	5.5

* Track width near end of test (~100 m sliding distance).

** Calculated using equation C.1.

C.1. SEM micrograph of the worn surface of annealed monolithic aluminum film (D=98 nm) at 200 m sliding distance. The Al film is wearing out and is starting to break exposing the substrate beneath.

Publications\Presentations Derived From This Work

Publications:

1) Z. N. Farhat, Y. Ding, D. O. Northwood and A. T. Alpas, ***The Effect of Grain Size on The Friction and Wear of Nanocrystalline Aluminum***, Material Science and Engineering, A206, 1996, p. 203.

2) Z. N. Farhat, Y. Ding, D. O. Northwood and A. T. Alpas, ***Nanoindentation and Friction studies on Ti-Based Nanolaminated Composite Films***, accepted to Surface Coatings Technology, 1996, in press.

3) Z. N. Farhat, A. T. Alpas and D. O. Northwood, ***Contribution of Crystallographic Texturing to the Friction and Wear Behaviour of FCC and HCP Metals***, submitted to Materials Characterization, 1996.

4) Z. N. Farhat, Y. Ding, A. T. Alpas and D. O. Northwood, ***The Processing and Testing of new and advanced Materials for Wear Resistant Coatings***, submitted to the Journal of Materials Processing Technology, 1996.

5) Z. N. Farhat, A. T. Alpas and D. O. Northwood, ***Application of X-ray Diffraction Techniques to the Understanding of Dry Sliding Wear Behaviour of Aluminum and Titanium***, Proceedings of The Asian Conference on X-ray and Related Techniques in Research and Industry (ACXRI 96), eds., B. Suraj, A. Zainal, J. Zul Azhar, Malaysia, 1996, p. 86.

6) Y. Ding, Z. Farhat, D. O. Northwood and A. T. Alpas, ***Mechanical Properties and Tribological Behaviour of Nanolayered Al/Al_2O_3 and Ti/TiN Composites***,

Surface Coatings Technology, 68/69, 1994, p. 459

7) Y. Ding, Z. Farhat, D. O. Northwood and A. T. Alpas, ***Tribological Properties of microlaminated Al/Al$_2$O$_3$ composites***, New Horizons for Materials, ed., P. Vincenzini, Florence, 4, 1995, p. 353.

8) Y. Ding, Z. Farhat, D. O. Northwood and A. T. Alpas, ***The Preparation, Mechanical properties and Wear Behaviour of Monolithic TiN and Microlaminated Ti/TiN Surface Coatings***, Proceedings of The International Conference on Surface Science and Engineering, ed., Z. Rizhang, Beijing, China, 1995, p. 494.

9) Z. N. Farhat and A. T. Alpas, ***Tribological Behaviour of Nanocrystalline Aluminum***, Technical Report submitted to Liburdi Engineering, Hamilton, Ontario, 1993, 18 pages.

10) Z. N. Farhat, Y. Ding, D. O. Northwood and A. T. Alpas, ***Nanoindentation and Dry Sliding Friction Tests on TiN Coatings Produced by Reactive Ion Plating***, Technical Report submitted to Liburdi Engineering, Hamilton, Ontario, 1994, 13 pages.

11) ***Development of Microlaminate Composites for Wear Resistant Coatings***, Final Report on a Strategic Grant Project, submitted to The Natural Science and Engineering Research Council of Canada (NSERC), 1995, 10 pages.

Oral Presentations

12) Z. Farhat, Y. Ding, D. O. Northwood and A. T. Alpas, ***Preparation and***

Mechanical Properties of Microlaminated Al/Al$_2$O$_3$ Composites for Tribological Applications by RF Sputtering, presented at the 5th Canadian Materials Science Conference, Kingston, Ontario, Canada, 1993.

13) Y. Ding, Z. Farhat, D. O. Northwood and A. T. Alpas, ***Microstructure and Mechanical Properties of Nanocrystalline Laminates Al/Al$_2$O$_3$***, presented at Interfaces II, Australia, 1993.

VITA AUCTORIS

Name	Zoheir N. Farhat.
Birth	September 27th, 1962, Tripoli, Libya.
Education	B.A.Sc. (1989), Engineering Materials, University of Windsor.
	M.A.Sc. (1991), Engineering Materials, University of Windsor.
	Ph.D. (1996), Engineering Materials, University of Windsor.

IMAGE EVALUATION
TEST TARGET (QA-3)

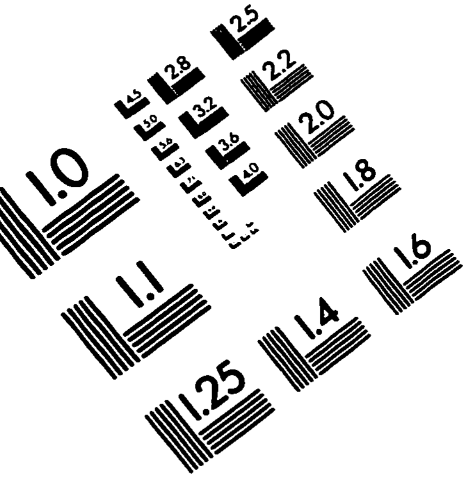
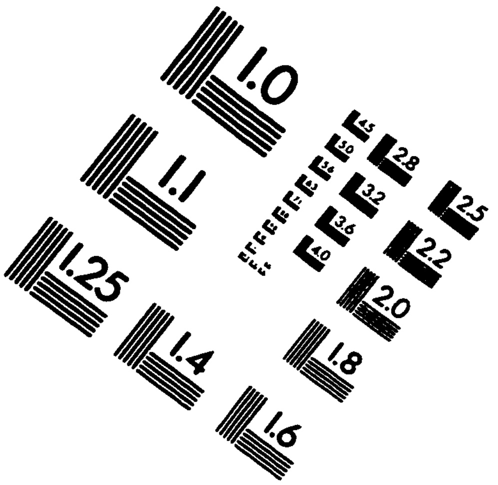
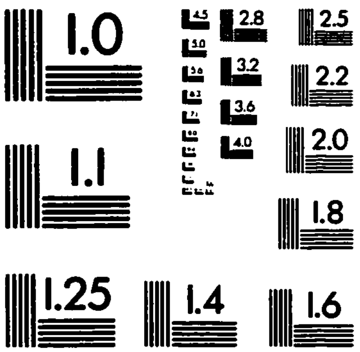

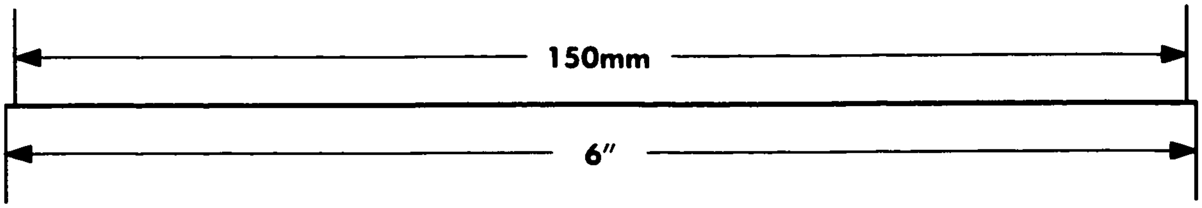

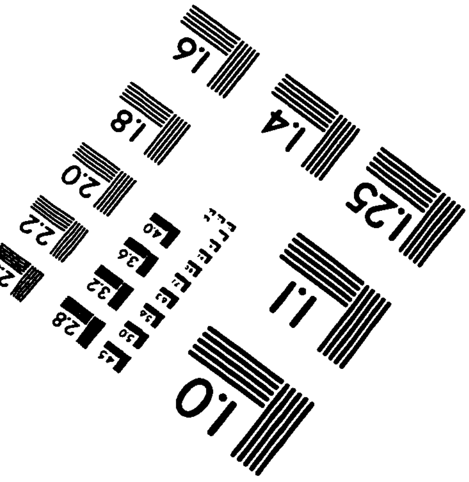

APPLIED IMAGE . Inc
1653 East Main Street
Rochester, NY 14609 USA
Phone: 716/482-0300
Fax: 716/288-5989